Spring 2019

Emergent Properties and Applications of Self-Assembled Benzophenone-Containing Materials

Baillie A. DeHaven

Recommended Citation

DeHaven, B. A.(2019). *Emergent Properties and Applications of Self- Assembled Benzophenone-Containing Materials.* (Doctoral dissertation). Retrieved from https://scholarcommons.sc.edu/etd/5119

EMERGENT PROPERTIES AND APPLICATIONS OF SELF-ASSEMBLED BENZOPHENONE-CONTAINING MATERIALS

by

Baillie A. DeHaven

Bachelor of Arts
University of West Florida, 2014

Submitted in Partial Fulfillment of the Requirements

For the Degree of Doctor of Philosophy in

Chemistry

College of Arts and Sciences

University of South Carolina

2019

Accepted by:

Linda S. Shimizu, Major Professor

Sheryl Wiskur, Chair, Examining Committee

Hans-Conrad zur Loye, Committee Member

Peisheng Xu, Committee Member

Cheryl L. Addy, Vice Provost and Dean of the Graduate School

DEDICATION

This work is dedicated to my Nan, who encouraged a young and confused community college student to keep on learning. Love you Lots.

ACKNOWLEDGEMENTS

First and foremost I would like to thank Professor Linda Shimizu for her unwavering support. She pushed me to be the best scientist that I can be, and was the best mentor I could have ever asked for. You put your students first and for that I am truly one of the lucky graduate students. I am looking forward to working together in the future.

Next, I would like to acknowledge my family. My incredible boyfriend, Chris Smith, has been through this journey with me every step of the way. He has been there for every up and down on this journey. I cannot wait to spend more time with you and less time worrying about what I'm forgetting about. I would like to think my Dad, Ron DeHaven, for calling me Dr. Baillie since I was 5 years old – it may not be the doctorate you had in mind but I know you are just as proud. I would also like to thank my Mom; we literally talked almost every day after work and those conversations kept me sane. You all were my motivation.

Now for the Shimizu group. It all started with Arthur Korous and Dr. Sahan Salpage, thank you both for being fantastic mentors and all around people. Ammon and Dustin, you both have become like lab brothers to me and I will really miss our lunches and good times. I would also like to acknowledge my undergrad army, especially Anna Chen, Craig Conklin, Emily Shimizu, Emily Souza, and Jack Orlandi. Finally, I want to thank Kayla Lantz, I am truly thankful for all the margaritas and nachos; I literally could not have done this without you.

ABSTRACT

Supramolecular assembly of benzophenone through urea hydrogen bonding interactions facilitates the formation of remarkably persistent triplet radical pairs upon UV-irradiation at room temperature, whereas no radicals are observed in solution. The generation of organic radicals is correlated to the microenvironment around the benzophenone carbonyl, the types of proximal hydrogens, and the rigid supramolecular network. High-Field EPR and variable temperature X-band EPR accompanied by simulations suggest a resonance stabilized radical pair through hydrogen abstraction. Previous work has shown that UV-irradiation of self-assembled benzophenone *bis*-urea host results in low quantities of radical pairs that can be used to enhance NMR signals by a factor of 4 for both the host and the encapsulated guest using a dynamic nuclear polarization (DNP) technique. This result suggests that even low levels of endogenous radicals can facilitate the study of host-guest relationships in the solid-state.[2] Additionally, the photochemical formation of reactive oxygen species (ROS) by the host was examined, which was found to generate both superoxide and singlet oxygen in similar quantities. The host was then applied as a nanoreactor to mediate photooxidations of 1-methyl-1-cyclohexene while suspended in solution and as a solvent free host:guest complex.

TABLE OF CONTENTS

LIST OF TABLES

LIST OF FIGURES

CHAPTER 1

ENHANCING THE STABILITY OF PHOTOGENERATED BENZOPHENONE TRIPLET RADICAL PAIRS THROUGH SUPRAMOLECULAR ASSEMBLY*

---

* DeHaven, B. A.; Goodlet, D. W.; Sindt, A. J.; Noll, N.; De Vetta, M.; Smith, M. D.; Martin, C. R.; Gonzalez, L.; Shimizu, L. S. *J. Am. Chem. Soc.* **2018**, *140*, 13064-13070. Reprinted here with permission of publisher.

1.0 ABSTRACT

Supramolecular assembly of urea-tethered benzophenone molecules results in the formation of remarkably persistent triplet radical pairs upon UV-irradiation at room temperature, whereas no radicals were observed in solution. The factors that lead to emergent organic radicals are correlated with the microenvironment around the benzophenone carbonyl, types of proximal hydrogens, and the rigid supramolecular network. The absorption spectra of the linear analogs were rationalized using time dependent density functional theory calculations on the crystal structure and in DMSO employing an implicit solvation model to describe structural and electronic solvent effects. Inspection of the natural transition orbitals for the more important excitation bands of the absorption spectra indicates that crystallization of the benzophenone containing molecules should present a stark contrast in photophysical properties versus solution, which was indeed reflected by their quantum efficiencies upon solid-state assembly. Persistent organic radicals have prospective applications ranging from OLED technology to NMR polarizing agents.

1.1 INTRODUCTION

The supramolecular assembly of small molecules through non-covalent interactions is proving to be a convenient approach in the design of hierarchical materials.[1-3] Controlled organization of discrete functional groups can enhance chemical and physical properties. For example, the solid-state assembly of perylene bisimide dyes to form transistors with n-type charge transport properties[4,5] and π-conjugated materials that exhibit enhanced luminescence.[6,7] Thus, further insight into how structure influences physical function is of great importance for the design of synergistic materials with properties tailored to specific applications. Here, we compare the impact solid-state assembly has on the photophysics of three benzophenone (BP) containing molecules. We report that organization of BP units within distinct solid-state environments quenches the lifetime and modulates the quantum yield of phosphorescence. Moreover, remarkably persistent radicals are generated upon UV-irradiation at room temperature. The quantity and stability of these radicals vary with the chemical environment that surrounds the key carbonyl unit (Figure 1.1). Thus, control over solid-state assembly of BP molecules can alter photophysical properties and lead to the generation of persistent radical pairs with potential applications ranging from OLED technology to NMR polarizing agents.[8-10]

Benzophenone, a prominent photosensitizer was first reported to generate organic ketyl radicals in 1891.[11] Although inherent high reactivity makes electron paramagnetic resonance (EPR) characterizations difficult as they are known to dimerize in solution forming benzopinacol.[12] Radicals generated by BP in solution are unstable and are typically only observed using EPR at low temperatures or through one-electron reduction to form the radical anion.[13,14] Previously, we reported a *bis*-urea macrocycle (**1**) that contains two BP units, which assembles into hexagonally packed columnar structures via robust urea hydrogen-bonding interactions.[15]

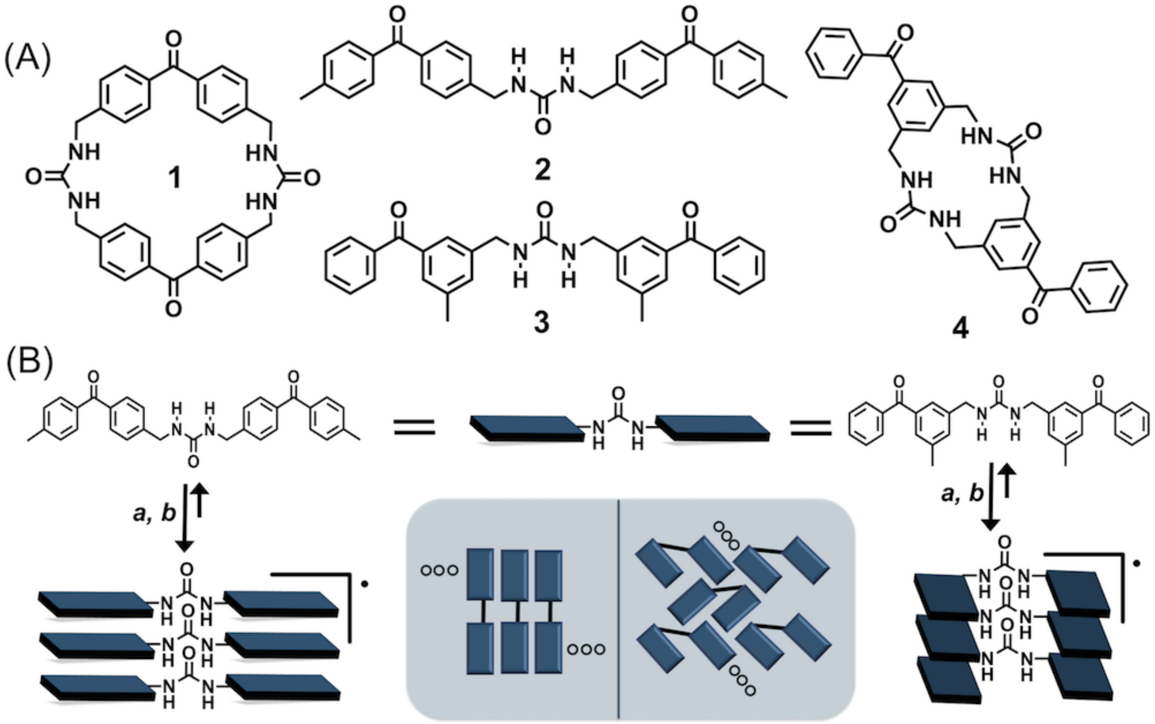

Figure 1.1. Self-assembly modulates the photophysics of BP derivatives and gives rise to emergent organic radicals. (A) Structures of urea-based BP containing macrocycles and linear analogs, **1**-**4**. (B) Monomers **2** and **3**, presented as planar for simplicity, assemble through hydrogen bonding interactions. UV-irradiation gives rise to persistent radicals as an emergent property. *Reagents and conditions: a. crystallization; b. UV-irradiation* (360 nm, rt, under N_2). Inset: top down assembly motif of the BP sensitizer in each crystal structure, **2** (left) and **3** (right).

Preorganization of the sensitizer impacted its photophysical properties by dramatically decreasing the quantum yield and lifetime.[16] Most intriguingly, UV-irradiation of this crystalline solid gave rise to organic radicals that persisted for weeks at room temperature when stored in the dark.[10] High-field and variable temperature X-band EPR studies accompanied by simulations suggested that UV irradiation of the crystals results in a resonance stabilized radical pair through hydrogen abstraction.[10] Our hypothesis is that BP in the excited state abstracts a hydrogen atom from a nearby molecule to form ketyl containing radical pairs.

Herein, we examine the chemical and photophysical properties of self-organized structures of BP-containing linear analogs and macrocycles (Figure 1.1A). Macrocycles **1** and **4** vary the position of BP within the cyclic framework to probe how orientation of the chromophore influences its crystalline packing. Linear analogs, **2** and **3**, are comprised of two BP molecules covalently tethered through a single methylene urea group and assemble through urea hydrogen-bonding interactions. The positions of the methyl substituents, *meta* or *para* with respect to the BP carbonyl, were varied across two different structures in order to explore their influence on crystal packing as well as determine the types of H-abstraction sites near carbonyl oxygen. Our goal is to examine how orientation of the BP sensitizer, as well as its relative position with respect to H-abstraction sites, impacts subsequent photophysical properties and if these assembled benzophenone also display the ability to form persistent radicals upon UV irradiation or if this emergent property is a function of the assembled macrocycles.

1.2 RESULTS AND DISCUSSION

The macrocycles and linear counterparts were synthesized in three to four steps using a simple alkylation of a protected urea (triazinanone) as the key step.[16] Protected analog **2** and macrocycle **4** were structurally characterized (see experimental). Colorless solvent-free crystals of **2** and **3** were obtained by recrystallization. Unfortunately, attempts to crystallize **4** through slow cooling, vapour diffusion, and microcrystallization techniques did not yield single crystals. We are currently screening a wide range of crystallization techniques including conditions with potential co-crystal formers.

Crystals of **2** were obtained as transparent plates through slow cooling in a hot acetic acid solution (120 °C, 6 mg/mL). The sample crystallized in the triclinic system in the acentric space group P1 (No. 1). The conformation of **2** is linear with the two BP units outstretched on both sides of the urea tether (Figure 1.2A). The two BP carbonyl groups of the monomer are aligned anti-parallel, likely to minimize the dipole moment.

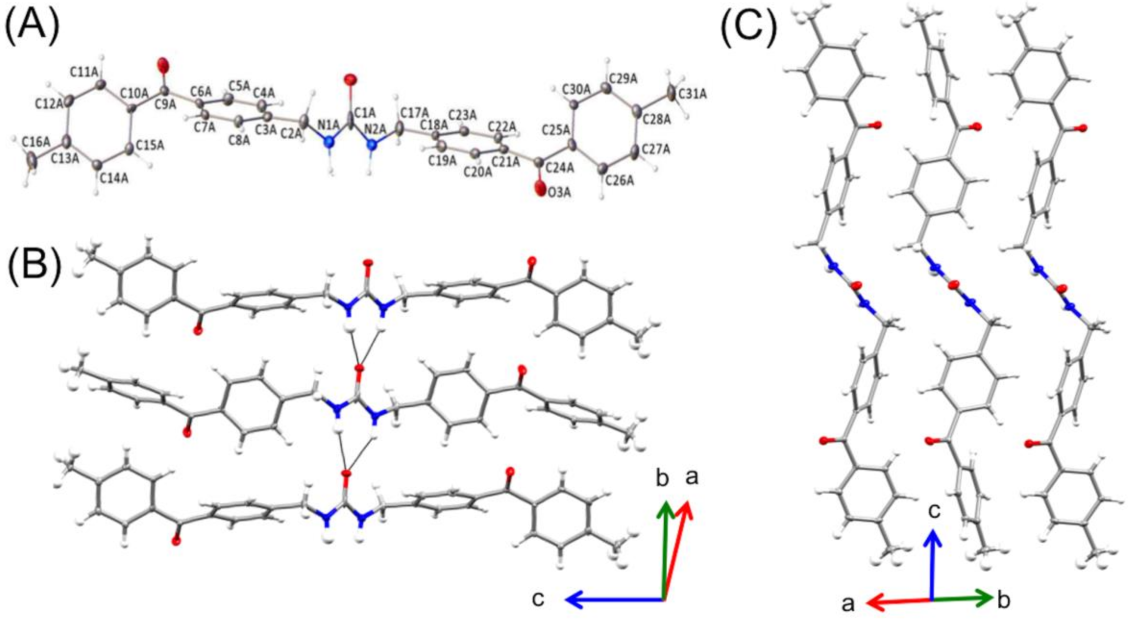

Figure 1.2. Single crystal X-ray diffraction (SC-XRD) of linear analog **2**, which crystallizes through slow cooling in acetic acid in the triclinic system as transparent platelets. (A) Thermal ellipsoid plot. (B) View of the urea hydrogen-bond interactions that stack BP units on top of each other and orient the aryl rings in an edge-to-face motif down the urea tape. (C) Top down view of the urea groups showing that the edge-to-face aryl packing pattern is maintained between neighboring BP units in two directions

Bifurcated urea hydrogen-bond interactions guide the assembly of **2** with N-H···O distances ranging from 2.873(2)-2.968(2) Å (Figure 1.2B & C). The BP sensitizer is ordered down the *ab* crystallographic plane resulting in a lamellar packing motif with aryl groups organized in an edge-to-face pattern and $C_g \cdots C_g$ distances (C_g = ring centroid) ranging from 4.601(2)-4.825(2) Å. The $C\text{-}H \cdots C_g$ distances vary from 3.419(4)-3.637(3) Å with angles ranging from 127-135°. The BP carbonyl oxygens reside in close proximity to aryl protons on closely packed molecules of **2** with C=O···H distances as close as 2.60 Å.

Slow evaporation of **3** in dichloromethane (1 mg/1.6 mL) resulted in the formation of transparent needle-like crystals in the monoclinic system in the acentric $P2_1$ space group. The profile of **3** is distinct, conforming to a C-shape with both BP components oriented in close proximity and $C_g \cdots C_g$ distances of 8.94 Å between alkyl substituted aryl groups (Figure 1.3). The two BP carbonyls of **3** are oriented in the same direction, although the carbonyls on neighboring molecules are opposing in direction. Predictable bifurcated urea-urea hydrogen bonding interactions stack the sensitizer down the *a*-axis with N-H···O distances ranging from 2.800(6)-2.809(6) Å, Figure 1.3A. This assembly orients the BP units in a herringbone pattern along the *b*-axis, while the aryl rings are parallel displaced down the *a*-axis with a distance of 4.511(3) Å from centroid to centroid. The carbonyl oxygens reside in close proximity to benzyl and aryl protons on proximal

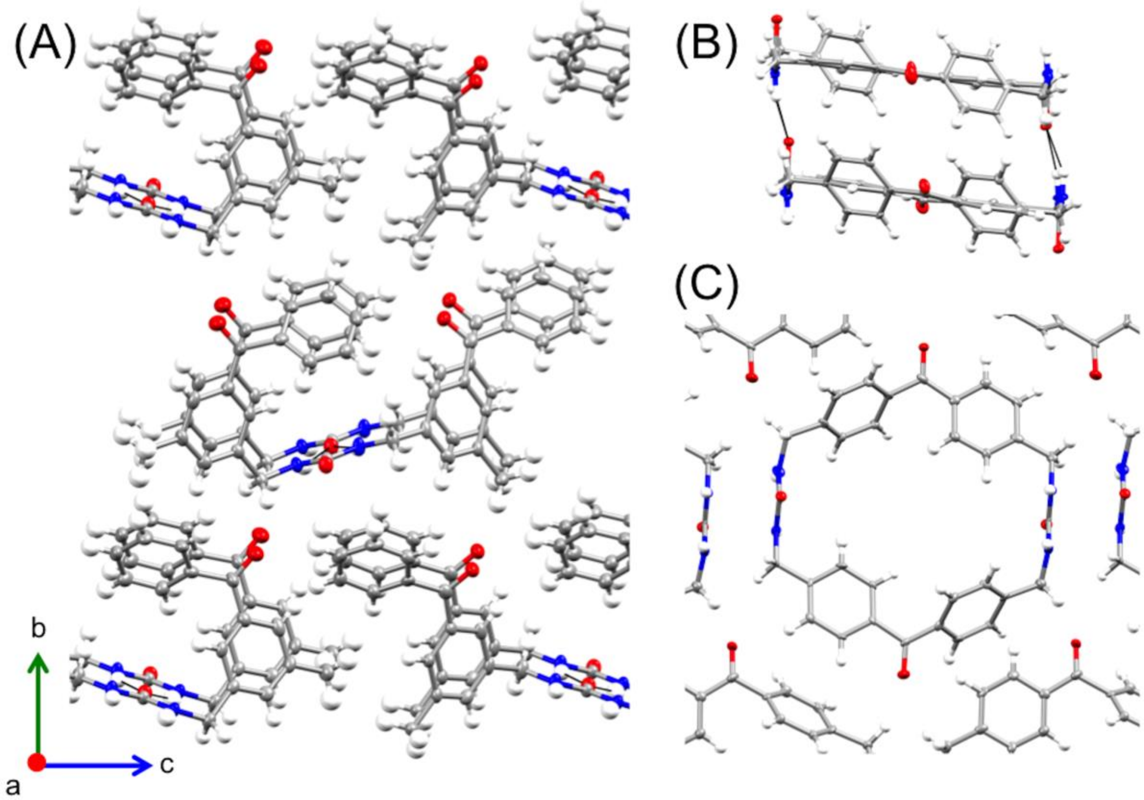

Figure 1.3. SC-XRD analysis of analogue **3** and macrocycle **1**. (A) Slow evaporation of **3** forms transparent needle-like crystals in the monoclinic system with BP units assembled in a herringbone pattern along the *b*-axis. The aryl rings are parallel displaced down the *a*-axis. (B) Macrocycle **1** crystallizes in the monoclinic system as needle-like crystals with BP units stacked down the *a*-axis resulting in edge-to-face aryl packing down the column. (C) The columns pack hexagonally staggering BP units across the *c*-axis.

molecules of **3** with C=O···H distances of 2.60 Å to methyl hydrogens, 2.88 Å to methylene protons, and 2.64 Å to aryl hydrogens.

In comparison, previously reported **1** crystallizes as transparent needle-like crystals in the monoclinic system in the $P2_1$ space group by slow-cooling a hot DMSO solution from 120 °C.[15] The two BP carbonyl carbons of the monomer are 10.2 Å apart and orient the carbonyl oxygens pointing outward towards the exterior of the macrocycle. Urea-urea hydrogen-bond interactions drive assembly stacking the BP molecules down the *a*-axis aligning the aryl rings in an edge-to-face motif with $C\text{-}H\cdots C_g$ distances ranging from 3.559(6)-3.597(7) Å and angles from 124-130° (Figure 1.3B). The columns encapsulate disordered DMSO molecules. The macrocycles are hexagonally packed and the BP units are staggered like brickwork along the *c*-axis.[15] The BP carbonyl oxygens are in close proximity to neighbouring methylene and aryl hydrogens with $C{=}O\cdots H$ distances of 2.41 Å and 2.68 Å, respectively (Figure 1.3C).

To probe how crystal packing of BP units impacts the overall photophysics, we measured the absorption, emission, lifetime, and quantum yield for each sample in the solid-state and in argon-purged solutions of DMSO.[‡,16] Table 1 compares these measurements with unsubstituted BP and **1**. For both linear analogs and macrocycles, the absorption spectra in solution maintained

Table 1.1. Measured photophysical properties of BP and the BP-urea molecules in DMSO solution compared to the solid-state.

PHOTOPHYSICAL PROPERTIES		**1**	**2**	**3**	**4**	**BP**
ε ($M^{-1}cm^{-1}$)		622[a]	449	317	297	342[a]
λ_{max}, Abs (nm)	Solution	ππ*, 270[a] nπ*, 345[a]	ππ*, 260 nπ*, 335	ππ*, 256 nπ*, 340	ππ*, 265 nπ*, 340	ππ*, 270[a] nπ*, 345[a]
	Crystals	ππ*, 355[a]	ππ*, 382	ππ*, 374	--	ππ*, 381
λ_{max}, Em (nm)	Solution	435[a]	474	465	502	435[a]
	Crystals	489[a]	528	526	--	450[a]
τ (ns)	Solution	--	1.5	2.0	1.5	--
	Crystals	0.32[a]	0.94	1.3	--	23,000[a]
φ (%)	Solution	--	<0.3	<0.3	<0.3	--
	Crystals	<0.1[a]	5.0	<0.3	--	0.5[a]

[a] Values obtained from reference 16.

the major spectroscopic properties of BP, with a strong ππ* band ranging from 256-270 nm and a weak spin forbidden nπ* transition from 335-345 nm. The molar absorptivity for these compounds range from 297-622 M^{-1} cm^{-1} with the *para*-substituted compounds exhibiting values higher than unsubstituted BP and the *meta*-substituted values being lower (Figure 1.30 - 1.32). In comparison, solid-state assembly of **1**-**3** induces an overall bathochromic shift in the spectrum λ_{max} = 355-382 nm, with broadening in the UV/vis region. This red shift is similar to what is observed upon formation of J-aggregates with dyes;[17] although this is not a perfect analogy as the BP chromophore is not planar.

The absorption properties of **2** and **3** were examined through time dependent density functional theory (TD-DFT) calculations to characterize the excited states of these molecules. This was done by calculating the absorption spectra of **2** and **3** using the crystal structures in the gas phase and an optimized geometry with the polarized continuum model (PCM)[18] in DMSO. The excited states were calculated at the ωB97XD[19]/6-31+G**[20] level of theory. More computational details are given in the SI. During optimization of **2**, the average dihedral angle between the two rings of the BP unit shifted from 26.9° to 31.3° (Figure 1.41). Additionally, the benzenes directly connected to the urea spacers move from being in plane with each other and roughly perpendicular to the urea unit to a more contorted structure. Nevertheless, the spectrum calculated with implicit solvation in DMSO shows good agreement with the experimental being only slightly blue-shifted (5 nm) with respect to the main absorption peak raised by ππ* transitions. The computations also find the dark nπ* transition as the lowest excited state. In comparison, the spectrum of **2** calculated for the crystal structure in the gas phase is shifted by 119 nm to higher energies with respect to the experimental solid-state spectrum (Figure 1.4A). Even though the excitation energies differ, the shape of the experimental spectra is reproducible and allows for the assignment of the lower energy absorption peaks to their corresponding electronic excitations. Similarly, the computed absorption spectra for **3** using the crystal structure geometry in the gas phase gave roughly the same shape with two intense absorption bands raised by the ππ* transitions (Figure 1.4B). Similar to **2**, this spectrum was blue-shifted by 135 nm compared to the experiment. As seen before, the nπ* transition was found as the lowest excited state. The calculated spectrum for the structure optimized in solution was again only slightly shifted in comparison to the experiment (4 nm).

As seen in Figure 1.4C and D there is a stark contrast between the occupied natural transition orbitals (NTOs) for **2** and **3**. In solution, the occupied NTO of **2** covers the entire BP unit including both benzene rings, while the corresponding occupied NTO in gas phase with the crystal structure geometry, shows contributions from only one of the BP benzene rings. Moreover, many of the NTOs contributing to the finer structure for the gas phase spectrum show the electron density localized on only one of

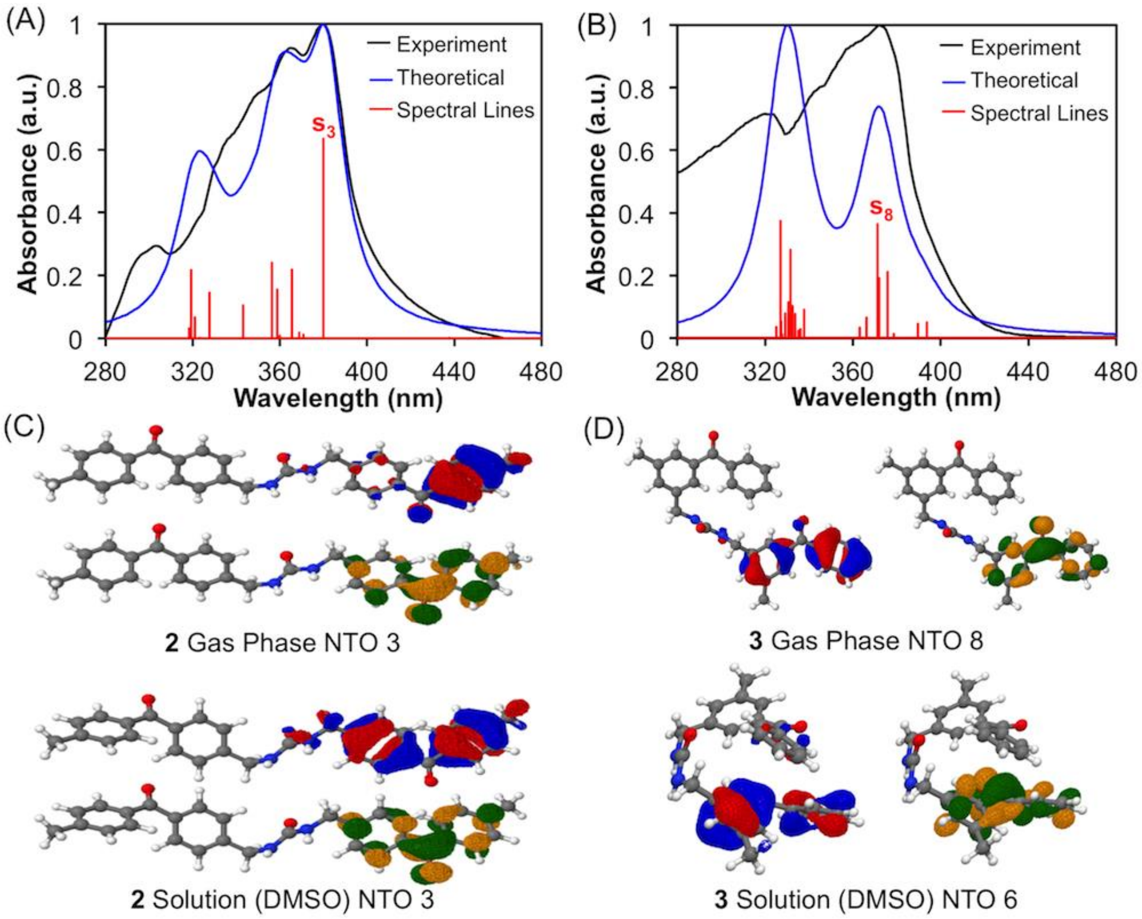

2 Gas Phase NTO 3

3 Gas Phase NTO 8

2 Solution (DMSO) NTO 3

3 Solution (DMSO) NTO 6

Figure 1.4. The excited states of **2** and **3** were characterized using TD-DFT calculations. The normalized experimental solid-state absorption spectra of (A) **2** and (B) **3** are compared to their calculated spectra in the gas phase including the corresponding spectral lines; the numbers indicate the electronic excited state. NTOs for the main transitions of (C) **2** and (D) **3** in gas phase compared to solution, where red/blue = occupied orbital and yellow/green = virtual orbital.

the two aromatic rings of the BP units (Figure 1.37). In comparison, **3** shows little difference in the electron density distribution moving from gas phase to solution. In both cases for **3**, the occupied NTO covers the entire BP unit. These calculations suggest that **2** should present a stark contrast in its photophysical properties when in the solid-state versus in solution, while we do not expect strong media effects for **3**.

The emission spectra recorded in solution (DMSO, 0.9 - 1.0 mM) exhibited transitions ranging from 435-502 nm and displayed an overall red shift upon solid-state assembly, λ_{em} = 450-528 nm. The phosphorescence lifetime of **2** and **4** in solution (DMSO, 0.9 mM) were the shortest at 1.5 ns, while **3** exhibited a slightly longer lifetime at 2.0 ns. Upon solid-state assembly the lifetimes of **2** and **3** were slightly quenched to 0.94 ns and 1.3 ns, respectively. Such deactivation in lifetime suggests that these compounds are prone to intermolecular self-quenching similar to other BP compounds.[21,22] A comprehensive study on this phenomenon by the Garcia-Garibay group demonstrated that the lifetime of BP nanocrystals with electron donating substituents are dramatically shorter than in solution, varying over 9 orders of magnitude depending on the electron donating ability of the substituents.[22] This is attributed to intermolecular self-quenching via a charge transfer mechanism.[22] The shorter observed lifetimes for **2** and **3** in the crystals are consistent with these prior reports, as the alkyl groups are mildly donating.

The phosphorescent quantum yields of **2**-**4** in DMSO solution (25 μM and 1 mM) displayed efficiencies of less than 0.3% in all cases. The low quantum efficiency is attributed to unrestricted rotation and vibrations of the sensitizer when allowed to move freely in solution. Interestingly, crystallization of **2** dramatically increased its quantum yield to 5.0% but did not influence **3** as predicted by computation. The calculations suggest that the solid-state geometry of **2** forces each of BPs benzene rings to act independently, whereas in solution the linear analog is able to orient itself so that both benzenes participate in the excitation of the π bands resulting in a loss of independent chromophores. This demonstrates that the higher quantum yield observed for **2** upon solid-state assembly is likely due to suppressed mobility when locked within the crystalline lattice. Literature reports also correlate suppressed mobility with increased quantum yields.[23-25] Recent studies have shown that halo-substituted BP units exhibit enhanced phosphorescence when organized in the solid-state.[23] In solution, the quantum yields were sufficiently diminished but they became highly emissive when frozen with liquid nitrogen.[23] Here, we show that restricting molecular motion of BP enriched a radiative decay pathway of the triplet excited state when only one of BP's benzene ring participates in the excitation process.

Typically, upon Franck-Condon excitation, BP undergoes rapid intersystem crossing (ISC) from $S_1 \rightarrow T_2 \rightarrow T_1$ excited states,[26] which can abstract nearby hydrogens to form ketyl containing radical pairs as well as undergo other excited state (ES) or thermal processes.[27] Scheffer proposed that intramolecular photochemical H-abstraction is preferred when the C=O···H distance is below the sum of the van der Waals radii of the oxygen and hydrogen atoms (2.72 Å),[28] while others have observed intermolecular H-abstraction by BP with C=O···H distances as far as 3.13 Å.[29,30] Figure 1.5 compares the microenvironment around the BP groups in the three systems and shows that there are, indeed, closely preorganized hydrogens (<2.72 Å to BP oxygen). The BP carbonyl in **1** is organized more closely to neighboring benzyl protons (2.41 Å) versus the harder to abstract aryl protons (2.68 Å). In comparison, in **2** the carbonyl oxygen is in close proximity to only the aryl protons (2.60 Å), which have a higher bond dissociation energy (BDE). BP has been found to abstract hydrogen atoms from benzene rings, albeit slowly.[31] Our hypothesis is that UV irradiation of **2** crystals may produce a triplet radical pair in low efficiency versus **1**. Finally, for **3** there are proximal benzylic CH_3 (2.60 Å), benzylic methylenes (2.88 Å), and aryl protons (2.64 Å), which suggests that several different triplet radical pairs could be formed. Simple BDE arguments predict the ketyl radicals may be formed more easily in compounds **1** and **3** as compared with **2**, which only contains close aryl hydrogens; as homolytic BDEs are lower for benzyl protons versus aryl (88 kcal/mol vs 111 kcal/mol, respectively).[32] Despite this, BP has been known to abstract all three types of protons.[29-31]

In an effort to correlate structure with the formation and stability of the UV-generated triplet radical pairs, we turned to X-band EPR spectroscopy. First, EPR spectra were recorded on solutions of **2** and **3** in dichloromethane (1 mM) pre and post UV-irradiation (1 h).[§] As expected, no EPR signal was observed pre or post UV indicating that any ketyl radical formed is quickly terminated in solution (Figure 1.44). Upon UV irradiation the linear analog solutions yellowed and showed only minor spectroscopic changes by absorption spectroscopy (Figure 1.49).

Next, solid-state EPR spectra were recorded on triply recrystallized samples of **2** and **3** (~10 mg) pre and post UV.[§§] After one hour of UV irradiation, the transparent crystals of **2** turned reddish-brown in color (Figure 1.6A), while the needle-like crystals of **3** became opaque upon removal from the mother liquor and showed a slight yellowing in color upon

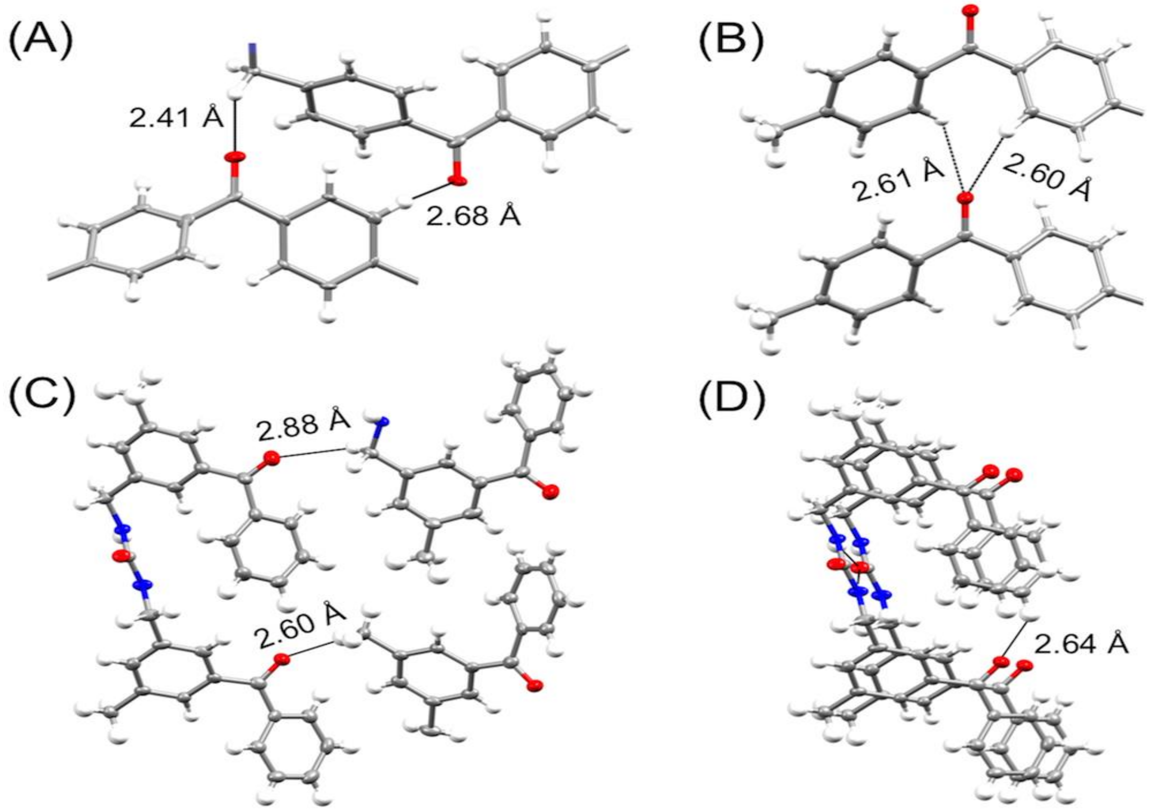

Figure 1.5. Comparison of the microenvironments around the BP carbonyl obtained from the SC-XRD of compounds **1-3**. (A) **1** has neighboring aryl and benzyl CH_2 protons. (B) The carbonyl of **2** resides in close proximity to only neighboring aryl protons. (C) The more complex structure of **3** is oriented close in space to two types of benzyls protons (CH_3 and CH_2) as well as (D) aryl protons.

UV irradiation (Figure 1.6B). UV irradiation of the crystals resulted in the formation of radicals in both **2** and **3** with *g* values of 2.005 and 2.007, respectively (Figures 1.6 and 1.45). Irradiation of **2** crystals gave rise to an isotropic EPR signal. The EPR line width of **3** was similar, but a weak second transition was observed at *g* = 2.003. A *g* value of 2.003 has previously been attributed to the BP ketyl.[33]

The concentration of radical pairs generated after one hour of UV-irradiation was approximated using a calibration of standard solutions of TEMPO in benzene (Figure 1.46).[10,34] Double integration of the EPR

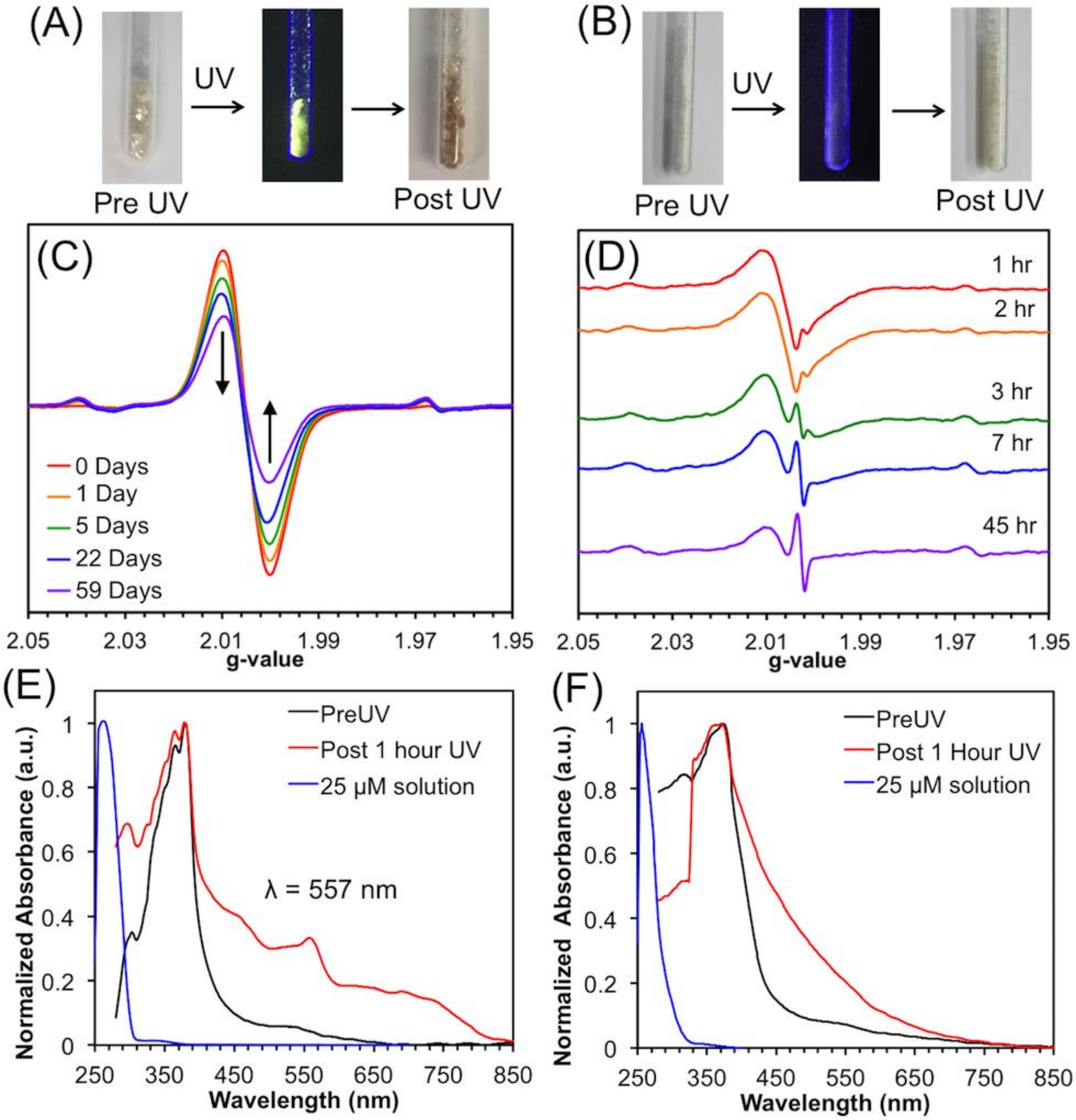

Figure 1.6. Photophysical properties of the triply recrystallized samples of **2** and **3** pre and post UV-irradiation. (A) The transparent crystals of **2** exhibit green fluorescence under UV light and become brown-red upon UV-irradiation. (B) The needle-like crystals of **3** show quenched emission and only slightly yellow in color after UV-irradiation. (C) EPR of **2** post UV and subsequent dark decay study demonstrating that the radicals are persistent for several days at rt. (D) EPR of **3** exhibits persistent radicals after irradiation with a significant change in EPR line shape within 2 h post UV. Comparison of absorption spectra of (E) **2** and (F) **3** in solution and their recrystallized solids pre and post UV irradiation for one hour, the new absorbance band in **2** at λ = 557 nm is labelled.

signals provides the overall area of the spectra, which were then compared to the TEMPO calibration. One hour UV-irradiation of **2** generated the same amount of radical as a 0.053 mM solution of TEMPO in benzene, suggesting that approximately 1 in 5,000 molecules of **2** have a radical. In comparison, after similar UV-irradiation host **1** showed ~1 in 30,000 molecules have a radical,[10] whereas the linear analog **3** shows radicals in ~1 in 25,000 molecules (similar to a 0.009 mM TEMPO solution). The amount of UV-generated radical formed increases with longer irradiation times. This result shows that **2** generates approximately five times more radical than **3** after one hour of UV irradiation and demonstrates that radical formation is not deterred by higher homolytic BDEs. Though, it is possible that the persistence of the radical pair is playing a role in the observed concentration difference.

Therefore, the persistence of the radicals was probed using dark decay studies where the samples were stored at room temperature in the dark after irradiation and EPR spectra were recorded over time. The dark decay study of **2** shows that there was little change in line shape and g-value (2.005) 140 days post UV-irradiation (Figure 1.6C). Sixty days after UV-irradiation, the area of the EPR signal retained half its initial amount, demonstrating the remarkable persistence of the radicals of **2** (Figure 1.47). In comparison, dark decay studies on recrystallized **3** showed a faster decay and exhibited dramatic changes in the EPR line shape (Figure 1.6D). Post UV the broad EPR line exhibited a g-value of 2.007 with a weak transition at g = 2.003. Two hours after irradiation the EPR signal retained a similar line shape although a stark change was observed between 2 and 3 hours after irradiation with an increase in population of radicals at g = 2.003. The overall line width of the spectra remained similar, but the area of the signal was decreased by half just 45 hours after UV irradiation (Figure 1.48). In contrast, macrocycle **1** displays a persistent radical, which exhibits a modest amount of radical 26 days after irradiation. In accordance with the spin selection rule, recombination reactions of triplet geminate radical pairs are forbidden and must first undergo ISC to yield a singlet radical pair in order to form products.[27,33] In solution, H-abstraction by BP generally occurs in 10-100 ns while recombination is considered the rate-limiting step (>1 μs).[27] The enhanced stability of these emergent radicals in the solid-state post UV-irradiation is attributed to delocalization of the radical pairs, which is further stabilized by the rigidity of the BP units upon assembly. Studies have shown that self-recombination reactions of the BP ketyl have a rate constant that is an order of magnitude lower than cross-reactions.[27] This seems to be reflected in the stability of **3** as the ketyl radical signal (g = 2.003) became more prominent the longer the sample remained at room temperature.

Figure 1.6E-F compares the absorption spectra of triply recrystallized samples (**2** and **3**) before and after 1h irradiation. The absorption spectra of both crystalline samples post UV retained their major spectroscopic properties, although both signals broadened into the visible region. Most intriguingly, irradiation of **2** afforded a new absorbance band at 557 nm which is consistent with where both the triplet and resulting ketyl absorb.[12,35,36] It should be noted that the triplet state of BP's absorption peak significantly overlaps with its corresponding ketyl, however the triplet is known to absorb out to wavelengths >600 nm.[35,36] This long wavelength absorption was not observed in the spectra of **3** or **1**,[10] again suggesting that UV-irradiation of **2** affords increased amounts of radicals versus the other derivatives. Samples of **2** and **3** were analysed by SC-XRD after UV irradiation and revealed no significant structural changes. Similarly, ^{1}H NMR spectra were obtained on irradiated samples showing no spectral changes, which is consistent with the estimated concentration of the radicals (Figure 1.50 - 1.51). Finally, the emission behaviour of the UV irradiated crystals was also investigated with no major changes observed upon excitation at 355 nm (Figure 1.33).

We have demonstrated that UV-irradiation of self-assembled BP containing molecules can give rise to persistent organic radicals in marked contrast to their behaviour in solution. The concentration of the radicals is low but is influenced by structure and assembly, as is their persistence. *Para*-substitution of BP containing radical pairs resulted in longer-lived radical species while *meta*-substituted radical pairs displayed decreased stability. A comprehensive study on a library of BP containing crystals with varying substituent patterns may be fruitful to further elucidate the rules that govern ketyl radical pair formation and their subsequent stability.

1.3 CONCLUSIONS

In summary, three new BP-containing molecules were synthesized and two afforded single crystals that assembled the photosensitizer through urea-urea hydrogen bonding interactions. We investigated the impact solid-state assembly has on their photophysics and explored their ability to form persistent radicals as a result of UV-irradiation. Solid-state assembly of the materials resulted in a bathochromic shift in both their absorption and emission spectra and quenched their phosphorescent lifetime, which is attributed to BPs self-quenching character. The quantum efficiency of **2** and **3** was <0.3% in solution, although crystallization influenced their quantum yield differently. Crystallization of **2** enhanced its quantum efficiency by an order of magnitude but did not influence **3**. TD-DFT calculations on the crystal structures of **2** and **3** in the gas phase and in solution were consistent with these experimental observations. The computations suggested that crystallization of **2** and **3** would influence their photophysical properties differently, predicting a dramatic change in photophysics for **2** and little or no difference was expected for **3**.

Self-assembly of compounds **1**-**3** resulted in three distinct crystal structures that vary the microenvironment around the BP carbonyl. Remarkably, all of the crystalline compounds exhibit persistent radicals upon UV-irradiation even though no radicals were observed in solution. The radical formation is attributed to BP carbonyls' close proximity to neighboring H-abstractions sites within the crystal structures. The amount of radicals generated after UV-irradiation (1 h) varied six-fold with **2** surprisingly showing the largest amount even though only aryl protons with higher BDE are close in proximity (2.60 Å) for abstraction, while macrocycle **1** exhibited the least amount of radicals. Radicals of **2** also displayed the greatest persistence, exhibiting approximately half the EPR signal after 140 days. In each case, the persistence of the UV-generated radicals was attributed to resonance stabilization about the rigid crystalline framework and may shed light on the impact solid-state assembly has on the recombination of ketyl containing radical-pairs.

1.4 FUTURE WORK

Future work will be focused on elucidating the factors that govern the formation, stability, and applications of the radicals. An interesting and speedy way to do this is through machine learning. All data for compounds **1** – **4** will be given to the Machine Learning Evolution Laboratory (MLEG) where they will data mine to determine the physical and structural similarities that may contribute to the persistent radical. Next, using the Cambridge Structural Database (CSD) all benzophenone-containing structures can be surveyed and those that contain similar attributes to **1**-**4** can be further investigated through crystal growth and EPR experiments to fine tune and further develop the factors that are important for persistent radical formation. It is also of interest to examine the ability of **2**-**4** to undergo triplet-triplet annihilation pathways with molecular oxygen to generate reactive oxygen species (ROS). In the case of linear analogs **2** and **3**, they exhibit enhanced solubility allowing us to directly compare the how solid-state assembly influences ROS generation. In the case of **4**, only the crystals can be examined, as they are only soluble in DMSO, a well-known chemical quencher of singlet oxygen.

1.5 EXPERIMENTAL

SYNTHESIS AND CHARACTERIZATION OF COMPOUNDS: All commercial reagents and solvents were purchased from Alfa Aesar®, Sigma-Aldrich®, VWR®, or TCI America® and were used as received without further purification unless otherwise stated. Reactions were conducted in oven-dried glassware under nitrogen atmosphere. Reactions were carried out using Thermofisher Isotemp® digital stirring hotplates in dimethicone oil baths. Slow cooling crystallizations were performed by heating the sample in a pressure vessel to 120 °C in the selected solvent and cooling 1 °C per hour to rt. All solid-state photophysical and EPR measurements were carried out on triply recrystallized samples unless otherwise stated. ^{1}H-NMR and ^{13}C-NMR spectra were recorded on Bruker Avance III-HD spectrometers (300-400 MHz). Chemical shifts are reported as (δ ppm) with the corresponding integration values (integration is not listed for ^{13}C-NMR spectra), while coupling constants (*J*-values) are reported in hertz (Hz). Standard abbreviations indicating multiplicity were used as follows: s (singlet), br (broad), d (doublet), t (triplet), q (quartet), m (multiplet). High-resolution mass spectrum data was recorded using a direct exposure probe (DEP) in electron ionization (EI) mode on a Waters QTOF-I quadrupole time-of-flight mass spectrometer. **PHOTOPHYSICAL PROPERTIES:** UV-irradiation of all materials was carried out with a Hanovia 450 W medium pressure mercury arc lamp cooled in a quartz immersion well. All IR analysis was performed using a Perkin Elmer Spectrum 100 IR Spectrometer. Diffuse reflectance spectra were recorded on the solid-state samples using a Perkin Elmer Lambda 45 UV/vis spectrometer equipped with UV Winlab software and were referenced to Spectralon®. Absorption spectra in solution were recorded on a Molecular Devices Spectramax M2. Quantum yield measurements were acquired on an Edinburgh FS5 fluorescence spectrometer equipped with a 150 W Continuous Wave Xenon Lamp source for excitation (SC-30: Integration Sphere module), as well as steady-state emission spectra on solutions (SC-05: Standard Cuvette Holder). Solid-state emission analysis was performed using a Perkin Elmer LS 55 fluorescence spectrometer equipped with a pulsed high-energy source for excitation (Front-Face mode). Phosphorescence lifetimes were measured using a Mini-τ lifetime spectrometer from Edinburgh Instruments equipped with a 365- S12 nm picosecond-pulsed-light-emitting diode (EPLED 365). **EPR STUDIES:** EPR experiments were performed using a Bruker EMX plus equipped with a Bruker X-band microwave bridgehead and Xenon software (v 1.1b.66). The double integration to obtain peak areas was performed in the Xenon software. Samples were sealed under N_2 and UV-irradiated in Norell Suprasil Quartz EPR tubes. **X-RAY STRUCTURE DETERMINATION:** X-ray intensity data was collected at 100(2) K using a Bruker D8 QUEST diffractometer equipped with a PHOTON-100 CMOS area detector and an Incoatec microfocus source (Mo K_α radiation, $\lambda = 0.71073$ Å). The raw area detector data frames were reduced and corrected for absorption effects using the Bruker APEX3, SAINT+ and SADABS programs.[37,38] Final unit cell parameters were determined by least-squares refinement of reflections taken from the data set. The structure was solved by direct methods with SHELXT.[39] Subsequent difference Fourier calculations and full-matrix least-squares refinement against F^2 were performed with SHELXL-2014[40] using OLEX2.[42] Powder X-ray diffraction patterns were recorded on a Rigaku Miniflex II diffractometer with accelerating voltage (30 kV) and current (15 mA).

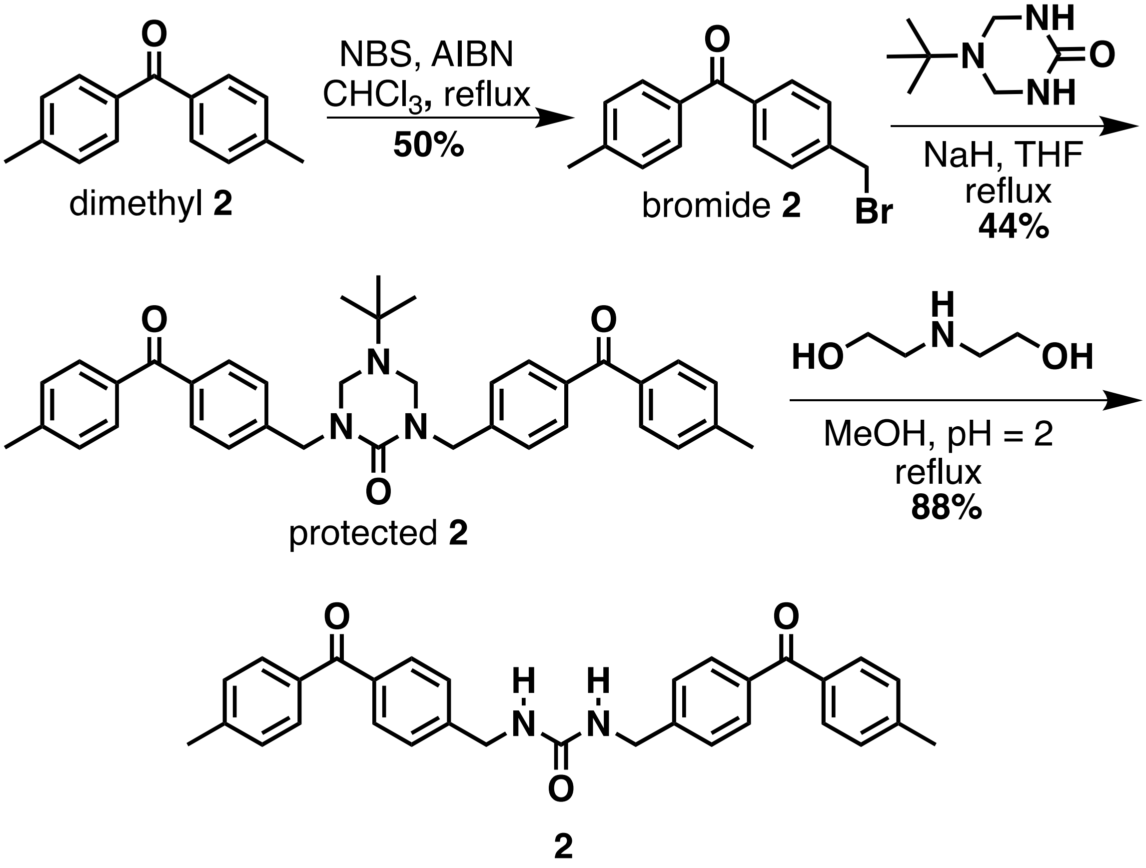

Scheme 1.1. Synthesis of 1,3-bis(4-(4-methylbenzoyl)benzyl) urea, **2**. *Reagents and Conditions*: 4,4-dimethylbenzophenone was brominated with N-bromosuccinimide (NBS, 1 eq) and 2,2'- azobis(isobutyronitrile) (AIBN) in chloroform to produce 4-(bromomethyl)-4'-methyl benzophenone, bromide **2**. The resultant bromide was then substituted using triazinanone and NaH in refluxing THF to give (((5-(*tert*-butyl)-2-oxo-1,3,5-triazinane-1,3-diyl)bis(methylene))bis(4,1-phenylene))bis(*p*-tolylmethanone), protected **2**. The product was then deprotected in an acidic diethanol amine aqueous/methanol mixture to yield the desired 1,3-bis(4-(4-methylbenzoyl)benzyl)urea (**2**).

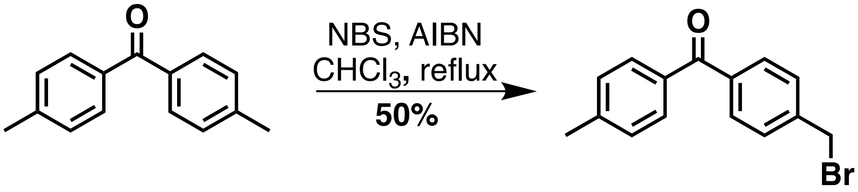

4,4’-dimethylbenzophenone (2.01 g, 9.54 mmol) was dissolved in chloroform (30 mL). Next, N-bromosuccinimide (NBS, 0.849 g, 4.77 mmol) and azobisisobutyronitrile (AIBN, 0.0157 g, 0.0954 mmol) were added and the reaction mixture was heated at reflux under N_2 for 20 h. The reaction was cooled to rt and the organic layer was washed with DI water (3 x 25 mL) to remove succinimide byproduct and dried over $MgSO_4$. Silica gel was added to the organic layer and the solvent removed under vacuum. The silica adhered crude reaction mixture was loaded onto a silica gel column packed with hexanes. The product was isolated via column chromatography using a gradient: (pure hexanes which were slowly tapered to a 90:10 hexanes: ethyl acetate mixture) as the second spot off the column to yield a white solid. (1.379 g, 50%). ^{1}H NMR (300 MHz; CD_2Cl_2) δ 7.75 (2H, d, J = 8.3), 7.70 (2H, d, J = 8.3), 7.52 (2H, d, J = 8.3), 7.31 (2H, d, J = 8.3), 4.57 (2H, s), 2.44 (3H, s). ^{13}C NMR (400 MHz; CD_2Cl_2) δ 195.36, 143.57, 141.98, 137.83, 134.66, 130.28, 130.10, 128.99, 128.87, 32.56, 21.37. HRMS (ESI) *m/z*: $[M+H]^+$ calc’d for $[C_{15}H_{11}OBr]^+$, 288.0150; found, 288.0145.

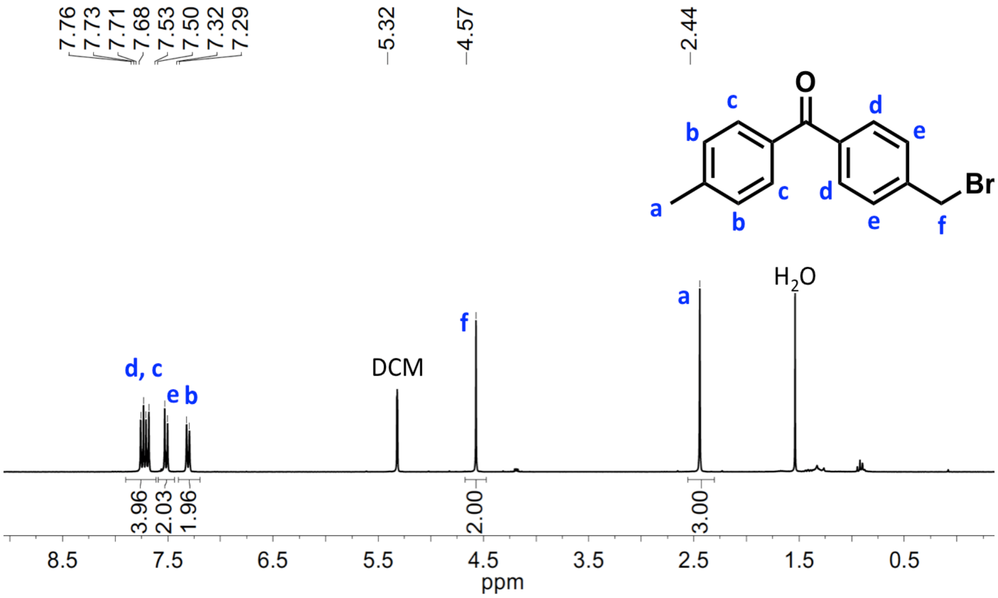

Figure 1.7. ^{1}H NMR (300 MHz; CD_2Cl_2) of bromide **2**.

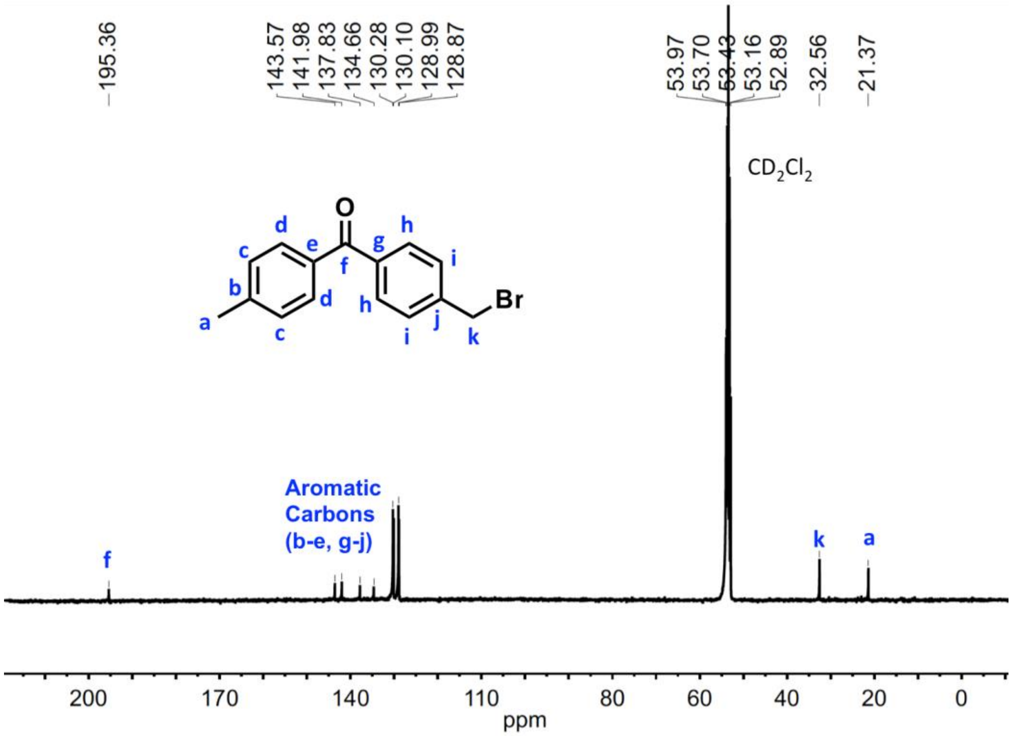

Figure 1.8. ^{13}C NMR (400 MHz; CD_2Cl_2) of bromide **2**.

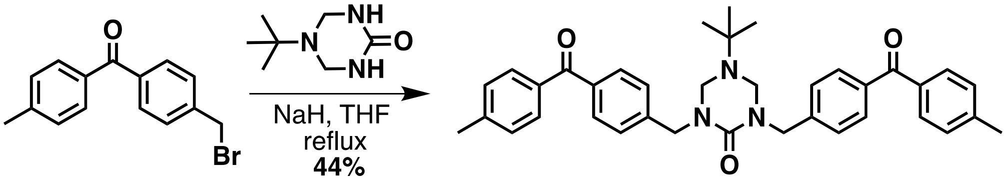

To a dry round bottom flask, still-dried THF (75 mL) was added. Next, triazinanone (0.334 g, 2.12 mmol) and NaH (60 % suspension in mineral oil, 0.206 g, 8.48 mmol) were added. The mixture was heated to reflux under N_2 atmosphere for two hours. The suspension was cooled to rt and a solution of bromide **2** (1.23 g, 4.24 mmol) in dry THF (15 mL) was added to the stirring mixture all at once. The mixture was then heated to reflux for 19 h. Next, the reaction mixture was cooled to rt, neutralized with 1N HCl, and diluted with water (100 mL). THF was removed under vacuum until an aqueous suspension remained. Crude product was extracted with methylene chloride (3 x 100 mL), washed with brine (150 mL), and dried with anhydrous $MgSO_4$. The product was purified via flash silica gel column chromatography (95:5 dichloromethane:methanol) and obtained as a white solid (0.265 g, 44%). ^1H NMR (300 MHz; CD_2Cl_2) δ 7.77 (4H, d, *J* = 8.0), 7.71 (4H, d, *J* = 8.2), 7.49 (4H, d, *J* = 8.0), 7.31 (4H, d, *J* = 8.0), 4.63 (4H, s), 4.30 (4H, s), 2.44 (6H, s), 1.05 (s, 9H). HRMS (ESI) *m/z*: $[M+H]^+$ calculated for $[C_{37}H_{39}N_3O_3]^+$, 574.3068; found, 574.3064.

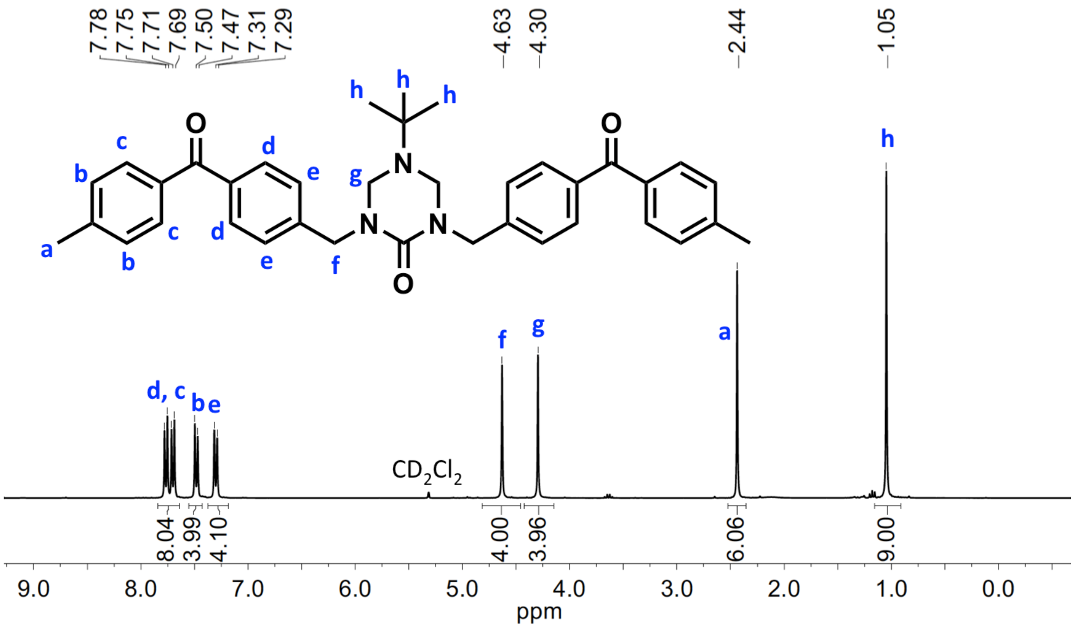

Figure 1.9. ^{1}H NMR (300 MHz; CD_2Cl_2) of protected **2**.

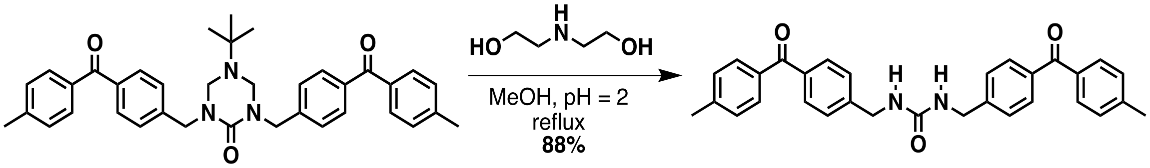

A deprotection solution was prepared by adding diethanol amine (20 mL) and deionized water (50 mL) to an Erlenmeyer flask and its pH was adjusted to pH 2 via drop-wise addition of 12.1 N HCl. Next, triazinanone protected **2** (0.265 g, 0.462 mmol) was added to a 1:1 v/v mixture of the deprotection solution (120 mL) and methanol (120 mL) was refluxed as a suspension for 48 h. The precipitate (varying in color from yellow to white) was collected via vacuum filtration and was washed with 1N HCl (20 mL), distilled water (3 x 100 mL), and dried under vacuum (0.194 g, 88%). ^{1}H NMR (300 MHz; DMSO-d6) δ 7.66 (8H, m), 7.43 (4H, d, *J* = 8.2), 7.36 (4H, d, *J* = 8.0), 6.68 (4H, t, *J* = 6.1), 4.35 (4H, d, *J* = 6.0), 2.41(6H, s). ^{13}C NMR (400 MHz; DMSO-d6) δ 195.60, 158.56, 146.40, 143.45, 136.16, 134.97, 130.25, 130.12, 129.56, 127.33, 40.62, 21.62. HRMS (ESI) *m/z*: $[M+H]^+$ calculated for $[C_{31}H_{28}N_2O_3]^+$, 477.2173; found, 477.2173.

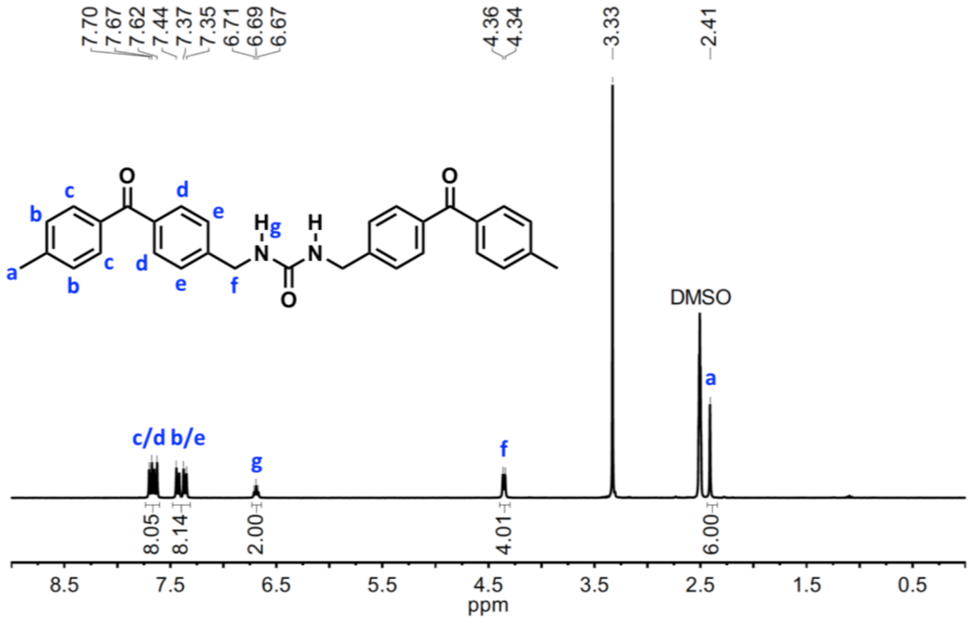

Figure 1.10. ^{1}H NMR (300 MHz; DMSO) of **2**.

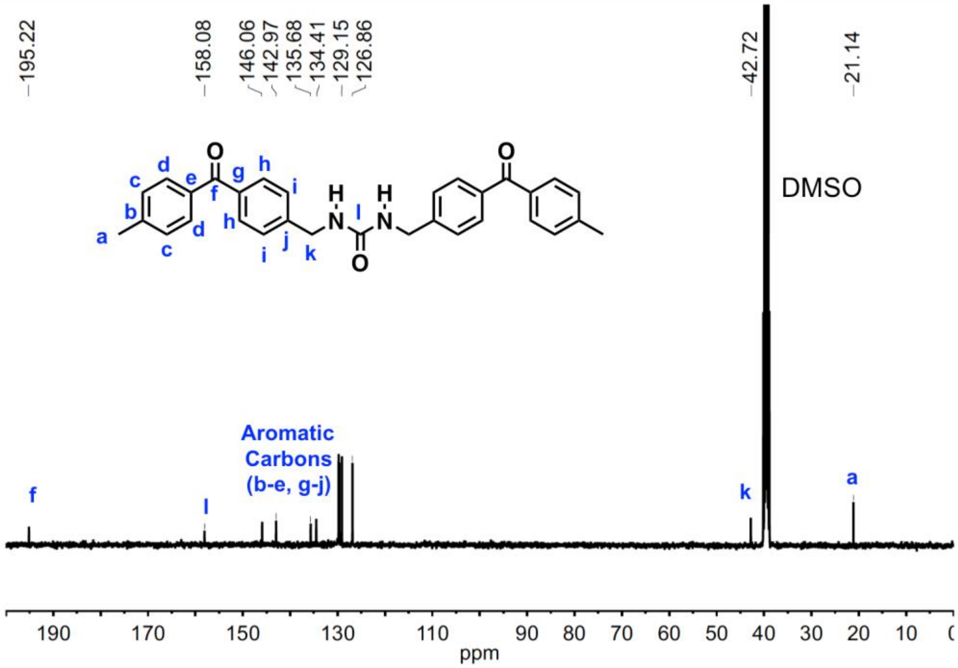

Figure 1.11. ^{13}C NMR (400 MHz; DMSO) of **2**.

Crystallization of 2: Crystals of **2** were obtained by dissolving the sample (6 mg/mL) in a hot acetic acid solution (120 °C). The sample was slow cooled at 1 °C per hour to rt to obtain transparent plates. The crystals (50 mg) were filtered using a vacuum filtration apparatus, were washed with DI water (100 mL), and dried under vacuum.

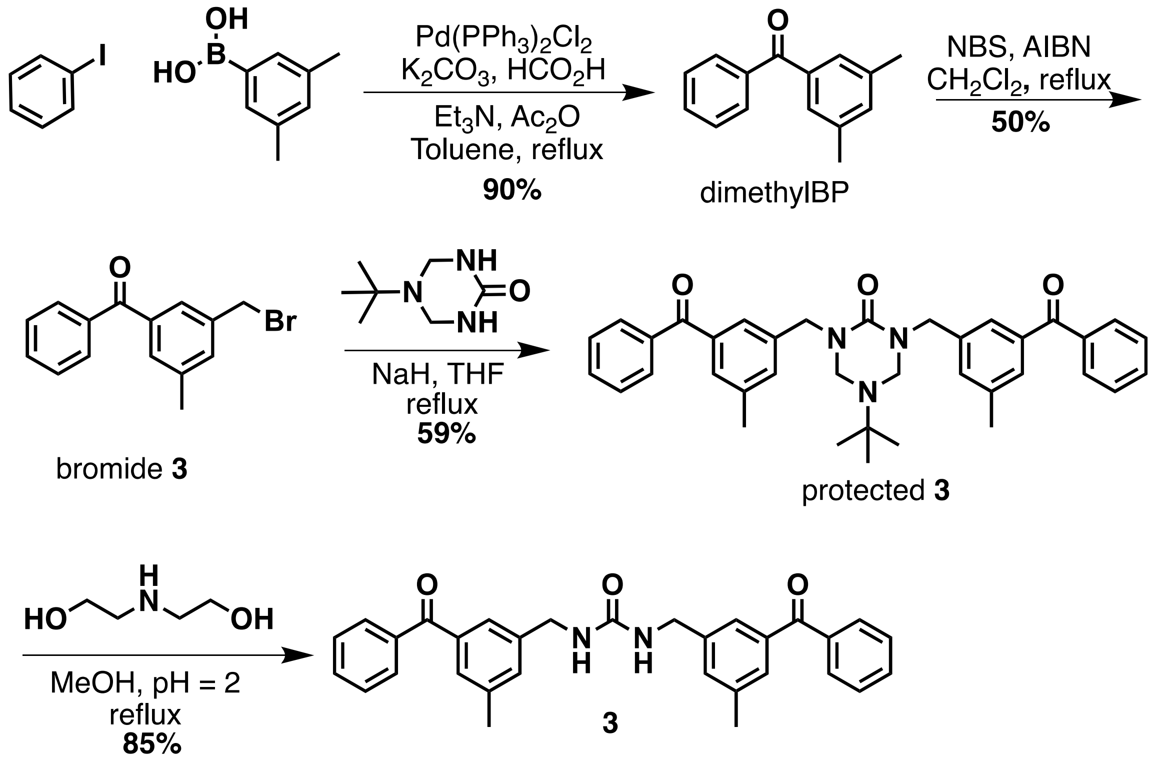

Scheme 1.2. Synthesis of 1,3-bis(3-(5-methyl)(benzoyl)benzyl)urea, **3**. *Reagents and Conditions*: (3,5-phenyl)boronic acid and iodobenzene were coupled via carbonylative Suzuki Coupling[43] to yield 3,5-dimethylbenzophenone, dimethylBP. The resultant product was brominated with N-bromosuccinimide (NBS, 1 eq) and 2,2'- azobis(isobutyronitrile) (AIBN) in DCM to produce 3-bromomethyl-5-methylbenzophenone, bromide **3**. The bromide was then substituted using triazinanone and NaH in refluxing THF to give 5-(tert-butyl)-2-oxo-1,3,5-triazinane-1,3-diylbis(3-benzoyl-5-methylphenylmethane), protected **3**. The product was then deprotected in an acidic diethanol amine aqueous/methanol mixture to yield the desired 1,3-bis(3-(5-methyl)(benzoyl)benzyl)urea (**3**).

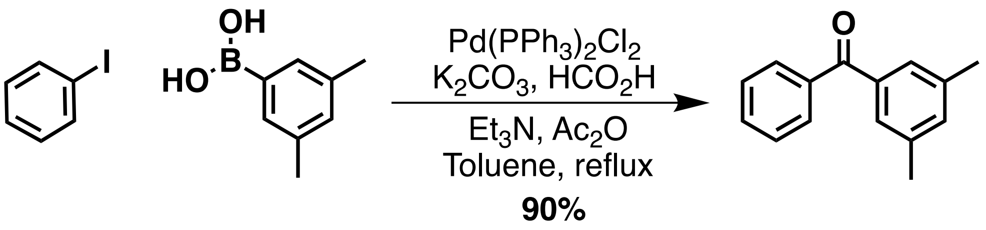

3,5-dimethylphenylboronic acid (0.149 g, 1.00 mmol), palladium(II)*bis*(triphenyl phosphine) dichloride (0.030 g, 0.040 mmol), and potassium carbonate (0.415 g, 3 mmol) were transferred to an oven dried Schlenk tube filled with N_2. Dry, degassed toluene (10 ml), triethyl amine (0.558 ml, 4 mmol), and iodobenzene (0.336 ml, 3 mmol) were added to the tube and the resulting suspension was sonicated followed by stirring at 100 ˚C. A premixed solution of formic acid (0.113 ml, 3 mmol) and acetic anhydride (0.283 ml, 3 mmol) (stirred under N_2 at 30 ˚C for 2 h) was then added to the Schlenk tube dropwise. The reaction was allowed to run for two days at 100 ˚C and checked via TLC (90:10 hexanes:ethyl acetate), an alizarin stain was used to monitor the loss of boronic acid.[44] Upon completion, the reaction mixture was filtered, and the filtrate was evaporated under reduced pressure. The product was then isolated via flash silica gel column chromatography (98:2 Hexanes:EtOAc → 96:4 Hexanes:EtOAc) to yield a white solid (0.188 g, 90%). Spectra matched that as previously reported.[43] ^{1}H NMR (300 MHz; $CDCl_3$) δ 7.81 (2 H, d, *J* = 7.1 Hz), 7.59 (1 H, t, *J* = 7.3 Hz), 7.48 (2 H, t, *J* = 7.5 Hz), 7.41 (2 H, s), 7.22 (1 H, s), 2.38 (6 H, s).

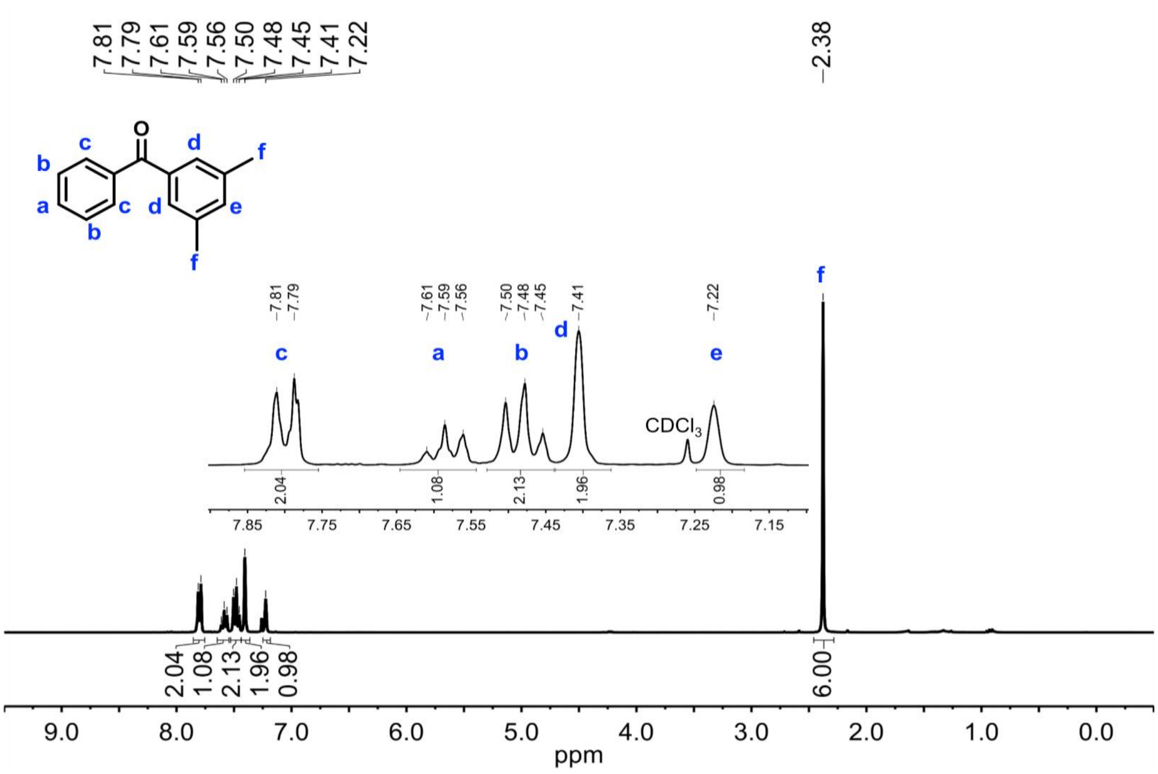

Figure 1.12. ^{1}H NMR (300 MHz; $CDCl_3$) of 3,5-dimethyl benzophenone.

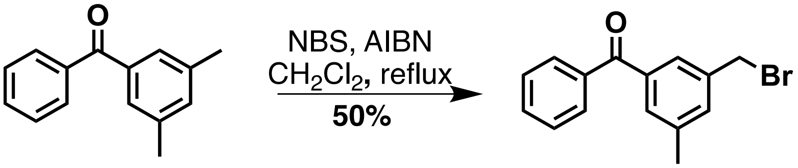

3,5-dimethyl benzophenone (0.750 g, 3.57 mmol), *N*-bromosuccinimide (0.635 g, 3.57 mmol), and azobisisobutyronitrile (0.006 g, 0.036 mmol) were transferred to a flask containing 33 mL DCM and was heated at reflux for 24 h under N_2 (with an initial irradiation period of 2 h with a sun lamp). Upon completion, the reaction mixture was filtered, and the filtrate was washed with H_2O (3 x 50 mL). The combined organic layers were evaporated under reduced pressure. The product was then isolated via silica gel column chromatography

(100 Hexanes → 90:10 Hexanes:EtOAc) to yield a white solid (0.513 g, 50%). ^{1}H NMR (300 MHz; CDCl$_3$) δ 7.81 (2 H, d, *J* = 7.4 Hz), 7.60 (2 H, t, *J* = 7.2 Hz), 7.54–7.44 (4 H, m) 4.50 (2 H, s), 2.42 (3 H, s). ^{13}C NMR (300 MHz; CDCl$_3$) δ 196.42, 139.06, 138.36, 138.11, 137.58, 133.82, 132.70, 130.76, 130.17, 128.50, 127.89, 32.86, 21.39. HRMS (ESI) *m/z*: $[M+H]^+$ calculated for $[C_{15}H_{13}BrO]^+$, 288.0150; found, 288.0156.

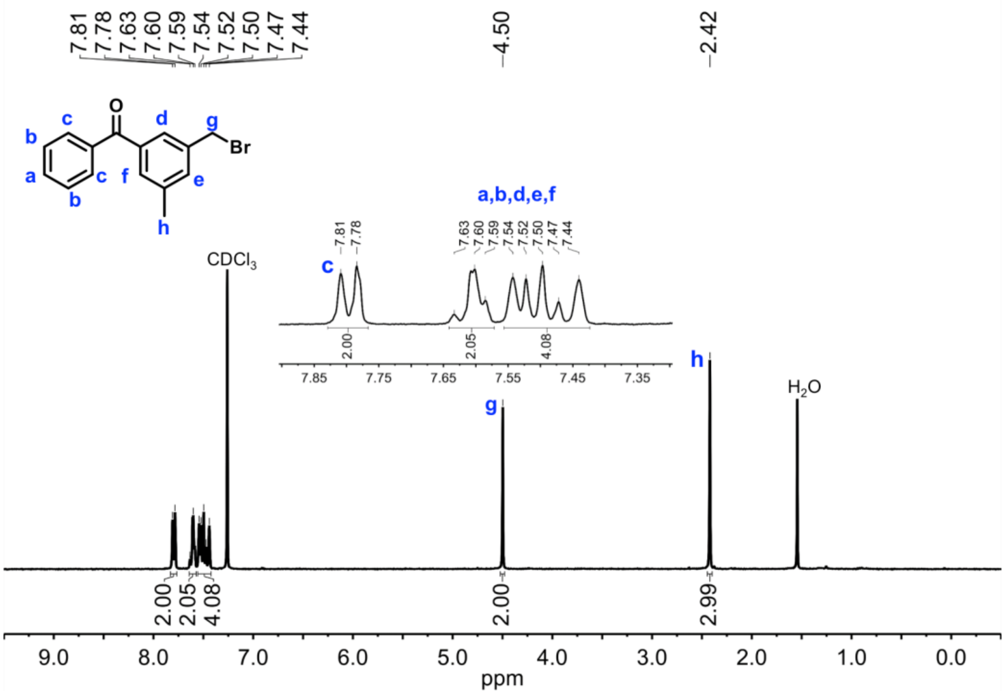

Figure 1.13. ^{1}H NMR (300 MHz; CDCl$_3$) of bromide **3**.

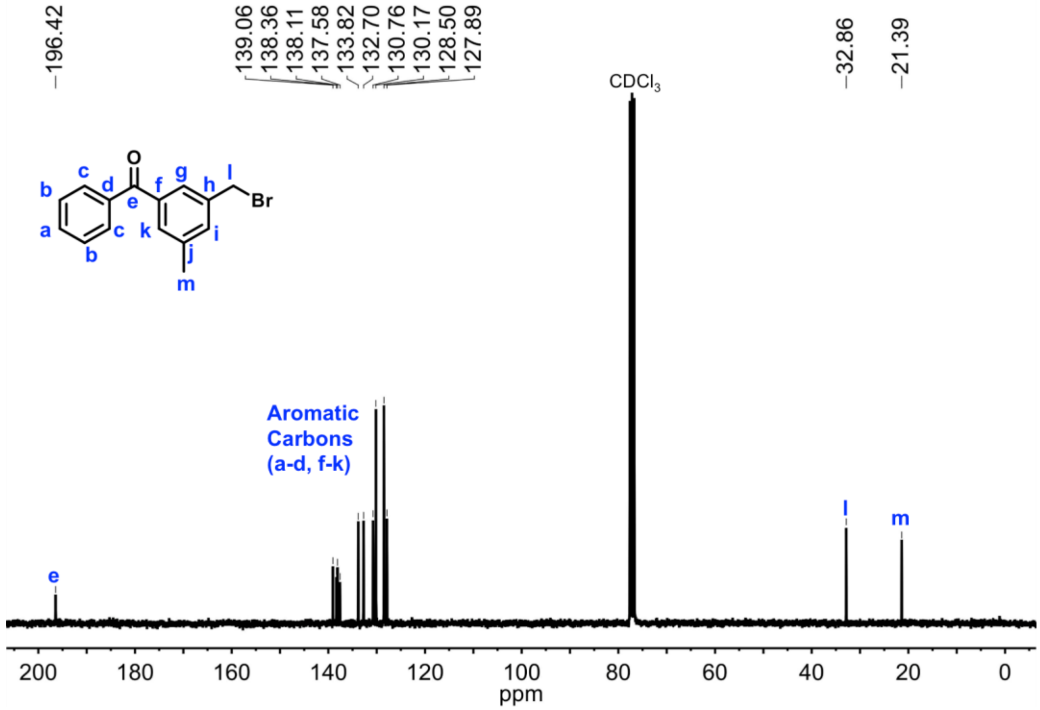

Figure 1.14. ^{13}C NMR (300 MHz; CDCl$_3$) of bromide **3**.

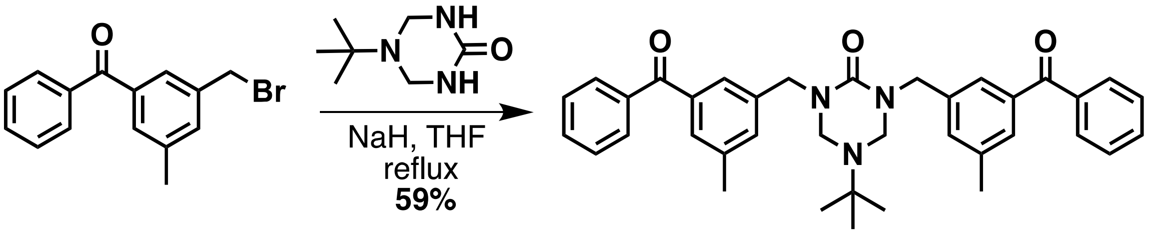

Triazinanone (0.128 g, 0.814 mmol) and NaH (60% suspension in paraffin oil, 0.131 g, 3.28 mmol) were suspended in dry THF (10 mL) and allowed to stir at rt for 5 min under N_2. Afterwards, a solution of 3-bromomethyl-5-methyl benzophenone (0.472 g, 1.63 mmol) in dry THF (10 mL) was added. The reaction was then allowed to reflux for 72 h. Upon completion the reaction was cooled to rt and neutralized with 1 N HCl. H_2O (10 mL) was added and the solution was extracted with DCM (3 x 25 mL), washed with brine (1 x 25 mL), and dried over $MgSO_4$. The solvent was then evaporated under reduced pressure, and the product was isolated via flash silica gel column chromatography (50:50 Hexanes:Ethyl Acetate) to yield a sticky solid (0.278 g, 59%). ^1H NMR (300 MHz; $CDCl_3$) δ 7.80 (4 H, d, *J* = 7.2 Hz), 7.58 (2 H, t, *J* = 7.3 Hz), 7.51 – 7.45 (10 H, m), 4.57 (4 H, s), 4.22 (4 H, s), 2.39 (6 H, s), 1.00 (9 H, s). ^{13}C NMR (300 MHz; $CDCl_3$) δ 196.85, 156.16, 138.64, 138.45, 137.87, 137.68, 133.15, 132.46, 132.40, 130.05, 129.78, 128.29, 126.76, 61.92, 54.24, 48.75, 28.30, 21.36. HRMS (ESI) *m/z*: $[M+H]^+$ calculated for $[C_{37}H_{39}N_3O_3]^+$, 574.3064; found, 574.3057.

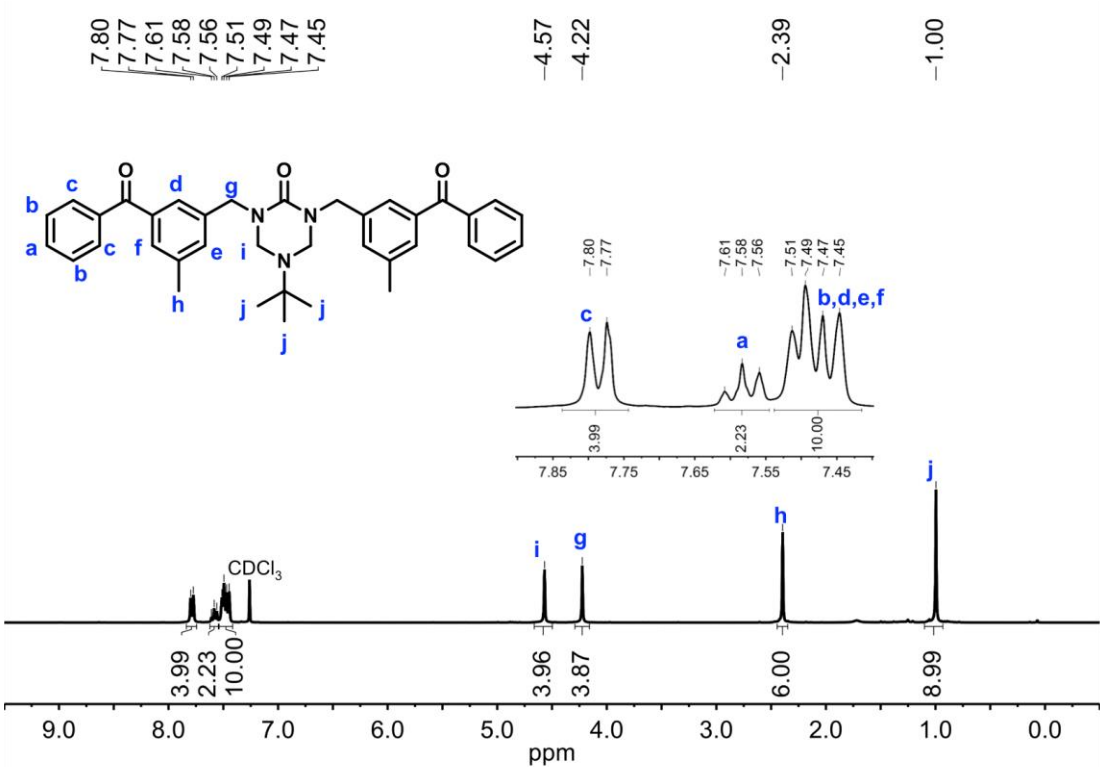

Figure 1.15. ^1H NMR (300 MHz; $CDCl_3$) of protected **3**.

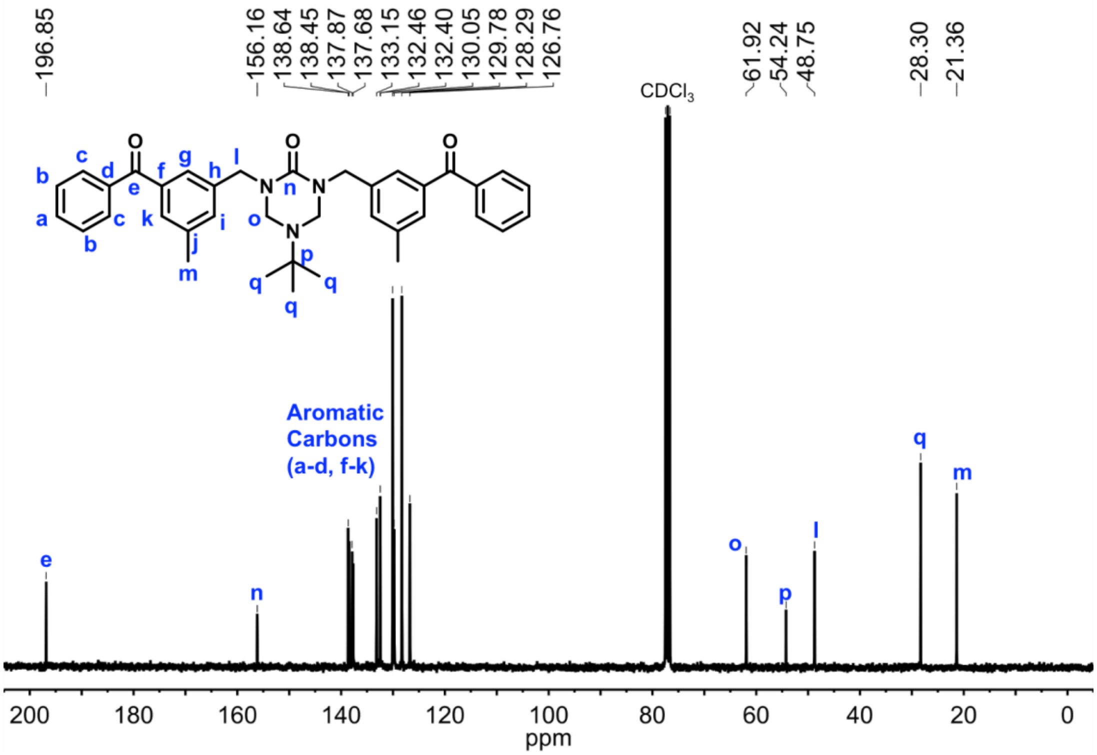

Figure 1.16. ^{13}C NMR (300 MHz; $CDCl_3$) of protected **3**.

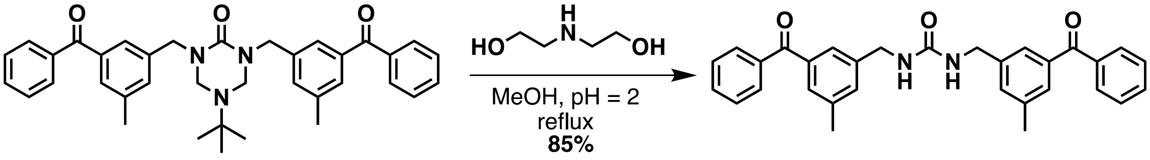

The protected linear analog (0.225 g, 0.392 mmol) was added to 50:40:10 v/v mixture of methanol, water, and diethanol amine (pH ~2, 60 mL) and heated to reflux as a suspension for 72 h. The pH was readjusted to 2 as needed using HCl. After cooling to rt, the precipitate was collected via vacuum filtration and was washed with 1 N HCl (20 mL), DI water (3 x 100 mL), and was dried under vacuum (0.160 g, 85%). ^{1}H NMR (300 MHz; $CDCl_3$) δ 7.78 (4 H, d, *J* = 7.9 Hz), 7.58 (2 H, t, *J* = 6.7 Hz), 7.49-7.44 (8 H, m), 7.34 (2 H, s), 4.72 (2 H, s), 4.44 (4

H, d, *J* = 5.7 Hz), 2.38 (6 H, s). HRMS (ESI) *m/z*: $[M+H]^+$ calculated for $[C_{31}H_{28}N_2O_3]^+$, 477.2173; found, 477.2175.

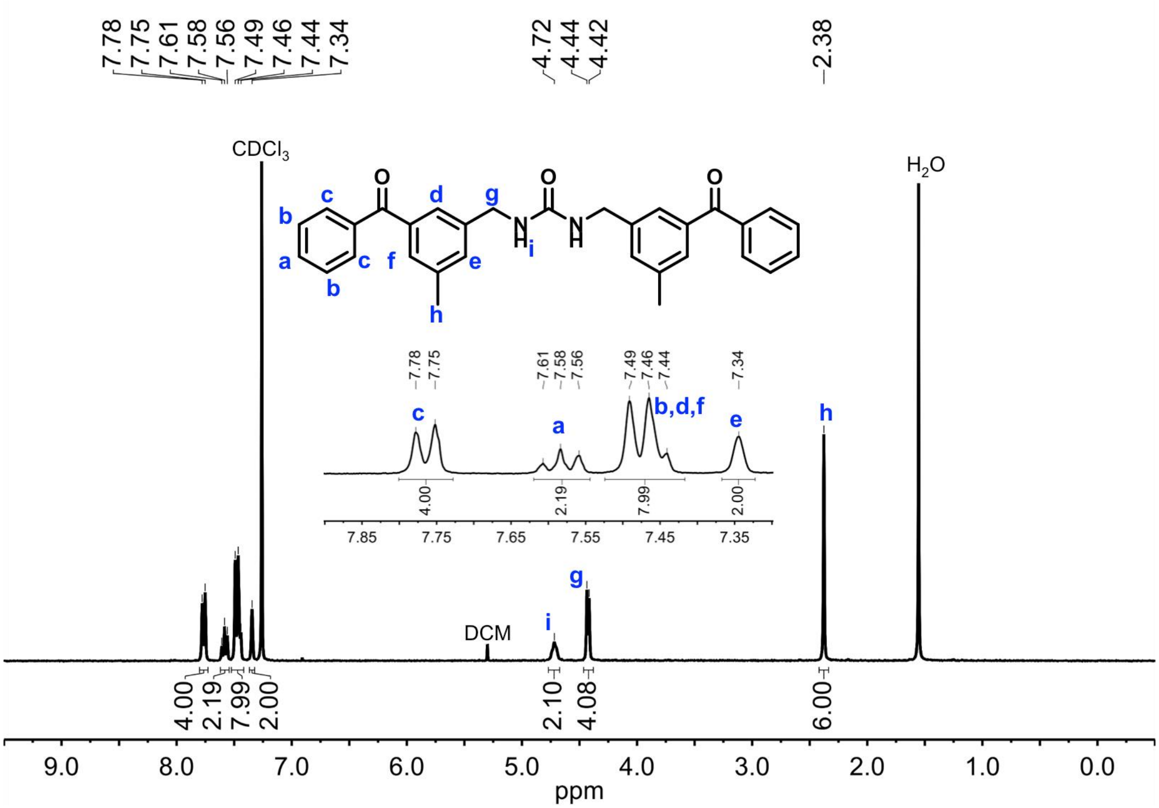

Figure 1.17. ^1H NMR (300 MHz; $CDCl_3$) of **3**.

Crystallization of 3: Crystals of **3** were obtained by dissolving the sample (1 mg/ 1.6 mL) in dichloromethane and the sample was allowed to slowly evaporate to form white needle-like crystals.

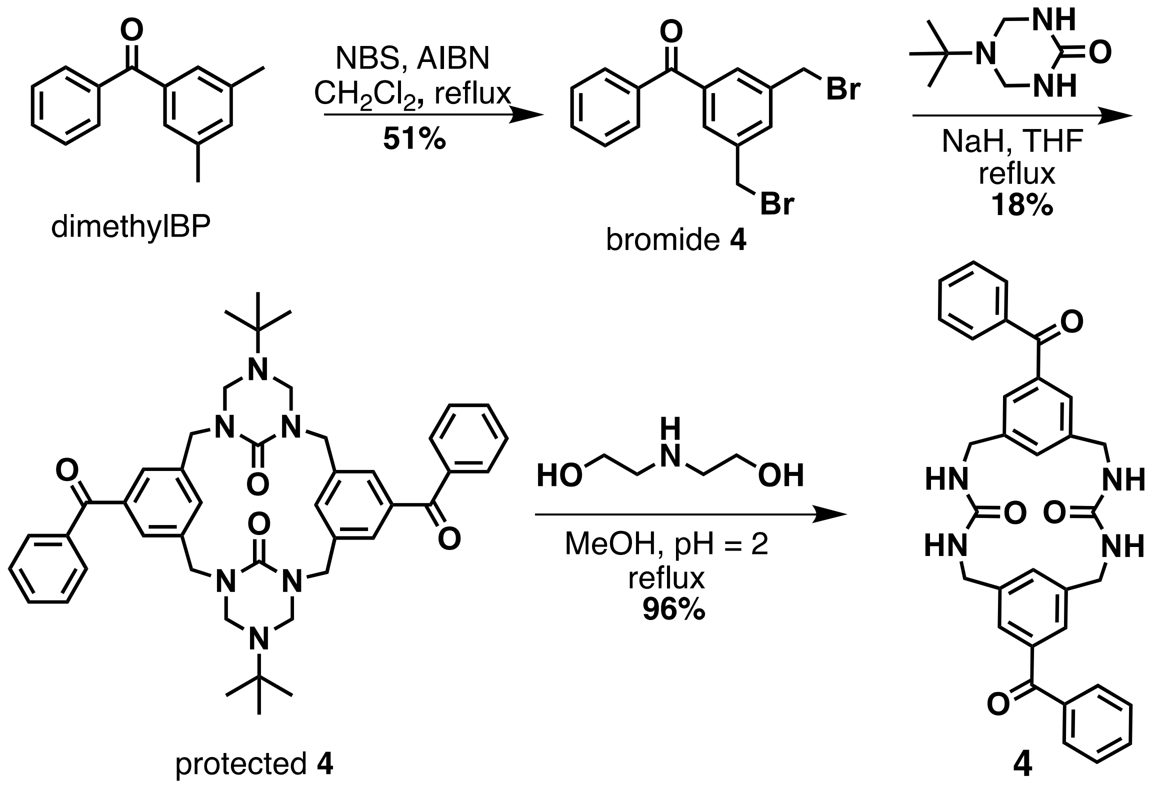

Scheme 1.3. Synthesis of macrocycle **4**. *Reagents and Conditions*: 3,5-dimethylbenzophenone (dimethylBP) was brominated with N-bromosuccinimide (NBS, 2.5 eq) and 2,2'- azobis(isobutyronitrile) (AIBN) in DCM to produce 3,5-bis(bromomethyl)benzophenone, bromide **4**. The resultant bromide was then substituted using triazinanone and NaH in refluxing THF to give protected **4**. The product was then deprotected in an acidic diethanol amine aqueous/methanol mixture to yield the desired macrocycle (**4**).

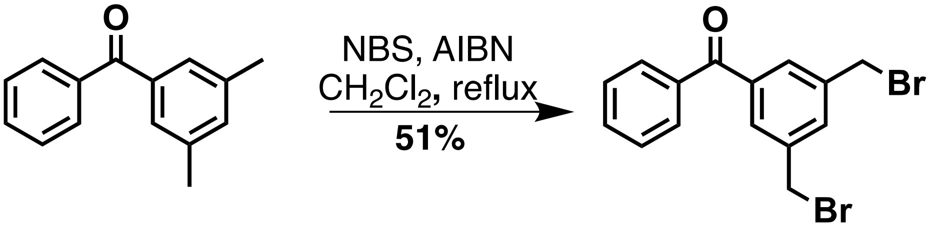

3,5-dimethyl benzophenone (0.584 g, 2.78 mmol), *N*-bromosuccinimide (1.24 g, 6.97 mmol), and azobisisobutyronitrile (0.005 g, 0.028 mmol) were suspended in 30 mL DCM and heated at reflux for 72 h under N_2 (with an initial irradiation period of 2 h with a sun lamp). Upon completion, the reaction mixture was filtered, and the filtrate was washed with H_2O (3 x 50 mL). The combined organic layers were evaporated under reduced pressure. The product was then isolated via silica gel column chromatography (100 Hexanes → 90:10 Hexanes:EtOAc) to yield a white solid (0.521 g, 51%). ^{1}H NMR (300MHz; CDCl$_3$) δ 7.81-7.78 (2 H, m), 7.75 (2 H, s), 7.69-7.58 (2H, m), 7.51 (2 H, t, *J* = 7.5), 4.52 (4 H, s). ^{13}C NMR (300MHz; CDCl$_3$) δ 195.55, 139.02, 138.92, 137.13, 133.42, 133.02, 130.50, 130.18, 128.66, 32.05. HRMS (ESI) *m/z*: [M+H]$^+$ calculated for [$C_{15}H_{12}Br_2O$]$^+$, 365.9255; found, 365.9260.

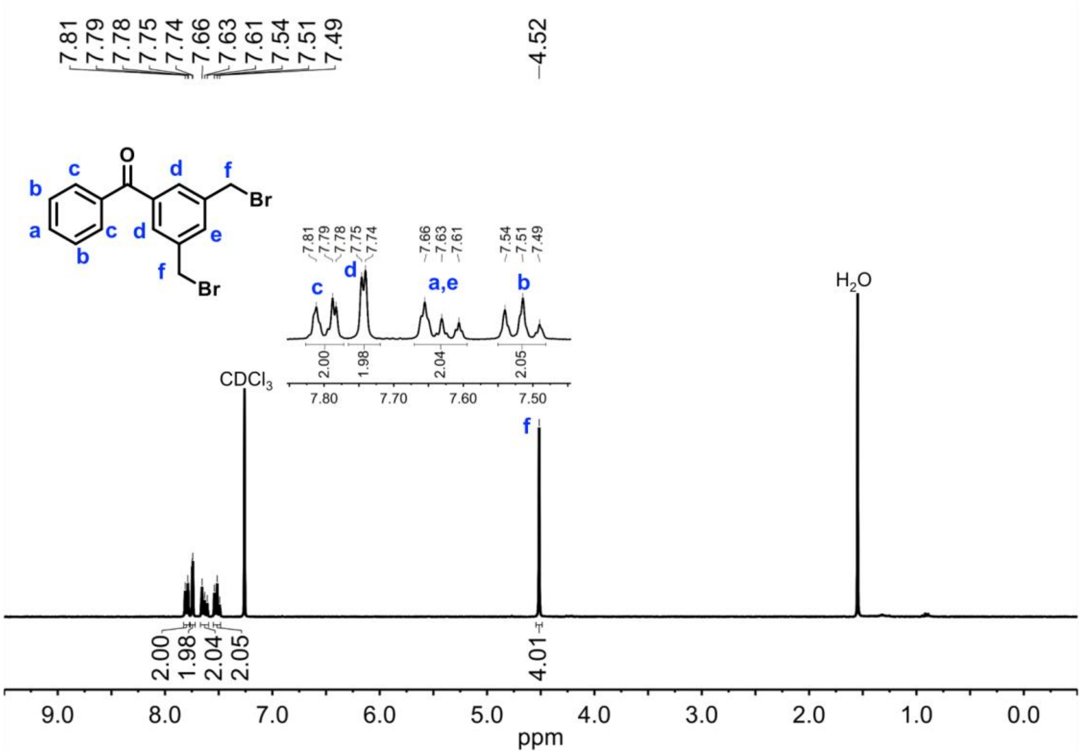

Figure 1.18. ^{1}H NMR (300 MHz; CDCl$_3$) of bromide **4**.

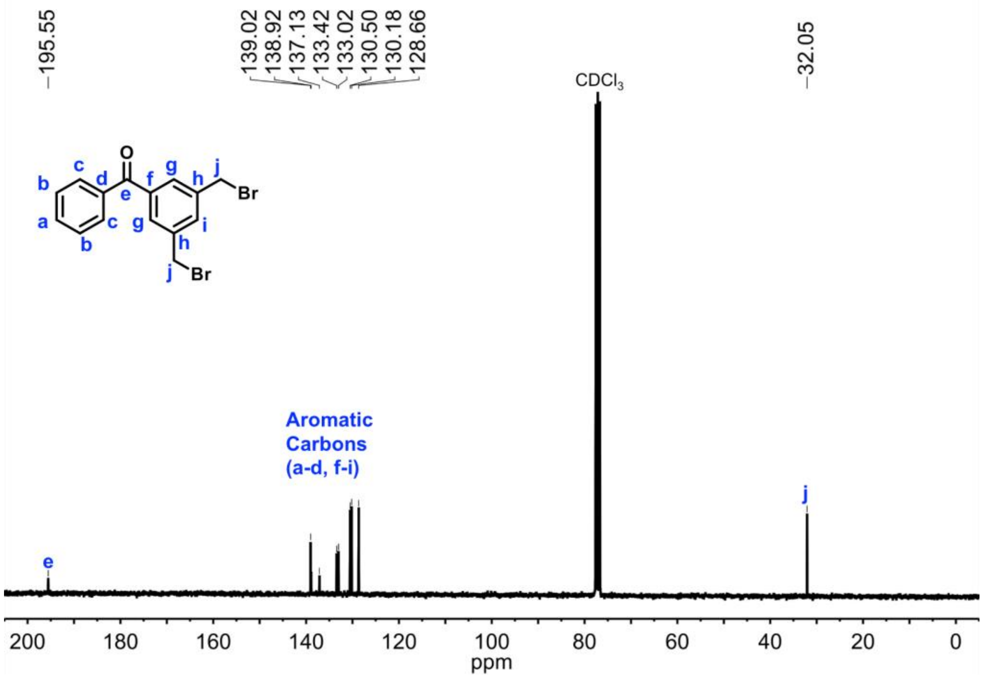

Figure 1.19. ^{13}C NMR (300 MHz; CDCl$_3$) of bromide **4**.

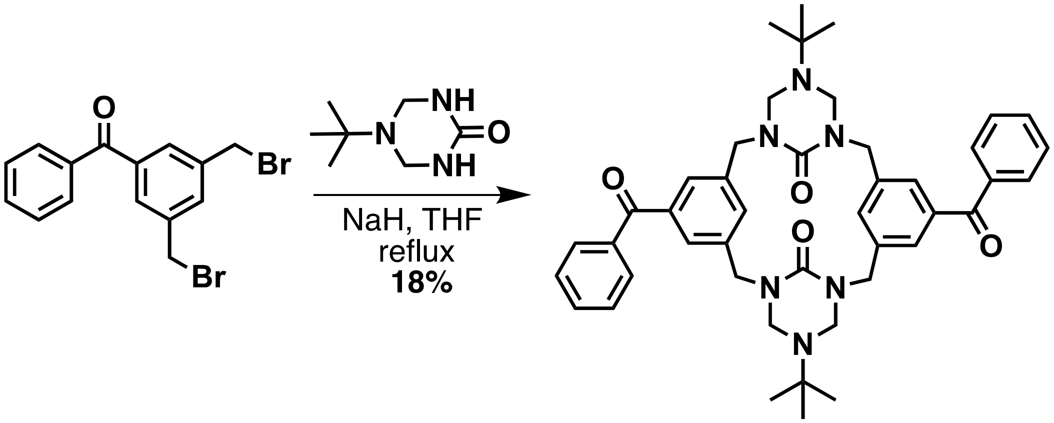

Triazinanone (0.546 g, 3.47 mmol) and NaH (60% suspension in paraffin oil, 0.558 g, 14.0 mmol) were suspended in dry THF (260 mL) and allowed to stir at rt for 10 min under N$_2$. Afterwards, a solution of 3,5-*bis*(bromomethyl) benzophenone (1.28 g, 3.47 mmol) in dry THF (70 mL) was added. The reaction was then allowed to reflux for 72 h. The reaction was then cooled to rt and neutralized with 1 N HCl. H_2O (65 mL) was added and the THF was removed via rotary evaporation. The solution was then extracted with DCM (3 x 55 mL), washed with brine (100 mL) and dried over $MgSO_4$. The combined organic layers were evaporated under reduced pressure. The product was then recrystallized via solvent diffusion of MeOH into a saturated $CHCl_3$ solution to yield colorless crystals (0.227 g, 18%). ^1H NMR (400 MHz; 120°C; DMSO-d6) δ 7.77-7.74 (6 H, m), 7.67 (2 H, t, *J* = 7.6 Hz), 7.58-7.52 (8 H, m), 4.64 (8 H, s), 4.25 (8 H, s), 1.07 (18 H, s). ^{13}C NMR (400 MHz; 80°C; DMSO-d6) δ 195.29, 154.59, 139.64, 137.02, 136.72, 132.10, 129.05, 128.92, 128.09, 126.85, 61.68, 53.24, 47.29, 27.59.

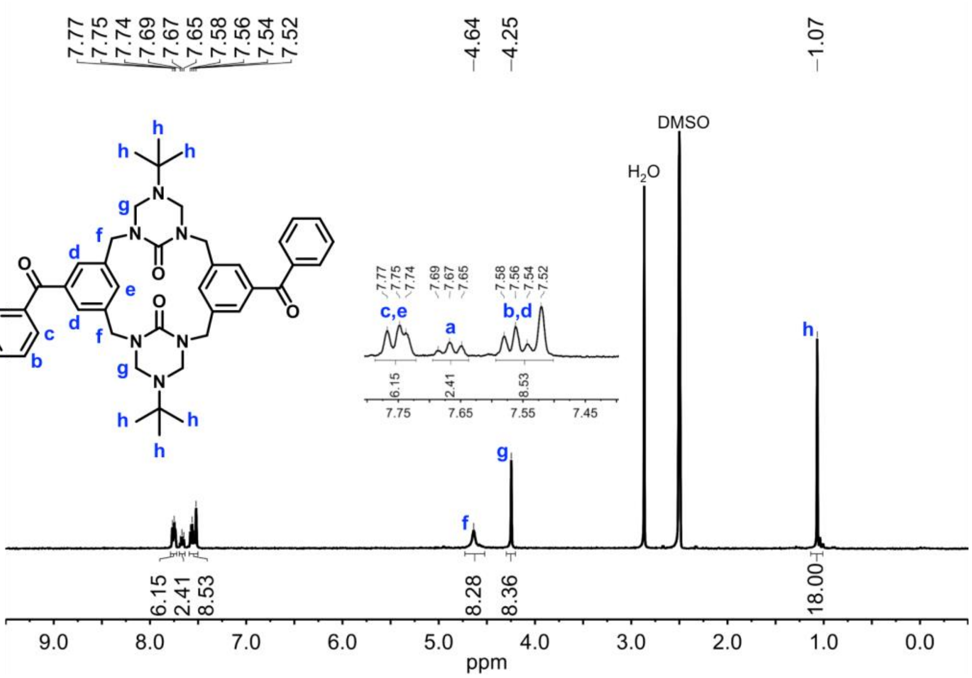

Figure 1.20. ^1H NMR (300 MHz; DMSO) of protected **4**.

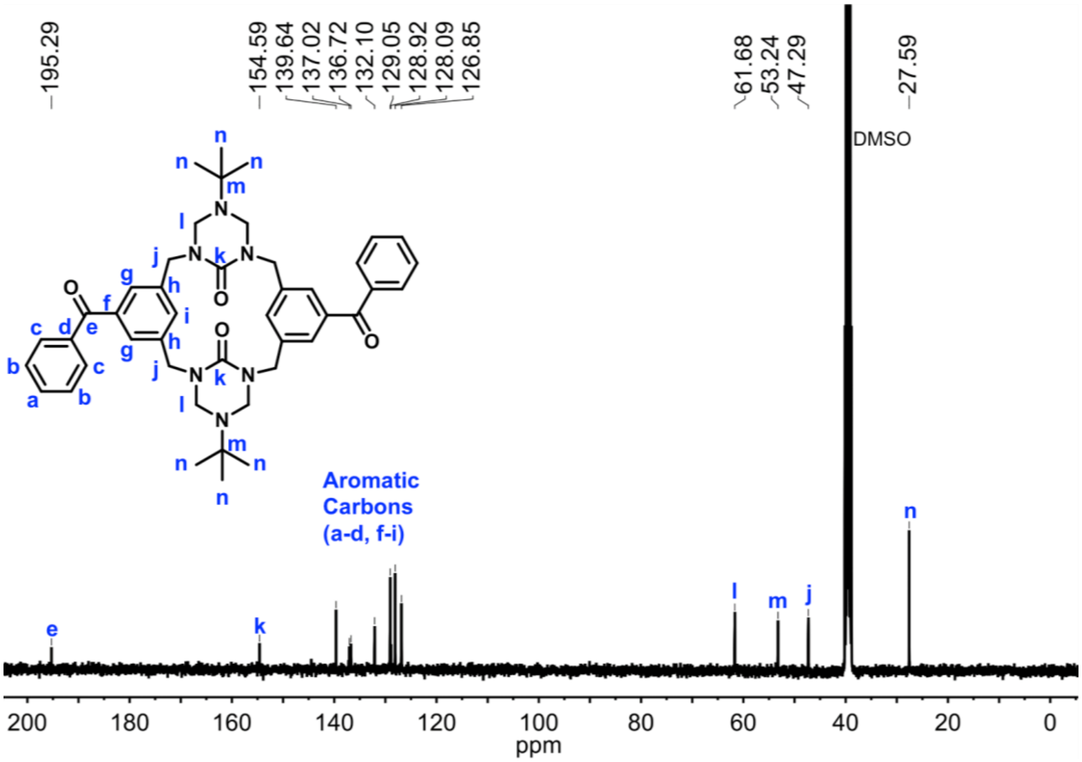

Figure 1.21. ^{13}C NMR (300 MHz; DMSO) of protected **4**.

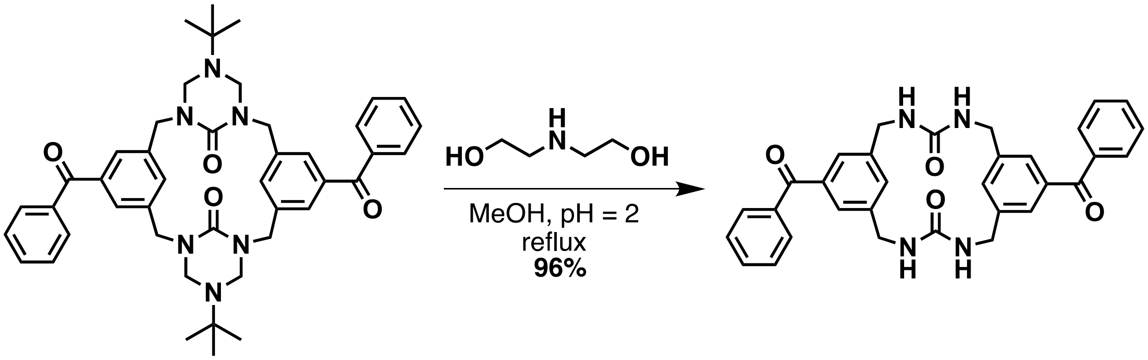

The previous protected macrocycle (0.227 g, 0.312 mmol) was added to 50:40:10 v/v mixture of methanol, water, and diethanol amine (pH ~2, 160 mL) and was refluxed as a suspension for 96 h. The pH was readjusted to 2 as needed using HCl. After cooling to rt, the precipitate was collected via vacuum filtration and was washed with 1 N HCl (20 mL), distilled water (3 x 100 mL), and was dried under vacuum to yield a white solid (0.160 g, 96%). ^{1}H NMR (300 MHz; DMSO-d6) δ 7.75 (4 H, d, *J* = 7.8 Hz), 7.69 (2 H, d, *J* = 7.3 Hz), 7.62-7.55 (6 H, m), 7.41 (4 H, s), 6.65 (4 H, s), 4.61 - 4.14 (8 H, br s). ^{13}C NMR (300 MHz; DMSO-d6) δ 195.87, 157.93, 142.41, 137.18, 136.51, 132.66, 129.56, 128.59, 127.91, 126.19, 42.28.

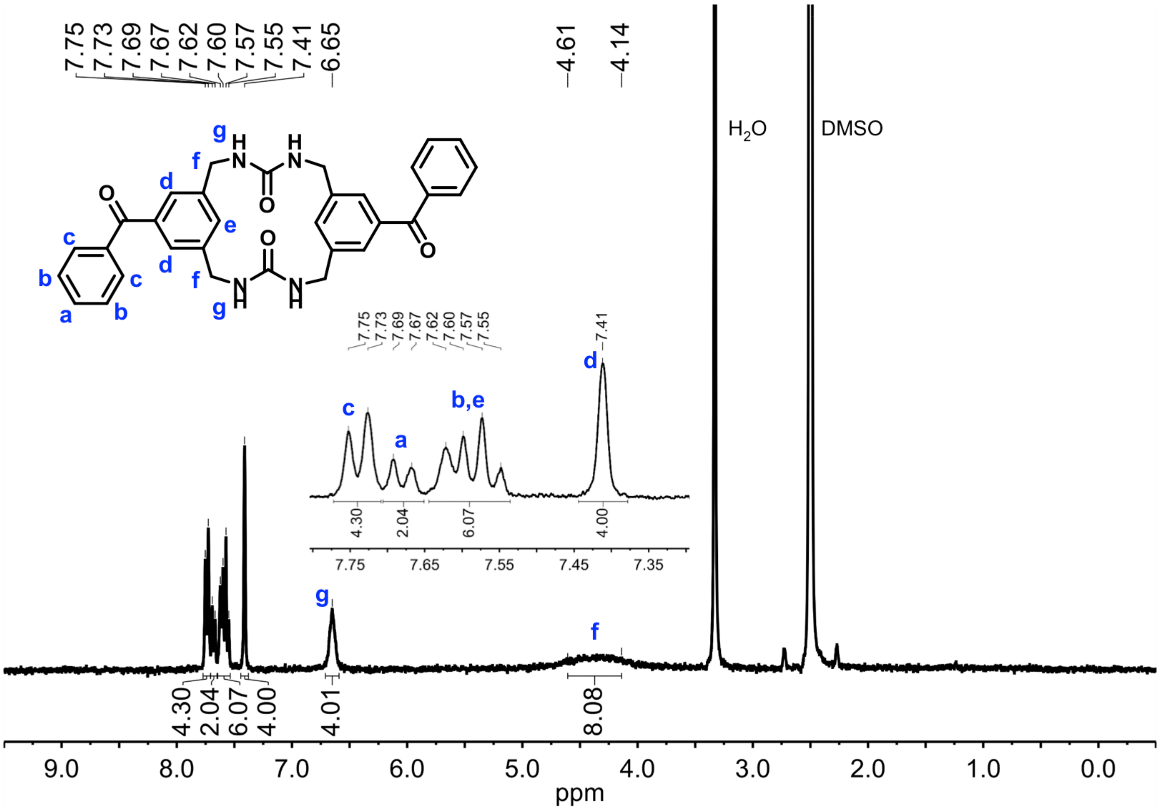

Figure 1.22.^{1}H NMR (300 MHz; DMSO) of **4**.

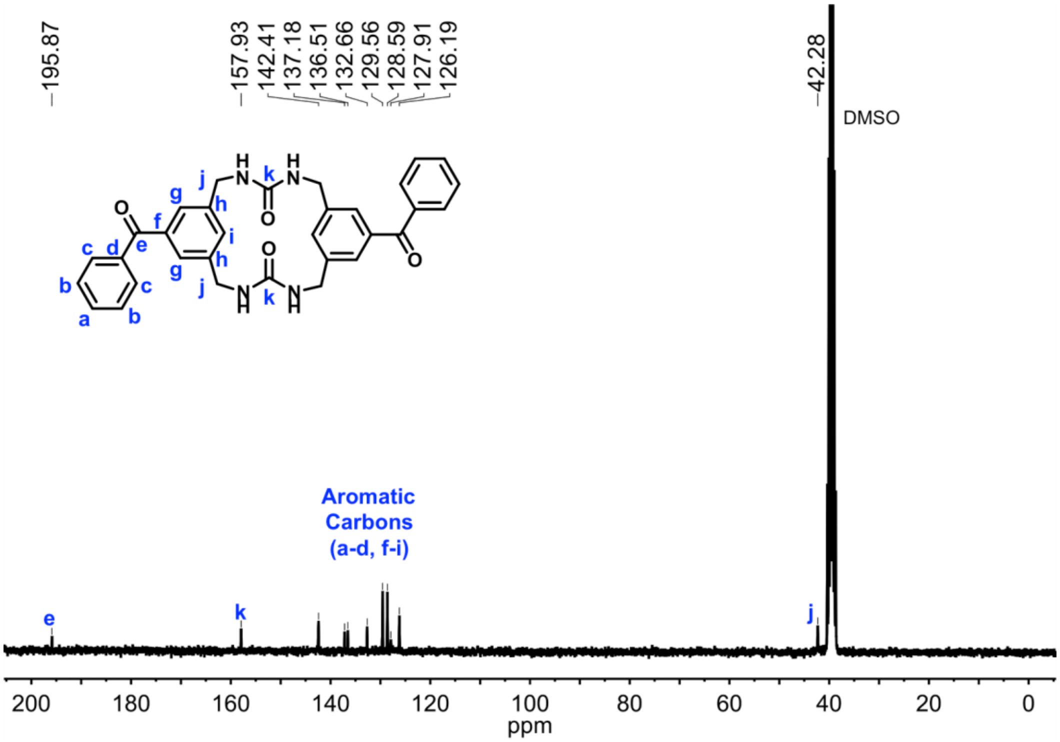

Figure 1.23. ^{13}C NMR (300 MHz; DMSO) of **4**.

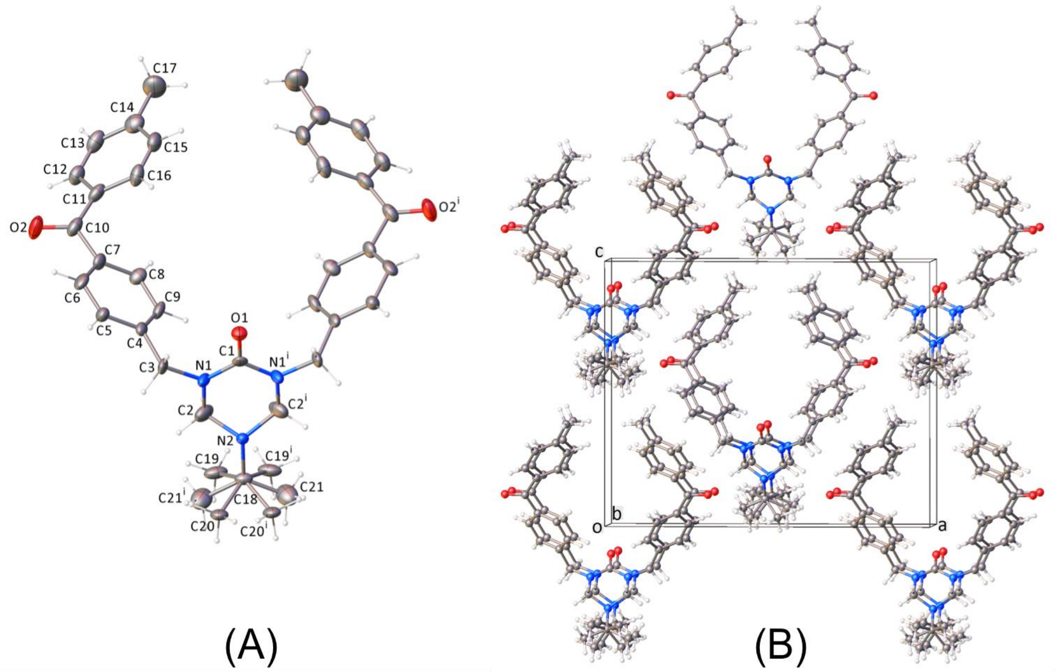

(A)

(B)

Figure 1.24. X-ray crystal structure and data of protected **2**. (A) Molecular structure and (B) crystal packing.

The compound crystallizes in the orthorhombic system. The pattern of systematic absences in the intensity data was consistent with the space groups Pmn2_1 and Pmmn. Structure solution using the intrinsic phasing method SHELXT generated a reasonable solution in the non-centrosymmetric group Pmn2_1. Pmn2_1 was confirmed by further refinement of the obtained model and also with the ADDSYM program.[45-48] The asymmetric unit consists of half of one $C_{37}H_{39}N_3O_3$ molecule and a region of disordered solvent molecules. The $C_{37}H_{39}N_3O_3$ molecule is located on a crystallographic mirror plane. Atoms C19-C21 of the *tert*-butyl group are disordered across the mirror plane and were refined with half-occupancy. Distances from the three disordered methyl carbons to C18 were restrained to be similar. Efforts to model the solvent disorder were unsuccessful. Trial modeling attempts suggest a mixture of ethanol and other unknown solvents, possible methanol and water. The Squeeze program in PLATON was used to account for these species.[48,49] The solvent-accessible volume was calculated to be 189 Å^3 per unit cell (11.5% of the total cell volume), containing the equivalent of 52 electrons per unit cell. The scattering contribution of this electron density was added to the structure factors computed from the known part of the structure during refinement. For comparison, the residual factors were R1/*w*R2 = 0.068/0.163 for the best disorder model, and R1/*wR2* = 0.058/0.127 after applying Squeeze. The reported crystal density and *F.W.* are calculated from the known part of the structure only. All non-hydrogen atoms were refined with anisotropic displacement parameters. Hydrogen atoms bonded to carbon were placed in geometrically idealized positions and included as riding atoms with (C-H) = 0.95 Å and *U*iso(H) = 1.2Ueq(C) for aromatic hydrogen atoms, *d*(C-H) = 0.99 Å and *U*iso(H) = 1.2Ueq(C) for methylene hydrogen atoms, and *d*(C-H) = 0.98 Å and *U*iso(H) = 1.5*U*eq(C) for methyl hydrogens. The largest residual electron density peak in the final difference map is 0.19 e-/Å^3, located 1.80 Å from H20B.

Crystal data structure and refinement for protected **2**. The .CIF file has been deposited CCDC 1855195.

Empirical formula	$C_{37}H_{39}N_3O_3$
Formula weight	573.71
Temperature/K	100(2)
Crystal system	orthorhombic
Space group	$Pmn2_1$
a/Å	19.855(2)
b/Å	5.3006(6)
c/Å	15.6536(18)
α/°	90
β/°	90
γ/°	90
Volume/Å^3	1647.4(3)
Z	2
ρcalcg/cm^3	1.157
μ/mm^{-1}	0.074
F(000)	612.0

Crystal size/mm^3	0.24 × 0.06 × 0.04
Radiation	MoK$_\alpha$ (λ = 0.71073)
2Θ range for data collection/°	6.63 to 48.484
Index ranges	$-22 \leq h \leq 22$, $-6 \leq k \leq 6$, $-18 \leq l \leq 17$
Reflections collected	11495
Independent reflections	2726 [R_{int}=0.0848, R_{sigma}=0.0638]
Data/restraints/parameters	2726/4/215
Goodness-of-fit on F^2	1.057
Final R indexes [I>=2σ (I)]	R_1 = 0.0577, wR_2 = 0.1156
Final R indexes [all data]	R_1 = 0.0891, wR_2 = 0.1269
Largest diff. peak/hole / e Å^{-3}	0.19/-0.23

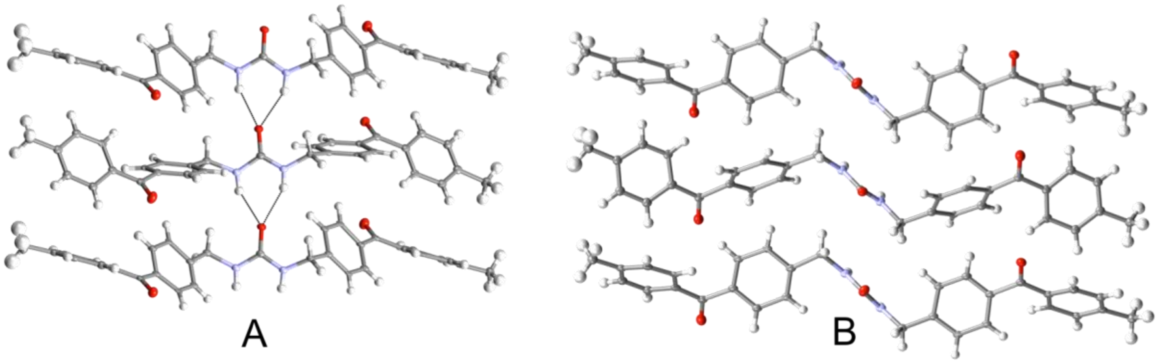

Figure 1.25.X-ray crystal structure and data of **2**. (A) Molecular structure and (B) crystal packing.

The compound crystallizes in the triclinic system. A reasonable, non-disordered solution was obtained in *P*1 (No. 1). The asymmetric unit in *P*1 consists of two independent $C_{31}H_{28}N_2O_3$ molecules, which were numbered identically except for label suffixes A or B. All non-hydrogen atoms were refined with anisotropic displacement parameters. Hydrogen atoms were placed in geometrically idealized positions and included as riding atoms with *d*(N-H) = 0.88 Å and *U*iso(H) = 1.2*U*eq(N) for urea hydrogen atoms, *d*(C-H) = 0.95 Å and *U*iso(H) = 1.2*U*eq(C) for aromatic hydrogen atoms, *d*(C-H) = 0.99 Å and *U*iso(H) = 1.2*U*eq(C) for methylene hydrogen atoms, and *d*(C-H) = 0.98 Å and *U*iso(H) = 1.5*U*eq(C) for methyl hydrogens. The methyl hydrogens were allowed to rotate as a rigid group to the orientation of maximum observed electron density. The largest residual electron density peak in the final difference map is 1.10 $e^-/Å^3$ located 1.06 Å from H2A. This and the other several largest peaks likely represent minor disorder components of the urea group oxygen and nitrogen atoms. Such disorder could not be successfully modeled because of the small magnitude of the residual density. Because of the absence of heavy atoms in the crystal, Friedel opposites were merged during refinement and no attempt made to determine the absolute structure. A check of the final structural model with ADDSYM showed no missed symmetry elements.[44-47]

Crystal data structure and refinement for triply recrystallized **2**. The .CIF file has been deposited CCDC 1855192.

Empirical formula	$C_{31}H_{28}N_2O_3$
Formula weight	476.55
Temperature/K	100(2)
Crystal system	triclinic
Space group	P1 (No. 1)
a/Å	6.0098(3)

b/Å	7.2615(3)
c/Å	27.0654(11)
α/°	93.9470(10)
β/°	90.4050(10)
γ/°	91.1100(10)
Volume/$Å^3$	1178.07(9)
Z	2
ρcalcg/cm^3	1.343
μ/mm^{-1}	0.087
F(000)	504.0
Crystal size/mm^3	0.54 × 0.36 × 0.03
Radiation	MoK_{α} ($\lambda = 0.71073$)
2Θ range for data collection/°	4.526 to 60.128
Index ranges	$-8 \le h \le 8$, $-10 \le k \le 10$, $-38 \le l \le 38$
Reflections collected	72515
Independent reflections	13721 [$R_{int}=0.0447$, $R_{sigma}=0.0458$]
Data/restraints/parameters	13721/3/657
Goodness-of-fit on F^2	1.028
Final R indexes [I>=2σ (I)]	$R_1 = 0.0560$, $wR_2 = 0.1464$
Final R indexes [all data]	$R_1 = 0.0868$, $wR_2 = 0.1642$
Largest diff. peak/hole / e $Å^{-3}$	1.10/-0.31

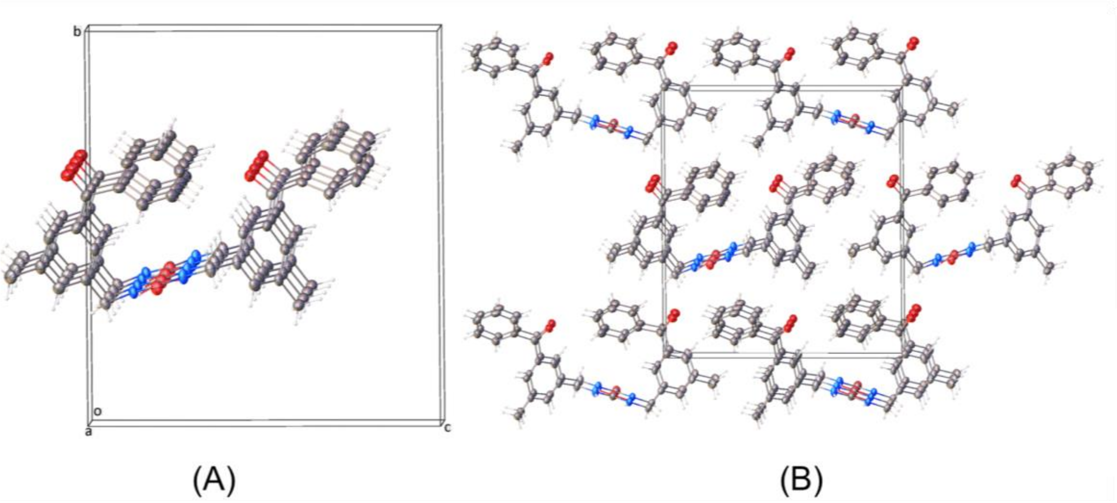

Figure 1.26. X-ray crystal structure and data of **3**. (A) Molecular structure and (B) crystal packing.

The compound crystallizes in the monoclinic system. The pattern of systematic absences in the intensity data positively ruled out a glide plane, leaving space groups $P2_1$ and $P2_1/m$ as possibilities. Intensity statistics suggested an acentric structure. The solution program XT returned a chemically and crystallographically stable solution in $P2_1$, which was verified by refinement and further with ADDSYM.[44-47] The asymmetric unit consists of one molecule. All non-hydrogen atoms were refined with anisotropic displacement parameters. Hydrogen atoms bonded to carbon were located in Fourier difference maps before being placed in geometrically idealized positions and included as riding atoms with d(C-H) = 0.95 Å and Uiso(H) = 1.2Ueq(C) for aromatic hydrogen atoms, d(C-H) = 0.99 Å and Uiso(H) = 1.2Ueq(C) for methylene hydrogen atoms, and d(C-H) = 0.98 Å and Uiso(H) = 1.5Ueq(C) for methyl hydrogens. The methyl hydrogens were allowed to rotate as a rigid group to the orientation of maximum observed electron density. Hydrogen atoms bonded to nitrogen were located and refined freely. Because of the absence of heavy atoms in the crystal, Friedel opposites were merged during refinement and no attempt made to determine the absolute structure. The largest residual electron density peak in the final difference map is 0.67 $e^-/Å^3$, located 0.58 Å from H21.

Crystal data structure and refinement for **3**. The .CIF file has been deposited CCDC 1855193.

Empirical formula	$C_{31}H_{28}N_2O_3$
Formula weight	476.55
Temperature/K	100(2)
Crystal system	monolinic
Space group	$P2_1$
a/Å	4.5113(3)
b/Å	17.3791(10)
c/Å	15.5995(9)
α/°	90
β/°	94.788(3)
γ/°	90
Volume/$Å^3$	1218.77(13)
Z	2
$\rho_{calc}g/cm^3$	1.299
μ/mm^{-1}	0.084

F(000)	504.0
Crystal size/mm^3	0.44 × 0.05 × 0.02
Radiation	MoK$_\alpha$ (λ = 0.71073)
2Θ range for data collection/°	4.688 to 50.112
Index ranges	$-5 \le h \le 5$, $-20 \le k \le 20$, $-18 \le l \le 18$
Reflections collected	18116
Independent reflections	4313 [R$_{int}$=0.0791, R$_{sigma}$=0.0870]
Data/restraints/parameters	4313/1/336
Goodness-of-fit on F^2	1.022
Final R indexes [I>=2σ (I)]	R$_1$ = 0.0602, wR$_2$ = 0.1338
Final R indexes [all data]	R$_1$ = 0.1058, wR$_2$ = 0.1494
Largest diff. peak/hole / e Å^{-3}	0.67/-0.20

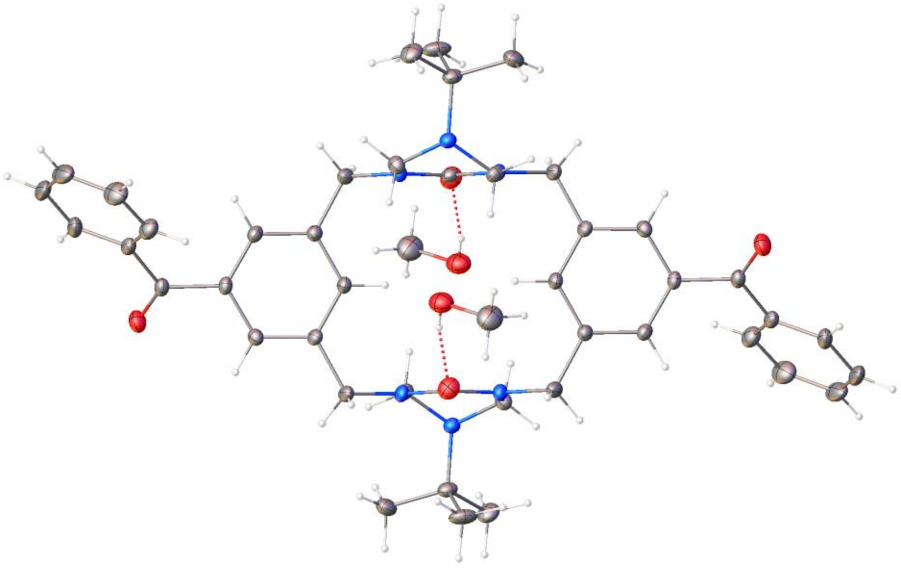

Figure 1.27. X-ray crystal structure and data of protected **4**, which was crystallized via solvent diffusion of MeOH into a saturated solution of protected **4** in $CHCl_3$.

The compound crystallizes in the monoclinic system. The pattern of systematic absences in the intensity data was consistent with the space group $P2_1/c$, which was verified by structure solution. The asymmetric unit consists of half of one $C_{44}H_{50}N_6O_4$ cycle and one methanol molecule. The $C_{44}H_{50}N_6O_4$ cycle is located on a crystallographic inversion center. All non-hydrogen atoms were refined with anisotropic displacement parameters. Hydrogen atoms bonded to carbon were located in Fourier difference maps before being placed in geometrically idealized positions and included as riding atoms with d(C-H) = 0.95 Å and Uiso(H) = 1.2Ueq(C) for aromatic hydrogen atoms, d(C-H) = 0.99 Å and Uiso(H) = 1.2Ueq(C) for methylene hydrogen atoms, and d(C-H) = 0.98 Å and Uiso(H) = 1.5Ueq(C) for methyl hydrogens. The methyl hydrogens were allowed to rotate as a rigid group to the orientation of maximum observed electron density. The hydrogen atom bonded to the methanol oxygen was located in a difference map and refined isotropically with a d(O-H) = 0.85(2) Å distance restraint. The largest residual electron density peak in the final difference map is 0.57 e^-/Å^3, located 0.80 Å from H22C.

Crystal data structure and refinement for protected **4**. The .CIF file has been deposited CCDC 1855194.

Empirical formula	$C_{46}H_{58}N_6O_6$
Formula weight	790.98
Temperature/K	100(2)
Crystal system	monolinic
Space group	$P2_1/c$

a/Å	14.4912(6)
b/Å	9.6735(4)
c/Å	16.1330(10)
α/°	90
β/°	115.788(3)
γ/°	90
Volume/Å^3	2050.76(15)
Z	2
$\rho_{calc}{}^{g}/cm^{3}$	1.281
μ/mm^{-1}	0.086
F(000)	848.0
Crystal size/mm^3	0.38 × 0.34 × 0.12
Radiation	MoK$_\alpha$ (λ = 0.71073)
2Θ range for data collection/°	5.048 to 60.242
Index ranges	$-20 \leq h \leq 20$, $-13 \leq k \leq 13$, $-22 \leq 1 \leq 22$
Reflections collected	110998
Independent reflections	6044 [R_{int}=0.0372, R_{sigma}=0.0159]
Data/restraints/parameters	6044/1/270
Goodness-of-fit on F^2	1.045
Final R indexes [I>=2σ (I)]	R_1 = 0.0468, wR_2 = 0.1229
Final R indexes [all data]	R_1 = 0.0590, wR_2 = 0.1313
Largest diff. peak/hole / e Å^{-3}	0.57/-0.32

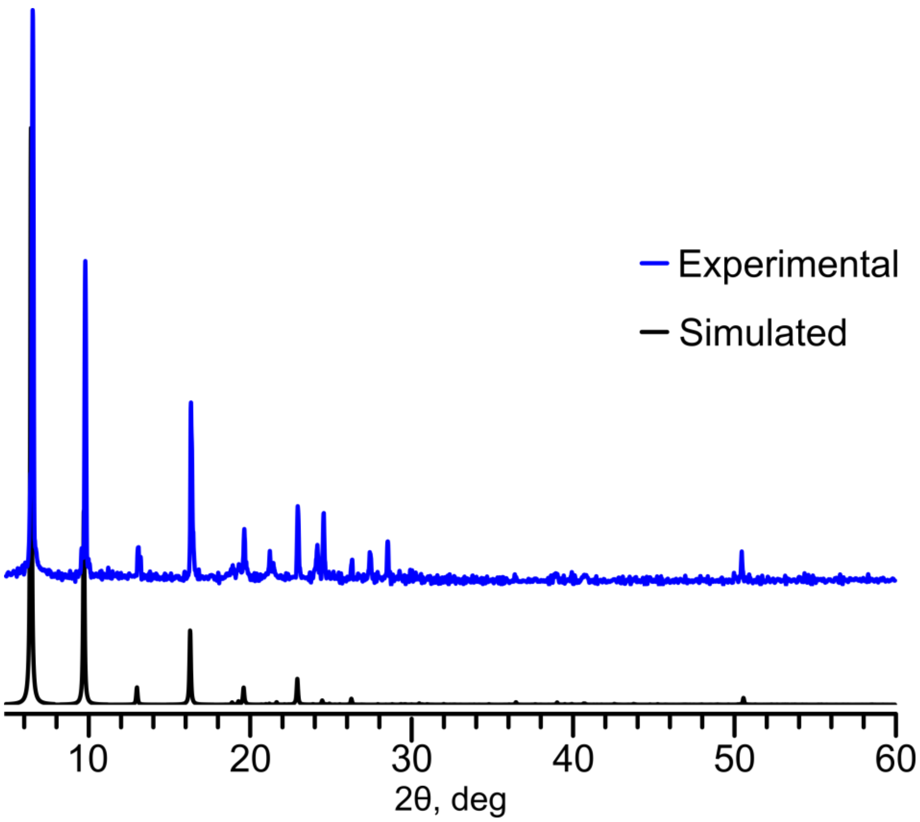

Figure 1.28. PXRD pattern of triply recrystallized **2**.

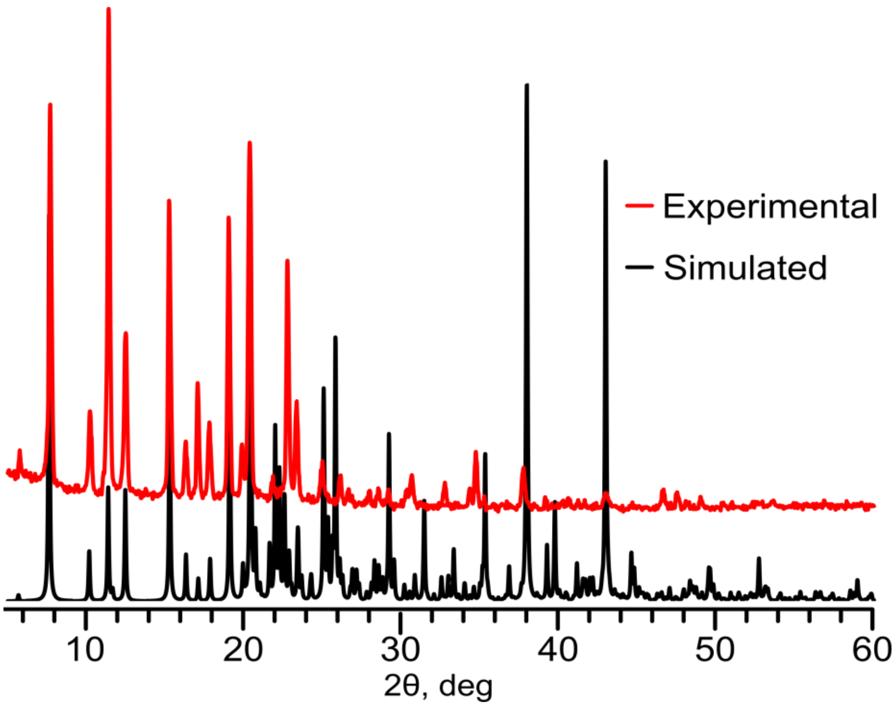

Figure 1.29. PXRD pattern of triply recrystallized **3**.

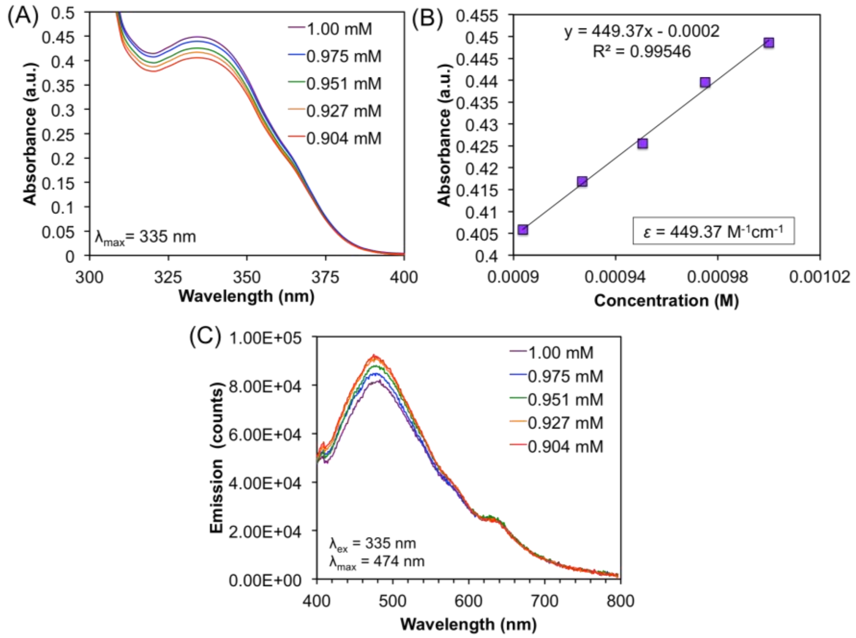

Figure 1.30. Absorption and emission spectra of **2** in DMSO (0.904 – 1.00 mM). (A) Absorbance spectra, λ_{max} = 335 nm. (B) Plot of concentration vs. absorbance used to calculate the molar absorptivity (C) emission spectra, λ_{ex} = 335 nm exhibiting a transition at 474 nm.

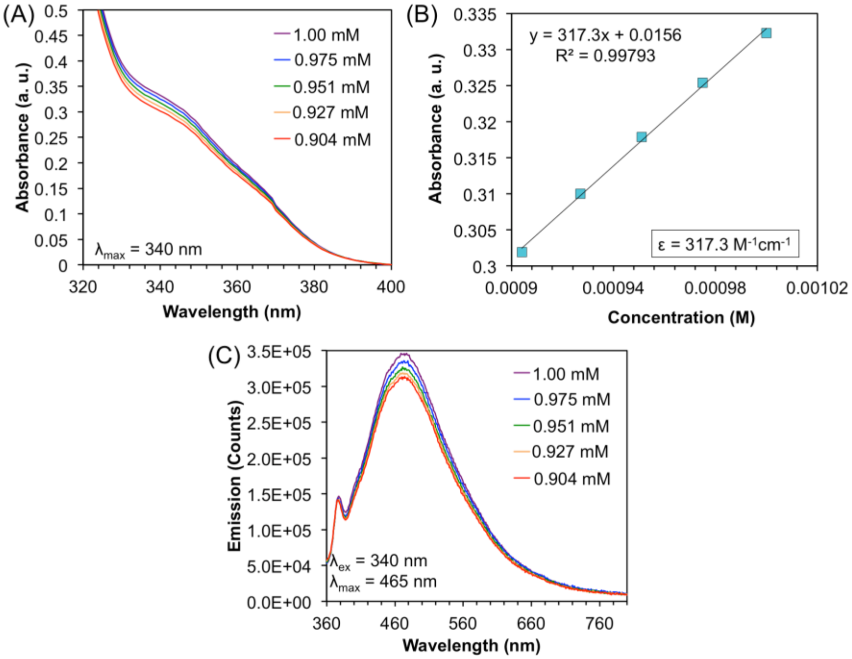

Figure 1.31. Absorption and emission spectra of **3** in DMSO (0.904 – 1.00 mM). (A) Absorbance spectra, λ_{max} = 340 nm. (B) Plot of concentration vs. absorbance used to calculate the molar absorptivity (C) emission spectra, λ_{ex} = 355 nm exhibiting a transition at 465 nm.

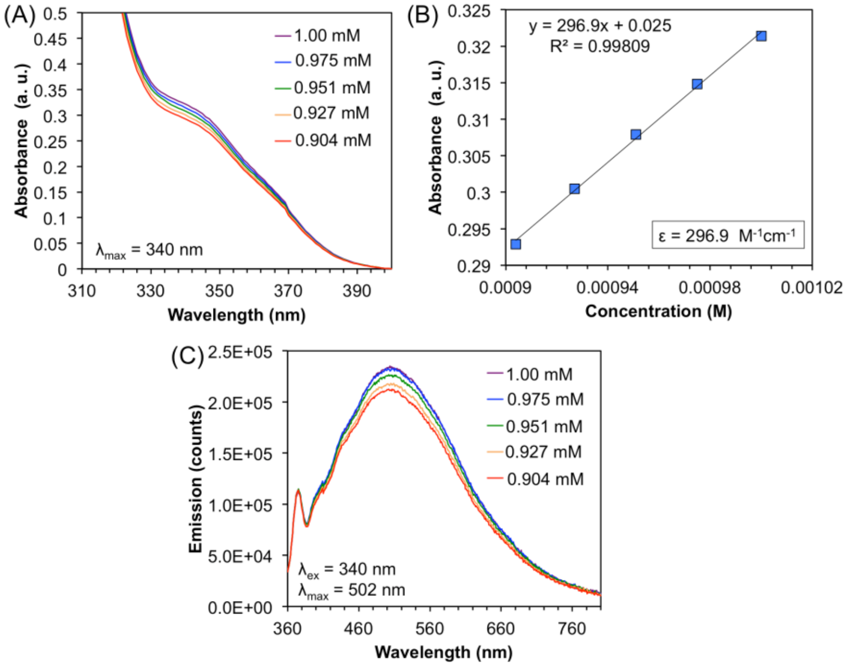

Figure 1.32. Absorption and emission spectra of **4** in DMSO (0.904 – 1.00 mM). (A) Absorbance spectra, λ_{max} = 340 nm. (B) Plot of concentration vs. absorbance used to calculate the molar absorptivity (C) emission spectra, λ_{ex} = 340 nm exhibiting a transition at 502 nm.

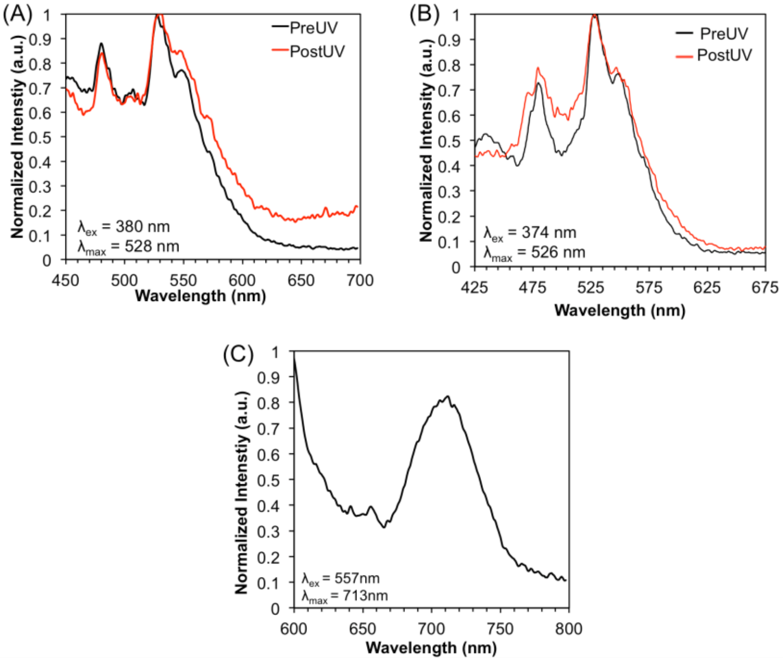

Figure 1.33. Solid-state emission spectra recorded on triply recrystallized samples of (A) **2** excited at 380 nm, λ_{max} = 528 nm, (B) **3** excited at 374 nm, λ_{max} = 526 nm, and (C) 557 nm excitation of the UV-irradiated sample of **2** exhibiting a transition at 713 nm.

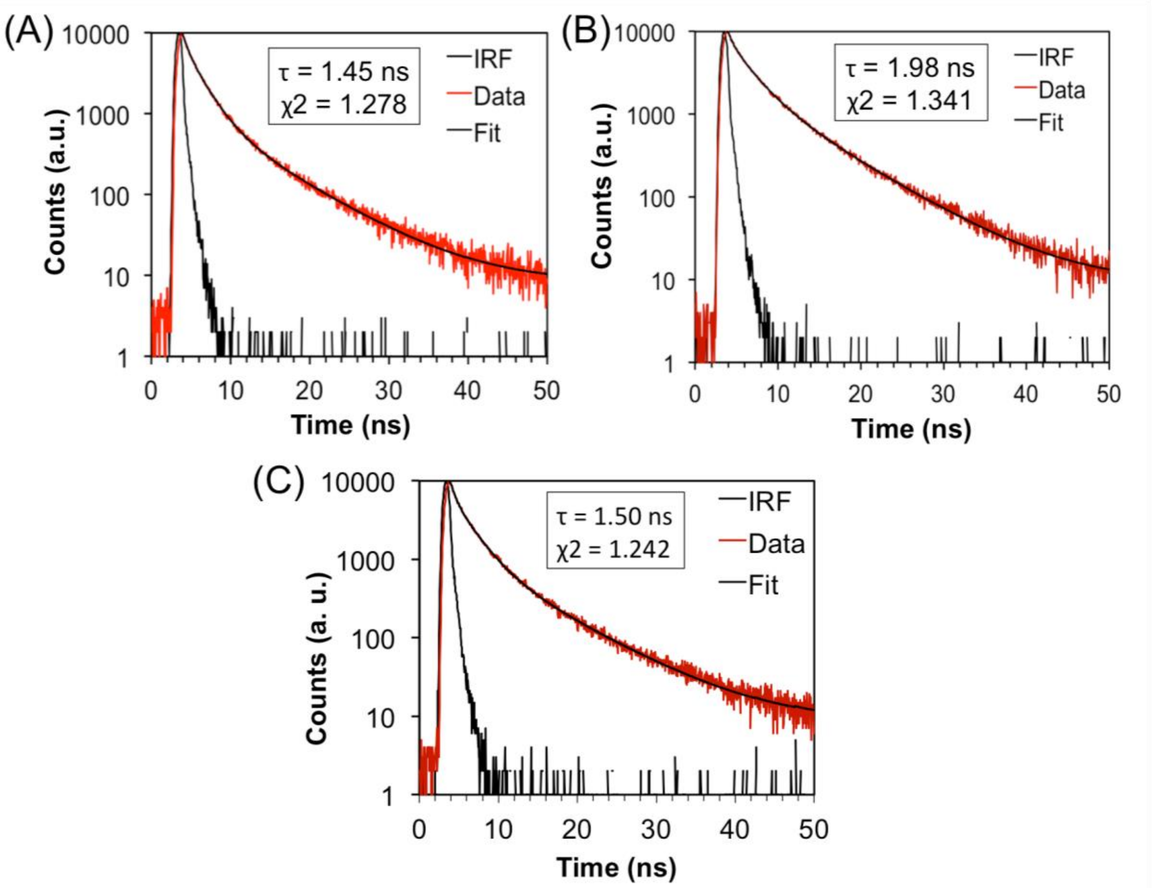

Figure 1.34. Lifetime decay of (A) **2**, (B) **3**, and (C), **4** in DMSO solutions, 0.904 mM.

The lifetime decays were fit with the triexponential function. The amplitude-weighted average lifetimes were calculated based on the following equation:

$$< \tau_{av} > = \frac{B_1\tau_1+B_2\tau_2+B_3\tau_3}{B_1+B_2+B_3} \qquad \text{(Eq'n 1.1)}$$

Table 1.2. Time constants (τ_i) and amplitude (B_i) values obtained in solution.

Samples	B_1	τ_1 (ns)	B_2	τ_2 (ns)	B_3	τ_3 (ns)	$<\tau_{av}>$ (ns)
2	0.0626	0.431	0.0429	2.086	0.0062	7.375	1.45
3	0.0617	0.385	0.0333	2.463	0.0153	7.379	1.98
4	0.0706	0.454	0.0357	2.393	0.0067	7.793	1.50

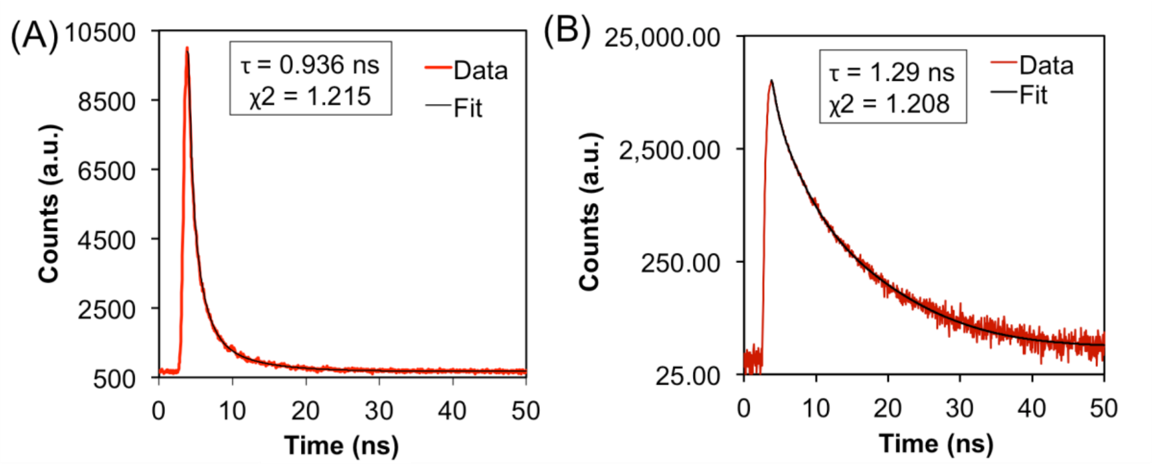

Figure 1.35. Lifetime decay of triply recrystallized (A) **2** and (B) **3**.

Table 1.3. Time constants (τ_i) and amplitude (B_i) values obtained for the triply recrystallized samples

Samples	B_1	τ_1 (ns)	B_2	τ_2 (ns)	B_3	τ_3 (ns)	$<\tau_{av>}$ (ns)
2	0.0918	0.312	0.0338	1.521	0.0076	5.879	0.934
3	0.0794	0.501	0.0311	2.234	0.0053	7.465	1.33

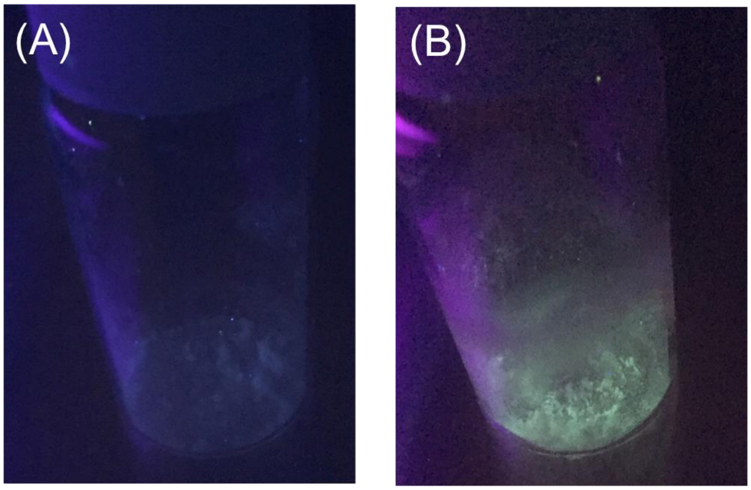

Figure 1.36. Triply recrystallized **3** under TLC lamp, (A) at room temperature (B) after freezing in a dry ice/acetone cooling-bath.

Computational Details:

The TDDFT calculations were performed with the ωB97XD[50] exchange-correlation functional and the double zeta polarized basis set including diffused functions 6-31+G**.[51] Such a long-range corrected functional can partially describe excitations with charge transfer character and includes dispersion corrections. Natural transition orbitals (NTOs) are calculated, together with a charge transfer descriptor and the electron/hole population analysis as implemented in the Theodore software package (http://theodore-qc.sourceforge.net/), to characterize the nature of such electronic transitions.[52] The solvent DMSO and its effects on the compounds absorption and structural properties were described by the implicit solvation model PCM.[53] First, the geometry of the linear analogs were preoptimized at the DFT ωB97XD/6-31G** level of theory because the presence of diffuse functions in the basis set prevented convergence of the optimization in solvent. To compute the absorption of the analogs 25 excited states (15 for **2** in gas phase) were sufficient to reproduce the main features of the experimental spectrum. Convoluted spectra were generated using Lorentzian line shapes at a full width half maximum of 10 nm for the gas phase and 15 nm for solution. The calculations have been performed with the Gaussian09 software package.[54]

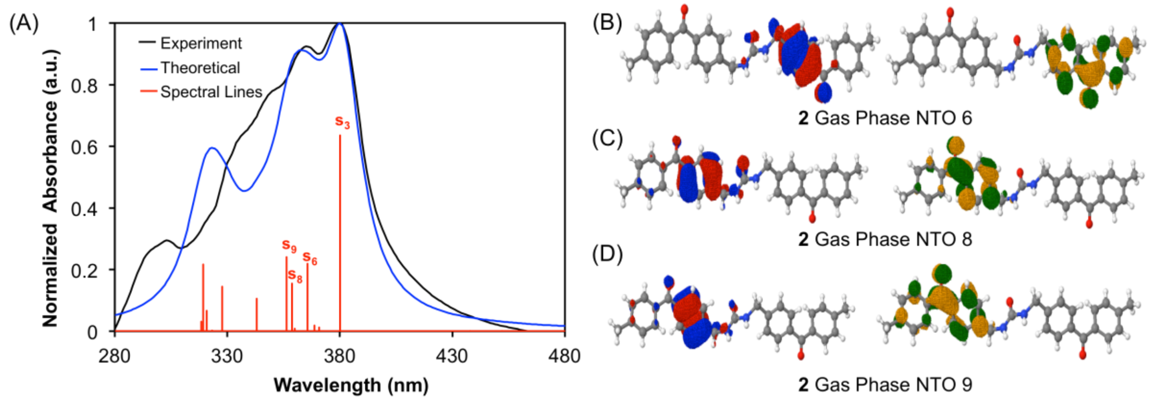

Figure 1.37. (A) Solid-state experimental absorption spectrum, theoretical absorption in the gas phase and corresponding spectral lines of **2**. The excited states are labeled. NTO pairs corresponding to the (B) S_6, (C) S_8, and (D) S_9 excited states of **2** in the gas phase.

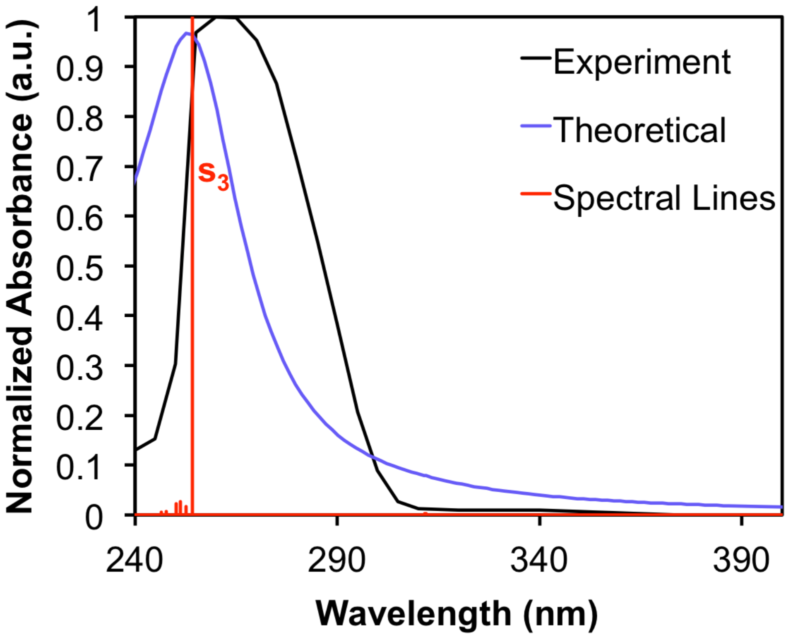

Figure 1.38. Experimental absorption spectrum (solution), theoretical absorption in DMSO and corresponding spectral lines of **2**. The spectral lines were normalized due to high oscillator strength. The S_3 excited state, responsible for the absorption is labeled.

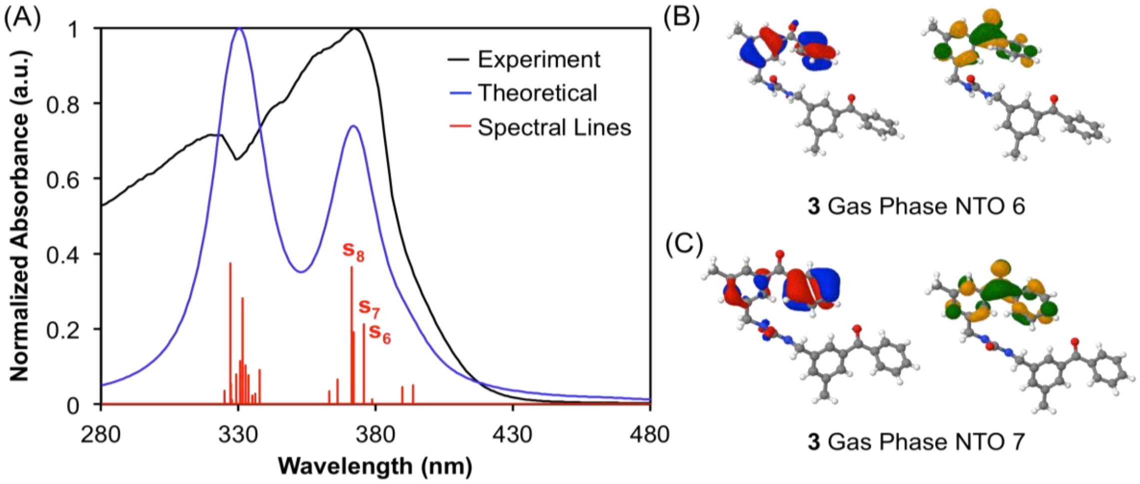

Figure 1.39. (A) Experimental absorption spectrum (solid-state), shifted (135 nm) theoretical absorption in the gas phase and corresponding spectral lines of **3**. The S_6, S_7, and S_8 excited states are labeled. NTO pairs corresponding to the (B) S_6 and (C) S_7 excited states of **3** in the gas phase.

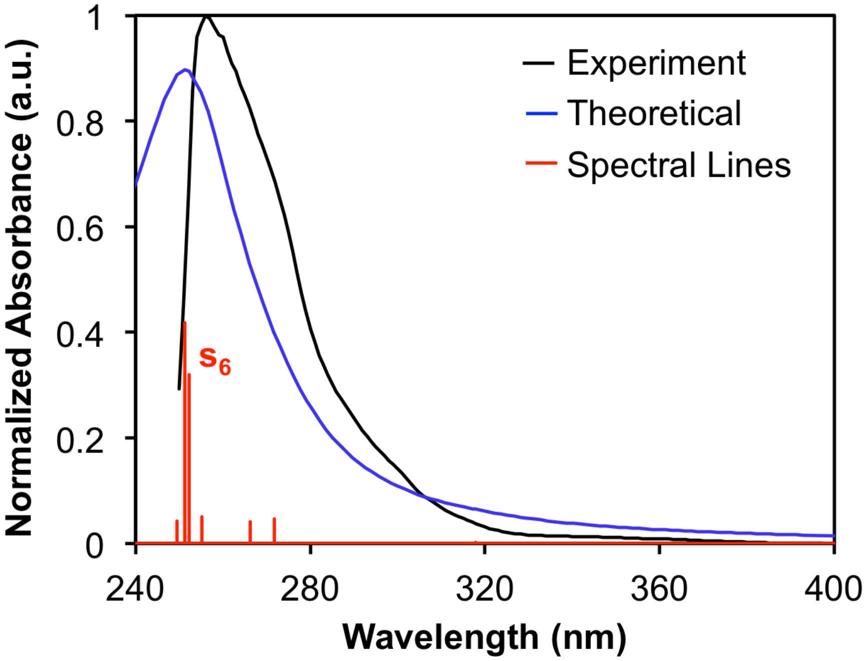

Figure 1.40. Experimental absorption spectrum (solution), theoretical absorption in DMSO and corresponding spectral lines of **3**. The S_6 excited state is labeled.

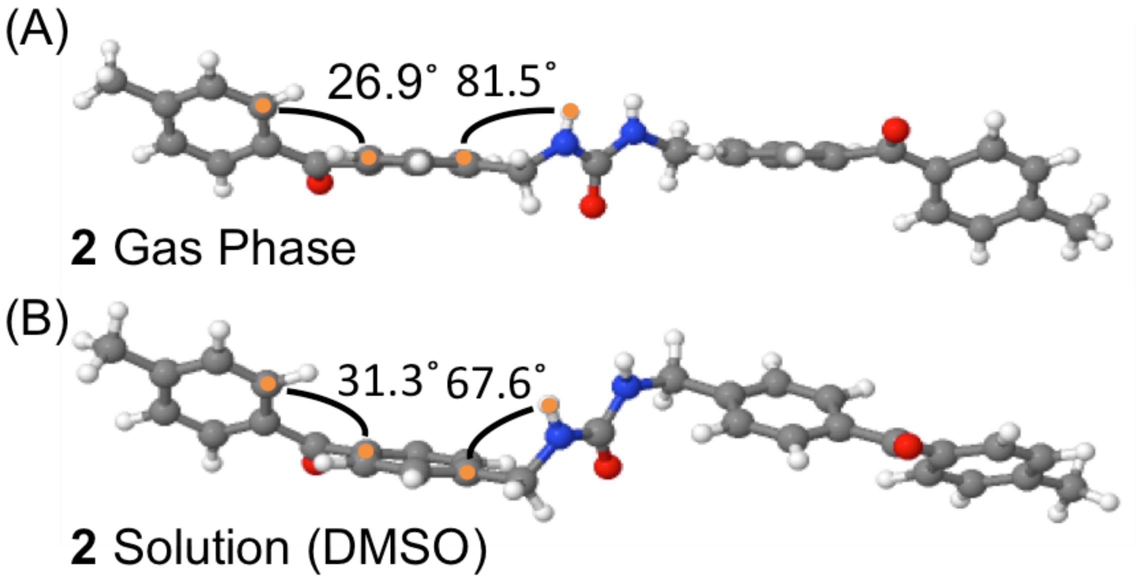

Figure 1.41. Difference in geometry between the crystal (gas phase, A) and the optimized structure in solution (B), for **2**. From left to right the torsion angles correlate to the angle between the benzenes on the benzophenones and the angle between the inner benzophenone benzene and urea hydrogen are reported, being the main geometrical difference between the two structures.

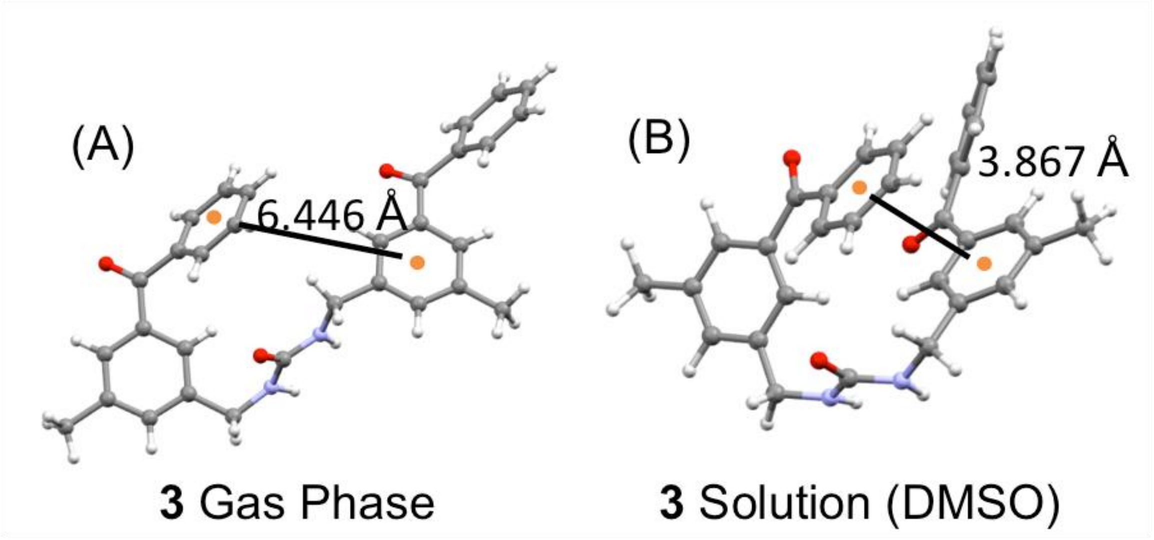

Figure 1.42. Geometry difference between (A) the crystal in the gas phase and (B) the optimized structure in solution for **2**. The main difference is the distance change between the highlighted benzene centroids.

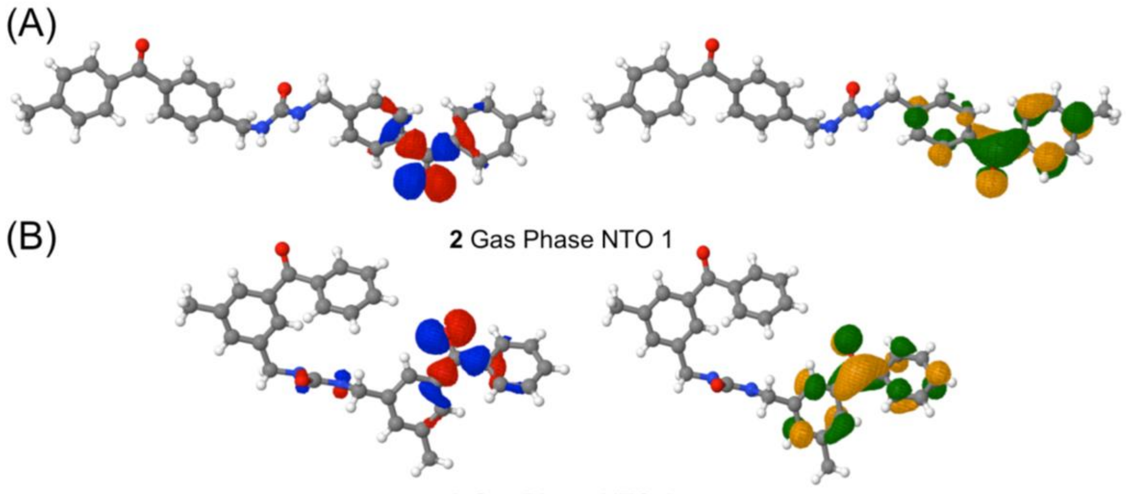

2 Gas Phase NTO 1

3 Gas Phase NTO 1

Figure 1.43. NTO pairs corresponding to the dark S_1 state (nπ*) for (A) **2** and (B) **3** in the gas phase.

Table 1.4. Optimized geometries used for excited state calculations for **2** and **3** given in Cartesian coordinates.

2				**3**			
Atom	X (Å)	Y (Å)	Z (Å)	Atom	X (Å)	Y (Å)	Z (Å)
O1	0.222	0.756	-0.608	O1	-2.721	-2.882	0.446
O2	-6.899	2.777	-0.212	O2	0.641	1.066	-1.693
O3	7.145	-2.438	-0.779	O3	-0.787	2.954	1.327
N4	-0.937	-1.215	-0.581	N4	-3.058	-2.129	-1.683
H5	-1.261	-1.966	0.009	H5	-2.598	-1.898	-2.55
N6	0.565	-0.718	1.100	N6	-1.215	-3.432	-1.186
H7	0.461	-1.676	1.398	H7	-0.959	-3.296	-2.152
C8	-0.036	-0.320	-0.067	C8	-2.351	-2.812	-0.726
C9	-1.769	-0.871	-1.720	C9	-0.136	-3.778	-0.283
H10	-1.929	-1.772	-2.316	H10	0.173	-4.815	-0.444
H11	-1.197	-0.165	-2.326	H11	-0.546	-3.711	0.729
C12	-3.101	-0.259	-1.337	C12	1.064	-2.86	-0.422
C13	-3.144	0.971	-0.668	C13	0.9	-1.514	-0.726
H14	-2.212	1.480	-0.439	H14	-0.087	-1.099	-0.892
C15	-4.358	1.535	-0.313	C15	2.001	-0.667	-0.853
H16	-4.393	2.496	0.191	C16	3.289	-1.189	-0.704
C17	-5.560	0.875	-0.596	H17	4.157	-0.557	-0.858
C18	-5.520	-0.349	-1.268	C18	3.479	-2.535	-0.389
H19	-6.441	-0.863	-1.522	C19	2.357	-3.354	-0.249
C20	-4.299	-0.905	-1.638	H20	2.497	-4.408	-0.019
H21	-4.281	-1.854	-2.167	C21	4.867	-3.092	-0.196

C22	-6.843	1.554	-0.237	H22	4.929	-4.131	-0.531
C23	-8.054	0.743	0.089	H23	5.146	-3.072	0.863
C24	-9.314	1.311	-0.135	H24	5.61	-2.508	-0.744
H25	-9.372	2.303	-0.570	C25	1.723	0.76	-1.207
C26	-10.468	0.615	0.190	C26	2.75	1.827	-0.985
H27	-11.438	1.064	-0.001	C27	2.742	2.925	-1.853
C28	-10.401	-0.659	0.769	H28	2.027	2.943	-2.669
C29	-9.141	-1.210	1.015	C29	3.639	3.97	-1.674
H30	-9.066	-2.187	1.482	H30	3.635	4.81	-2.361
C31	-7.980	-0.525	0.674	C31	4.538	3.942	-0.609
H32	-7.014	-0.971	0.889	H32	5.234	4.762	-0.464
C33	-11.659	-1.417	1.100	C33	4.538	2.865	0.273
H34	-12.072	-1.885	0.200	H34	5.226	2.846	1.112
H35	-12.428	-0.751	1.502	C35	3.654	1.807	0.082
H36	-11.47	-2.207	1.829	H36	3.651	0.979	0.781
C37	1.661	0.035	1.658	C37	-4.216	-1.34	-1.326
H38	1.641	-0.074	2.747	H38	-4.797	-1.916	-0.6
H39	1.477	1.090	1.438	H39	-4.839	-1.225	-2.218
C40	3.041	-0.340	1.145	C40	-3.915	0.025	-0.726
C41	3.224	-1.198	0.061	C41	-2.69	0.294	-0.124
H42	2.363	-1.640	-0.430	H42	-1.907	-0.449	-0.151
C43	4.502	-1.504	-0.388	C43	-2.468	1.502	0.534
H44	4.643	-2.183	-1.222	C44	-3.467	2.479	0.535
C45	5.625	-0.938	0.220	H45	-3.277	3.423	1.037
C46	5.443	-0.081	1.312	C46	-4.694	2.244	-0.082
H47	6.302	0.345	1.821	C47	-4.905	1.006	-0.697
C48	4.165	0.205	1.771	H48	-5.868	0.805	-1.162
H49	4.038	0.860	2.628	C49	-5.771	3.299	-0.101
C50	6.978	-1.334	-0.277	H50	-6.754	2.864	0.101
C51	8.124	-0.382	-0.163	H51	-5.823	3.782	-1.082
C52	9.419	-0.906	-0.082	H52	-5.58	4.076	0.643
H53	9.549	-1.983	-0.067	C53	-1.179	1.798	1.233
C54	10.517	-0.063	-0.017	C54	-0.376	0.687	1.843
H55	11.515	-0.485	0.058	C55	0.976	0.936	2.103
C56	10.359	1.328	-0.054	H56	1.385	1.906	1.841
C57	9.066	1.846	-0.161	C57	1.78	-0.044	2.667
H58	8.922	2.921	-0.212	H58	2.83	0.157	2.856
C59	7.959	1.006	-0.208	C59	1.239	-1.286	2.996
H60	6.967	1.434	-0.304	H60	1.869	-2.055	3.43
C61	11.554	2.239	0.041	C61	-0.111	-1.532	2.773
H62	12.419	1.813	-0.474	H62	-0.544	-2.49	3.043
H63	11.838	2.391	1.088	C63	-0.919	-0.553	2.202
H64	11.343	3.221	-0.390	H64	-1.968	-0.769	2.042

Table 1.5. Calculated excited states of **2** in gas phase. Energies (nm), oscillator strengths (f_{OSC}), charge transfer numbers among fragments, and hole/electron differences as calculated by Theodore.[52]

State	Energy (nm)	Oscillator Strength (f_{OSC})	Charge Transfer*	Hole*			Electron*		
				1	2	3	1	2	3
S_1	333	0.001	0.005	0.000	0.001	0.999	0.000	0.003	0.996
S_2	318	0.001	0.007	0.999	0.001	0.000	0.993	0.007	0.000
S_3	261	0.635	0.009	0.003	0.005	0.997	0.003	0.004	0.998
S_4	252	0.012	0.021	0.000	0.008	0.992	0.000	0.013	0.987
S_5	249	0.018	0.010	0.001	0.004	0.996	0.001	0.006	0.994
S_6	246	0.219	0.056	0.962	0.033	0.007	0.967	0.027	0.007
S_7	240	0.008	0.004	0.997	0.001	0.003	0.995	0.003	0.003
S_8	239	0.155	0.049	0.046	0.037	0.919	0.046	0.014	0.942
S_9	237	0.240	0.060	0.923	0.037	0.040	0.933	0.026	0.041
S_{10}	224	0.105	0.014	0.996	0.006	0.000	0.993	0.008	0.001
S_{11}	208	0.145	0.040	0.002	0.027	0.976	0.002	0.014	0.989
S_{12}	204	0.002	0.035	0.000	0.023	0.975	0.000	0.014	0.984
S_{13}	201	0.066	0.088	0.922	0.077	0.003	0.971	0.027	0.003
S_{14}	200	0.217	0.017	0.002	0.013	0.995	0.002	0.004	1.004
S_{15}	199	0.031	0.446	0.006	0.452	0.541	0.004	0.031	0.963

*Hole and electron were calculated from the following pieces of **2**, where 1 = one benzophenone unit, 2 = methylene urea unit and 3 = the other benzophenone unit. Charge transfer was calculated from this as well.

Table 1.6. Calculated excited states of **2** in solution. Energies (nm), oscillator strengths (f_{OSC}), charge transfer numbers among fragments, and hole/electron differences as calculated by Theodore.[52]

State	Energy (nm)	Oscillator Strength (f_{OSC})	Charge Transfer*	Hole*			Electron*		
				1	2	3	1	2	3
S_1	312	0.003	0.008	0.998	0.001	0.001	0.992	0.007	0.001
S_2	312	0.003	0.007	0.001	0.001	0.998	0.001	0.006	0.993
S_3	254	1.512	0.041	0.405	0.032	0.562	0.413	0.015	0.571
S_4	253	0.026	0.035	0.563	0.025	0.412	0.570	0.012	0.417
S_5	251	0.041	0.024	0.991	0.009	0.001	0.985	0.015	0.001
S_6	250	0.033	0.012	0.001	0.004	0.996	0.001	0.008	0.992
S_7	248	0.011	0.026	0.991	0.009	0.000	0.983	0.018	0.000
S_8	247	0.008	0.028	0.000	0.010	0.990	0.000	0.018	0.983
S_9	239	0.176	0.044	0.195	0.033	0.774	0.201	0.015	0.786
S_{10}	239	0.032	0.060	0.755	0.047	0.201	0.779	0.019	0.204
S_{11}	209	0.013	0.609	0.332	0.656	0.010	0.908	0.089	0.002
S_{12}	205	0.116	0.014	0.999	0.006	0.001	0.996	0.008	0.001
S_{13}	204	0.100	0.063	0.002	0.058	0.945	0.001	0.009	0.995
S_{14}	203	0.018	0.723	0.023	0.731	0.244	0.004	0.046	0.949
S_{15}	202	0.143	0.061	0.014	0.048	0.942	0.016	0.015	0.973
S_{16}	202	0.179	0.164	0.827	0.159	0.017	0.959	0.025	0.019
S_{17}	196	0.359	0.034	0.959	0.020	0.020	0.964	0.015	0.020
S_{18}	195	0.191	0.021	0.021	0.010	0.968	0.021	0.011	0.967
S_{19}	194	0.054	0.059	0.960	0.036	0.003	0.971	0.025	0.003
S_{20}	193	0.026	0.048	0.002	0.029	0.968	0.002	0.021	0.976
S_{21}	189	0.361	0.038	0.963	0.019	0.018	0.960	0.022	0.017
S_{22}	188	0.396	0.028	0.022	0.016	0.962	0.023	0.018	0.959
S_{23}	184	0.070	0.146	0.848	0.145	0.004	0.968	0.026	0.003
S_{24}	184	0.002	0.148	0.047	0.252	0.699	0.105	0.163	0.730
S_{25}	184	0.094	0.284	0.124	0.562	0.311	0.260	0.385	0.353

*Hole and electron were calculated from the following pieces of **2**, where 1 = one benzophenone unit, 2 = methylene urea unit and 3 = the other benzophenone unit.

Table 1.7. Calculated excited states of **3** in gas phase. Energies (nm), oscillator strengths (f_{OSC}), charge transfer numbers among fragments, and hole/electron differences as calculated by Theodore.[52]

State	Energy (nm)	Oscillator Strength (f_{osc})	Charge Transfer*	Hole*			Electron*		
				1	2	3	1	2	3
S_1	334	0.001	0.004	0.998	0.001	0.001	0.998	0.001	0.001
S_2	329	0.002	0.005	0.000	0.002	0.997	0.001	0.002	0.997
S_3	259	0.051	0.050	0.002	0.036	0.965	0.003	0.015	0.985
S_4	255	0.046	0.043	0.972	0.027	0.003	0.984	0.015	0.004
S_5	244	0.013	0.002	1.001	0.000	0.001	1.000	0.001	0.001
S_6	241	0.212	0.019	0.004	0.009	0.987	0.006	0.006	0.988
S_7	238	0.191	0.019	0.018	0.009	0.973	0.020	0.007	0.973
S_8	237	0.365	0.017	0.973	0.012	0.016	0.979	0.004	0.017
S_9	232	0.066	0.020	0.011	0.010	0.982	0.012	0.008	0.984
S_{10}	229	0.034	0.031	0.967	0.021	0.015	0.978	0.007	0.017
S_{11}	203	0.091	0.050	0.971	0.023	0.009	0.966	0.026	0.010
S_{12}	202	0.028	0.038	0.007	0.021	0.974	0.013	0.013	0.975
S_{13}	201	0.023	0.883	0.090	0.336	0.573	0.960	0.021	0.018
S_{14}	199	0.077	0.453	0.499	0.127	0.374	0.919	0.024	0.056
S_{15}	199	0.002	0.166	0.014	0.119	0.865	0.132	0.023	0.844
S_{16}	198	0.103	0.483	0.414	0.371	0.215	0.872	0.027	0.101
S_{17}	197	0.282	0.078	0.755	0.058	0.188	0.774	0.031	0.197
S_{18}	196	0.115	0.088	0.251	0.068	0.682	0.254	0.020	0.727
S_{19}	195	0.079	0.080	0.884	0.067	0.049	0.900	0.028	0.072
S_{20}	193	0.012	0.713	0.031	0.719	0.249	0.076	0.058	0.864
S_{21}	193	0.054	0.861	0.004	0.065	0.930	0.817	0.020	0.162
S_{22}	193	0.374	0.202	0.018	0.061	0.923	0.144	0.039	0.820
S_{23}	191	0.002	0.263	0.101	0.845	0.051	0.236	0.670	0.092
S_{24}	191	0.035	0.038	0.900	0.088	0.013	0.904	0.079	0.018
S_{25}	191	0.018	0.114	0.008	0.162	0.828	0.025	0.093	0.881

*Hole and electron were calculated from the following pieces of **3**, where 1 = one benzophenone unit, 2 = methylene urea unit and 3 = the other benzophenone unit. Charge transfer was calculated from this as well.

Table 1.8. Calculated excited states of **3** in solution. Energies (nm), oscillator strengths (f_{OSC}), charge transfer numbers among fragments, and hole/electron differences as calculated by Theodore.[52]

State	Energy (nm)	Oscillator Strength (f_{OSC})	Charge Transfer*	Hole*			Electron*		
				1	2	3	1	2	3
S_1	318	0.002	0.018	0.975	0.002	0.022	0.966	0.002	0.032
S_2	317	0.001	0.015	0.021	0.004	0.975	0.028	0.002	0.970
S_3	272	0.046	0.104	0.919	0.061	0.021	0.966	0.011	0.025
S_4	266	0.041	0.063	0.009	0.041	0.952	0.015	0.012	0.975
S_5	255	0.050	0.080	0.228	0.010	0.763	0.224	0.005	0.772
S_6	252	0.320	0.057	0.767	0.010	0.223	0.778	0.005	0.217
S_7	251	0.418	0.046	0.014	0.012	0.974	0.021	0.006	0.972
S_8	249	0.043	0.025	0.988	0.004	0.009	0.983	0.001	0.016
S_9	239	0.111	0.116	0.892	0.004	0.105	0.962	0.003	0.037
S_{10}	238	0.069	0.074	0.026	0.009	0.967	0.049	0.006	0.948
S_{11}	220	0.012	0.900	0.544	0.078	0.378	0.395	0.006	0.598
S_{12}	219	0.028	0.842	0.334	0.142	0.523	0.637	0.007	0.354
S_{13}	217	0.021	0.895	0.117	0.021	0.861	0.833	0.006	0.160
S_{14}	213	0.013	0.851	0.650	0.256	0.092	0.241	0.011	0.746
S_{15}	211	0.007	0.851	0.414	0.490	0.095	0.642	0.016	0.340
S_{16}	208	0.027	0.381	0.111	0.156	0.731	0.374	0.020	0.605
S_{17}	207	0.015	0.634	0.323	0.419	0.256	0.283	0.018	0.698
S_{18}	205	0.104	0.555	0.712	0.106	0.180	0.458	0.020	0.521
S_{19}	205	0.005	0.769	0.131	0.056	0.812	0.711	0.010	0.278
S_{20}	204	0.020	0.891	0.167	0.067	0.765	0.697	0.007	0.294
S_{21}	203	0.011	0.554	0.588	0.194	0.217	0.502	0.013	0.484
S_{22}	202	0.154	0.244	0.764	0.144	0.092	0.845	0.054	0.102
S_{23}	200	0.127	0.140	0.916	0.024	0.061	0.868	0.006	0.128
S_{24}	199	0.193	0.153	0.028	0.060	0.912	0.082	0.037	0.880
S_{25}	199	0.250	0.216	0.192	0.043	0.765	0.149	0.012	0.840

*Hole and electron were calculated from the following pieces of **3**, where 1 = one benzophenone unit, 2 = methylene urea unit and 3 = the other benzophenone unit. Charge transfer was calculated from this as well.

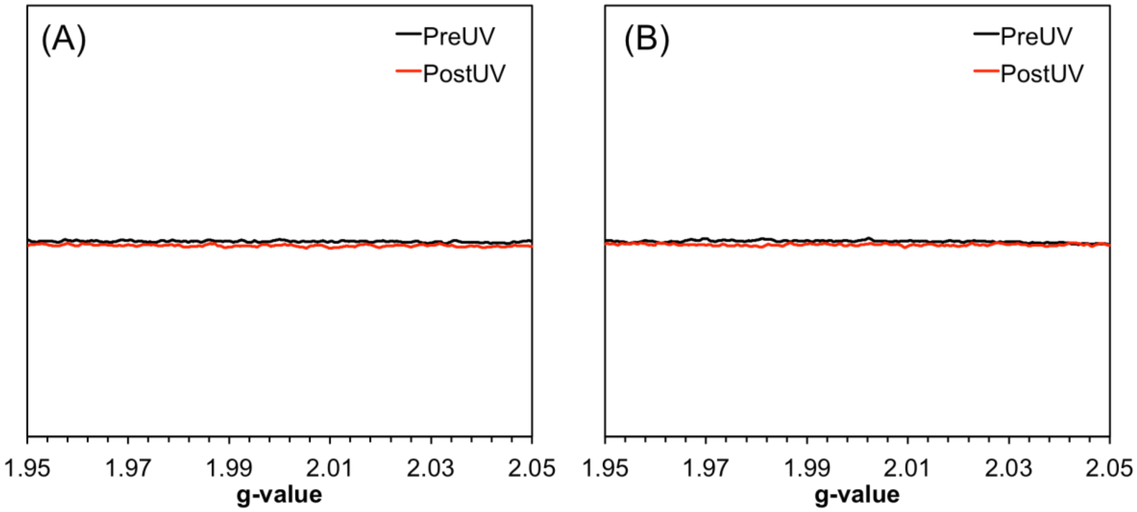

Figure 1.44. EPR spectra recorded in solution of (A) **2** and (B) **3** in dichloromethane pre and post UV.

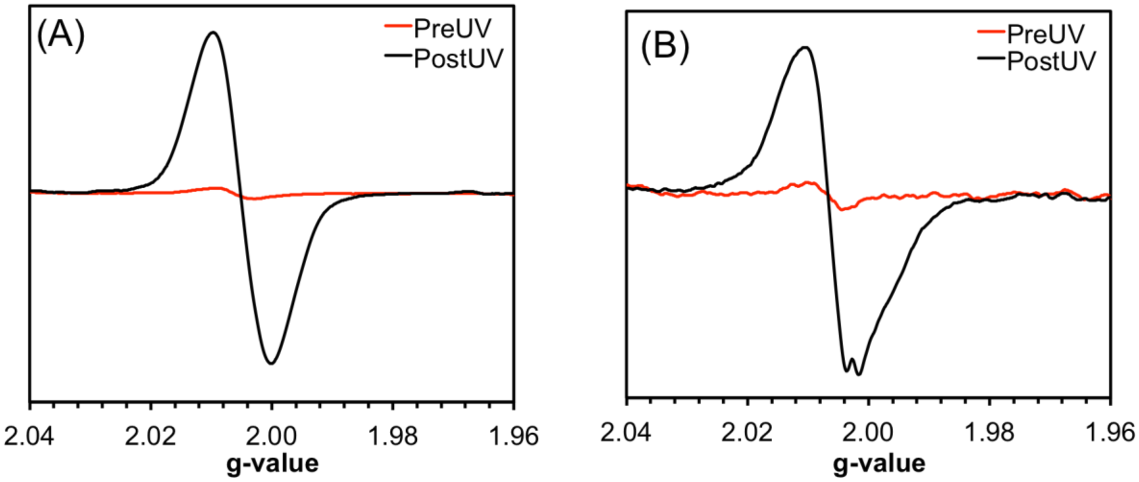

Figure 1.45. EPR spectra of triply recrystallized samples of (A) **2** and (B) **3** pre and post UV irradiation.

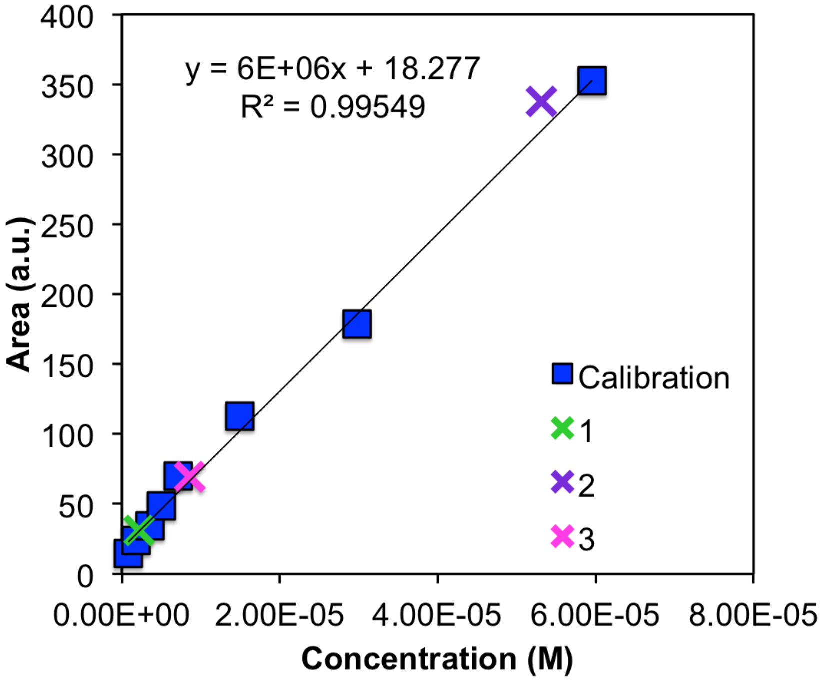

Figure 1.46. Radical concentration determination. The TEMPO calibration curve (■) is overlaid with the area and determined concentration of **1** (X), **2** (X), and **3** (X) after 1 hour of UV-irradiation.

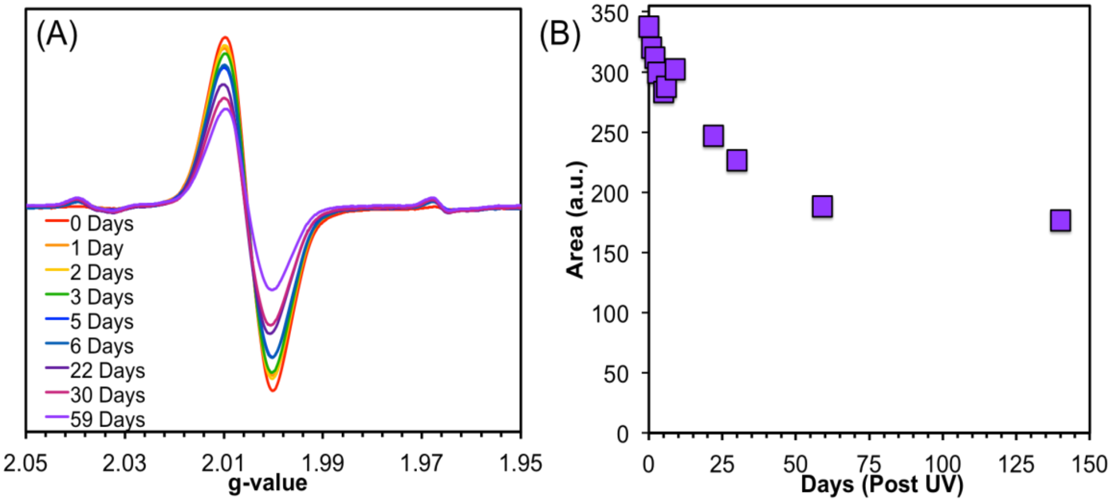

Figure 1.47. Dark decay study of the triply recrystallized samples **2** (A) EPR spectra post UV irradiation for 1 hour and (B) area of each curve plotted against days post irradiation.

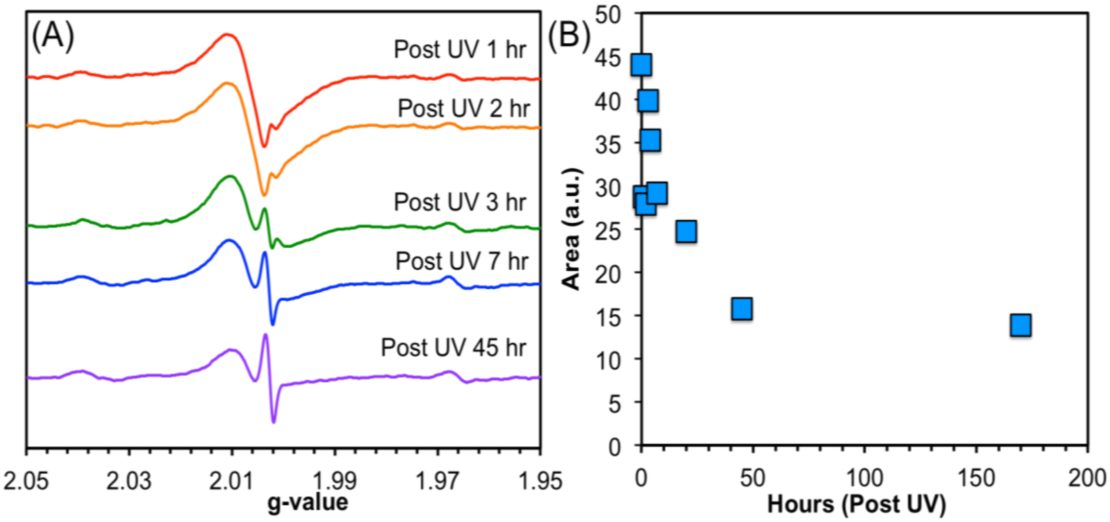

Figure 1.48. Dark decay study of the triply recrystallized samples **3** (A) EPR spectra post UV irradiation for 1 h and (B) area of each curve plotted against hours post irradiation.

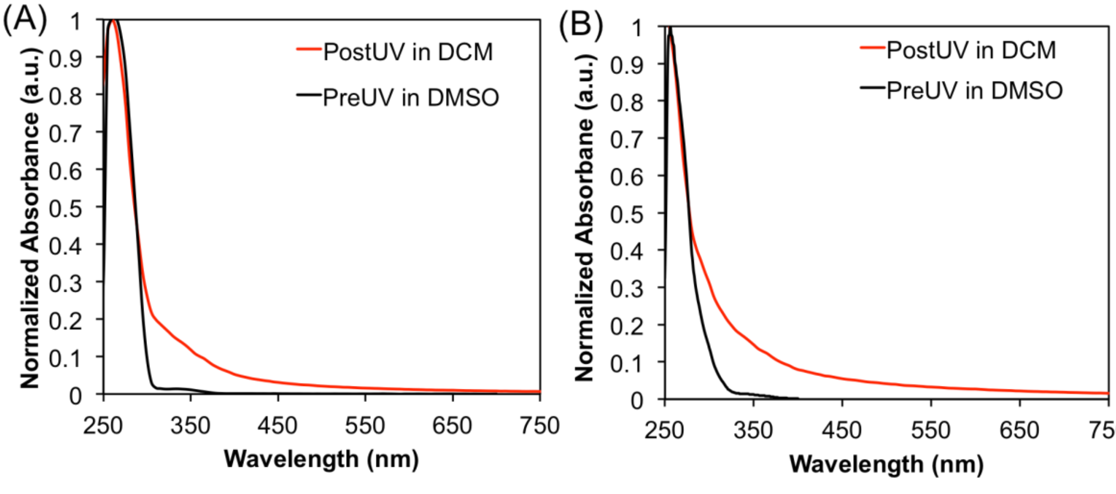

Figure 1.49. Normalized UV/vis spectra of EPR solutions (A) **2** and (B) **3** post irradiation compared to unirradiated samples in DMSO.

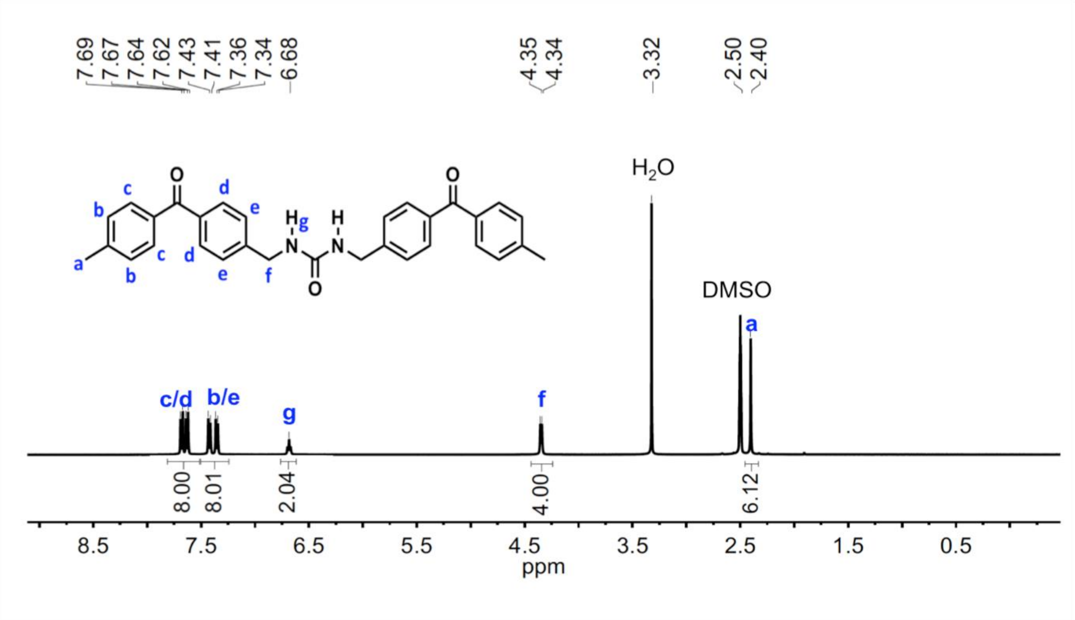

Figure 1.50. ^{1}H NMR (300 MHz; DMSO) of **2** crystals post UV irradiation showing that no changes were observed after irradiation upon dissolution, see figure 1.10.

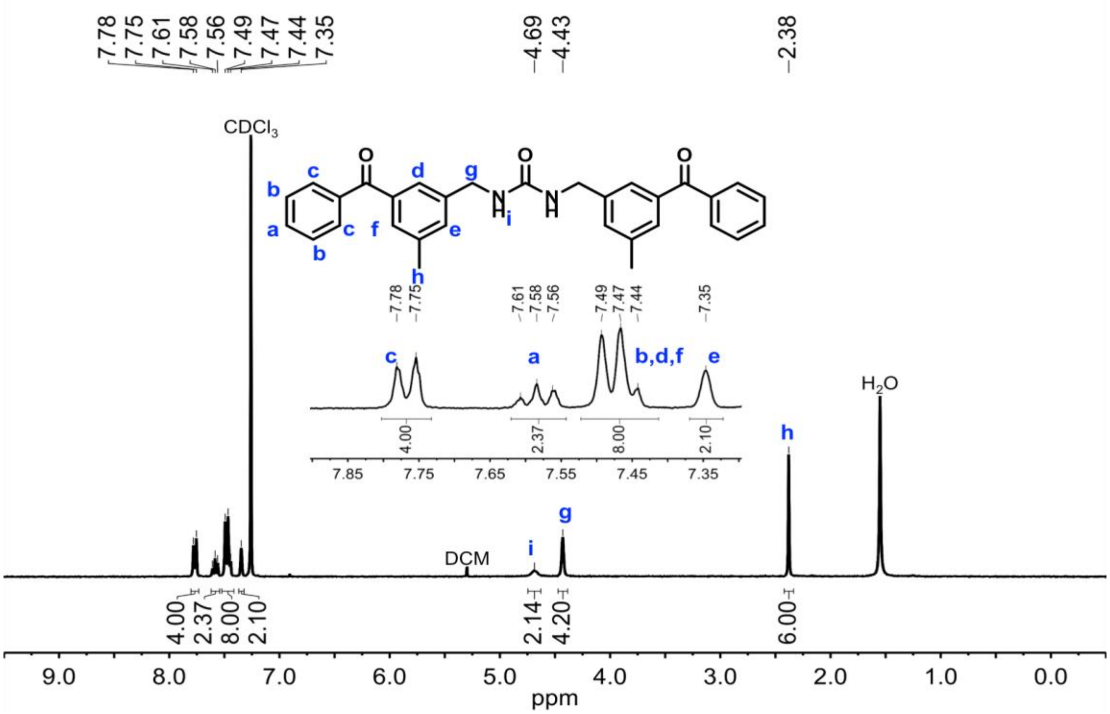

Figure 1.51. ^{1}H NMR (300 MHz; $CDCl_3$) of **3** crystals post UV irradiation showing that no changes were observed after irradiation upon dissolution, see figure 1.17.

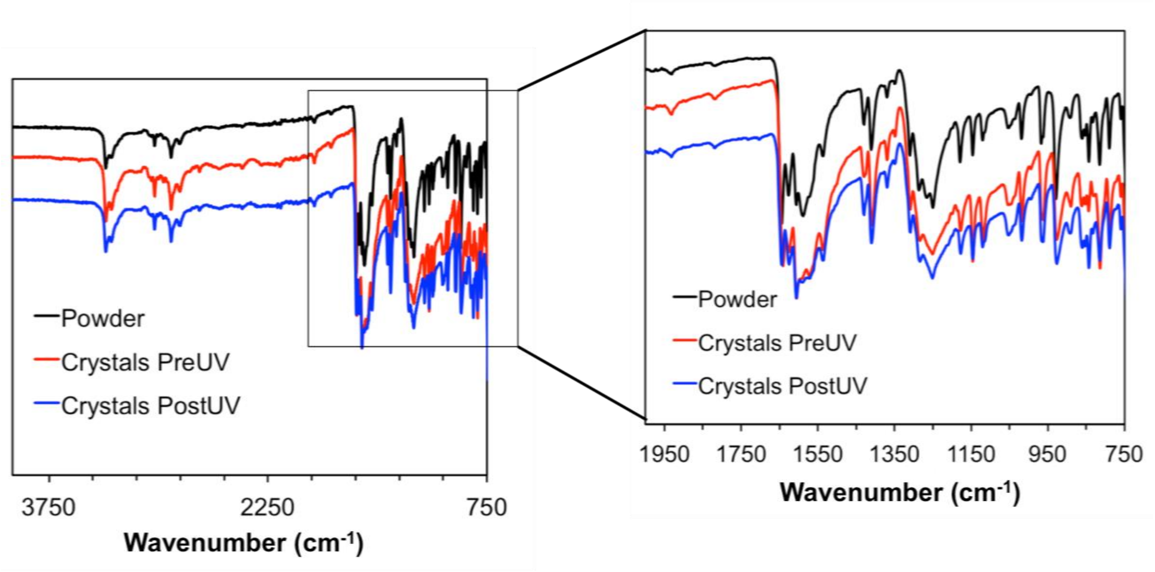

Figure 1.52. FT-IR on the triply crystallized samples of **2** pre and post UV compared to the powder before UV irradiation.

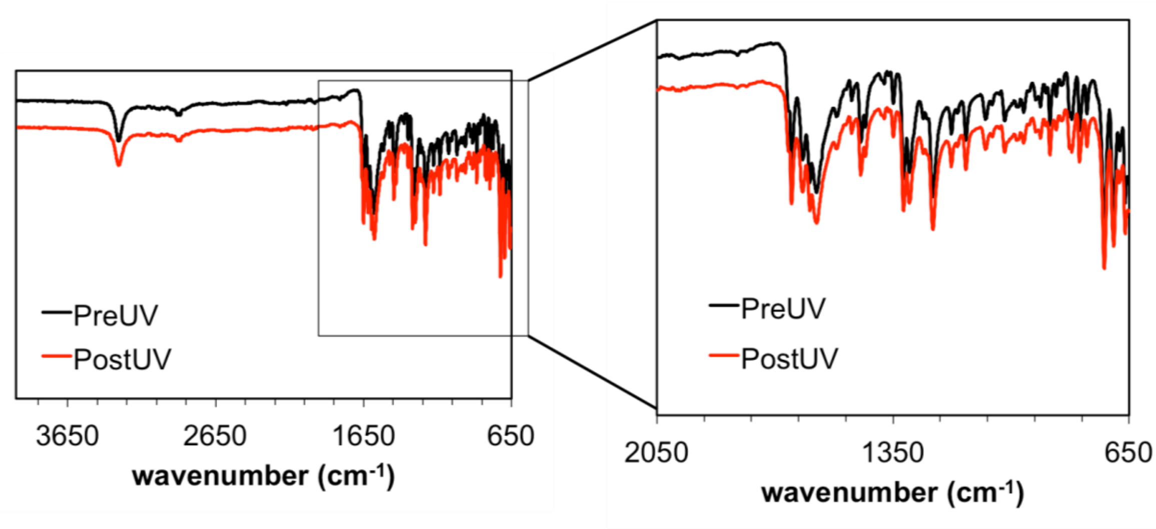

Figure 1.53. FT-IR on the triply crystallized samples of **3** pre and post UV.

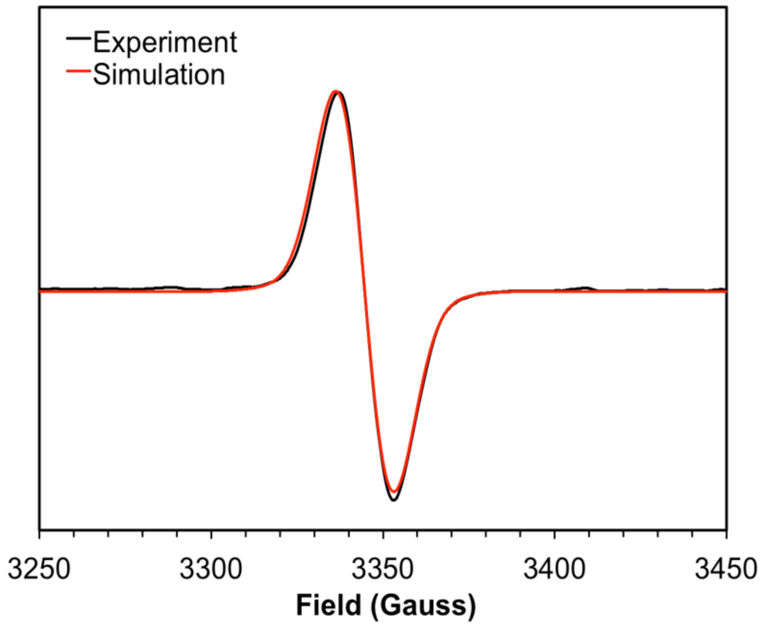

Figure 1.54. Simulation of the X-band EPR spectra recorded at 298 K for the triplet radical pair generated by **2** after UV-irradiation using the "pepper" package in MATLAB's EasySpin toolbox. The spectrum was fit for two spin ½ radicals from the experimental spectra using isotropic g-values of 2.007 and 2.003 for simplicity.

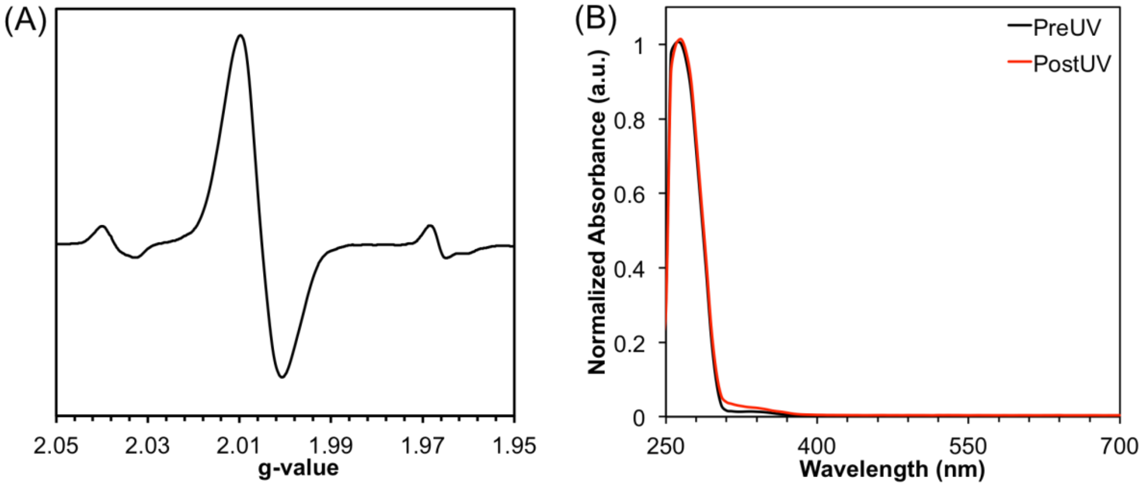

Figure 1.55. Dissolution of UV-irradiated **2** crystals (A) EPR spectra of **2** crystals recorded 140 days after UV irradiation. (B) Normalized UV/vis spectra of the sample in DMSO (25 μM) recorded pre and post UV-irradiation. The reddish brown crystals form a colorless solution and no changes are observed in the absorbance spectrum suggesting that the radicals dimerize and/or are scavenged by oxygen upon dissolution.

1.6 REFERENCES

1. Lehn, J. -M. *Proc. Natl. Acad. Sci. USA* **2002**, *99*, 4763-4768.
2. Stupp, S. I.; Palmer, L. C. *Chem. Mater.* **2014**, *26*, 507-518.
3. Adhikari, B.; Lin, X.; Yamauchi, M.; Ouchi, H.; Aratsu, K.; Yagai, S. *Chem. Commun.* **2017**, *53*, 9663-9683.
4. Würthner, F.; Kaiser, T. E.; Saha-Möller, C. R. *Angew. Chem. Int. Ed.* **2011**, *50*, 3376-3410.
5. Würthner, F.; Saha-Möller, C. R.; Fimmel, B.; Ogi, S.; Leowanawat, P.; Schmidt, D. *Chem. Rev.* **2016**, *116*, 962-1052.
6. Mei, J.; Leung, N. L. C.; Kwok, R. T. K.; Lam, J. W. Y.; Tang, B. Z. *Chem. Rev.* **2015**, *115*, 11718-11940.
7. Shi, J.; Aguilar Suarez, L. E.; Yoon, S. –J.; Varghese, S.; Serpa, C.; Park, S. Y.; Lüer, L.; Roca-Sanjuán, D.; Milián-Medina, B.; Gierschner, J. *J. Phys. Chem. C* **2017**, *121*, 23166-23183.
8. Lee, S. Y.; Yasuda, T.; Yang, Y. S.; Zhang, Q.; Adachi, C. *Angew. Chem. Int. Ed.* **2014**, *53*, 6402-6406.
9. Cao, W.; Wang, W. D.; Xu, H. -S.; Sergeryev, I. V.; Struppe, J.; Wang, X.; Mentink-Vigier, F.; Gan, Z.; Xiao, M. -X.; Wang, L.-Y.; Ding, S. -Y.; Bai, S.; Wang, W. *J. Am. Chem. Soc.* **2018**, *140*, 6969-6977.
10. DeHaven, B. A.; Tokarski III, J. T.; Korous, A. A.; Mentink-Vigier, F.; Brugh, A. M.; Forbes, M. D. E.; Makris, T. M.; van Tol, J.; Bowers, C. R.; Shimizu, L. S. *Chem. Eur. J.* **2017**, *23*, 8315-8319.

11. Scott, T. A.; Ooro, B. A.; Collins, D. J.; Shatruk, M.; Yakovenko, A.; Dunbar, K. R.; Zhou, H. -C. *Chem. Commun.* **2009**, 65-67.
12. Iwakura, Y.; Takeda, K.; Nakazawa, T.; Watarai, O. *J. Polymer Sci. C: Polymer Lett.* **1968**, *6*, 115-118.
13. Murai, H.; Imamura, T.; Obi, K. *Chem. Phys. Lett.* **1982**, *87*, 295-298
14. Fischer, P. H. H.; Zimmermann, H. *Z. Naturforsch A* **1968**, *23*, 1339-1342.
15. Dewal, M. B.; Xu, Y.; Yang, J.; Mohammed, F.; Smith, M. D.; Shimizu, L. S. *Chem. Commun.* **2008**, 3909-3911.
16. Geer, M. F.; Walla, M. D.; Solntsev, K. M.; Strassert, C. A.; Shimizu, L. S. *J. Org. Chem.* **2013**, *78*, 5568-5578.
17. Cai, K.; Xie, J.; Zhang, D.; Shi, W.; Yan, Q.; Zhao, D. *J. Am. Chem. Soc.* **2018**, *140*, 5764-5773.
18. Mennucci, B. *Wiley Interdiscip. Rev.: Comput. Mol. Sci.* **2012**, *2*, 386-404.
19. Chai J. D.; Head-Gordon, M. *Phys. Chem. Chem. Phys.* **2008**, *10*, 6615-6620.
20. Ditchfield, R.; Hehre, R. W.; Pople, J. A. *J. Chem. Phys.* **1971**, *54*, 724-728.
21. Simoncelli, S.; Kuzmanich, G.; Gard, M. N.; Garcia-Garibay, M. A. *J. Phys. Org. Chem.* **2010**, *23*, 376-381.

22. Kuzmanich, G.; Simoncelli, S.; Gard, M. N.; Spänig, F.; Henderson, B. L.; Guldi, D. M.; Garcia-Garibay, M. A. *J. Am. Chem. Soc.* **2011**, *133*, 17296-17306.
23. Yuan, W. Z.; Shen, X. Y.; Zhao, H.; Lam, J. W. Y.; Tang, L.; Lu, P.; Wang, C.; Liu, Y.; Wang, Z.; Zheng, Q.; Sun, J. Z.; Ma, Y.; Tang, B. Z. *J. Phys. Chem. C* **2010**, *114*, 6090-6099.
24. Yang, J.; Zhen, X.; Gao, X.; Ren, Z.; Wang, J.; Xie, Y.; Li, J.; Peng, Q.; Pu, K.; Li, Z. *Nat. Commun.* **2018**, *9*, 1-10.
25. Gong, Y.; Tan, Y.; Li, H.; Zhang, Y.; Yuan, W.; Zhang, Y.; Sun, J.; Tang, B. Z. *Sci. China Chem.* **2013**, *56*, 1183-1186.
26. Marazzi, M.; Mai, S.; Roca-Sanjuán, D.; Delcey, M. G.; Lindh, R.; González, L.; Monari, A. *J. Phys. Chem. Lett.* **2016**, *7*, 622-626.
27. Dormán, G.; Nakamura, H.; Pulsipher, A.; Prestwich, G. D. *Chem. Rev.* **2016**, *116*, 15284-153998.
28. Scheffer, J. R. *Acc. Chem. Res.* **1980**, *13*, 290-296.
29. Ito, Y.; Matsuura, T.; Tabata, K.; Ji-Ben, M.; Fukuyama, K.; Sasaki, M.; Okada, S. *Tetrahedron* **1987**, *43*, 1307-1312.
30. Koshima, H.; Hessler Bittl, D. P.; Miyoshi, F.; Yang, Y.; Matsuura, T. *J. Photochem. Photobiol. A: Chem.* **1995**, *86*, 171-176.
31. Buettner, A. V.; Dedinas, J. *J. Phys. Chem.* **1971**, *75*, 187-191.
32. McMillen, D. F.; Golden, D. M. *Ann. Rev. Phys. Chem.* **1982**, *33*, 493-532.
33. Woodward, J. R. *Prog. React. Kinet. Mech.* **2002**, *27*, 165-207.

34. Danielsson, R.; Albertsson, P.-A.; Mamedov, F. Styring, S. *Biocimica. Et Biophysica. Acta.* **2004**, *1608*, 53-61.
35. Turro, N. J.; Ramamurthy, V.; Scaiano, J. C. *Modern Molecular Photochemistry of Organic Molecules*; University Science Books: Sausalito, 2010; pp 483 – 624.
36. Encinas, M. V.; Scaiano, J. C. *J. Am. Chem. Soc.* **1981**, *103*, 6393-6397.
37. **APEX3** Version 2016.9-0 and **SAINT+** Version 8.37A. Bruker AXS, Inc., Madison, Wisconsin, USA, 2016.
38. **SADABS**-2016/2: Krause, L.; Herbst-Irmer, R.; Sheldrick, G. M.; Stalke, D. *J. Appl. Cryst.* **2015**, *48*, 3-10.
39. **SHELXT**: Sheldrick, G. M. *Acta Cryst*. **2015**, *A71*, 3-8.
40. **SHELXL:** Sheldrick, G. M. *Acta Cryst*. **2008**, *A64*, 112-122.
41. **OLEX2**: Dolomanov, O. V.; Bourhis, L. J.; Gildea, R. J.; Howard, J. A. K.; Puschmann, H. *J. Appl. Cryst.* **2009**, *42*, 339-341.
42. Qi, X.; Jian, L. B.; Li, H. P.; Wu, X. F. *Chem. Eur. J.* **2015**, *21*, 17650-17656.
43. Duval, F.; van Beek, T. A.; Zuilhof, H. *Synlett* **2012**, *23*, 1751-1754.
44. LePage, Y. *J. Appl. Crystallogr.* **1987**, *20*, 264-269.
45. Spek, A. L. *J. Appl. Crystallogr.* **1988**, *21*, 578-579.
46. Spek, A. L. *Acta Crystallogr. Sect A* **1990**, *46*, C34.
47. **PLATON**: Spek, A. L. *Acta Cryst.* **2009**, *D65*, 148-155.
48. van der Sluis, P.; Spek, A. L. *Acta Crystallogr. Sect. A* **1990**, *46*, 194-201.

49. **PLATON SQUEEZE**: Spek, A. L. *Acta Cryst.* **2015**, *C71*, 9-18.
50. Chai, J. D. Head-Gordon, M. *Phys. Chem. Chem. Phys.* **2008**, *10*, 6615-6620.
51. Ditchfield, R.; Hehre, R. W.; Pople, J. A. *J. Chem. Phys.* **1971**, *54*, 724-728.
52. Plasser, F.; Bappler, S. A.; Wormit, M.; Dreuw, A. *J. Chem Phys.* **2014**, *141*, 1 -13.
53. Mennucci, B. *Wiley Interdiscip. Rev. Comput. Mol. Sci.* **2012**, *2*, 386-404.
54. Frisch, M. J.; Trucks, G. W.; Schlegel, H. B.; Scuseria, G. E.; Robb, M. A.; Cheeseman, J. R.; Scalmani, G.; Barone, V.; Petersson, G. A.; Nakatsuji, H.; Li, X.; Caricato, M.; Marenich, A.; Bloinio, J.; Janesko, B. G.; Gomperts, R.; Mennucci, B.; Hratchian, H. P.; Ortiz, J. V.; Izmaylov, A. F.; Sonnenberg, L.; Williams-Young, D.; Ding, F.; Lipparini, F.; Egidi, F.; Goings, J. Peng, B.; Petrone, A.; Henderson, T.; Ranasinghe, D.; Zakrzewski, V. F.; Gao, J.; Rega, N.; Zheng, G.; Liang, W.; Hada, M.; Ehara, M.; Toyota, K.; Fukuda, R.; Hasegawa, J.; Ishida, M.; Nakajima, T.; Honda, Y.; Kitao, O.; Nakai, H.; Vreven, T.; Throssell, K.; Montgomery, J. A.; Peralta, J. E.; Ogliaro, F.; Bearpark, M; Heyd, J. J.; Brothers, E.; Kudin, K. N.; Staroveroy, V. N.; Keith, T.; Kobayashi, R.; Normand, J.; Raghavachari, K.; Rendell, A.; Burant, J. C.; Iyengar, S. S.; Tomasi, J.; Cossi, M; Millam, J. M.; Klene, M.; Adamo, C.; Cammi, R.; Ochterski, J. W.; Martin, R. L.; Morokuma, K.; Farkas, O.; Foresman, J. B.; Fox, D. J. Gaussian 09, Revision D.01, Gaussian, Inc., Wallingford, CT, 2009.

CHAPTER 2

PERSISTENT RADICALS OF SELF-ASSEMBLED BENZOPHENONE *BIS*-UREA MACROCYCLES: CHARACTERIZATION AND APPLICATION AS A POLARIZING AGENT FOR SOLID-STATE DNP MAS SPECTROSCOPY[§]

[§] DeHaven, B. A.; Tokarski, J. T.; Korous, A. A.; Mentink-Vigier, F.; Makris, T. M.; Brugh, A. M.; Forbes, M. D. E.; van Tol, J.; Bowers, C. R.; Shimizu, L. S. *Chem. Eur. J.* **2017**, *23* (34), 8315 – 8319. Reprinted here with permission by the publisher.

2.0 ABSTRACT

UV-irradiation of a self-assembled benzophenone *bis*-urea macrocycle generates μM amounts of radicals that persist for weeks under ambient conditions. High-Field EPR and variable temperature X-band EPR studies suggest a resonance stabilized radical pair through H-abstraction. These endogenous radicals were applied as a polarizing agent for magic angle spinning (MAS) dynamic nuclear polarization (DNP) NMR enhancement. The field-stepped DNP enhancement profile exhibits a sharp peak with a maximum enhancement of $\varepsilon_{on/off} = 4$ superimposed on a nearly constant DNP enhancement of $\varepsilon_{on/off} = 2$ over a broad field range. This maximum coincides with the high field EPR absorption spectrum, consistent with an Overhauser effect mechanism. DNP enhancement was observed for both the host and guests, suggesting that even low levels of endogenous radicals can facilitate the study of host-guest relationships in the solid-state.

2.1 INTRODUCTION

Dynamic Nuclear Polarization (DNP) has gained widespread use as a means to improve the sensitivity of nuclear magnetic resonance (NMR) signals.[1-3] In material science, solid-state DNP methods primarily rely on exogenous radicals, such as TOTAPOL and AMUPol, which are typically introduced by incipient wetness impregnation in mM concentrations.[4] Recent work suggests that high field DNP enhancement may also be observed with endogenous radicals.[5] This manuscript probes the structure of an unusually persistent endogenous radical in *bis*-urea macrocycle **1** and its use as a polarizing agent for DNP enhancement. The photogenerated radical was first noted when investigating the applications of benzophenone *bis*-urea macrocycle **1** to facilitate selective photooxidations.[6, 7] The prolonged stability of these endogenous radicals at room temperature appears to be a consequence of the columnar assembly and crystal packing of the porous organic crystals, where as no evidence of radical formation is observed in solution.[6] Herein, we probe the structure of the radical, estimate its quantity, and evaluate its lifetime by EPR spectroscopy. Finally, we demonstrate that the low levels of endogenous radicals in **1** can be applied to hyperpolarize nuclei and enhance the NMR signals of both the host and its encapsulated DMSO guest (Figure 2.1).

Solutions of exogenous stable radicals such as AMUPol, known as “DNP juice”, are typically used in mM concentration as polarizing agents for solid-state DNP MAS NMR at ~100 K.[1, 4] Under microwave irradiation, the exogenous radical transfers its spin polarization to neighbouring protons. The large spin polarization of the protons generates a spin polarization gradient leading to spin diffusion to nearby protons resulting in a uniform proton hyperpolarization throughout the sample.[8] The proton spin polarization can be transferred to other nuclei, such as ^{13}C, using a Cross-Polarization (CP) pulse sequence. Recently, Eichorn *et al.* demonstrated DNP in pyruvic acid following low temperature UV-irradiation without any exogenous radical.[9,10] Instead, the quasi-stable, short-lived UV-induced radicals were shown to afford sizeable DNP enhan-

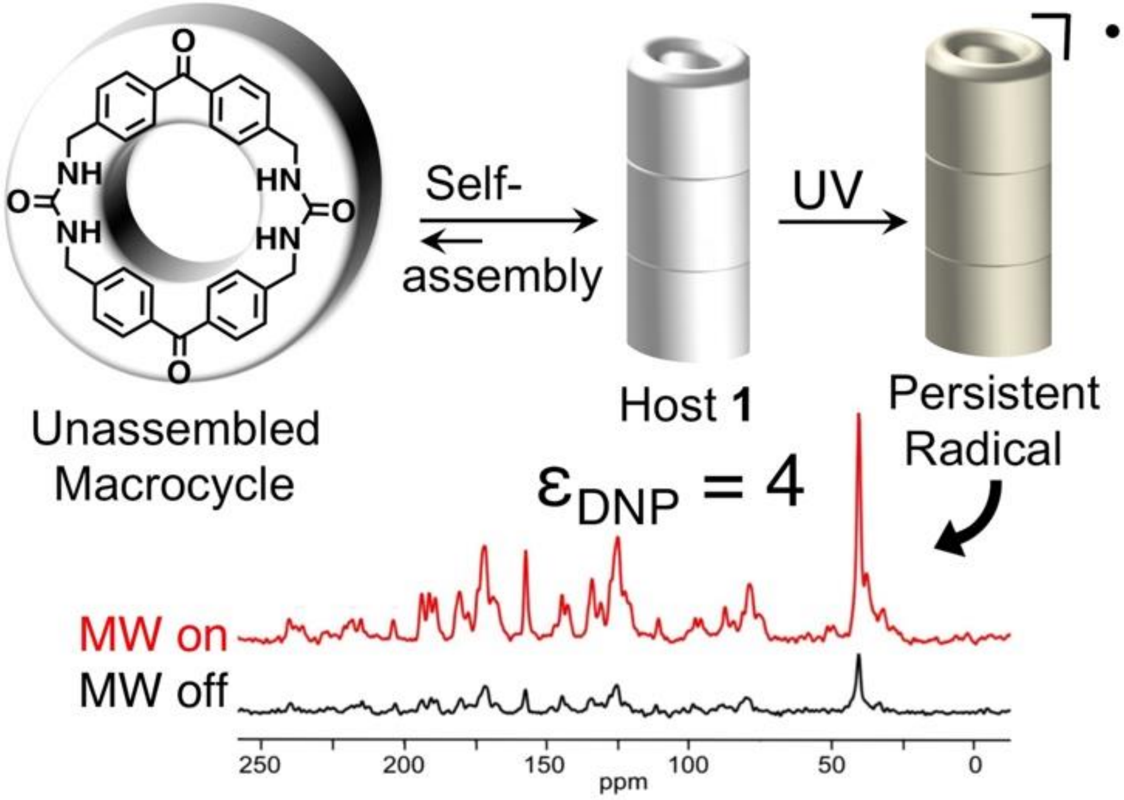

Figure 2.1. A benzophenone *bis*-urea macrocycle self-assembles from DMSO to form host **1** with encapsulated DMSO. A persistent paramagnetic species is generated when **1** is UV irradiated at 350 nm with a Hanovia 450 W medium pressure mercury arc lamp. This long-lived intermediate was used to create DNP enhancement over a broad field range in MAS NMR experiments.

cements at low temperatures.[9, 10] Larger DNP enhancements are possible in solution and have been observed in frozen media under constant irradiation (photochemically induced DNP).[11] With exogenous radicals, optimum concentration is key, as high radical concentration can result in excessive paramagnetic relaxation and line broadening. [4, 12] Few studies have examined DNP using endogenous radicals in the solid-state or single crystals.[5, 9, 10]

Recently, the Shimizu group found columnar supramolecular assembly of benzophenone altered its photophysics and lead to the formation of stable radicals as an emergent property. Benzophenone is an extensively studied chromophore with promising applications ranging from photosensitization to genome sequencing and materials chemistry.[13] Its photochemistry affords a triplet state as a result of fast intersystem crossing, which can rapidly undergo H-abstraction to yield a ketyl radical. The radical is only observed at low temperatures (77 K) as a doublet with a g value of 2.0061 or as a radical anion *via* 1-electron reductions.[14]

Compound **1** preorganizes two benzophenones within a macrocycle. Upon recrystallization from hot DMSO, **1** assembles in needle-like crystals through predictable bifurcated urea hydrogen-bonding interactions to afford columns (Figure 2.1). [7] The crystals are robust and contain accessible channels that are filled with DMSO guests (Figure 2.3b). DMSO guests can be removed by heating and other solvents and substrates can be readily loaded in the channels.[7] The assembled structure enforces close contacts between the benzophenone groups to the methylene H's on neighbouring columns (2.44 – 2.81 Å, Figure 2.9) and orients individual benzophenone units close in space. [6] Molecular self-assembly and crystal packing in **1** dramatically quenches the phosphorescence lifetime from μs to < 1 ns, likely through a non-radiative pathway.[6] Mechanistic investigations suggest that columnar assembly and packing stabilizes some type of photogenerated radical that is stable for weeks in the dark at room temperature. No evidence of radical formation is observed in solution where the molecule only exists in monomer form. Our hypothesis is that the solid-state structure may facilitate an H-abstraction reaction to form the ground state triplet radical pair (RP) shown in Figure 2.2A.

2.2 RESULTS AND DISCUSSION

We probed the structure of the photogenerated radicals of **1** through solid–state X-band EPR studies on **1** and on a fully ^{15}N-labeled derivative. Both samples exhibited nearly identical broad peaks (g = 2.006, Figures 2.2B and 2.15). A simulation using parameters for a weakly exchange–coupled RP (see inset Figure 2.2B and 2.18 for more details and parameters) shows that the overall spectral width and main features of the experimental spectrum can be accounted for with such a model. This also rules out the presence of a photochemically excited (or thermally relaxed) molecular triplet state, which would be expected to exhibit much broader line widths >1000 G. The similar broad peak observed for the ^{15}N-labeled derivative suggests that the triplet RP, drawn in Figure 2.2A, adopts a conformation where the ^{15}N hyperfine is less than half of the natural line width (~14 G, Figure 2.18), which is reasonable for the benzylic radical structure shown.

The stability of the photoinduced RP was investigated through dark decay studies, which were performed by UV irradiating **1** (1 h, rt) and recording the EPR spectra over time (0 h – 26 days) while storing the sample in the dark. The double integration of the EPR signal is plotted vs.

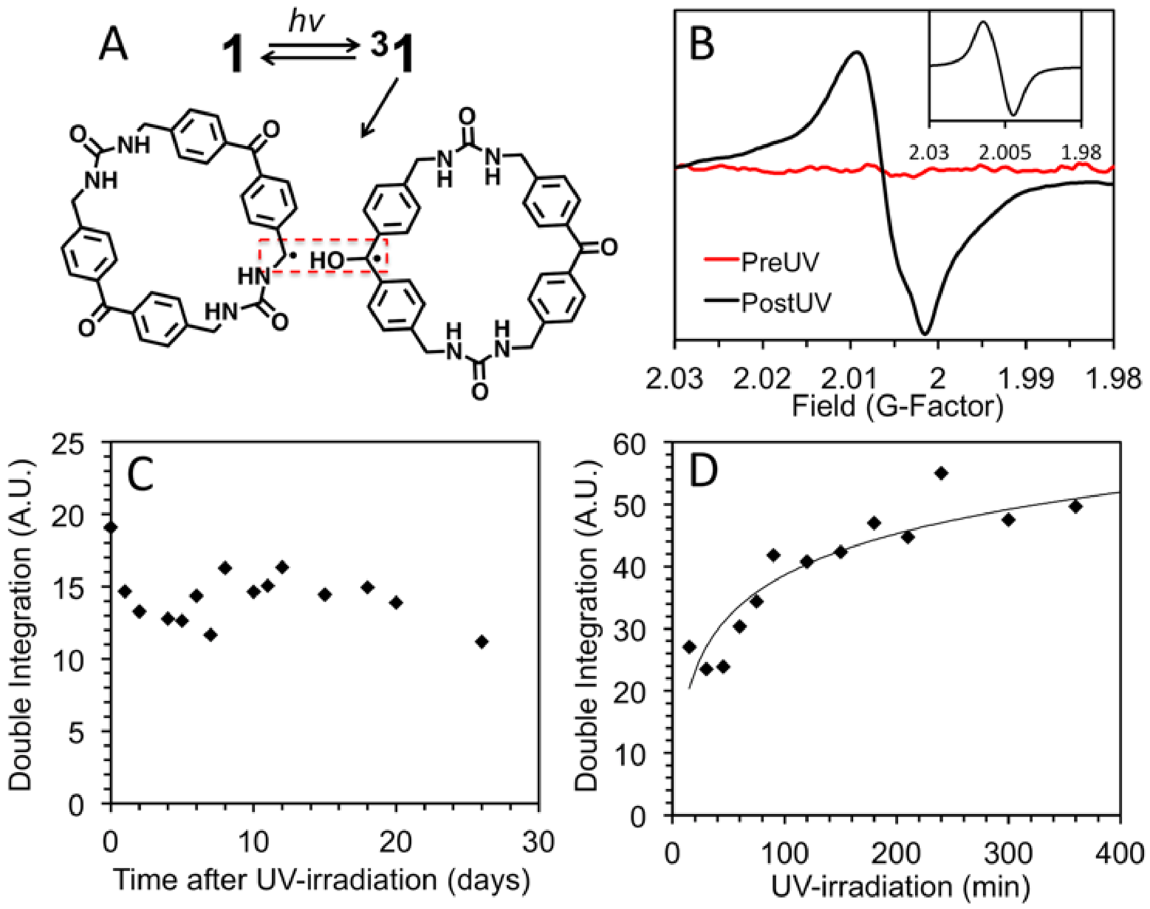

Figure 2.2. (A) Proposed photochemistry of **1**, which suggests the known photoreaction of benzophenone in the presence of an H donor. (B) X–band EPR signal, pre- and post-UV exposure (simulation inset) centered at an average g value of 2.006. (C) Dark-decay study of **1** (5 mg) after 1 h of UV irradiation. (D) Radical generation study shows that radical signal reaches a maximum intensity after 5h.

time after UV-irradiation in Figure 2.2C. Little to no loss of signal intensity is observed, suggesting that once generated, the radicals created in **1** are stable for weeks. The small fluctuations in the observed EPR signal intensity are likely due to variations in the orientation of the crystalline sample with respect to the magnetic field.[15] The stability of the photogenerated radical is likely a consequence of two effects. First, it is probable that once generated, the radicals are unable to terminate as benzophenone is known to do in solution, due to the rigid structure of the macrocycles. Second, the proposed photochemistry suggests that the radicals are generated in positions that allow resonance stabilization into the neighbouring benzene rings resulting in enhanced stabilization of the radicals.

The concentration dependence of the radicals generated by UV-irradiation of **1** was monitored for exposures from 30 min to 7 h. Figure 2D plots the double integration of the EPR signal vs. irradiation time and indicates that the number of radicals reaches a maximum after 5-7 h. After 7 h of UV-irradiation, **1** was slightly yellow in colour but still suitable for single crystal X-ray diffraction. No changes were observed in the X-ray structure (Figure 2.19) or in the ^{1}H NMR, indicating that **1** is stable and the absolute radical concentration is low. The maximum concentration was approximated by calibration with standard solutions of TEMPO in benzene under identical conditions (Figure 2.20).[10, 16] The number of radicals generated by **1** (4.5 mg) is similar to a 5.4 μM stock solution(0.1 mL), which is equivalent to a radical forming in ~0.01% of the macrocycles.

Variable temperature EPR spectra were recorded to resolve hyperfine couplings that may not be observed at rt. First, spectra were recorded at high temperatures (293, 348 and 398K, Figure 2.21) for **1** and the ^{15}N labelled **1**. No change in the *g*-factor or the coupling pattern was observed, although the intensity of the signal decreased with increasing temperature. Cooling the sample to 100K did not markedly change the g-

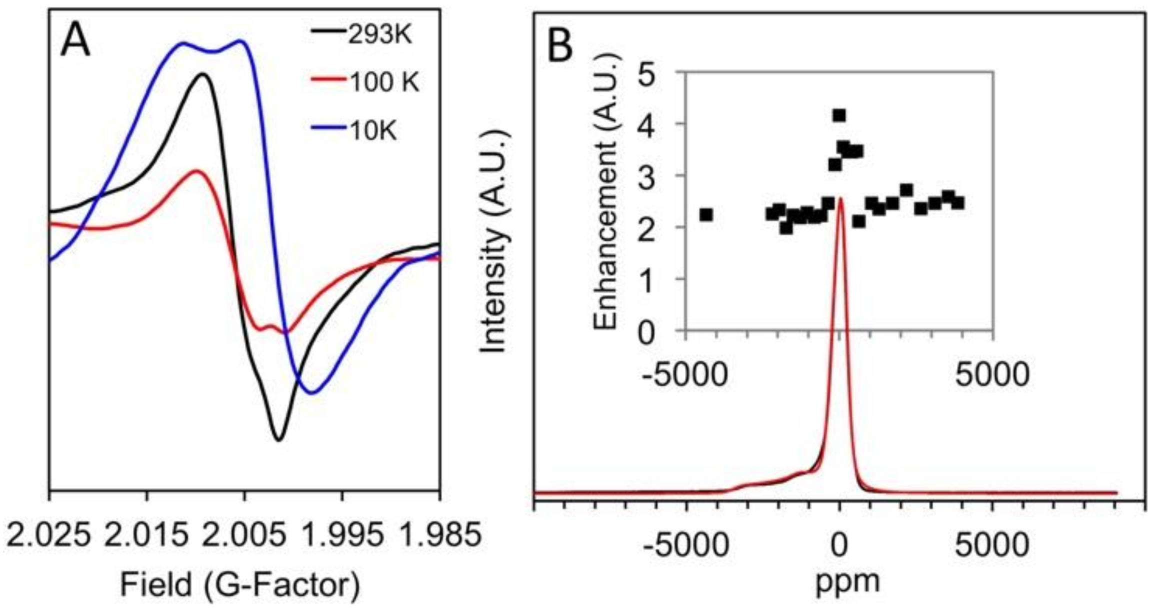

Figure 2.3. Steady-state EPR studies of **1**. (A) Variable temperature X-band EPR study of **1** at 293 K (black line), 100 K (red line) and 10 K (blue line) (B) CW high-field (240 GHz) EPR absorption curve of **1** at 6 K vs. ppm (black line, see ESI for plot in mT). An EasySpin simulation of the high field EPR (red line) for two S=1/2 electron spins, one weighted x4. Inset: Plot of DNP enhancement vs. ppm observed in a field-step study.

factor, although a slight anisotropy was observed at g = 2.001 (Figure 2.3A, red spectra). Further cooling to 10 K resulted in a change in the EPR spectrum, leading to a powder pattern shape with an overall shift in g-factor to 2.001 and a slight anisotropy. This can be explained by the orientation-dependent dipolar contribution of rigid radical pairs, which are often further complicated by hyperfine interactions ultimately resulting in line broadening due to motional averaging. By cooling the sample, we were able to overcome the Boltzmann distribution and rebuild the g-factor matrix leading to the significant over population of the lower energy states. The lack of hyperfine interactions at low temperatures is consistent with delocalized radicals, since hyperfine interactions are described by the probability of finding an electron at the site of a nucleus (i.e. Fermi contact interaction). For a delocalized radical the probability is small resulting in an averaged effect.[17]

The high field EPR shown in Fig. 2.3B was acquired on the NHMFL's 240 GHz spectrometer and converted to a ppm scale to assist in our interpretation of the field-stepped DNP data. The solid-state high-field CW absorbance EPR spectra of UV-irradiated **1** (25 mg) at 6K shows a broad baseline component at g = 2.006 with a sharper transition at g = 2.003. Spectral simulations carried out using the EasySpin software are in agreement with two S=½ radical species with a sharp isotropic signal at g = 2.003 as well as a second broad anisotropic signal. An extrapolated simulation to X-band indicates that the lines would overlap at low field, consistent with the observations in Figure 2.3. Variable temperature EPR and high-field experiments both suggest the assignment as two radicals, possibly a delocalized RP.

The thermally polarized CP MAS NMR spectra were recorded at a spinning speed of 11.3 kHz after 0h, 2h and 4h of UV-irradiation (Figure 2.4). The ^{13}C NMR peaks are surprisingly sharp for both the host and included DMSO. The spectra before and after UV-irradiation are nearly identical and no paramagnetic broadening is observed, consistent with the low estimated radical concentration and a well-ordered structure.[12] The THF loaded host crystals, also show a sharp thermally polarized CP MAS NMR spectra under similar conditions (Figure 2.29).

Solid-state MAS DNP experiments gave a maximum enhancement factor $\varepsilon_{on/off}$ = 4. The DNP enhancement profile, shown in the inset of Figure 2.3B, demonstrates that nearly constant DNP enhancement $\varepsilon_{on/off}$ = 2 is obtained over a broad field range of approximately 120 mT with a sharp peak in the enhancement factor of $\varepsilon_{on/off}$ = 4. DNP enhancement profiles are more typically limited to a much smaller field range of 30-40 mT compared to our experimentally observed 120 mT range for **1**.[2,18] Given the broad EPR signal observed by **1**, this profile is not surprising. Figure 2.5 depicts the optimized DNP CP-MAS NMR spectrum at the magnetic field that optimized the DNP enhancement, where $\varepsilon_{on/off}$ = 4 was recorded at 112K and a spinning speed of 7.0 kHz. Similar enhancement factors were observed for all NMR peaks including the encapsulated DMSO. The spinning side bands are a result of the low spinning speed required to keep the sample stabilized at the low temperature temperatures employed. The non-irradiated sample showed no DNP enhancement, which indicates that the enhancement results from irradiation of the sample and is not a microwave induced heating artifact (Figure 2.30). The constant and positive sign of this field-stepped study suggests an Overhauser mechanism.[19] Much larger DNP enhancements can be observed through traditional impregnation methods; therefore, the UV-irradiated sample was impregnated with AMUPol (10 mM, 10-12 μL of a 6:3:1 glycerol-d_8, D_2O,H_2O solution) and the DNP CP-MAS NMR spectrum acquired using the optimal field conditions for **1** (Figure 2.32). A

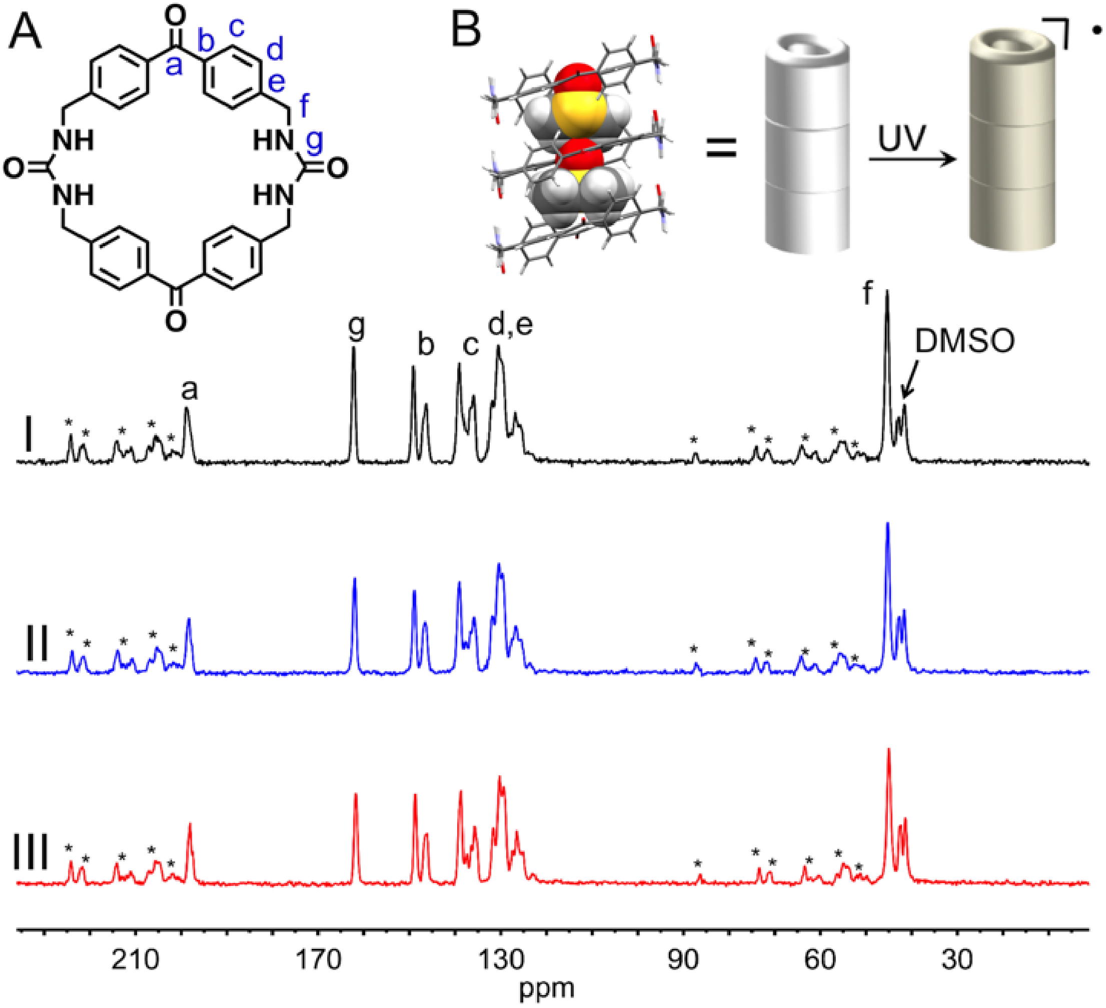

Figure 2.4. Top: (A) Peak assignment of the benzophenone *bis*-urea macrocycle, which self-assembles to form **1**. (B) XRD structure of **1** depicting the encapsulated DMSO (space fill), the assembly of **1** promotes the formation of a stable radical upon UV irradiation. Bottom: CP MAS NMR spectra of thermally polarized **1** recorded at a spinning speed of 11.3 kHz. (I) no UV, (II) 2 h. UV and (III) 4 h. UV.

DNP enhancement of $\varepsilon_{on/off}$ ~ 6 was observed for all peaks with the exception of the glycerol peaks which were enhanced by a factor of $\varepsilon_{on/off}$ ~ 20. This higher observed enhancement is likely due to the dual effect of the endogenous and exogenous radicals in this sample. The larger observed enhancement for glycerol is expected because the exogenous

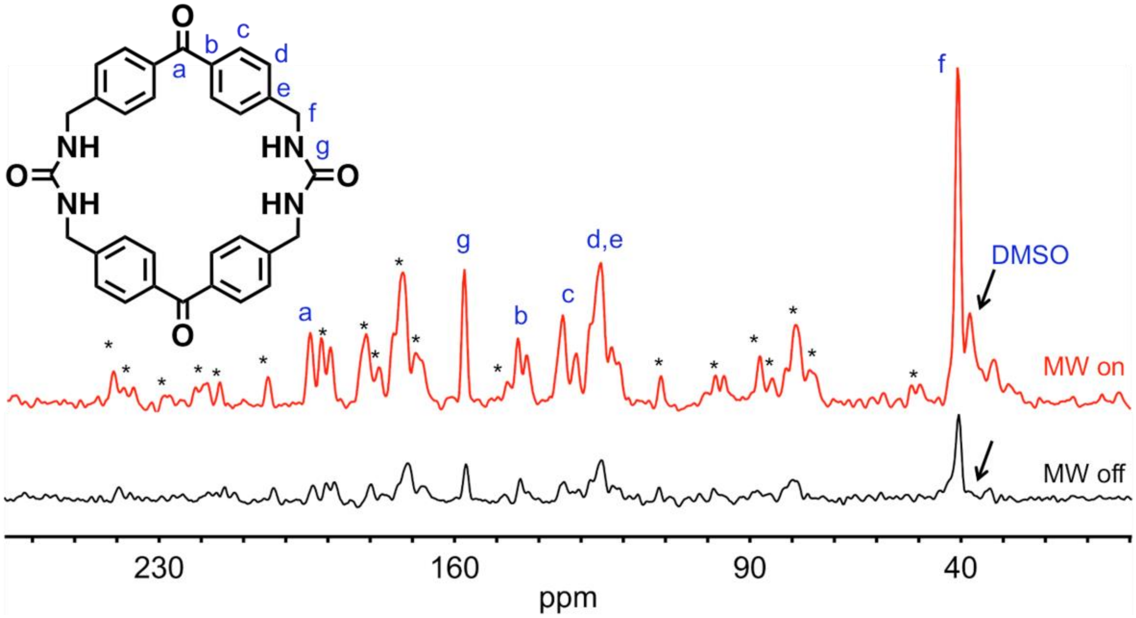

Figure 2.5. Optimized DNP CP-MAS NMR enhancement observed at 14.085 T under CP DNP MAS NMR conditions demonstrating a total enhancement of $\varepsilon_{on/off}$ = 4. Recorded at 112 K and a spinning speed of 7.0 kHz, microwave on (red line) vs. microwave off (black line). *Indicates spinning sidebands.

radical is in more direct contact with glycerol molecules present in the bulk DNP juice. It should be noted that impregnating the sample did not yield much higher polarization levels while introducing solvent signals. These results suggest that in these porous organic crystals, it may be more fruitful to use the endogenous radicals formed by **1** to enhance the NMR signals of the host:guest materials as opposed to traditional impregnation methods. Such DNP enhancement may be observable in other structures.

2.3 CONCLUSIONS

We have demonstrated that UV-irradiation of assembled benzophenone *bis*-urea macrocycles can generate low ~µM concentrations of long-lived RPs that persist for weeks at room temperature in the dark. Labelling experiments ruled out nitrogen-centered radicals. High field EPR data and variable temperature X-band EPR studies suggest the formation of two radicals. Our hypothesis is that the columnar assembled structure of **1** facilitates an H-abstraction reaction and significantly stabilizes the triplet RP. Stable and persistent organic radicals are rare and typically belong to four structural classes.[20] These results suggest that additional organic radicals may be stabilized by similar supramolecular assembly. Thus, we are currently exploring building blocks that contain other known sensitizers to investigate if their crystalline solids also afford stable radicals upon photolysis.

In summary, we have demonstrated that the photo-induced radical species generated by **1** can be utilized as a polarizing agent to significantly enhance NMR signals for both the host and its encapsulated guest DMSO, even though the concentration of endogenous radicals in **1** is orders of magnitudes below typical quantities of exogenous agents used for DNP NMR. UV-irradiated **1** showed a surprisingly broad DNP enhancement profile of over 120 mT, demonstrating that it is not necessary to tune the microwave frequency in order to observe DNP enhancement. The contribution of the cross-effect mechanism appears to be insignificant, since the field-stepped DNP profile exhibits only a single maximum with $\varepsilon_{on/off} > 0$. These results suggest that the design and incorporation of low levels of endogenous radicals into host frameworks may be broadly applied for NMR signal enhancement. Future DNP studies will focus on investigating a variety of guest molecules to see if such systems can be widely applied to study host: guest interactions in the solid-state.

2.4 FUTURE WORK

The future work on this project is obvious. It will be fruitful to load different guests inside the host and use it to study host-guest relationships in the solid-state. Moreover, current DNP polarizing agents are not reusable and are difficult to synthesize. So an interesting venture may be to take advantage of the insolubility of these materials accompanied by their radicals persistence at room temperature to develop resuable and regnerable DNP polarizing agents. This venture may require a host material that generates higher quantities of radical, but would be of extreme interest in the time of DNP.

2.5 EXPERIMENTAL

Materials and Instrumentation: All chemicals were purchased from Sigma Aldrich, VWR, or TCI Inc. and were used without further purification. ^{1}H-NMR spectroscopy in solution was performed on a Bruker Avance III HD 300 NMR spectrometer. UV-irradiation of host **1** was carried out with a Hanovia 450 W medium pressure mercury arc lamp cooled in a quartz immersion well. Thermogravimetric analysis (TGA) was carried out using TA instruments SDT-Q600 simultaneous DTA/TGA at a rate of 4º/min from 25-180 ºC with 5 min isotherms before and after temperature increase. EPR experiments were performed using a Bruker EMX plus equipped with a Bruker X-band microwave bridgehead and Xenon software (v 1.1b.66). Low temperature EPR experiments were carried out on the same instrument with a cavity cooled with liquid nitrogen for the 100 K study and liquid helium for the 10 K study. High temperature EPR analysis were performed in collaboration with Dr. Malcolm Forbes group on a JEOL USA Inc. JES-RE1X X-band EPR spectrometer equipped with a wide bandwidth preamplifier and a low-noise GaAsFET microwave amplifier. High-field EPR experiments were performed on a 240 GHz spectrometer at 6K under CW conditions. The high-field simulation was carried out using EasySpin and MATLAB, ML VERSION. ^{13}C CP MAS NMR and DNP NMR Experiments were carried out using a ramped CP-MAS pulse sequence on a 600 MHz Bruker DNP spectrometer (3.2 mm sapphire rotor) at the National High Magnetic Field Laboratory in Tallahasee, FL. CCDC structures: 684400 and 1534513.

EPR Sample Preparation: Neat crystals of 1 were added to a Norell quartz EPR tube, purged under Argon gas, sealed under Parafilm, and capped. The samples were UV-irradiated at 350 nm at rt with a Hanovia 450 W medium pressure mercury arc lamp cooled in a quartz immersion well. EPR signals were doubly integrated three times and averaged from the 3305 G to 3370 G range using Xenon software (v 1.1b.66).

MAS DNP NMR Sample Preparation: <u>UV irradiated sample</u>: The sample was prepared by UV-irradiating a crystalline sample of **1** (25 mg) for 7 hours using a medium pressure Hanovia Hg lamp using Corning glass filters to isolate the 366 nm Hg line. After UV irradiation, the sample was packed neat into a 3.2 mm sapphire rotor and DNP experiments were performed. **<u>Non-irradiated sample:</u>** The sample was prepared by packing a neat unirradiated crystalline sample of **1** (25 mg) into a 3.2 mm sapphire rotor and DNP experiments were performed. **AMUPol impregnated sample:** The previously packed UV-irradiated host **1** sample (25 mg) was unpacked from the sapphire rotor and impregnated with AMUPol (10 mM, 10-12 µL of a 6:3:1 glycerol-d_8, D_2O, H_2O solution) and the DNP CP-MAS NMR spectrum acquired using the optimal field conditions for **1**.

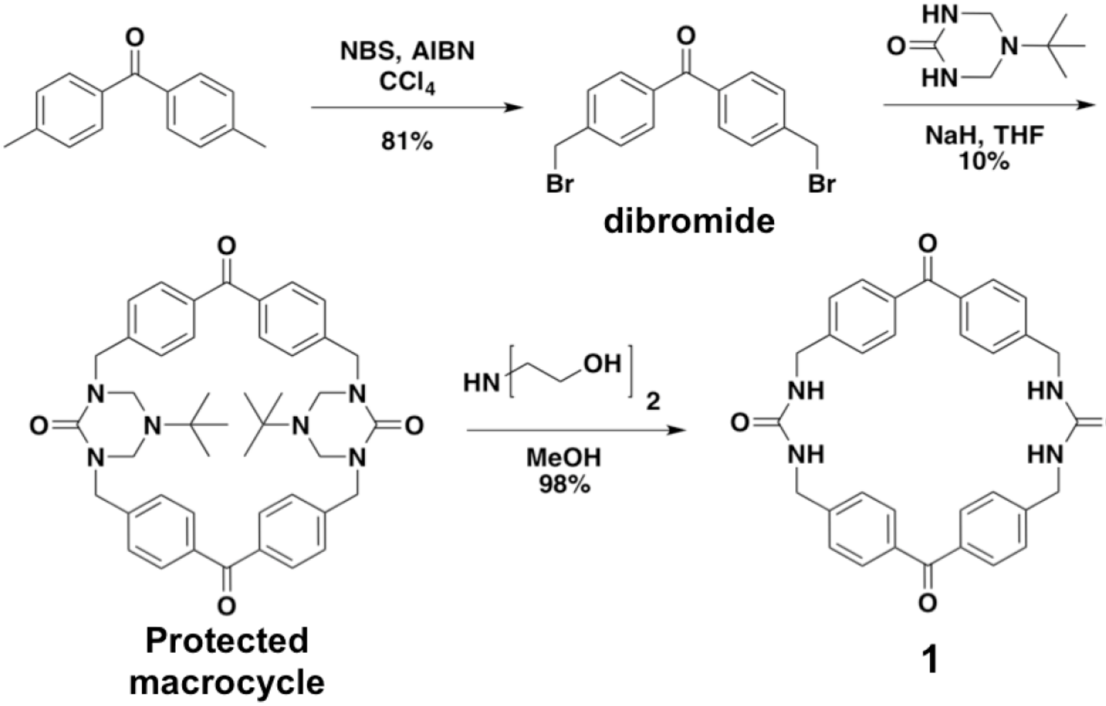

Scheme 2.1. Synthesis of benzophenone *bis*-urea macrocycle **1**. Host **1** was synthesized as previously reported.[21] Commercial 4,4'-*bis*(bromomethyl)benzophenone was brominated with N-bromosuccinimide **(**NBS) using 2,2'-azo*bis*(isobutyronitrile) (AIBN) as an initiator in CCl_4 to yield 4,4'- *bis*(bromomethyl) benzophenone (dibromide). The brominated c-shaped spacer was then cyclized with triazinanone and NaH in refluxing THF to form the protected macrocycle. Deprotected in an acidic diethanol amine aqueous/methanol mixture afforded the desired macrocycle **1**.

MAS DNP NMR Experimental: All ^{13}C NMR spectra were acquired using a ramped CP-MAS pulse sequence on a 600 MHz Bruker DNP spectrometer (3.2 mm sapphire rotor) at the National High Magnetic Field Laboratory. DNP experiments were conducted with a high-powered Cryomagnetics 394 GHz gyrotron with an output of 24 mW. The output was guided via quasi-optics to a corrugated waveguide and into the probe head. Experiments were conducted at 112 K with spinning speeds at 7.0 kHz.

Synthesis of 4,4'-*bis* (bromomethyl) benzophenone:

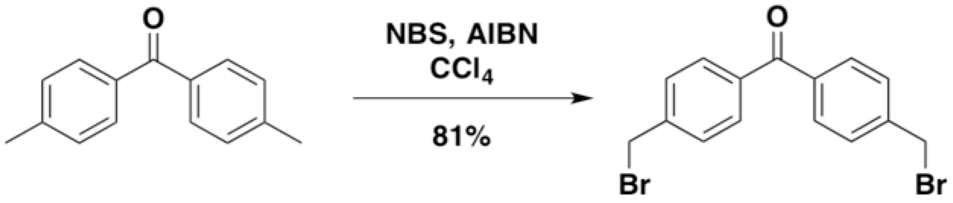

4,4'-*bis*(bromomethyl) benzophenone (2.0006 g, 9.51 mmol) was dissolved in CCl_4 (30 mL). Next, *N*-bromo succinimide (NBS, 4.2301 g, 23.8 mmol) and azobisisobutyronitrile (AIBN, 0.0104 g, 0.095 mmol) were added, and the reaction mixture was heated at reflux under N_2 for 18 h. Excess AIBN (~2 mg) and NBS (~30 mg) were added to the reaction mixture, which was stirred for a further two hours to push the reaction to completion. The reaction was cooled to rt, residual succinimide removed by filtration and washed with DCM. Silica gel was added, and the solvent was removed under vacuum and loaded onto a silica gel column packed with hexanes. The product was isolated *via* column chromatography (9:1 hexanes: ethyl acetate) as the last spot to yield a white solid that was further recrystallized from ethyl acetate. (2.3570 g, 67%). ^{1}H-NMR: (300 MHz; $CDCl_3$) δ=7.78 (4H, d, *J*=8.1), 7.51(4H, d, *J*=8.4), 4.54 (4H, s).

Synthesis of ^{15}N labeled triazinanone protected *bis*-urea benzophenone macrocycle:

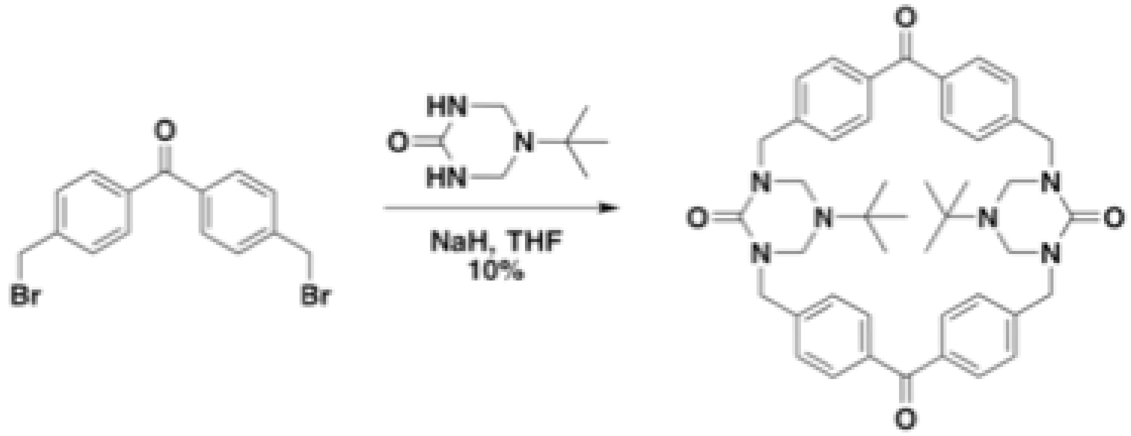

To a dry round bottom flask, still-dried THF (400 mL) was added. Next, ^{15}N labeled triazinanone (0.8578 g, 5.43 mmol) and NaH (60 % suspension in mineral oil, 0.8797 g, 21.72 mmol) were added. The mixture was heated to reflux under N_2 atmosphere for two hours. The suspension was cooled to rt and a solution of 4,4'-*bis*(bromomethyl)benzophenone (2.0078 g, 5.43 mmol) in dry THF (100 mL) was added to the stirring mixture all at once. The mixture was then heated to reflux for 48 h. Next, the reaction mixture was cooled to rt, neutralized with 1N HCl (~10 mL), and diluted with water (100 mL). THF was then removed under vacuum until an aqueous suspension remained. Crude product was extracted with methylene chloride (3 x 100 mL), washed with brine (150 mL), and dried with anhydrous Mg_2SO_4. Product was purified *via* flash silica gel column chromatography (9:1 ethyl acetate: methanol). Column fractions were left to evaporate for 3-7 days and white precipitate was collected and dried under vacuum to yield a white solid. (0.140 g, 3.5%). ^{1}H-NMR: ^{1}H-NMR (300 MHz, CD_2Cl_2) δ 7.81 (d, J = 8.1, 8H), 7.46 (d, J = 8.1, 4H), 4.64 (s, broad, 8H), 4.34 (s, 8H), 1.07 (s, 18H). ^{13}C-NMR: (75 MHz, $CDCl_3$) δ= 196.02, 155.69, 143.52, 136.62, 131.00, 127.35, 62.99, 54.35, 49.24, 28.45.

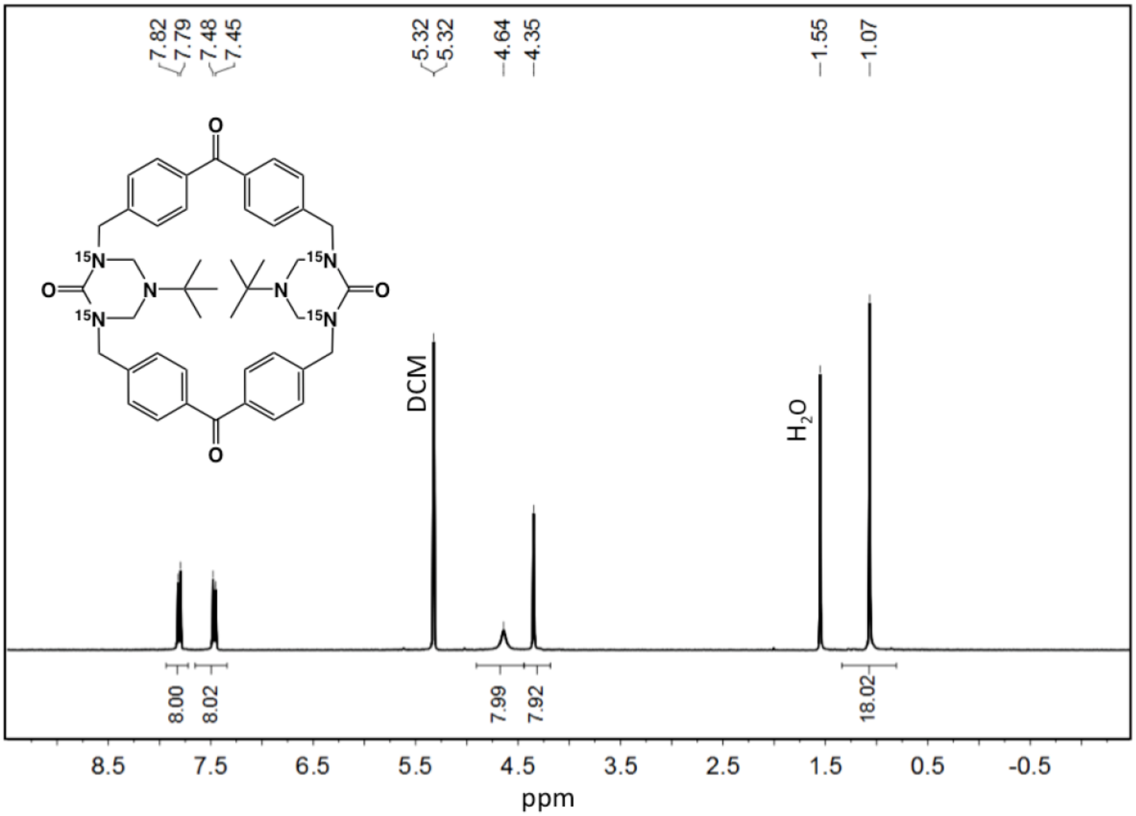

Figure 2.6. ^{1}H-NMR (300 MHz, δ_2 - CD_2Cl_2) of protected ^{15}N labeled host **1**.

Preparation of Deprotection Solution: A mixture of diethanol amine (20 mL) and deionized water (50 mL) was adjusted to pH 2 via drop-wise addition of 12.1 N HCl. The pH was monitored via litmus paper.

Deprotection of ^{15}N labeled triazinanone protected benzophenone *bis*-urea macrocycle (1):

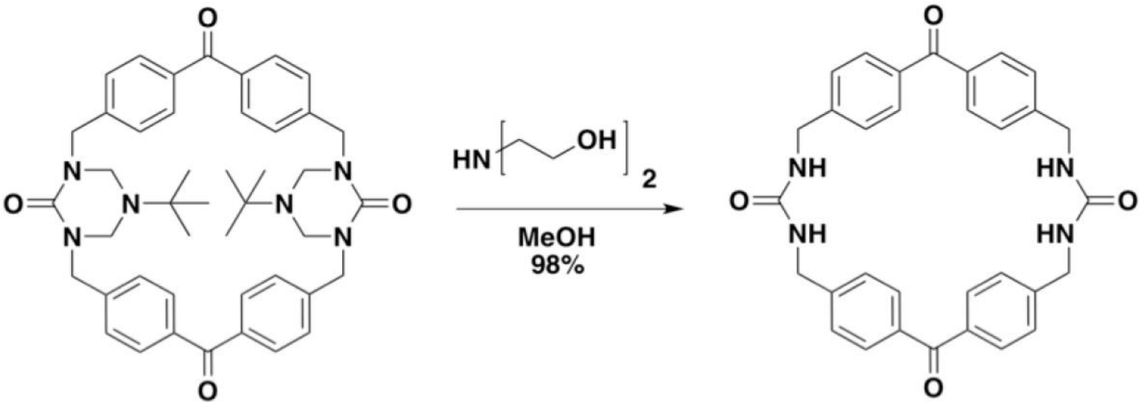

Triazinanone protected *bis*-urea benzophenone macrocycle (0.200 g, 0.275 mmol) was added to 1:1 v/v mixture of the deprotection solution (70 mL) and methanol (70 mL) was refluxed as a suspension for 48 h. The precipitate (varying in color from yellow to white) was collected via vacuum filtration and was washed with 1N HCl (20 mL), distilled water (3 x 100 mL), and dried under vacuum (0.135 g, 92%). ^{1}H-NMR (300 MHz, DMSO-d_6) δ 7.75 (d, J=8.0, 8H), 7.43 (d, J=7.9, 8H), 6.82 (d, J= 90.6, 4H), 4.384 (d, J= 5.5, 8H) ^{13}C-NMR (75 MHz, DMSO-d_6) δ 195.36, 158.42, 147.21, 135.74, 130.38, 126.70, 42.76.

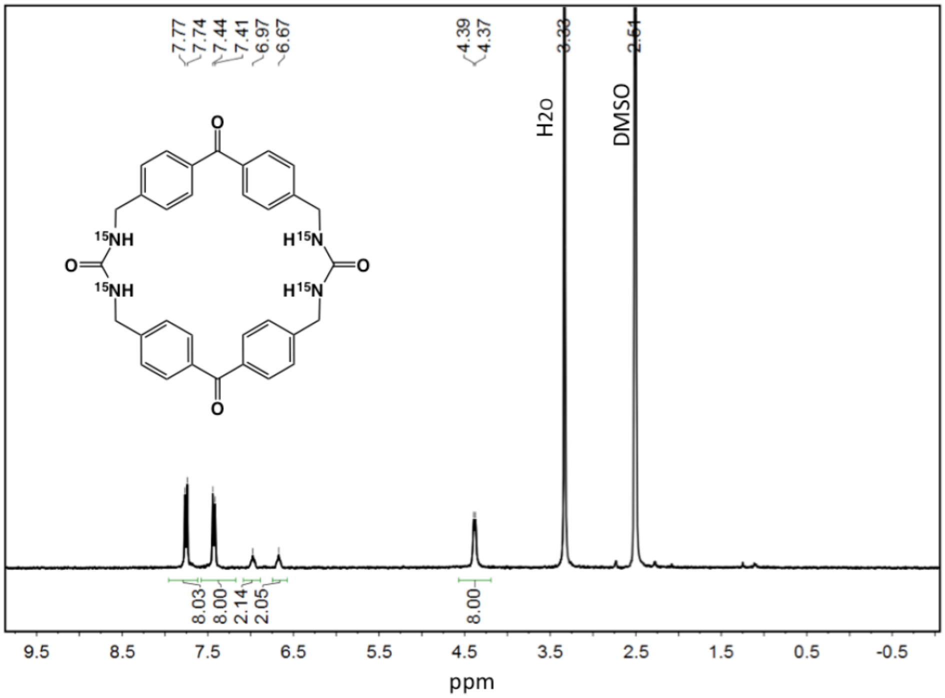

Figure 2.7. ^{1}H-NMR (300 MHz, δ_6-DMSO) of ^{15}N labeled host **1**.

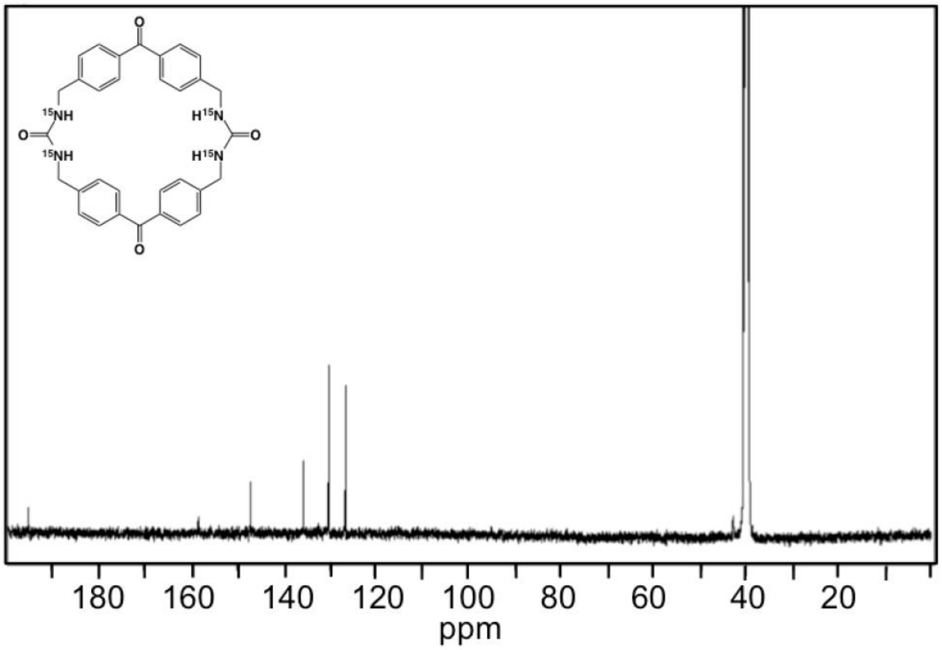

Figure 2.8. ^{13}C-NMR (75 MHz, δ_6-DMSO) of ^{15}N labeled host **1**.

Assembly of benzophenone *bis*-urea macrocycle to yield host 1: A suspension of benzophenone *bis*-urea macrocycle (0.135 g, 0.275 mmol) in DMSO (12 mL) was heated to 130°C and DMSO slowly added to the stirring mixture until all the material was dissolved. The colorless solution was hot gravity filtered into a pressure tube which was heated at 130°C for 1 hour and was slowly cooled to room temperature at a ramp rate of 1°C/hr. The white needle-like crystalline product was collected via vacuum filtration to yield host **1** (0.120 g, 92%). The same procedure was carried out on the ^{15}N labeled material.

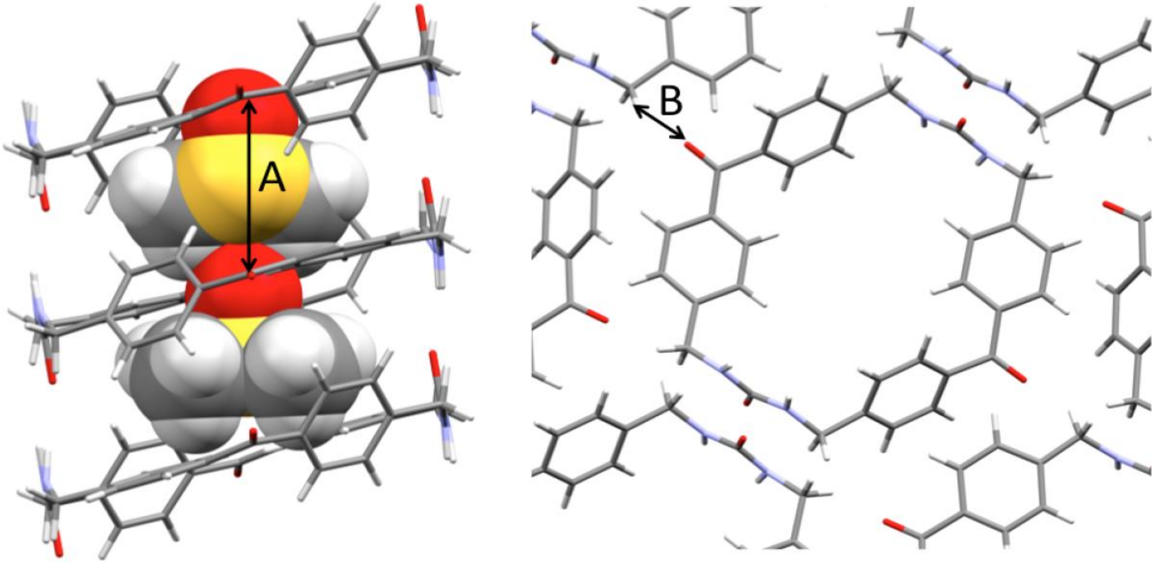

Figure 2.9. XRD of assembled host **1**. (A) View along a single column highlighting the 4.74 Å bond distance between the neighboring benzophenone carbonyl groups. (B) Crystal packing showing close contacts of the methylene-bridged hydrogens (2.44 Å) to benzophenone carbonyls, potential sites for H-abstraction – DMSO guests have been omitted for clarity.

Exchange of guests to form host 1•THF: Host **1** (25 mg) was heated to 180 °C via thermogravimetric analysis at a ramp rate of 4°C/min to remove DMSO from host channels. The emptied host was then soaked in neat THF (1 mL) overnight. The THF loaded crystals were collected via vacuum filtration and packed into a 3.2 mm sapphire rotor and investigated under ^{13}C CP MAS NMR conditions at room temperature.

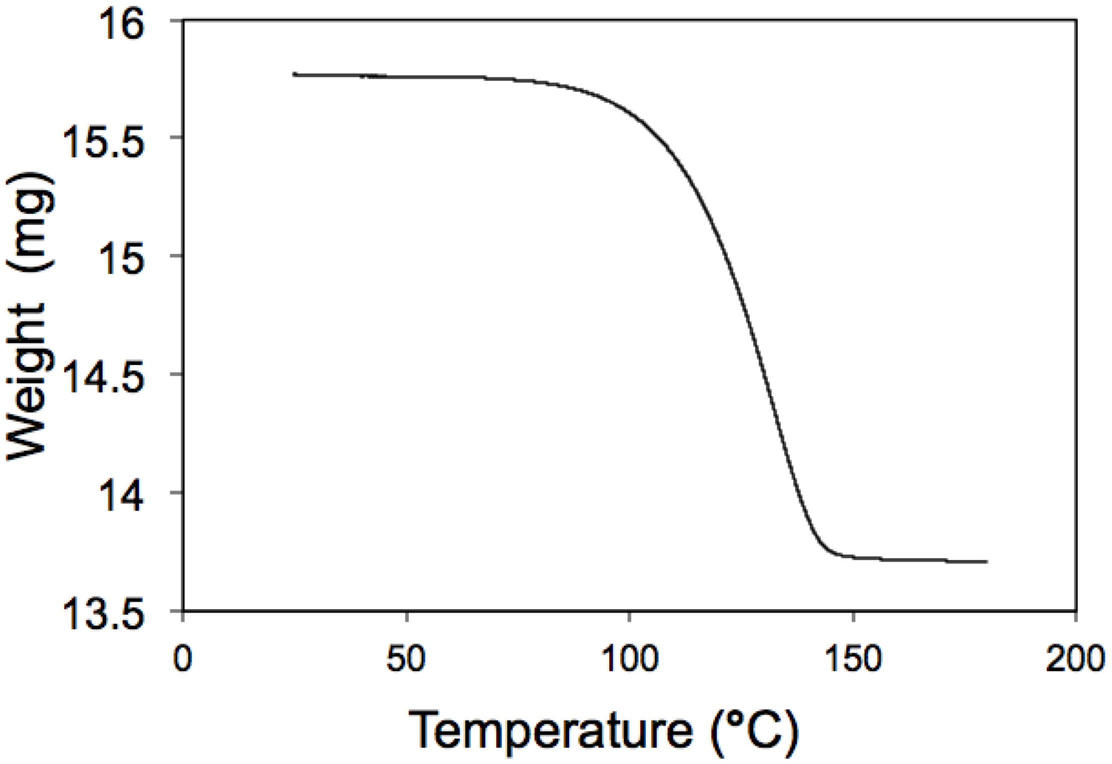

Figure 2.10. TGA graph with a one step desorption of DMSO from host **1**•DMSO at 130 °C. Host: guest ratio calculated to be 1:1.

IR spectroscopy studies. IR spectroscopy was performed on freshly evacuated host **1** crystals (host **1** empty) purified by one recrystallization cycle both before and after 30 min UV irradiation. Irradiation was performed as previously described using a Rayonet reactor. All IR analysis was performed using a Perkin Elmer Spectrum 100 IR Spectrometer.

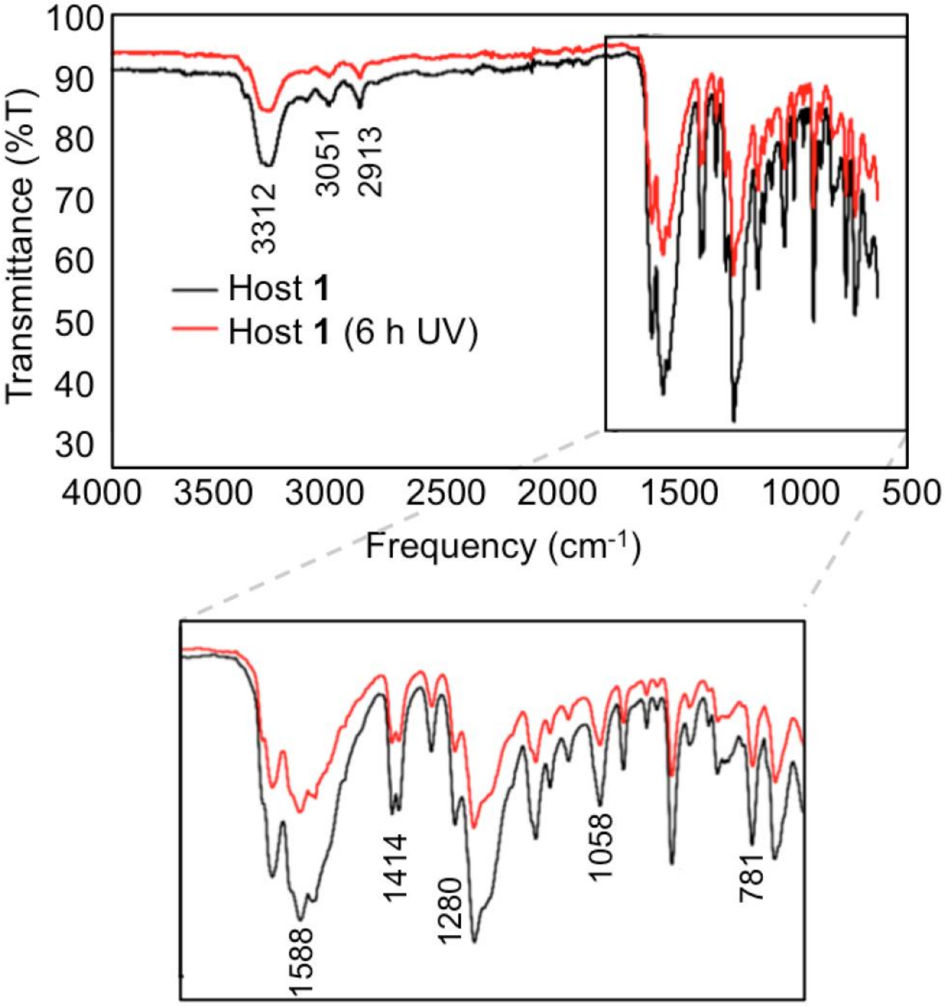

Figure 2.11. IR comparison of solid host **1** (empty) before (black line) and after (red line) 1 h of UV irradiation.

UV-vis studies. UV-vis spectroscopy was performed on freshly evacuated host **1** (10 mg) crystals purified by one recrystallization cycle recorded after 3 hours UV irradiation. Sample was analyzed using a 4 mm quartz well with a quartz cover plate. All UV-vis analysis was performed using a Perkin Elmer Lambda 35 UV-vis spectrometer with UV Winlab software. After 3h UV irradiation (Figure 2.13, red line) host **1** (empty) displays a nearly identical spectra with the initial host. The broad pi-pi* excitation absorption was slightly shifted at λ_{max} = 304 nm. The more intense n-pi* excitation was identical to that of the before UV-irradiation of the sample at λ_{max} = 355 nm. A weak absorption may be present at λ_{max} = 588 nm. In the literature, benzophenone ketyl radicals have been reported to have λ_{max} values at 330 and 545 nm.[22] These absorption bands are reported to shift to longer wavelengths as bulky substituents are attached. This can be seen through comparison ketyl radical derivatives such as benzophenone, naphthylphenylketone, 2-benzoylbiphenyl, and bis(bisphenyl-2-yl)methanone. These analogous possess λ_{max} absorptions relating to ketyl radical at 545, 585, 585, and 630 nm respectively.[22] The benzophenone radical anion has been reported at λ_{max} = 700 nm region[23] and was not observed in our system.

UV-vis studies DMSO loaded host 1 after UV irradiation. UV-vis spectroscopy was performed on host **1** (10 mg) crystals purified by one recrystallization cycle recorded after 3 hours UV irradiation. Sample was analyzed using a 4 mm quartz well with a quartz cover plate. All UV-vis analysis was performed using a Perkin Elmer Lambda 35 UV-vis spectrometer with UV Winlab software.

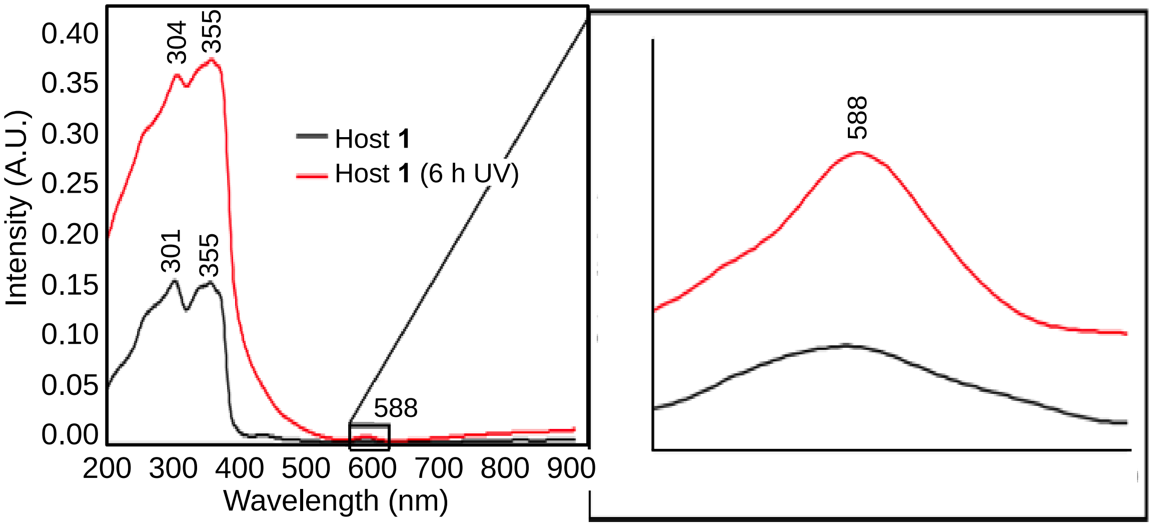

Figure 2.12. UV-vis comparison of solid host **1** (empty) before (black line) and after (red line) 3 h UV irradiation. UV irradiated host **1** shows similar λ_{max} values at 304 and 355 nm. The ketyl radical or other radical species is expected at λ_{max} at 588 nm.

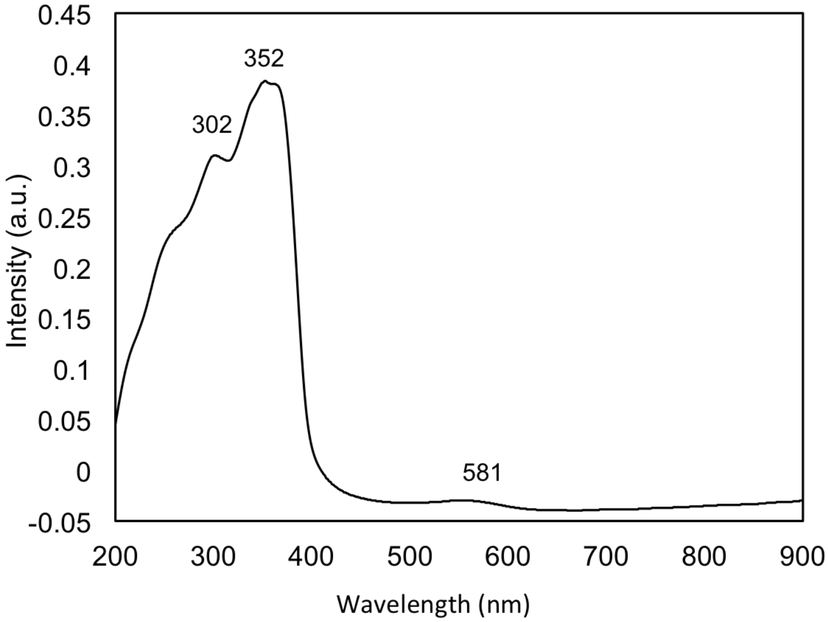

Figure 2.13. UV-vis comparison of solid host **1** with DMSO loaded in the channels after UV irradiation for 3 hours. UV irradiated host **1** shows similar λ_{max} values at 302 and 352 nm. The ketyl radical or other radical species is expected at λ_{max} at 581 nm.

Fluorescence studies. Fluorescence spectroscopy was performed on freshly evacuated host **1** (10 mg) crystals purified by one recrystallization cycle both before and after 30 min UV irradiation. Sample was analyzed using a 4 mm quartz well with a quartz cover plate. Solid-state fluorescence analysis was performed using a Perkin Elmer LS 55 fluorescence spectrometer with FL Winlab software with integrating sphere. Sample was analyzed over 375 – 525 nm range using an excitation wavelength of λ_{ex} = 355 nm.

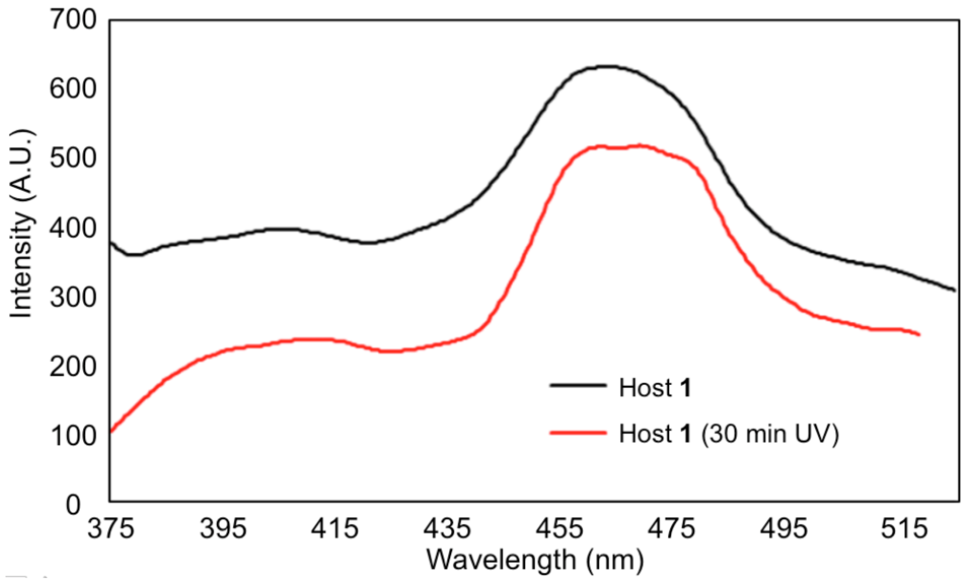

Figure 2.14. Emission spectra comparison of solid host **1** (empty) before (black line) and after (red line) UV irradiation. Scan range was 375 to 525 nm using λ_{ex}=355 nm as the excitation wavelength.

EPR comparison of ^{15}N host 1 vs. unlabeled host 1: Freshly evacuated crystals of host **1** and ^{15}N host **1** (5 mg) were loaded into separate EPR tubes and purged with Argon for 5 min. EPR analysis was then performed on both samples before UV exposure. As expected, neither sample yielded a positive EPR signal upon ambient light exposure. Crystals were then UV irradiated for 30 min using a Rayonet reactor equipped with 16 x 120 W lamps (350 nm) followed by EPR analysis. The very small changes observed upon ^{15}N substitution indicate that the contribution to spin density on the N is smaller than expected, which may reflect an orientation effect in the hyperfine tensor for the benzylic-type radical. The signal is also being broadened by spectral exchange and has a rather large natural line width, both of which may mask small changes in hyperfine splitting patterns due to isotopic substitution.

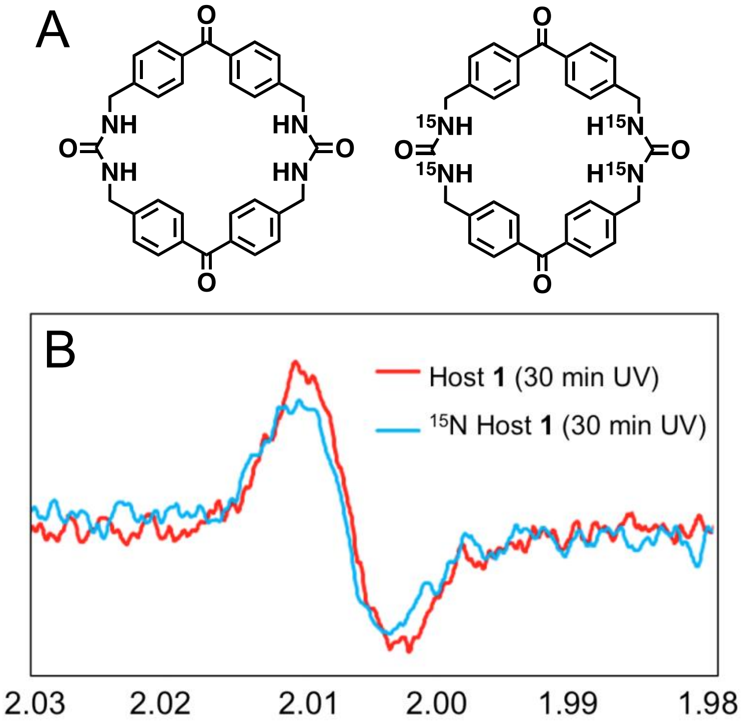

Figure 2.15. (a) Host **1** and its ^{15}N labeled analogue samples prepared under Ar (g) and (b) Comparison of their EPR spectra after 30 min UV irradiation.

EPR after multiple recrystallizations: To test that the photoinduced radical was not a result of impurity host **1** was subjected to three recrystallization cycles and EPR spectra were recorded. Signal was still observed after 3 recrystallization cycles indicating that the radical is not a result of impurity.

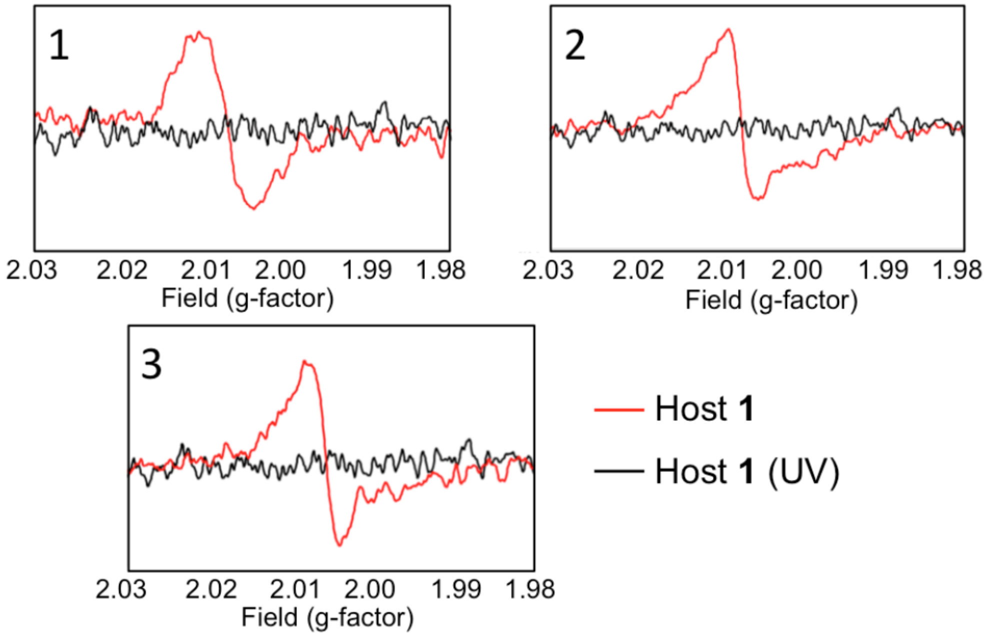

Figure 2.16. Host **1** (empty) EPR analysis before and after 30 min UV irradiation under Argon atmosphere after the (1) 1st , (2) 2nd, and (3) 3rd recrystallization cycles.

EPR of assembled vs. unassembled 1: Precipitate: **1** collected directly from the deprotection step was collected via Millipore vacuum filtration and washed with H_2O (25mL) and CH_2Cl_2 (25 mL). Sample was left to dry on the vacuum filtration apparatus for 30 min, and then the purity was verified via 1H-NMR spectroscopy. The precipitated host **1** (5 mg) was loaded into an EPR sample tube and purged with argon for 5 min then EPR spectra was recorded. Sample was then transferred to the Rayonet UV reactor and irradiated for 30 min and the EPR spectra was again recorded. Solution: Freshly recrystallized host **1** crystals (1 mg) were dissolved in DMSO (1 mL) by heating with a heat gun. Solution was transferred into an EPR tube and purged with argon gas (99.99%

purity) for 5 min and the EPR was recorded. Sample was then irradiated in a Rayonet UV reactor equipped with 3500 Å bulbs for 30 min and the EPR was again recorded. Assembled material: Host **1** crystals (5 mg), purified via 3x recrystallization cycles, were collected via Millipore vacuum filtration. Sample was then washed with CH_2Cl_2 (25 mL) and left to pull on the vacuum filtration apparatus for 30 min. Crystals were then loaded into an EPR tube, then purged with Argon for 5 min, and the EPR spectra was recorded. Sample was then transferred to the Rayonet UV reactor and irradiated for 30 min and the EPR spectra were again recorded. The lack of changes to the EPR signal when DMSO is loaded in the channels shows that the DMSO guest does not quench the radical. Radical formation does not appear to be altered or impacted by guests being loaded in the host channels, as observed by Geer in EPR samples of host **1**•cumene and host **1**•2-methyl-2-butene.[21]

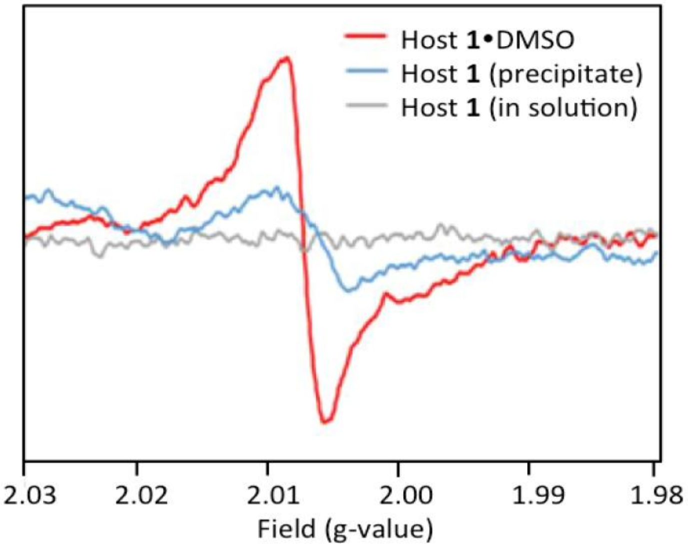

Figure 2.17. Comparison of crystallized host **1**, host **1** precipitate from deprotection solution, and host **1** in DMSO in solution after 30 min UV irradiation.

X-band EPR Simulations:

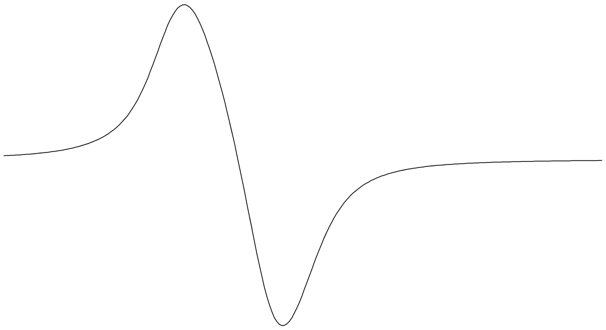

Figure 2.18. Computer simulation of the X-band EPR spectrum in Figure 2B. Total sweep width is 100 G. Other parameters given below.

X-band EPR Parameters:

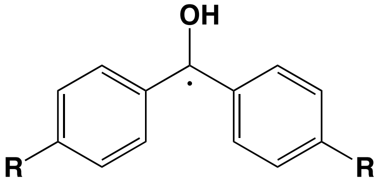

4 H $_{ortho}$ = 5.0 G

4 H $_{meta}$ = 2.0 G

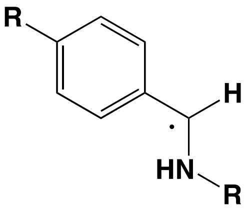

1 N = 6.0 G

1 H = 5.0 G

1 H = 3.0 G

4 H = 4.0 G

Other parameters: average g-factor = 2.0055, spin exchange interaction J = 3 G, natural line width = 14 G.

For simplicity, the simulation uses isotropic g-factors and hyperfine interactions. The overall spectral width and line shape support the existence of a weakly coupled radical pair rather than a molecular triplet state. Minor discrepancies in the fit almost certainly arise from hyperfine and g–factor anisotropies that are unaccounted for in the model. Also, it is not well established if the observed spin-spin coupling is of the exchange or dipole-dipole interaction type.

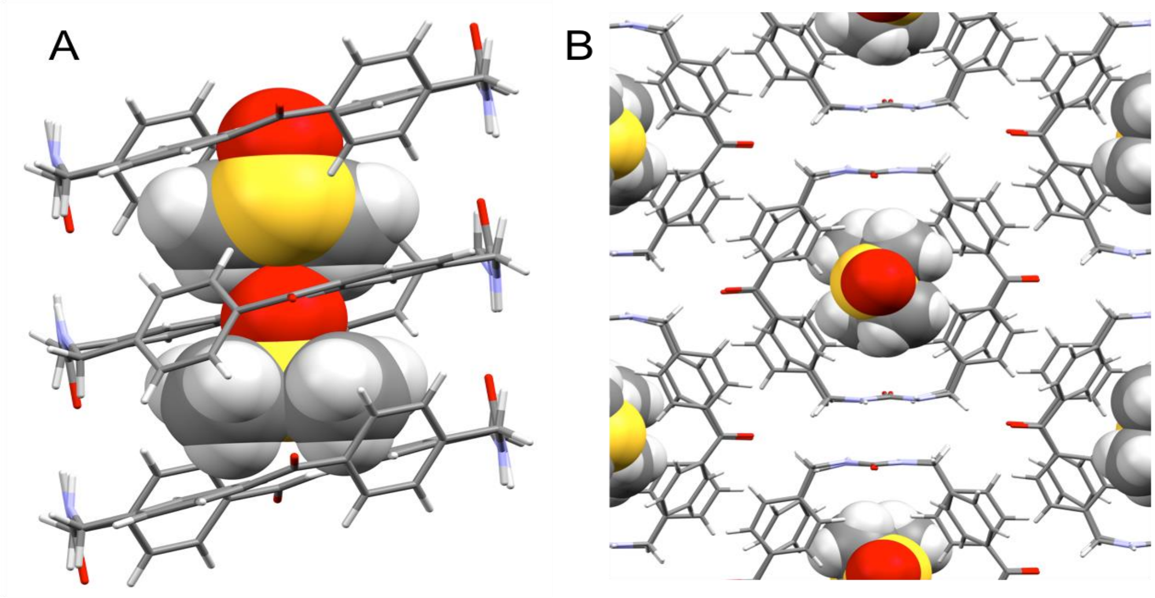

Figure 2.19. Views from the crystal structure of host **1** after 7 hours of UV irradiation. (A) View along a single column, DMSO is loaded in the channels. (B) View of crystal packing.

XRD of host 1 after 7 hours UV-irradiation: Crystal data structure and refinement of [$C_{32}H_{28}N_4O_4$, C_2H_6OS]. The .cif file has been deposited CCDC 1534513.

Empirical Formula	$C_{32}H_{28}N_4O_4$, C_2H_6OS
Temperature (K)	100 (2)

Formula Weight	532.60, 78.13
Space group	P 21
a/Å	9.4229 (7)
b/Å	23.0807 (15)
c/Å	13.2465 (9)
Volume/Å	2878.95
Z, Z’	4,0
Density (calculated)	1.322 Mg/m^3
Absorption coefficient	0.090
F(000)	1288.0
Crystal size/mm^3	0.44 x 0.08 x 0.06
Theta range for data collection	4.322 to 55.146
Index ranges	12≤h≤12,-30≤k≤ 30,-17≤l≤ 17
Reflections collected	83073
Independent reflections	13329[R_{int}=0.0339,R_{sigma}=0.0240]
Completeness to theta	100.0%
Absorption correction	None
Refinement method	Full matrix least-squares on F^2
Data / restraints / parameters	13329/13/856
Goodness-of-fit on F^2	1.065
Final R indices [I>2sigma(I)]	R_1 = 0.0350, wR_2 = 0.0864
R indexes (all data)	R_1 = 0.0420, wR_2 = 0.0910
Largest diff. peak and hole	0.26/-0.42

Dark Decay Experiment: Crystals of host **1** (12.5 mg) were added to a Norell quartz EPR tube, purged under Argon gas, and sealed under Parafilm. The sample was UV-irradiated at 350 nm for 1 h at rt. X-band EPR experiments were carried out for nearly 26 days after UV-irradiation, the sample was stored in the dark in between scans. Experiments were carried out under identical parameters at a microwave power of 1.589 dB with a modulation amplitude of 2. EPR signal was doubly integrated three times and averaged from the 3305 G to 3370 G range using Xenon software (v 1.1b.66).

UV-dependence Study: Crystals of host **1** (4.5 mg) were added to a Norell quartz EPR tube, purged under Argon gas, and sealed under Parafilm. The sample was UV-irradiated at 350 nm for 1 h at rt. X-band EPR experiments were carried at various time intervals during the UV-irradiation until radical generation plateaued. Experiments were carried out under identical parameters at a microwave power of 1.589 dB and 1.0 G modulation amplitude. EPR signal was doubly integrated three times and averaged from the 3305 G to 3370 G range using Xenon software (v 1.1b.66).

Calibration of TEMPO in benzene: A stock solution (3.2 mM) of TEMPO in benzene was prepared by dissolving TEMPO (0.005 mg) in benzene (10 mL). The solution was diluted to known concentrations and 0.1 mL aliquots were used for X-band EPR studies using identical parameters. The EPR samples were recorded in the same Norell EPR tube, which was washed and flame dried in between samples. The three line EPR spectra was doubly integrated three times and averaged from the 3305 G to 3370 G range using Xenon software (v 1.1b.66).

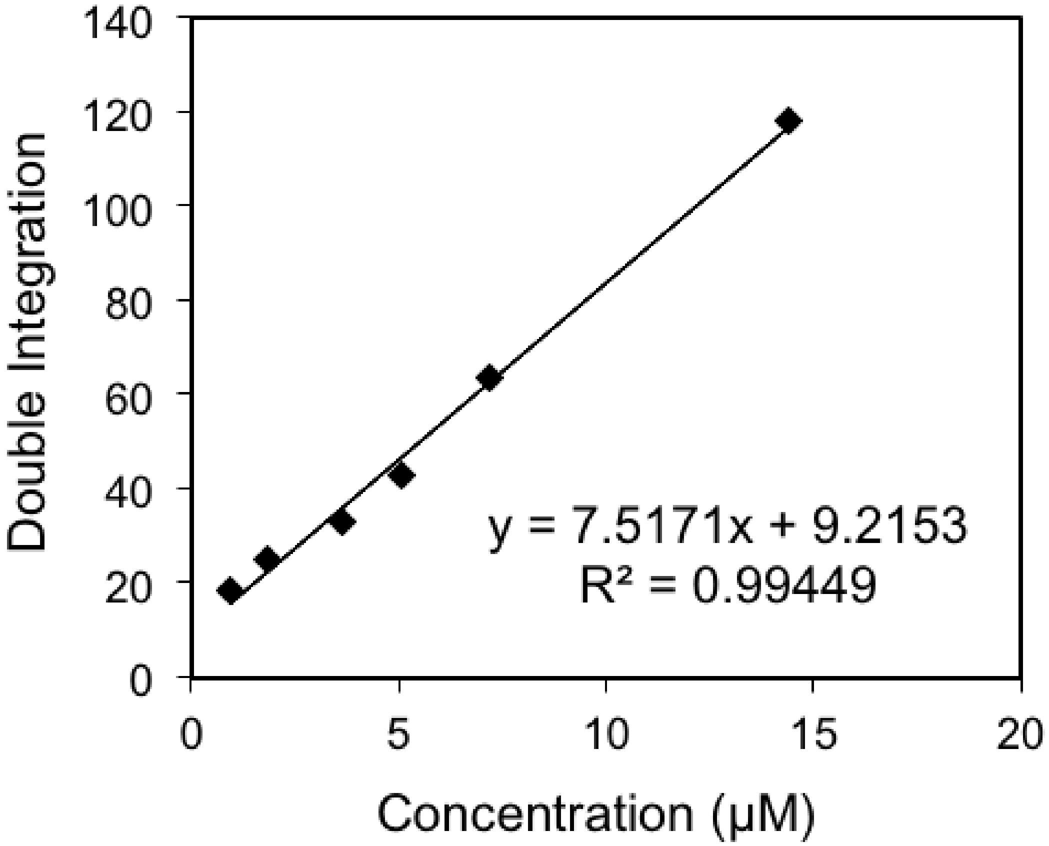

Figure 2.20. Calibration of EPR spectrometer using TEMPO in benzene. Signal intensities were doubly integrated in order to obtain the area under the absorption curve.

Calculation for approximate radical concentration:

Area under the curve (after 7 hours irradiation): 50.034629

Equation from TEMPO calibration: $y = 7.5171x – 9.2153$

Where, $y = 7.5171x - 9.2153$

x = concentration

y = area under the curve = 50.034629

$$50.034629 = 7.5171x - 9.2153$$

$$40.819329 = 7.5171x$$

$$x = 5.43 \times 10^{-06}\ \text{M} = 5.4\ \mu\text{M radical concentration}$$

Percentage of radical generated by 1 calculation: From the concentration we can find the mols of TEMPO.

$$\text{M} = \frac{\text{mol}}{\text{L}} = 5.43 \times 10^{-06}\ \text{M} = \frac{\text{mols of TEMPO}}{0.0001\ \text{L}}$$

$$\text{mols of TEMPO} = 5.43 \times 10^{-06}\ \text{M}\ (0.0001\ \text{L})$$

$$= 5.43 \times 10^{-10}\ \text{mols of TEMPO} \times 10^{-06}\text{M} = \frac{\text{mol of TEMPO}}{0.0001\text{L}}$$

From there we can find the approximate number of radicals that were generated. This is because for every one molecule of TEMPO there is one radical in the system.

1 TEMPO molecule = 1 Radical

5.43×10^{-10} mols of radicals generated by **1**

For 4.5 mg host **1**:

$$\frac{0.0045\ \text{g}}{1} \times \frac{1\ \text{mol}}{610.34\ \text{g}} = 7.37 \times 10^{-06}\ \text{mols host } \mathbf{1}$$

Now we can calculate the percentage of radical generated. To do that, we can divide the number of radicals of generated by UV irradiation by the number host molecules present.

$$\frac{5.43 \times 10^{-10}\ \text{mols radicals}}{7.37 \times 10^{-06}\ \text{mols host}} \times 100 = 0.007 = \sim 0.01\ \%\ \text{radical/host}$$

Variable temperature studies: Evacuated host **1** crystals (5 mg), purified via 3x recrystallization cycles, and evacuated ^{15}N labeled host **1** crystals (5 mg) were UV irradiated for 30 min. EPR spectra was recorded at 20, 50, and 100ºC. All variable temperature EPR analysis were performed on a JEOL USA Inc. JES-RE1X X-band EPR spectrometer equipped with a wide bandwidth preamplifier and a low-noise GaAsFET microwave amplifier.

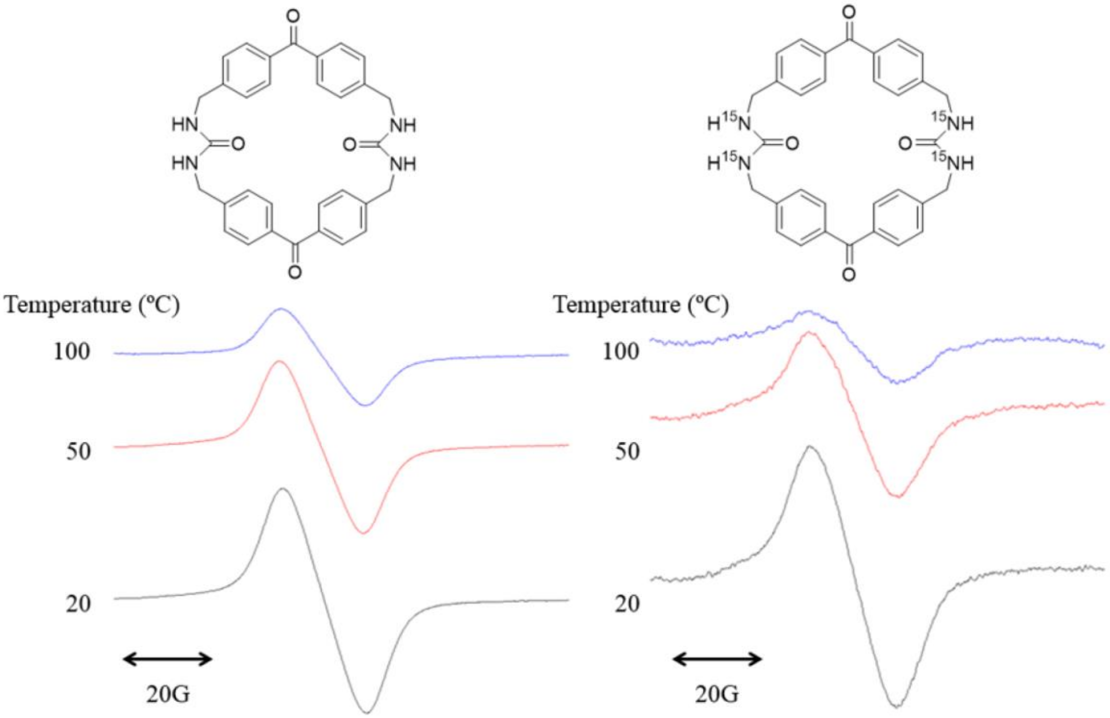

Figure 2.21. Variable Temperature EPR at 20, 50, and 100 ºC for host **1** (empty) and ^{15}N labeled host **1.**

^{15}N labeled 1 EPR recorded at 10K. EPR experiments were performed using a Bruker EMX plus equipped with a Bruker X-band microwave bridgehead and Xenon software (v 1.1b.66). Low temperature EPR experiments were carried out on the same instrument with a cavity cooled with liquid helium spectra was recorded at 10 K on 7.6 mg of ^{15}N labeled host crystals.

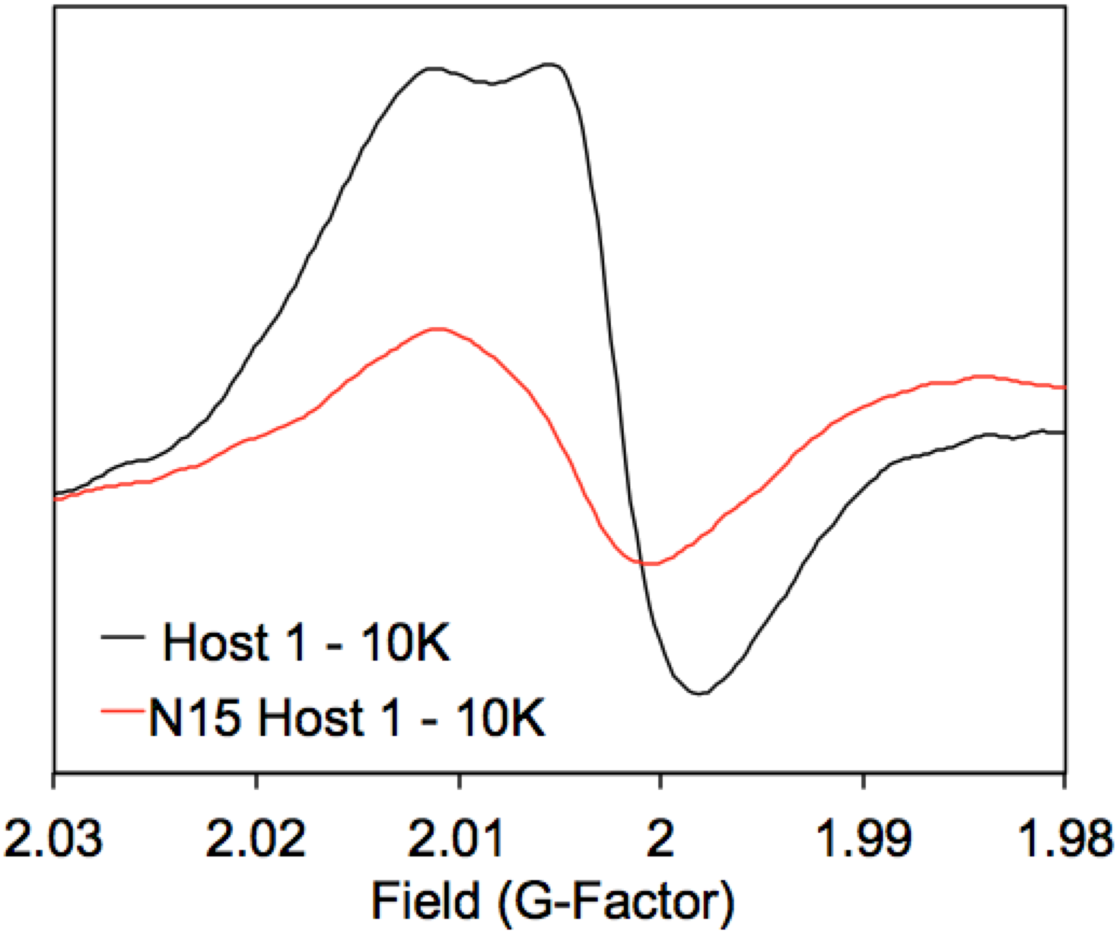

Figure 2.22. Low temperature EPR recorded at 10 K on ^{15}N labeled host **1** versus unlabeled host.

High Field EPR: High-field EPR experiments were performed on a 240 GHz spectrometer under CW conditions. Host **1** after 7 hours of UV irradiation (25 mg) was crushed and placed into the sample well, spectra was recorded at 6K. Easy Spin simulation was performed by John Tokarski, details and parameters given in Table 2.1.

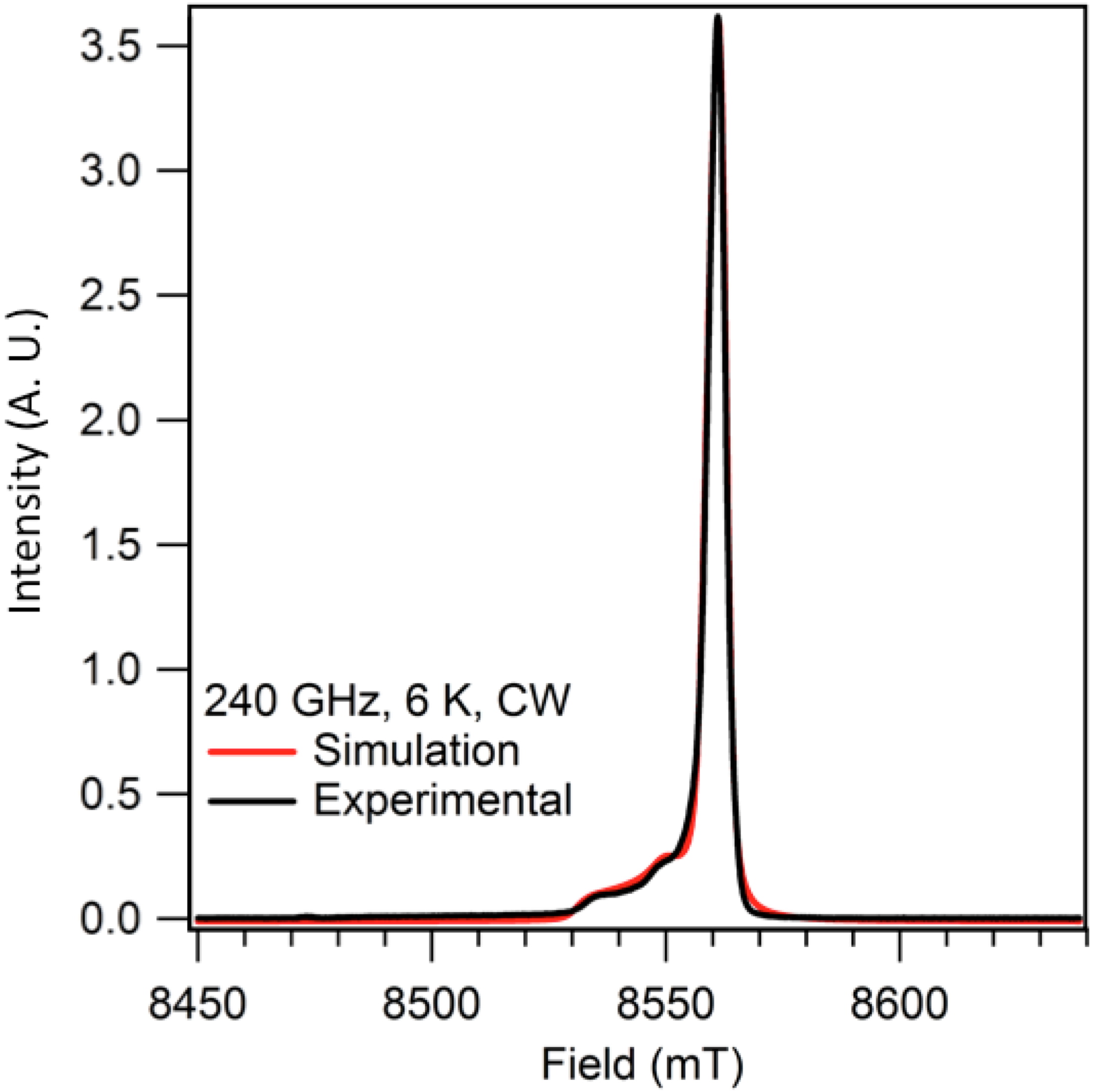

Figure 2.23. CW high-field (240 GHz) EPR absorption curve of **1** at 6 K vs. ppm.

High Field EPR Simulations: The high field EPR data was simulated using the MATLAB EasySpin toolbox. All simulations were performed using the "pepper" package at 6 K and 240 GHz. No field ordering was used in the simulations. Three separate simulations were performed: a single radical species with S=1/2, two radicals with S=1/2 for both species, and a single species with S=1. In the first case, the EPR data was not able to reproduce the smaller, low-field peaks, even by varying the g-anisotropy for one radical. The triplet state was able to reproduce the low-field peaks (D= -380 MHz, E= -10 MHz), but the intensities were inconsistent with respect to the acquired experimental data. However, it was the system with two spin ½ radicals that was able to properly fit the observed data.

MAS DNP NMR Conditions: All ^{13}C NMR spectra were acquired using a ramped CP-MAS pulse sequence on a 600 MHz Bruker DNP spectrometer (3.2 mm sapphire rotor) at the National High Magnetic Field Laboratory. DNP experiments were conducted with a high-powered Cryomagnetics 394 GHz gyrotron with an output of 24 mW. The output was guided via quasi-optics to a corrugated waveguide and into the probe head. Experiments were conducted at 112 K with spinning speeds at 7.0 kHz. The sample was prepared by UV-irradiating a crystalline sample of **1** (25 mg) for 7 hours using a medium pressure Hanovia Hg lamp using Corning glass filters to isolate the 366 nm Hg line in Dr. Jack Saltiel's lab at Florida State University under the supervision of Dr. Shipra Gupta. After UV irradiation, the sample was packed into a 3.2 mm sapphire rotor and DNP experiments were performed. For comparison, host **1** was also impregnated with AMUpol using identical conditions and at its optimal field strength. DNP experiments were also carried out on an unirradiated sample to ensure the enhancement observed was not a result of heating.

Build-up curve: The signal intensity was investigated as a function of irradiation time and plotted in Figure 2.25. The data fits to a bi-exponential function as the enhanced signal is comprised of a slow and fast component (6.7 s and 24.2 s). At shorter times, the enhancement is larger which allows the use of a shorter recycle delay and ultimately a shorter experimental time to achieve a quality signal to noise ratio.

MAS DNP NMR Field Sweep: A Lakeshore cryogenics power supply system was used to ramp the field of the magnet. Data for the field sweep was acquired with and without microwaves to analyze the enhancement as a function of field strength. Enhancement, ε was calculated as

$$\varepsilon = \frac{S_{on}}{S_{off}}$$

Where, S denotes the signal intensities with and without the microwaves. The field sweep data does not represent the typical solid effect, cross effect profiles. Furthermore, the enhancement seems to be constant, except for a slight maxima around 14.09 T. Therefore, due to the extremely broad enhancement, it could be postulated that the enhancement derives from the Overhauser effect.

Conversion from Tesla to ppm for Figure 2.3B. Due to the fact that the DNP field step study and High-field EPR were recorded on different magnetic fields (14.1 and 8.56 T respectively) we had to convert the two spectra to ppm to overlay them. PPM conversion was achieved in excel and performed on the field-stepped DNP study (Figure 2.26) and on the high-field EPR.

$\text{Field} – B_{max} = B_0$
$(B_0 / B_{\text{max}}) \text{ x } 10^{06} = \text{ppm scale}$

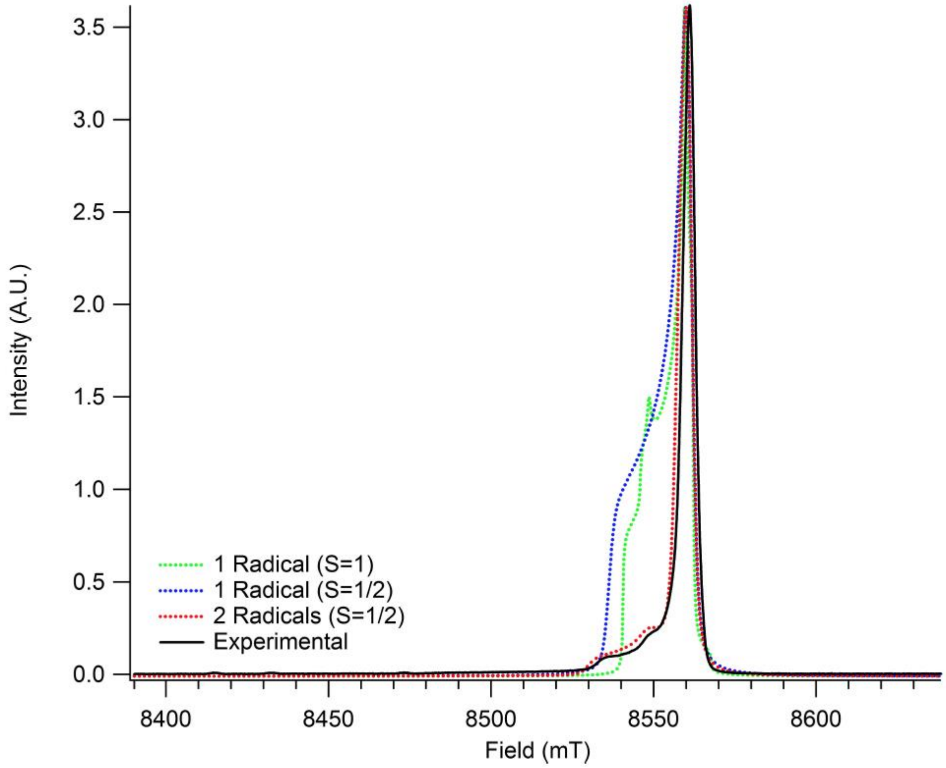

Figure 2.24. Simulation of the CW high field (240 GHz) EPR spectra recorded at 6K for a single radical species with S=1/2 (blue line); single radical species with S=1 (green line); two S=1/2 radicals (red line) with respect to the experimental data (black line) demonstrating that the data is consistent with triplet radical pair (two S=1/2 radicals).

Table 2.1. The g-values used to simulate the spectra which is consistent with a biradical system with S=1/2 for both species.

	Isotropic g-value	**PAS Components**	**Weighting Factor**
Radical 1	2.0030	[2.0027, 2.0027, 2.00365]	4
Radical 2	2.0061	[2.0027, 2.0056, 2.0100]	1

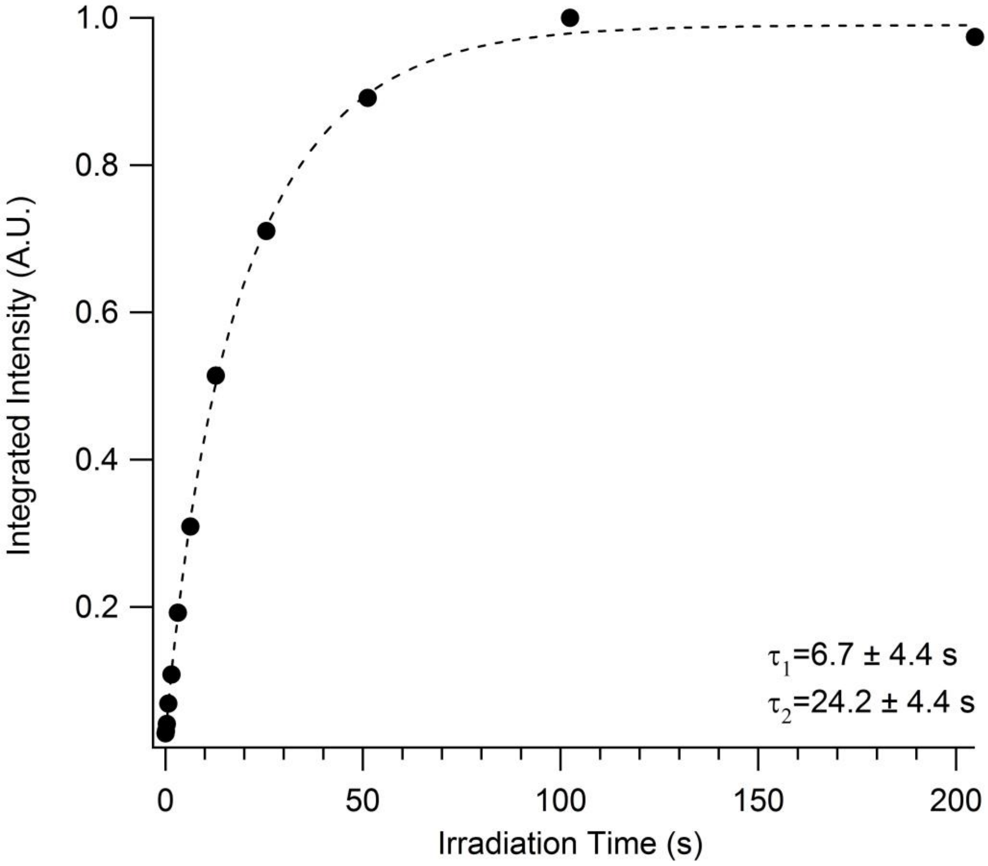

Figure 2.25. DNP signal as a function of irradiation time of the UV-irradiated **1.**

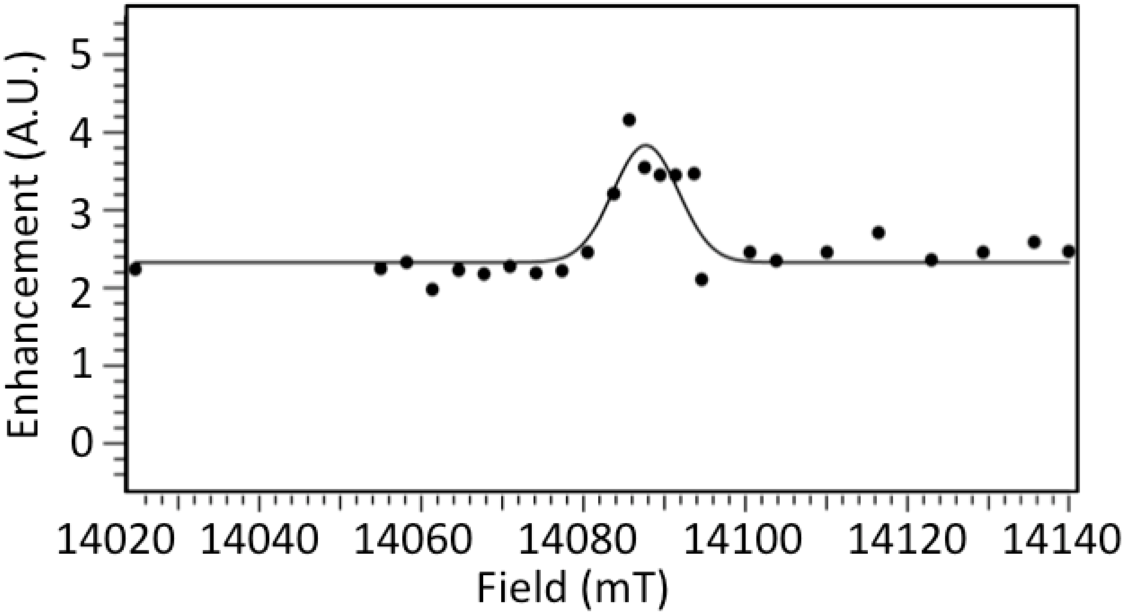

Figure 2.26. ^{13}C-MAS NMR field dependence of the DNP enhancement of UV-irradiated **1** (7 h, rt) as a function of magnetic field.

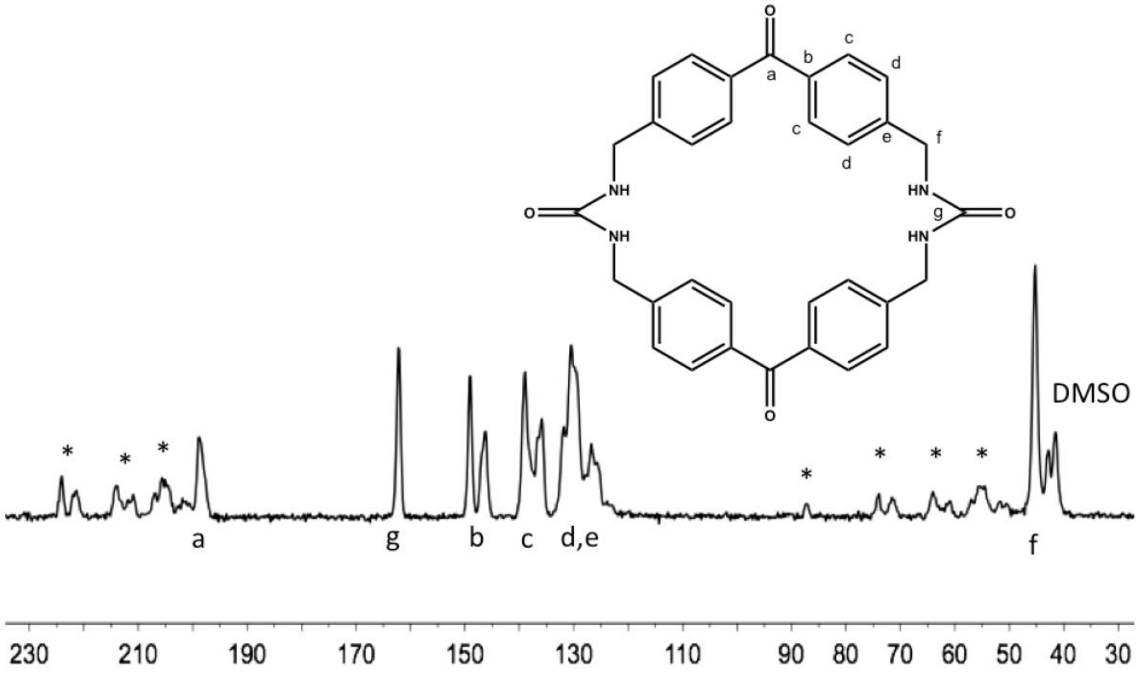

Figure 2.27. Thermally polarized ^{13}C-MAS NMR of UV-irradiated (2h, rt) host **1** recorded at a spinning speed of 11.3 kHz at room temperature. *indicates spinning side bands.

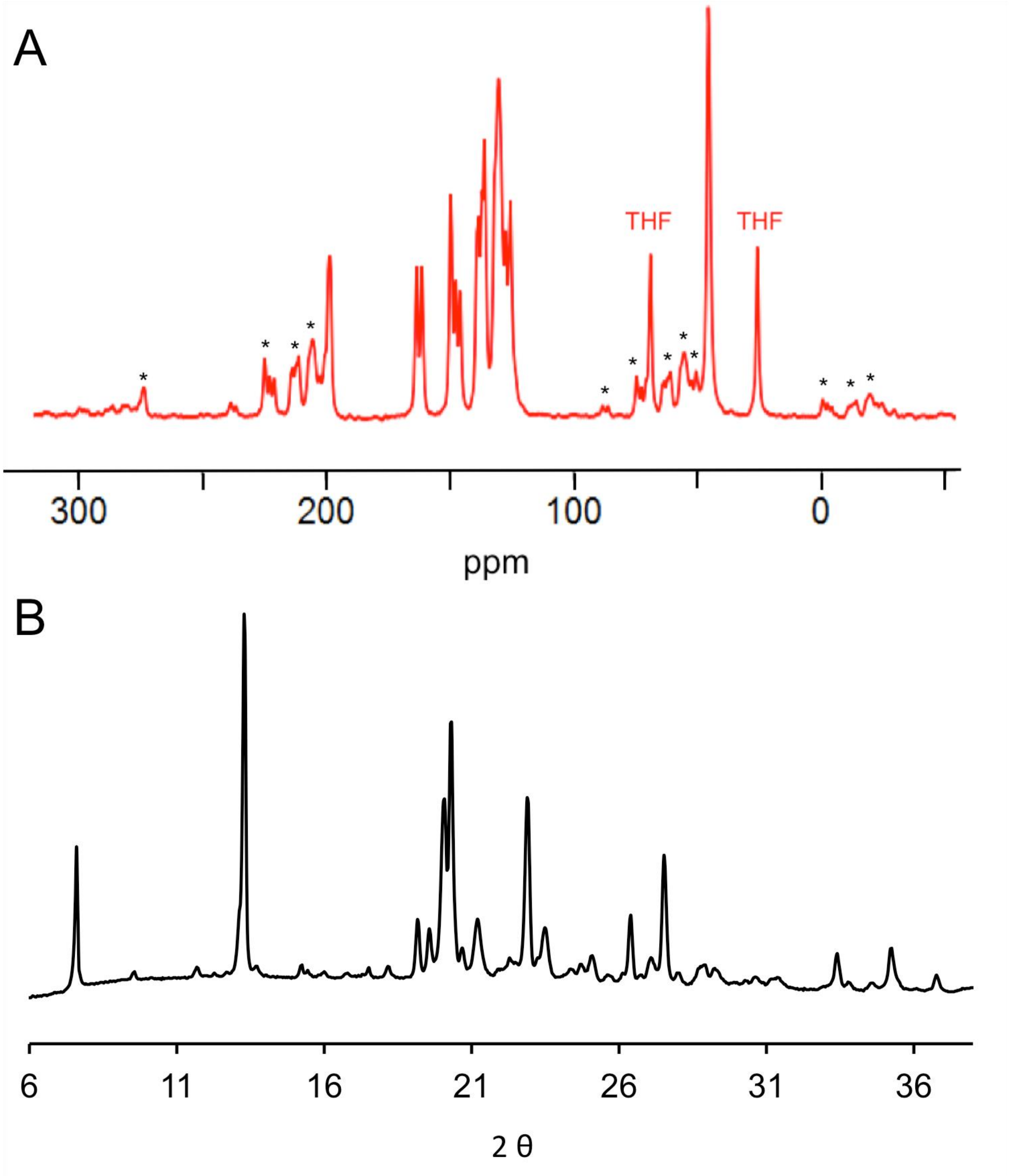

Figure 2.28. (A) Thermally polarized ^{13}C-MAS NMR of UV-irradiated (2h, rt) host **1•**THF recorded at a spinning speed of 11.3 kHz at room temperature. *Indicates spinning sidebands. (B) PXRD of of UV-irradiated (2h, rt) host **1•**THF.

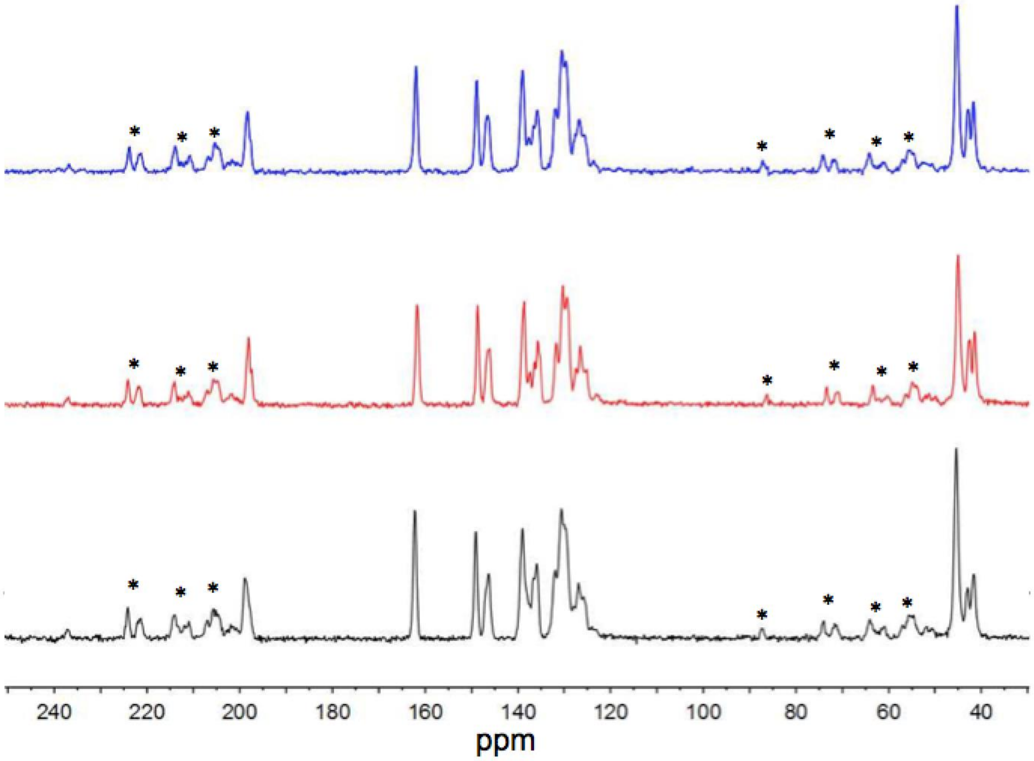

Figure 2.29. Complete CP MAS NMR spectra of thermally polarized **1** recorded at a spinning speed of 11.3 kHz. (I) no UV, (II) 2 h. UV and (III) 4 h. UV. *indicates spinning sidebands.

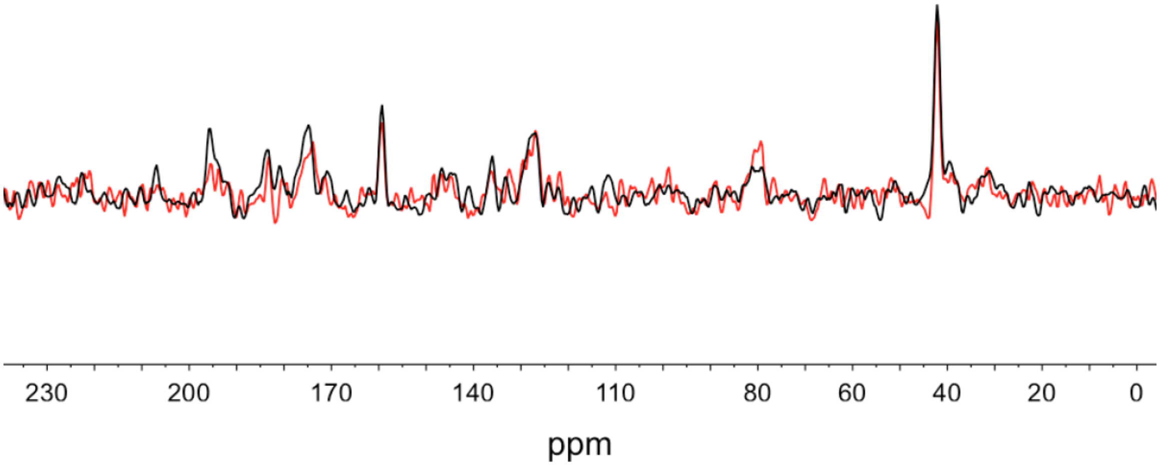

Figure 2.30. DNP CP-MAS NMR on unirradiated host **1**, performed to ensure the broad enhancement factor of 2 was not a result of heating. Enhancement was not observed on host **1** before UV-irradiation. Spectra performed at 14.085 T under exact CP DNP MAS NMR conditions with microwave on (red line) vs. microwave off (black line). Recorded at 112 K and a spinning speed of 7.0 kHz, microwave on (red line) vs. microwave off (black line).

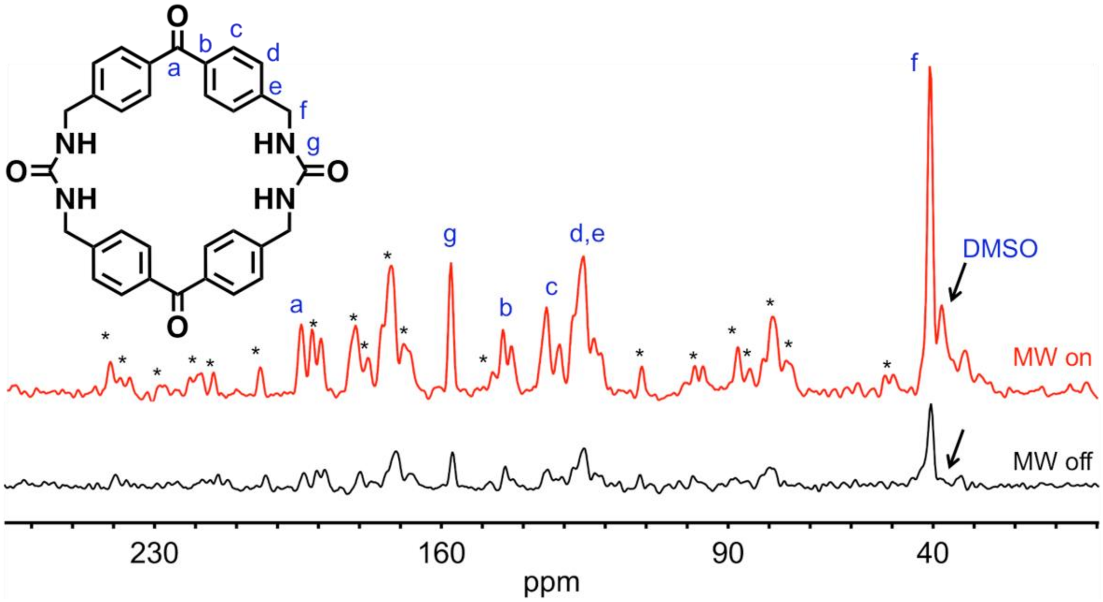

Figure 2.31. Optimized DNP CP-MAS NMR enhancement observed at 14.085 T under CP DNP MAS NMR conditions demonstrating a total enhancement of ε_{DNP} = 4. Recorded at 112 K and a spinning speed of 7.0 kHz, microwave on (red line) vs. microwave off (black line). *Indicates spinning sidebands.

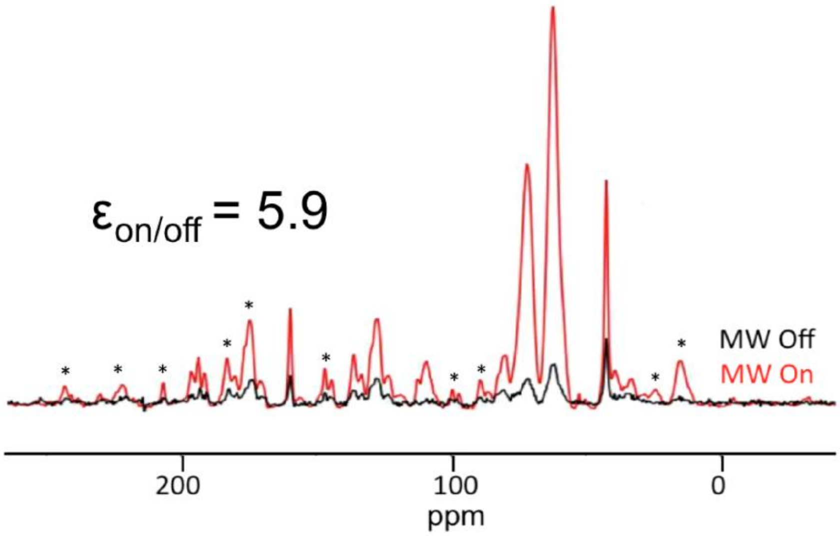

Figure 2.32. DNP CP-MAS NMR enhancement observed at 14.085 T under CP DNP MAS NMR conditions demonstrating on an AMUPol doped sample, demonstrating an enhancement of ~6. Recorded at 112 K and a spinning speed of 7.0 kHz, microwave on (red line) vs. microwave off (black line). *Indicates spinning sidebands.

^{13}C CP MAS DNP NMR AMUPol Impregnation: The UV-irradiated host **1** (25 mg) was impregnated with AMUPol (10 mM, 10-12 μL of a 6:3:1 glycerol-d_8, D_2O, H_2O solution) and the DNP CP-MAS NMR spectrum acquired using the optimal field conditions for **1**.

2.6 References

1. Lee, D.; Hediger, S.; De Paëpe, G. *Solid State Nucl. Magn.* **2015**, *66-67*, 6-20.
2. Smith, A. N.; Long, J. R. *Anal. Chem.* **2016**, *88*, 122−132.
3. Rossini, A. J.; Zagdoun, A.; Lelli, M.; Lesage, A.; Copéret, C.; Emsley, L. *Acc. Chem. Res.* **2013**, *46*, 1942 – 1951.
4. Akbey, Ü.; Franks, W. T.; Linden, A.; Orwick-Rydmark, M.; Lange, S.; Oschkinat, H. Dynamic Nuclear Polarization Enhanced NMR in the Solid-State. In *Topics in Current Chemistry* [Online]; Kuhn, L. T., Ed.; Springer: New York, 2013; Volume 6, pp 181–228. https://link.springer.com/chapter/10.1007%2F128_2013_436
5. (a) Maly, T.; Cui, D.; Griffin, R. G.; Miller, A. -F. *J. Phys. Chem. B* **2012**, *116*, 7055−7065. (b) Riikonen, J.; Rigolet, S.; Marichal, C.; Aussenac, F.; Lalevée, J.; Morlet-Savary, F.; Fioux, P.; Dietlin, C.; Bonne, M.; Lebeau, B.; Lehto, V. -P. J*. Phys. Chem. C* **2015**, *119*, 19272–19278.
6. Geer, M.; Walla, M.; Solntsev, K.; Strassert, C.; Shimizu, L. S. *J. Org. Chem.* **2013**, *78*, 5568−5578.

7. Dewal, M.; Xu, Y.; Yang, J.; Mohammed, F.; Smith, M.; Shimizu, L. S. *Chem. Commun.* **2008**, 3909–3911.

8. (a) Thurber, K. R.; Tycko, R.; *J. Chem. Phys.* **2012**, *137*, 84508. (b) Mentink-Vigier, F.; Akbey, U.; Hovav, Y.; Vega, S.; Oschkinat, H.; Feintuch, A. J. *Magn. Reson.* **2012**, *224*, 13–21. (c) F. Mentink-Vigier, F.; Paul, S.; Lee, D.; Feintuch, A.; Hediger, S.; Vega, S.; De Paëpe, G. *Phys. Chem. Chem. Phys*. **2015**, *17*, 21824-21836.

9. Eichhorn, T. R.; Takado, Y.; Salameh, N.; Capozzi, A.; Cheng, T.; Hyacinthe, J. -N.; Mishkovsky, M.; Roussel, C.; Comment, A. J. *Proc. Natl. Acad. Sci. U.S.A.* **2013**, *110*, 18064-18069.

10. Capozzi, A.; Hyacinthe, J. -N.; Cheng, T.; Eichhorn, T. R.; Boero, G.; Roussel, C.; van der Klink, J. J.; Comment, A. J. *Phys. Chem. C* **2015**, *119*, 22632−22639.

11. (a) Liu, G.; Levien, M.; Karchin, N.; Parigi, G;. Luchinat, C.; Bennati, M. *Nature Chem.* **2017**, DOI: 10.1038/NCHEM.2723. (b) Daviso, E.; Jacoba Janssen, G.; Alia, A.; Jeschke, G.; Matysik, J.; Tessari, M. *J. Am. Chem. Soc.* **2011**, *133*, 16754-16757.

12. Langea, S.; Linden, A. H.; Akbey, U.; Franks, W. T.; Loening, N. M.; van Rossum, B. –J.; Oschkinat, H. J. *Magn. Reson.* **2012**, *216*, 209-212.

13. (a) Baldovi, H. G.; Kruger, M.; Reinsch, H.; Alvaro, M.; Stock, N.; Garcia, H. J. *Mater. Chem. C* **2015**, *3*, 3607-3613. (b) Dormán, G.; Nakamura, H.; Pulsipher, A.; Prestwich, G. D. *Chem. Rev.* **2016**, *116*,

15284-15398. (c) Marazzi, M.; Mai, S.; Roca-Sanjuán, D.; Delcey, M.G.; Lindh, R.; González, L. Monari, A. J. *Phys. Chem. Lett.* **2016**, *7*, 622−626.

14. (a) Barash, L.; Wasserman, E.; Yager, W. A. *J. Am. Chem. Soc.* **1967**, *89*, 3931. (b) Lin, T. –S. *J. Chem. Phys*. **1972**, *57*, 2260. (c) Murai, H.; Imamura, T.; Obi, K. *Chem. Phys. Lett.* **1982**, *87*, 295. (d) Jones, C.; McDyre, L.; Murphy, D. M.; Stasch, A. *Chem. Commun*. **2010**, *46*, 1511-1513.
15. (a) Gast, P.; A Gottschalk, A.; Norris, J. R.; Closs, G. L. *FEBS Lett.* **1989**, *243*, 1-4. (b) Žilić, D.; Rakvin, B.; Dalal, N. S. *J. Appl. Phys.* **2011**, *110*, 1-5.
16. Prasad, A.; Ferretti, U.; Sedlářová, M.; Pospíšil, P. *Sci. Rep.* **2016**, *6*, 1 – 13.
17. Dyakonov, M. I. *Spin Physics in Semiconductors*; Springer: Verlag Berlin Heidelberg, 2008.
18. Kaushik, M.; Bahrenberg, T.; Can, T. V.; Caporini, M. A.; Silvers, R.; Heiliger, J.; Smith, A. A.; Schwalbe, H.; Griffin, R. G.; Corzilius, B. *Phys. Chem. Chem. Phys.* **2016**, *18*, 27205-27218.
19. Can, T. V.; Caporini, M. A.; Mentink-Vigier, F.; Corzilius, B.; Walish, J. J.; Rosay, M.; Maas, W. E.; Baldus, M.; Vega, S.; Swager T. M.; Griffin, R. G. *J. Chem. Phys*. **2014**, *141*, 1-8.
20. (a) Hicks, R. G. *Org. Biomol. Chem.* 2007, **5**, 1321–1338. (b) Rajca, A. *Chem. Rev.* **1994**, *94*, 871. (c) Rawson, J. M.; Alberola, A.; Whalley,

A. E. *J. Mater. Chem*. **2006**, *16*, 2560. (d) Nakatsuji, S.; Anzai, H. J. *Mater. Chem.* **1997**, *7*, 2161.

21. (a) Geer, M.; Walla, M.; Solntsev, K.; Strassert, C.; Shimizu, L. S. *J. Org. Chem.* **2013**, *78*, 5568−5578; (b) Dewal, M.; Xu, Y.; Yang, J.; Mohammed, F.; Smith, M.; Shimizu, L. S. *Chem. Commun.* **2008**, 3909–3911.
22. Sakamoto, M.; Cai, X.; Fujitsuka, M.; Majima, T. *Chem. Eur. J.* **2006**, *12*, 1610-1617.
23. (a) Miyasaka, H.; Morita, K.; Kamada, K.; Mataga, N. *Chem. Phys. Lett.* **1991**, *178*, 405-510; (b) Haselbach, E.; Jacques, P.; Pilloud, D.; Suppan, P.; Vauthey, E. *J. Phys. Chem.* **1995**, *95*, 7115-7117; (c) Khan, F. A.; Wang, D.; Pemberton, B.; Talipov, M. R.; Rathore, R. *J. Photoch. Photobio. A: Chem.* **2016**, *331*, 153-159.

CHAPTER 3

SYNERGISTIC EFFECTS OF HYDROGEN AND HALOGEN BONDING IN CO-CRYSTALS OF DIPYRIDYLUREAS AND DIIODOTETRAFLUOROBENZENE[†]

[†] DeHaven, B. A.; Chen, A. L.; Shimizu, E. A.; Salpage, S. R.; Smith, M. D.; Shimizu, L. S. *Supramol. Chem.* **2018**, *30* (4), 315-327. Reprinted here with permission by the publisher.

3.0 ABSTRACT

Herein, we investigate co-crystallization of three linear co-formers that contain urea and pyridyl groups with three regioisomers of diiodotetrafluorobenzene (DITFB) to afford eleven co-crystals. The linear *o*-, *m*-, and *p*- dipyridylureas vary distance and geometry between the urea carbonyl oxygen and two pyridyl nitrogen acceptors, while the donors consist of urea NH groups and the activated halides in DITFB. Electrostatic potential calculations suggest that the *o*-dipyridylurea co-former presents two significantly different acceptors. In comparison, the acceptors in the *m*- and *p*-dipyridylurea co-formers display electrostatic potentials within 5-6 kJ/mol and should be competitive, potentially leading to altered assembly motifs. Overall, ten of the co-crystals consistently display the urea assembly motif as the best acceptor/donor pair. Seven structures were obtained as the predicted 1:1 ratio with halogen bonding interactions linking ditopic halogen bond donors and the pyridyl units through N⋯I interactions ranging from 78.4-83.1% of the van der Waals radii. Modified structures were more likely when there was a structural mismatch with the geometrically challenging *o*-DITFB donor and *m*- or *p*-dipyridylurea co-former. The majority of the co-crystal structures (10/11) demonstrated fully satisfied hydrogen and halogen bonding interactions suggesting that these synthons can be used synergistically to generate complex solid-state structures.

3.1 INTRODUCTION

Co-crystallization is a technique that incorporates non-covalent interactions into the design of functional crystalline solids made up of two or more molecular components without compromising each co-formers' biological activity.[1-3] Co-crystals often give rise to synergistic effects, modulating physiochemical properties such as solubility, stability, and melting point. Therefore, they have applications in pharmaceuticals, energetic materials, and in templating solid-state photoreactions.[3-8] It is challenging to determine the precise rules for combining multiple individual supramolecular interactions to rationally predict solid-state structures, as complex intermolecular interactions act both competitively and collectively to drive crystallization. When designing molecular building blocks that self-assemble in high fidelity, one typically considers the strength, reversibility and directionality of the interactions. Hydrogen and halogen bond interactions are often selected to guide assembly as they are directional, although both are relatively weak and reversible.[9-10] Both involve an acceptor that is nucleophilic in nature, having at least one lone pair of electrons. They differ by the type of electrophilic donor present in the interaction; group XVII halogen atoms vs. a hydrogen atom, typically on or near an electronegative group.[9-10]

A pioneer in the field, Margaret Etter defined a broad set of rules for solid-state hydrogen bonding preferences (Etter's Rules) from investigation of co-crystals and demonstrated the importance of electrostatic potentials when predicting the structural outcome of co-crystals.[11-13.] Others showed that these simple calculations can be used to predict the structural outcome of multicomponent crystallizations with the best hydrogen bond acceptor interacting preferentially with the best donor.[14-17] Electrostatic potential surface maps can be used to determine the most negative electrostatic potential that general marks the best acceptor and the most positive values that indicate the best donor. These potentials also correlate with beta values, which can account for the competition of solvent molecules.[17] Our interest in examining the synergistic assembly of co-crystals originates from our work on pyridyl *bis*-urea macrocycles (Figure 3.1a), which demonstrate an unusual hydrogen bond assembly pattern, as well as a propensity to form co-crystals.[18-21] In the pyridyl *bis*-urea macrocycles, the urea oxygen is the better acceptor (□ = 8.3 for urea oxygen vs. 7.0 for pyridine nitrogen); however, the close proximity of these acceptors modulated the expected hydrogen bonding motif. The macrocycles form robust 1-dimensional pillars through two different hydrogen bonds (N-H···N and N-H···O) where the urea NH's interact with both the urea carbonyl oxygen and the pyridine nitrogen.[18] This leaves two oxygen lone pairs unsatisfied per macrocycle that can be employed orthogonally to organize DITFBs through C=O···I halogen

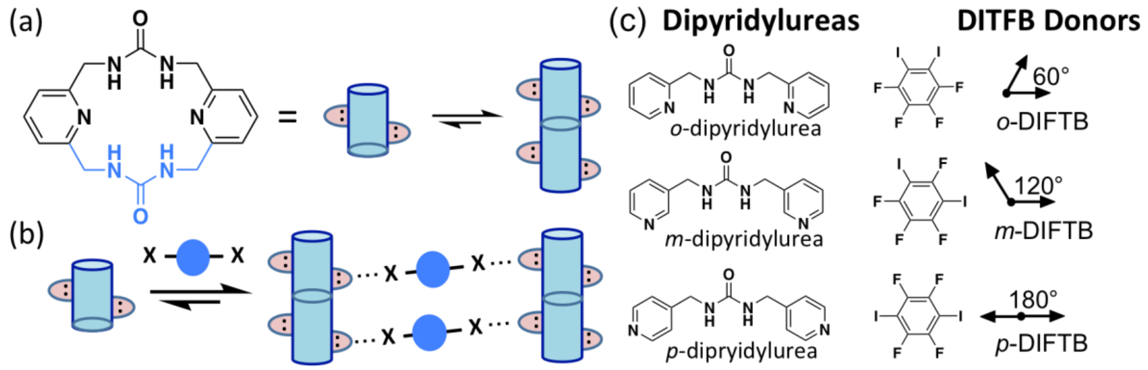

Figure 3.1. Dipyridylureas contain hydrogen bond donors and two potential acceptors. (a) The pyridyl *bis*-urea macrocycles form robust 1-dimensional pillars, the black color marks the dipyridylurea structural analogue studied in this manuscript. (b) Hydrogen and halogen bond formation drives the co-crystallization of the pyridyl *bis*-urea macrocycle and DITFBs. (c) Dipyridylurea co-formers that present both donors and acceptors and the DITFBs investigated in this manuscript

bonding interactions (Figure 3.1b).[20] In this example, proximity, electrostatics and geometric constraints imposed by the macrocycle may be individually or collectively responsible for the altered supramolecular pattern. Also, the presence of competing acceptors with similar electrostatic potentials can further complicate these issues.[21]

This manuscript explores the assembly of linear dipyridylurea co-formers that are closely related to the pyridyl *bis*-urea macrocycle with diidotetrafluorobenzenes (DITFBs). These co-formers present competitive donors and acceptors for hydrogen and halogen bond formation. Specifically, we investigated the co-crystallization of three linear dipyridylureas with *o-, m-,* and *p-*DITFB activated ditopic halogen bond donors (Figure 3.1c). The simple *o-*dipyridylurea is structurally most similar to the macrocycle; where as the *m-*dipyridylurea and *p-*dipyridylurea vary the distance and geometry between the pyridyls and the urea group. Reger *et al*. incorporated these dipyridylurea co-formers into the design and synthesis of europium and terbium metal complexes where they were found to exhibit luminescent properties following complexation.[22] Others also employed these ligands in metallo-supramolecular complexes and to assemble diacetylenes.[23-26] Similarly, the ditopic halogen bond donors, DITFBs, were selected as they present the iodine atoms at different distances and spatial dispositions. These systems were used to probe the relationship between hydrogen and halogen bonding moieties, to examine how their complex geometry governs supramolecular architecture, and to understand how the presence of halogen bond donors will complement and/or disrupt the urea-urea hydrogen-bonding motif.

3.2. RESULTS AND DISCUSSION

The urea-centered co-formers were used as previously synthesized.[22] NMR, IR, and high-resolution mass spectrometry was recorded before co-crystal screening (Figures 3.8-3.16). The halogen bond donors and organic solvents were ordered through VWR and used as received.

Co-crystals were obtained by grinding a 1:1 stoichiometric ratio of DITFBs (16.6 mg, 0.041mmol) and dipyridylurea ligands (10 mg, 0.041mmol) for 1-2 minutes with a few drops of $CHCl_3$. Method 1: Half of the ground mixture was dissolved in a minimal amount of DMSO. Water was allowed to vapor diffuse into the DMSO solution for 2-4 days. Small clusters of colorless needle-like co-crystals resulted and were submitted for single crystal X-ray diffraction analysis (SC-XRD). Method 2: The remaining half of the ground mixture was heated in a minimal amount of CH_3CN until complete dissolution and filtered using a syringe filter into a clean vial where they were left to slowly evaporate (3-7 days). All crystallizations that yielded a precipitate were collected, dissolved in CH_2Cl_2, and left to slowly evaporate once more. Crystals of the parent dipyridylureas were obtained by dissolving each compound (10-20 mg) in a minimal amount of CH_3CN. The solution was filtered using a syringe filter into a clean vial and left to slowly evaporate (3-7 days). Crystallizations that yielded a precipitate were collected, dissolved in CH_2Cl_2, and left to slowly evaporate. All suitable crystals obtained were submitted for SCXRD.

Electrostatic potentials were computed with the Spartan 10’ software package. The crystal structure files (CIFs) of the dipyridylureas were imported into the program. The DITFB molecules were drawn in the program and fully optimized without constraints. The co-former energies were directly calculated using DFT B3YLP level of theory, using a 6-311++G** basis set under vacuum. The electrostatic potentials of the best donor and acceptor were obtained from the electrostatic potential map (0.002 e a.u. isovalue) and were automatically distinguished by the software. The electrostatic potentials of the second best donor and acceptor were determined by clicking on the region of interest on the molecule until the highest (or lowest) value was obtained for each binding-site.

X-ray intensity data for all crystals were collected at 100(2) K using a Bruker D8 QUEST diffractometer equipped with a PHOTON 100 CMOS area detector and an Incoatec microfocus source (Mo Kα radiation, λ = 0.71073 Å). The raw area detector data frames were reduced and corrected for absorption effects using the Bruker APEX3, SAINT+ and SADABS programs.[27, 28] Final unit cell parameters were determined by least-squares refinement of large sets of strong reflections taken from each data set. The structures were solved using dual-space intrinsic phasing methods with SHELXT.[29] Subsequent difference Fourier calculations and full-matrix least-squares refinement against F^2 were performed with SHELXL-2014[29] using OLEX2.[30] Structures were deposited in the Cambridge Crystallographic Data Centre: CCDC 1552608-1552521.

FT-IR spectra were recorded on the crystalline samples using a PerkinElmer Spectrum 100 FT-IR Spectrometer. Background spectra were recorded in 4 scans from 650 to 4000 cm^{-1} and then the crystalline sample was loaded onto the IR sample stage. The crystalline sample was added until the transmittance of key signals was lower than 90% and 32 scans were taken from 650 to 4000 cm^{-1}.

Three flexible dipyridylurea ligands that consist of a central urea and two covalently attached pyridine ring 'arms' were investigated as co-formers with the three regioisomers of DITFB. As the structures of the dipyridylurea ligands were not in the CCDC, we first crystallized them to examine if the pyridyl moiety modulates the urea assembly motif compared to simple dibenzylurea. Next, we investigated co-crystal formation of each dipyridylurea with the three-ditopic halogen bond donors. Our hypothesis is that the central urea will form strong bifurcated urea-urea hydrogen bonding interactions leaving the pyridyl nitrogen free to act as a halogen bond acceptor. Specifically, we addressed the following questions: (1) Can we predict the structural outcome of the co-crystals through simple electrostatic potential calculations? (2) Is the urea-urea assembly motif conserved when the halogen-bond donors are introduced? (3) Does the position of the pyridyl nitrogen (*o*, *m*, *p*) impact the bond length, angle, and pattern of the urea assembly? (4) Do all halogen bond donors form interactions with suitable acceptors?

The homomeric assembly of the dipyridylureas was first screened by crystallization through slow evaporation from CH_2Cl_2 or CH_3CN to afford colorless needles of *o*-dipyridylurea ($C_{13}H_{14}N_4O$), *m*-dipyridylurea dihydrate ($C_{13}H_{14}N_4O\cdot(H_2O)_2$) and *p*-dipyridylurea hydrate ($C_{13}H_{14}N_4O\cdot H_2O$). As expected, all three compounds formed the typical three-centered bifurcated hydrogen bonding interactions between the urea NH and the carbonyl oxygen on the neighboring molecule (Figure 3.2). As compared with simple dibenzylurea, the hydrogen bonds distances are slightly shorter in these pyridyl systems with an average N-H···O distance = 2.83 Å versus 2.91 Å in the dibenzylurea, indicating a slightly stronger interaction.[31] The N-H···O are shorter in the *o*-dipyridylurea than in the hydrates of *m*-dipyridylurea and *p*-dipyridylurea, with average bond lengths ranging from 2.823 to 2.842 Å. The bond angles are also smaller in the *o*-urea with N-H···O (151.0°) then in the *m*-dipyridylurea (153.1° and 155.2°) or *p*-dipyridylurea (156.0°).

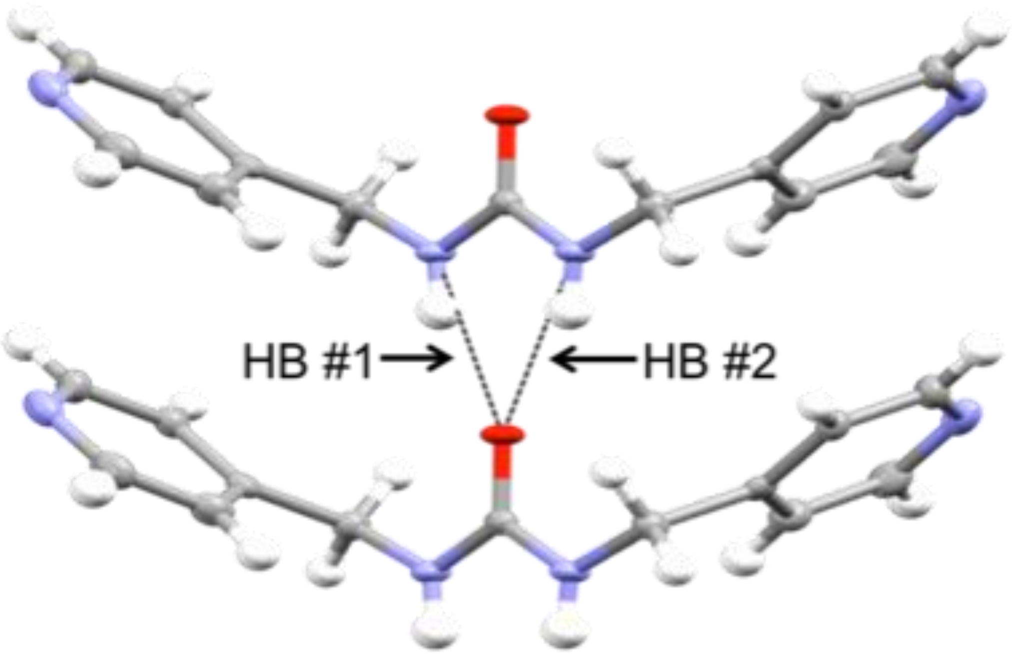

Figure 3.2. Crystal structure of *p*-dipyridylurea depicting the urea three-center hydrogen bonding interaction known as the urea tape. Each N-H···O hydrogen-bonding interaction (HB) is indicated by arrows.

In the crystal structure of *o*-dipyridylurea, one pyridine nitrogen is close in space to a weakly acidic methylene hydrogen on a neighboring dipyridylurea co-former while the other pyridine nitrogen is proximal to a hydrogen on a neighboring pyridine ring (Figure 3.17). The *m*-dipyridylurea crystallized as a dihydrate where the pyridine acceptor interacts with water through O-H···N hydrogen bonding interactions. Two water molecules interconnect nearby dipyridylureas through water-to-water and water-to-pyridine hydrogen bonding interactions resulting in zig-zagged strands of water along the *b*-axis. (Figure 3.18). Finally, the *p*-dipyridylurea displays similar water-to-pyridine hydrogen bonding interactions, although a single water molecule interconnects neighboring dipyridylurea molecules through O-H···N hydrogen bonds running along the *b*-axis (Figure 3.19).

To predict the probable co-crystallized structures of the three dipyridylurea co-formers with the regioisomers of DITFBs, we turned electrostatic computations. A simple prescreen of the co-formers allowed us to identify and compare the best donors and best acceptors present in these molecules in order to rank the binding sites and make general predictions about possible assembly motifs. The electrostatic potential of the co-formers were calculated using Spartan 10' with the DFT B3YLP level of theory and a 6-311++G** basis set under vacuum. Figure 3.3A displays the electrostatic potential maps showing areas with the most negative electrostatic potential (red) which are most capable of acting as acceptors and areas of most positive electrostatic potential (blue) that indicates the potential donors. The dipyridylureas present two urea N-Hs as

Table 3.1. Summary of hydrogen bond angles and distances obtained from crystal structures of the dipyridyl urea series

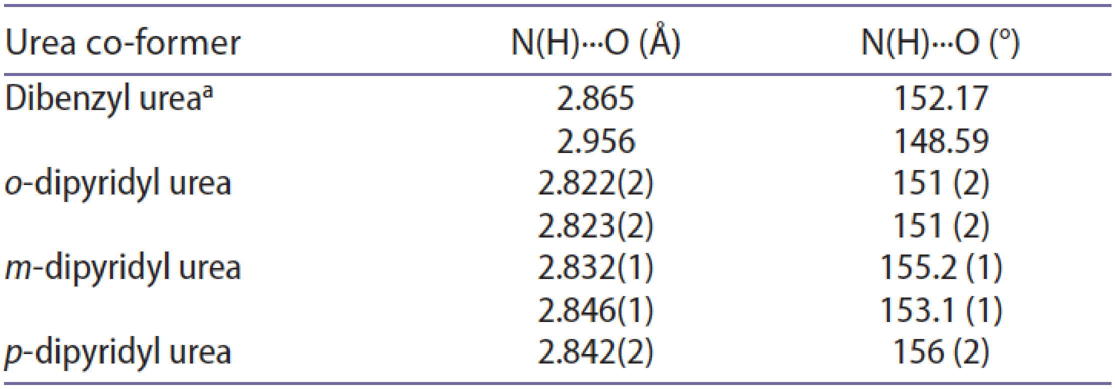

Urea co-former	N(H)···O (Å)	N(H)···O (°)
Dibenzyl urea[a]	2.865	152.17
	2.956	148.59
o-dipyridyl urea	2.822(2)	151 (2)
	2.823(2)	151 (2)
m-dipyridyl urea	2.832(1)	155.2 (1)
	2.846(1)	153.1 (1)
p-dipyridyl urea	2.842(2)	156 (2)

[a]Parameters obtained in Mercury from a crystal structure published by Watkinson *et* al. (31).

donors and three acceptors (the urea oxygen and two pyridyl nitrogens) while the DITFBs offer ditopic halogen bond donors (Figure 3.3B). Comparing the numerical molecular electrostatic potentials for all compounds in Table 3.2, the urea NH's are clearly the best donors with electrostatic potentials ranging from 254 to 290 kJ/mol. The activated iodines displayed values ranging from 161 to 169 kJ/mol, and are subsequently the second best donors. Among the potential acceptors, the *o*-dipyridylurea carbonyl oxygen is the clear winner with the most negative electrostatic potential at -237 kJ/mol versus its pyridyl nitrogen at -187 kJ/mol. However, when comparing the electrostatic potentials of the remaining dipyridylurea co-formers, the ranking is not straightforward. In the *m*-dipyridylurea, the potential difference between the carbonyl oxygen and pyridyl nitrogen acceptors is quite small, only 6.11 kJ/mol. This difference is even smaller, 5.31 kJ/mol, for *p*-dipyridylurea. Such a small difference in electrostatic potential between the two acceptors is problematic and may result in competition

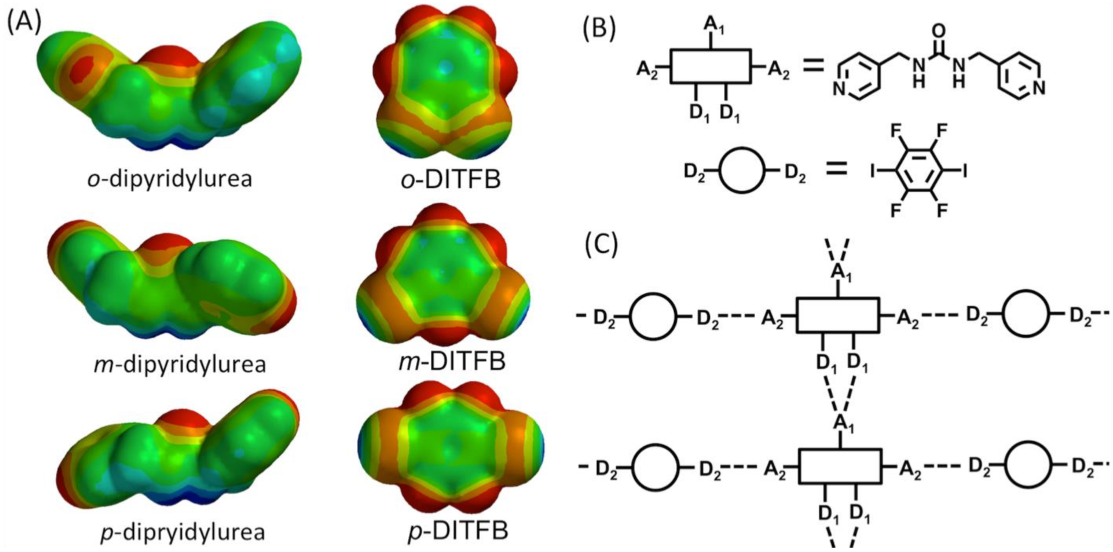

Figure 3.3. Dipyridylureas contain one hydrogen bond donor and two potential acceptors. (A) Electrostatic potential maps of the dipyridylurea series and DITFB regioisomers, the red areas indicate negative electrostatic potentials, which are capable of acting as acceptor sites. (B) Abbreviations of the co-formers investigated in this study. The best donors (D_1), best acceptors (A_1), second best donors (D_2), and second best acceptors (A_2) are labelled. (C) Co-formers assembly predicted from their electrostatic potential ranking.

between the acceptors for the best donor, the urea NH, which could lead to altered urea assembly or to multiple crystal forms as we attempt to co-crystallize these dipyridylureas with the DITFBs.[21] The small electrostatic potential differences between acceptors did not appear to impact the urea assembly motif in the homomeric crystals, likely due to urea oxygen's ability to engage in bifurcated hydrogen bonding with the urea NHs, which are energetically favorable as compared with pyridine nitrogen acceptor that can only engage in a the single linear hydrogen bond. In summary, these results suggest that the urea assembly as the best donor/best acceptor should be strongly favored in co-crystallizations of *o*-dipyridylurea and DITFBs; however, in *m*- and *p*-

Table 3.2. Molecular electrostatic potential values of each binding site (kJ/mol)

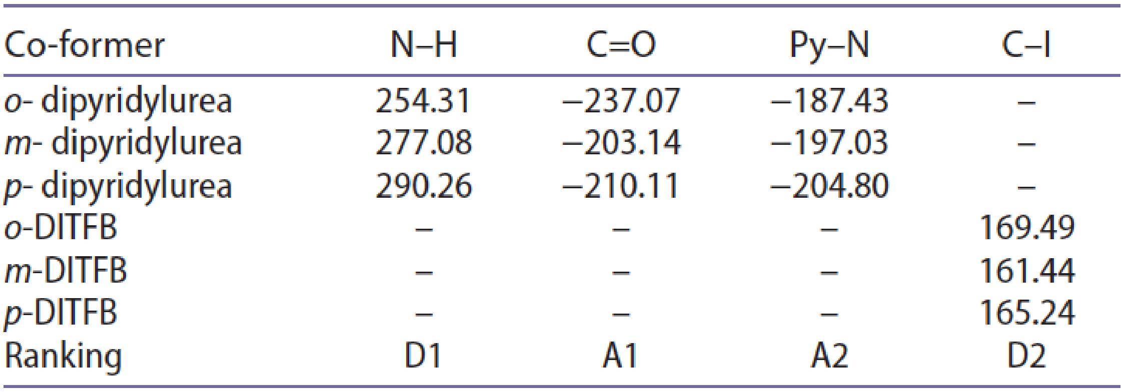

Co-former	N–H	C=O	Py–N	C–I
o- dipyridylurea	254.31	−237.07	−187.43	–
m- dipyridylurea	277.08	−203.14	−197.03	–
p- dipyridylurea	290.26	−210.11	−204.80	–
o-DITFB	–	–	–	169.49
m-DITFB	–	–	–	161.44
p-DITFB	–	–	–	165.24
Ranking	D1	A1	A2	D2

dipyridylureas the urea assembly is modestly favored leaving open the potential for competition between the acceptors.

Samples of the dipyridylureas (*o*-, *m*-, and *p*-) were mixed or ground with the ditopic halogen bond donors DITFB in 1: 1 molar ratio and crystallized by vapor diffusion and slow evaporation experiments, eleven X-ray quality co-crystals were obtained: *o*-dipyridylurea·*o*-DITFB, *o*-dipyridylurea·*m*-DITFB, *o*-dipyridylurea·*p*-DITFB, *m*-dipyridylurea·(*o*-DITFB)$_2$, (*m*-dipyridylurea)$_2$·(*o*-DITFB)$_7$, *m*-dipyridylurea·*m*-DITFB, *m*-dipyridylurea·*p*-DITFB, *p*-dipyridylurea·(*o*-DITFB)$_2$, *p*-dipyridylurea·*m*-DITFB, *p*-dipyridylurea·*p*-DITFB, and *p*-dipyridylurea·(*p*-DITFB)$_2$. The hydrogen bond angles and distances obtained from the co-crystals are summarized in Table 3.3. We will now analyze the co-crystal structures formed by the o-dipyridylurea, then turn to *m*-dipyridylurea co-crystals, and finally to the *p*-dipyridylurea structures.

Our electrostatic calculations predicted that the *o*-dipyridylurea co-former presents one clearly better acceptor, the urea oxygen, and two additional pyridyl nitrogen acceptors, which have significantly different electrostatic potentials. As anticipated, *o*-dipyridylurea formed co-crystals with all three regioisomers of DITFB with the conserved three-centered urea assembly and additional iodo to pyridyl halogen bonding interactions (Figure 3.4). The *o*-dipyridylurea formed a 1:1 co-crystal with *o*-DITFB, crystallizing in the orthorhombic system as *o*-dipyridylurea·*o*-DITFB (space group $P2_12_12_1$). The two urea NH hydrogen-bond donors form similar but not identical interactions with the neighboring urea carbonyl oxygen with N-H···O distances of 2.797(3) Å and 2.843(3) Å and dihedral angles of 153(3)° and 152(4)° respectively. The remaining pyridine acceptors interact with the *o*-DITFB with I···N distances of 2.892(2) Å and 2.831(2) Å and C-I···N angles of 169.5(1)° and 177.7(1)° respectively, resulting in a serpentine patterned sheet when looking down the *a*-axis (Figure 3.4A).

Crystallization of *o*-dipyridylurea with *m*-DITFB also afforded a 1:1 co-crystal *o*-dipyridylurea·*m*-DITFB in the monoclinic space group $P2_1/c$. The urea hydrogen bonding interactions were slightly shorter with N-H···O distances of 2.744(4) Å and 2.795(4) Å and the dihedral angles were 150(5)° and 161(5)° respectively. The pyridine acceptors interact with the *meta* substituted halogen bond donors with I···N distances of 2.935(7) Å and 2.893(7) Å and C-I···N angles of 165.2(6)° and 172.7(4)° (major *m*-DITFB disorder component only), resulting in corrugated 2D layers (Figure 3.4B). The 2D layers are assembled from 1D strands of urea-urea hydrogen bonded tapes running along the *a*-axis interlinked through halogen bonding interactions with DITFB molecules to the pyridyl nitrogen along the *bc* crystallographic plane.

Table 3.3. Hydrogen bond angles and distances obtained from the co-crystals.

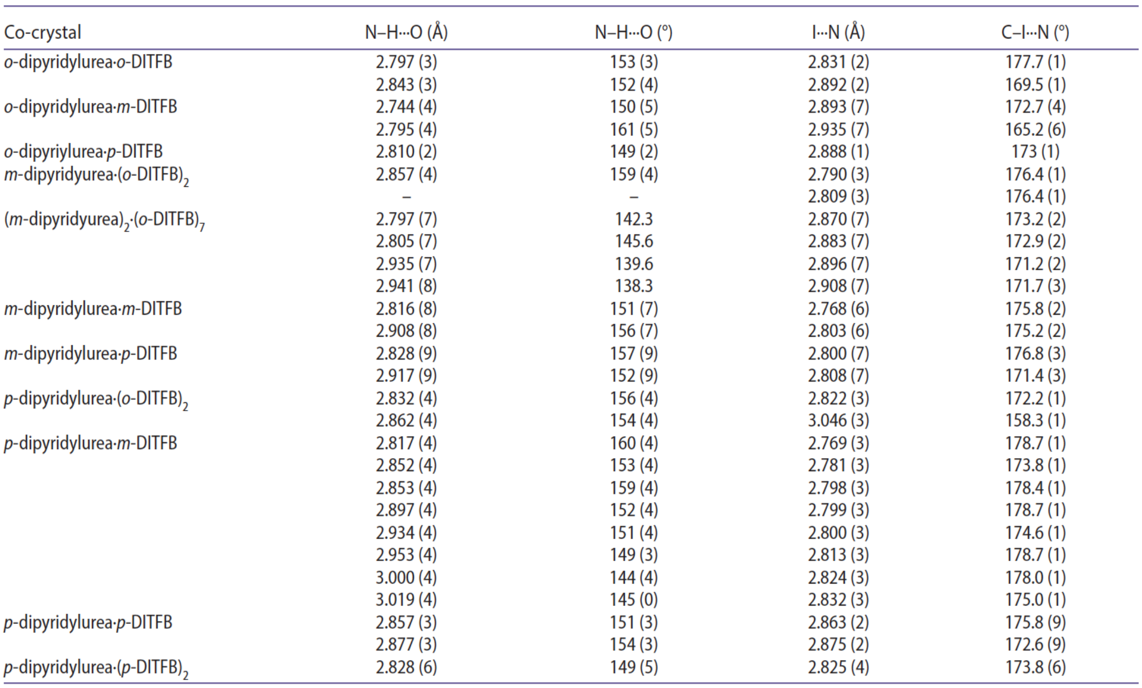

Co-crystal	N–H···O (Å)	N–H···O (°)	I···N (Å)	C–I···N (°)
o-dipyridylurea·*o*-DITFB	2.797 (3)	153 (3)	2.831 (2)	177.7 (1)
	2.843 (3)	152 (4)	2.892 (2)	169.5 (1)
o-dipyridylurea·*m*-DITFB	2.744 (4)	150 (5)	2.893 (7)	172.7 (4)
	2.795 (4)	161 (5)	2.935 (7)	165.2 (6)
o-dipyriylurea·*p*-DITFB	2.810 (2)	149 (2)	2.888 (1)	173 (1)
m-dipyridyurea·(*o*-DITFB)$_2$	2.857 (4)	159 (4)	2.790 (3)	176.4 (1)
	–	–	2.809 (3)	176.4 (1)
(*m*-dipyridyurea)$_2$·(*o*-DITFB)$_7$	2.797 (7)	142.3	2.870 (7)	173.2 (2)
	2.805 (7)	145.6	2.883 (7)	172.9 (2)
	2.935 (7)	139.6	2.896 (7)	171.2 (2)
	2.941 (8)	138.3	2.908 (7)	171.7 (3)
m-dipyridylurea·*m*-DITFB	2.816 (8)	151 (7)	2.768 (6)	175.8 (2)
	2.908 (8)	156 (7)	2.803 (6)	175.2 (2)
m-dipyridylurea·*p*-DITFB	2.828 (9)	157 (9)	2.800 (7)	176.8 (3)
	2.917 (9)	152 (9)	2.808 (7)	171.4 (3)
p-dipyridylurea·(*o*-DITFB)$_2$	2.832 (4)	156 (4)	2.822 (3)	172.2 (1)
	2.862 (4)	154 (4)	3.046 (3)	158.3 (1)
p-dipyridylurea·*m*-DITFB	2.817 (4)	160 (4)	2.769 (3)	178.7 (1)
	2.852 (4)	153 (4)	2.781 (3)	173.8 (1)
	2.853 (4)	159 (4)	2.798 (3)	178.4 (1)
	2.897 (4)	152 (4)	2.799 (3)	178.7 (1)
	2.934 (4)	151 (4)	2.800 (3)	174.6 (1)
	2.953 (4)	149 (3)	2.813 (3)	178.7 (1)
	3.000 (4)	144 (4)	2.824 (3)	178.0 (1)
	3.019 (4)	145 (0)	2.832 (3)	175.0 (1)
p-dipyridylurea·*p*-DITFB	2.857 (3)	151 (3)	2.863 (2)	175.8 (9)
	2.877 (3)	154 (3)	2.875 (2)	172.6 (9)
p-dipyridylurea·(*p*-DITFB)$_2$	2.828 (6)	149 (5)	2.825 (4)	173.8 (6)

Slow evaporation of *o*-dipyridylurea and *p*-DITFB from acetonitrile resulted in colorless needle-like 1:1 *o*-dipyridylurea·*p*-DITFB co-crystals in the monoclinic space group C2/c. The typical three-centered urea interactions were observed with identical N-H···O distances (2.810(2) Å) and angles (149(2)°). The halogen bonding interaction between the pyridine acceptor and *p*-DITFB showed I···N distance of 2.888(1) Å with C-I···N angle of 173(1)°. The 1D urea-urea hydrogen bonded tapes run along the *b*-axis and are linked through halogen bonding interactions to the pyridyl nitrogen, resulting in 2D layers that resemble a herringbone pattern on the *ac* crystallographic plane.

In the case of the *m*-dipyridylurea co-former, the electrostatic potential of urea oxygen acceptor was slightly more negative that the pyridyl group; however the difference was small (6.11 kJ/mol), which suggested there might be competion. Co-crystallization of *m*-dipyridylurea with the regioisomers of DITFB

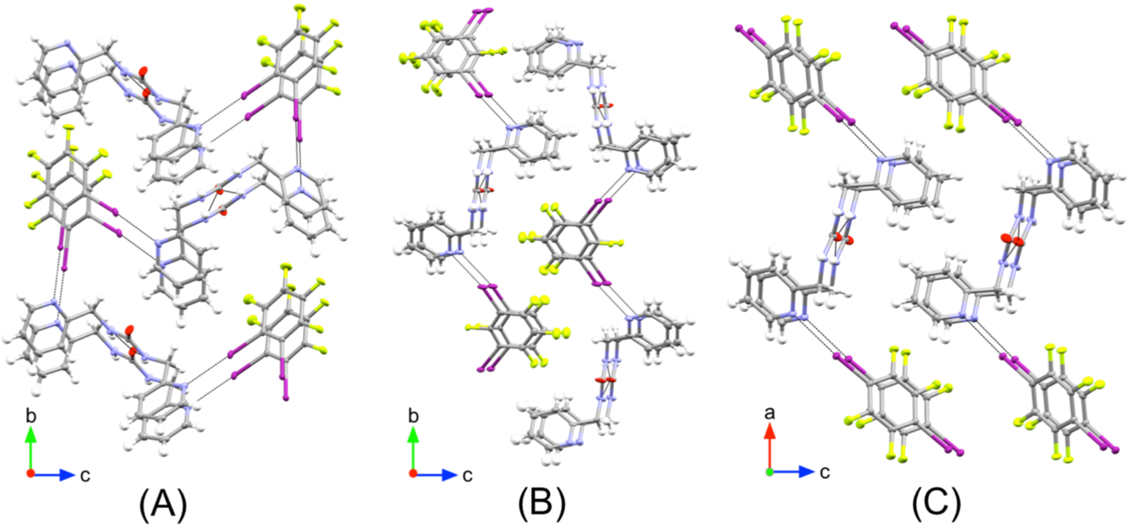

Figure 3.4. Comparison of structures from the 1:1 co-crystals of *o*-dipyridylurea with the regioisomers of DITFB show the conserved urea hydrogen bonded chains further assembled by halogen bonding interactions. Hydrogen and halogen bonds are shown as the thinner dotted bonds. (A) Views from *o*-dipyridylurea·*o*-DITFB structure show zig-zagged 2D layers. (B) Views from *o*-dipyridylurea·*m*-DITFB show similar 2D layers assembly. (C) Views from *o*-dipyridylurea·*p*-DITFB highlight the similar synergistic action of hydrogen and halogen bonding interactions

gave some unusual structures. Vapor diffusion of water into a 1:1 mixture of *m*-dipyridylurea and *o*-DITFB in DMSO afforded colorless, twinned needle-like crystals of *m*-dipyridylurea·(*o*-DITFB)$_2$, a 1:2 co-crystal in the monoclinic system with space group $P2_1/c$. Instead of the typical three-centered urea hydrogen bonding motif, the ureas form extended chains through amide like hydrogen bonds between one NH and the neighboring urea oxygen with N-H···O distance of 2.857(4) Å and angle of 159(4)°. This leaves the remaining NH donor and an oxygen lone pair unsatisfied (Figure 3.5A, top). Instead, the second best donor, an iodo from *o*-DITFB, forms halogen bonds with the pyridyl nitrogens with I···N distances of 2.790(3) and 2.809(3) Å (Figure 3.5A, bottom). An O···I interaction is formed between free oxygen lone pair and an iodo donor is present, similar to the interaction observed by the pyridyl *bis*-urea macrocycle. A 2016 CSD search performed by Cinčić et. al. indicated that there were only 12 reported entries involving C=O···I interactions for both *ortho* and *para* DITFBs.[32] Here, we observe an O···I interaction distance of 2.947(3) Å with an C=O···I angle of 123.8(2)°, very close to what one would expect (120°) for halogen bonding to an sp^2 hybridized oxygen atom.

Identical crystallization conditions also afforded a complex twinned (*m*-dipyridylurea)$_2$·(*o*-DITFB)$_7$ co-crystal in the monoclinic space group *P*2$_1$/n. There are two crystallographically independent *m*-dipyridylurea molecules and seven independent *o*-DITFBs in the structure. Here, the urea hydrogen-bonding motif is observed with four different urea N-H···O distances ranging from 2.797(7) to 2.941(8) Å. Multiple halogen bonding interactions organize the pyridine acceptors and the DITFBs through I···N distances of with distances ranging from 2.870(7)-3.392(7) Å indicating both halogen bonds and short contacts with the DITFB drive the unique assembly. Short halogen contacts are also observed between the urea oxygens and DITFB displaying I···O distances of 3.006(4) Å and 3.031(4) Å. Individual *o*-DITFB molecules are tilted irregularly within stacks with six-molecule repeating units. Interestingly, the seventh independent *o*-DITFB molecule is trapped in the elliptical pores nearly perpendicular to the other structural features (Figure 3.5B). Here, a C=O···I angle of 132.9° is observed which is larger than the expected angle of 120° for sp^2 hybridized atoms; however, wider C=O···I angles have been reported in a study of co-crystals

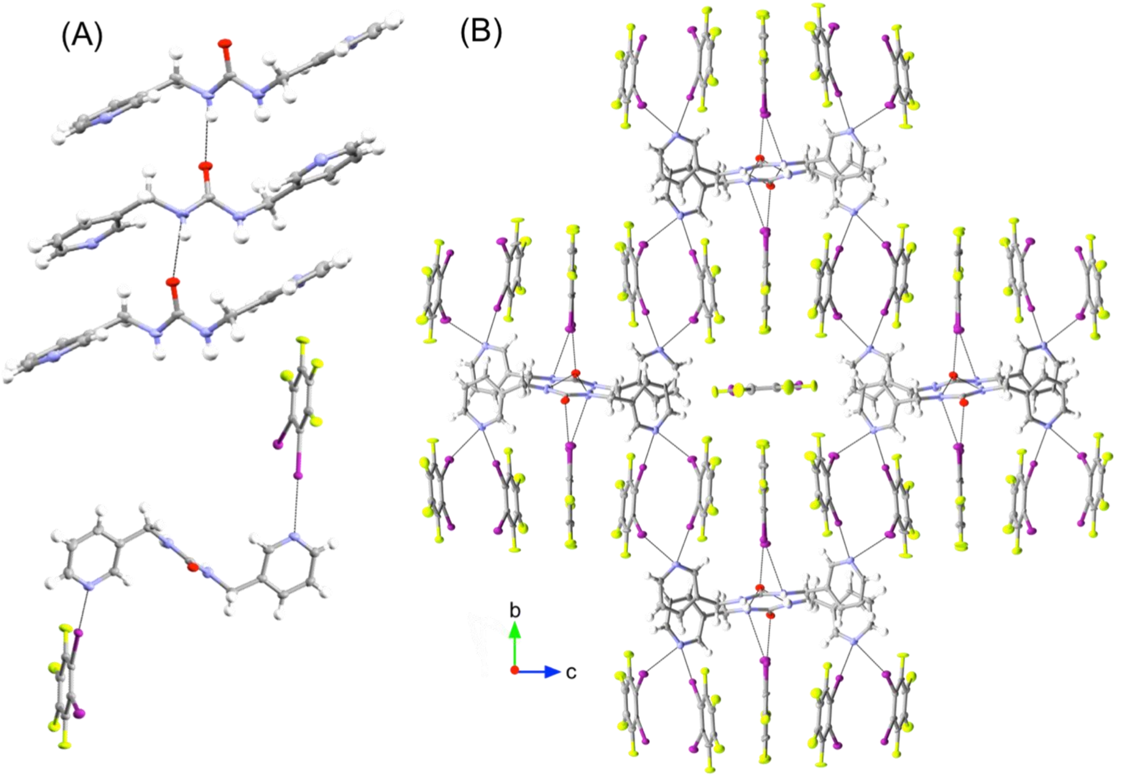

Figure 3.5. Comparison of the two crystal forms of *m*-dipyridylurea and *o*-DITFB co-crystals grown from a 1:1 stoichiometric mixture afford modified structures. (A) (Top) Views from *m*-dipyridylurea·(*o*-DITFB)$_2$ highlight the linear amide hydrogen bonded chain where one NH group is not involved in additional interactions. (Bottom) Both halogen donors form C-I···N interactions with the pyridyl nitrogens. (B) Views from the (*m*-dipyridylurea)$_2$·(*o*-DITFB)$_7$ co-crystal exhibiting the typical urea hydrogen bonding motif. Complex C-I···N and C-I···O halogen bonding interactions organize six *o*-DITFB molecules resulting in a pocket where a seventh *o*-DITFB molecule fits nearly perpendicularly.

formed from DITFB's and imines where C=O···I angles ranging from 120.6-142.7° were observed.[32]

Crystallization of *m*-dipyridylurea with *m*-DITFB through slow evaporation from CH_3CN afforded colorless needles of the expected 1:1 co-crystals *m*-dipyridylurea·*m*-DITFB in the monoclinic system with space group $P2_1/c$. The typical urea self association shows expected N-H···O distances of 2.816(8) and

2.908(8) Å and dihedral angles of 151(7)° and 156(7)°. Subsequent halogen bonding of these two *meta* co-formers forms a tetrameric macrocycle structure (Figure 3.6A). The halogen bonding interactions show I···N distances of 2.768(6) Å and 2.803(6) Å and C-I···N angles of 175.8(2)° and 175.2(2)°. Two urea components are halogen bonded through the pyridine moiety to the DITFB to form a tetrameric structure with no void in the cyclic co-crystal.

Slow evaporation of a 1:1 mixture of *m*-dipyridylurea and *p*-DITFB from CH_3CN yielded colorless twinned needles of the expected *m*-dipyridylurea·*p*-DITFB in the monoclinic system with space group $P2_1/c$. Figure 3.6B illustrates the consistent three-centered urea interactions N-H···O distances 2.828(9) and 2.917(9) Å with N-H···O angles of 157(9)° and 152(9)°. Similar to Figure 3.3C, halogen bonding interactions between the pyridyl nitrogen and the DITFBs afford in linear 2D layers with I···N distances of 2.800(7) Å and 2.808(7) Å and C-I···N angles of 176.8(3)° and 171.4(3)°. Overall, for the *m*-dipyridyl urea with the DITFB regioisomers, only the *o*-DITFB gave a structure that did not conserve the urea assembly motif, presumably due to the mismatch in geometry between these two building blocks.

For the *p*-dipyridylurea co-former, the difference in electrostatic potentials between the urea oxygen acceptor and the pyridyl acceptor was even smaller; however, the urea assembly was consistently conserved and the activated halides interacted with the pyridyl nitrogens to give the predicted assembly proposed in Figure 3.3C. Only the constrained *o*-DITFB exhibited additional short contacts (Figure 3.7A). Slow evaporation of the 1:1 mixture of *p*-

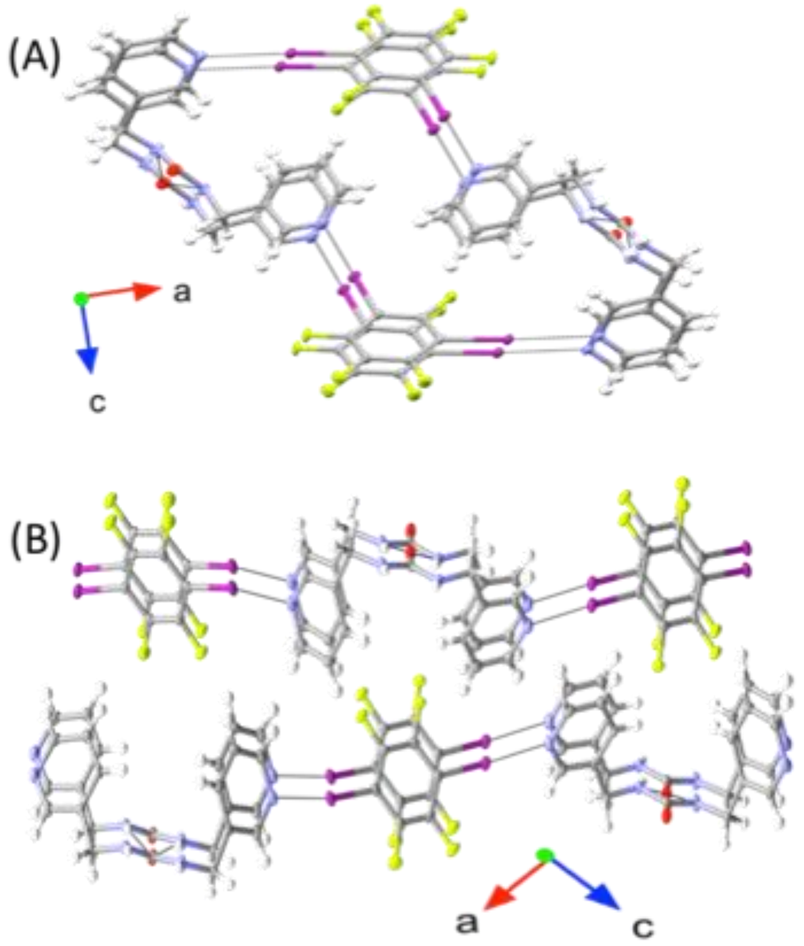

Figure 3.6. Comparison of 1:1 co-crystal structures: (A) *m*-dipyridylurea·*m*-DITFB resulting in a macrocyclic structure with no void and (B) *m*-dipyridylurea·*p*-DITFB which forms infinite polymeric chains along the *a*-axis.

dipyridylurea and *o*-DITFB from CH_2Cl_2 afforded the 1:2 *p*-dipyridylurea·(*o*-DITFB)$_2$ co-crystal in the monoclinic system with space group $P2_1/c$. Short I···N and I···O interactions define discrete $(p\text{-}C_{13}H_{14}N_4O)_2(o\text{-}C_6F_4I_2)_4$ clusters with halogen to pyridine interaction distances of I···N 2.822(3) Å and 3.046(3) Å and

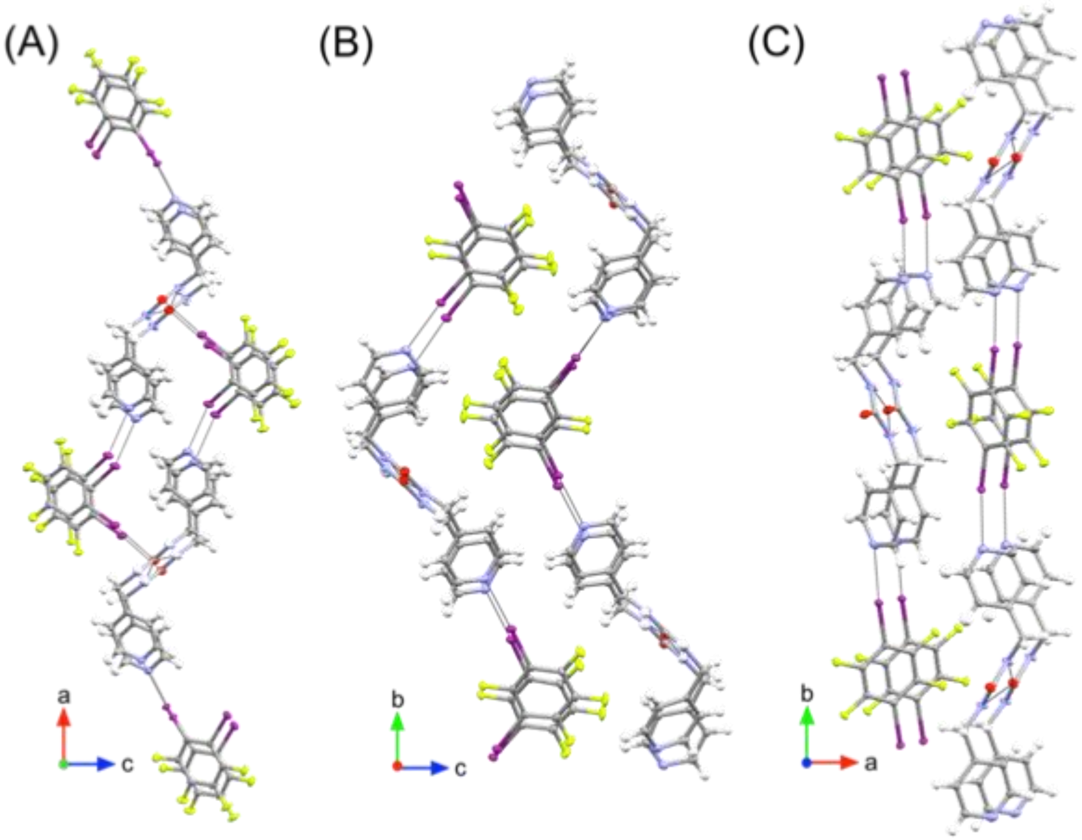

Figure 3.7. Crystal structures obtained by the *p*-dipyridylurea series with the regioisomers of DITFB afforded the expected urea chains. A) Views from *p*-dipyridylurea·(*o*-DITFB)$_2$ highlight the urea hydrogen bonded chains that are connected through C-I···N and C-I···O halogen bonding interactions. B) Views from the *p*-dipyridylurea·*m*-DITFB co-crystal exhibit typical urea hydrogen bonded chains further connected through C-I···N halogen bonding interactions. C) Views from the *p*-dipyridylurea·*p*-DITFB co-crystals showing 1D urea hydrogen bonded chains connected through halogen bonding interactions to form 2D layers.

C-I···N angles of 172.2(1)° and 158.3(1)° and short I···O distance of 3.025(2) Å (Figure 3.7A). The clusters are linked by three-center urea hydrogen bonding along the crystallographic [101] direction with typical N-H···O distances and angles (2.862(4) Å and 2.832(4) Å, 154(4)° and 156(4)°).

Vapor diffusion of water into a 1:1 mixture of *p*-dipyridylurea and *m*-DITFB in DMSO yielded *p*-dipyridylurea·*m*-DITFB co-crystal in the triclinic system with space group P-1. The asymmetric unit consisted of four crystallographically independent *p*-dipyridylurea moieties and four independent *m*-DITFBs. Undulating 2D layers are built from urea hydrogen-bond strands along the *a*-axis linked by short N···I interactions with the *m*-DITFBs that range from 78.4 to 80.2% of the van der Waals radii for N···I (Figure 3.7B). Typically urea N-H···O distances range from 2.817(4) Å and 3.019(4) Å with an average distance of 2.916 Å. The halogen bonding interactions between the *m*-DITFB donor and the pyridine acceptors show I···N distances from 2.769(3) Å and 2.833(3) Å and C-I···N angles of 178.7(1)° and 174.6(1)° resulting in a 2D layered structure with a herringbone pattern. The *m*-DITFB molecules are stacked into columns along the *a*-axis.

The crystal structure of *p*-dipyridylurea·*p*-DITFB was obtained through a slow evaporation technique from CH_3CN resulting in colorless 1:1 urea: DITFB co-crystals in the orthorhombic system with the space group *Fdd*2. As predicted, the structure (Figure 3.7C) displayed the expected urea hydrogen bonding columns, formed down the *b*-axis with N-H···O distances of 2.857(3) Å and 2.877(3) Å and N-H···O angles of N-H···O 151(3)° and 154(3)°. The halogen bonding interactions join the columns to form 2D layers parallel to the crystallographic (011) plane (I···N 2.863(2) Å and 2.875(2) Å, C-I···N 175.8(9)° and 172.6(9)°). A second crystal form, *p*-dipyridylurea·(*p*-DITFB)$_2$, was also obtained through a vapor diffusion of water into a 1:1 mixture of the *p*-dipyridylurea and *p*-DITFB in DMSO (Figure 3.23). In this structure, the typical urea assembly motif is conserved, as is the pyridyl to iodo C-I⋯N halogen bonding interaction.

Co-crystals are important in the pharmaceutical industry as they can alter the physicochemical properties and improve the stability of low melting pharmaceuticals.[33,34] Table 3.4 compares the melting points of the co-crystals and pyridylurea co-formers. The melting points of neat co-formers, *o*-DITFB and *p*-DITFB were recorded to be 58-60°C and 112-114°C respectively; while *m*-DITFB is a liquid at room temperature. The dipyridylureas co-formers displayed higher melting points with the hydrate *p*-DITFBs exhibiting the highest (183-184°C), consistent with literature reports.[35,36] Upon co-crystallization, all *o*-dipyridylurea·DITFB and *p*-dipyridylurea·DITFB co-crystals have higher melting points than their neat co-formers. These materials exhibit the common urea-urea interactions as well as pyridyl to iodine halogen bonds, suggesting that satisfying the full complement of donors and acceptors increases the melting point. In contrast, the co-crystals of the *m*-dipyridylurea with DITFBs varied widely in stability likely reflecting their different assembled structures. Co-crystals that maintain the urea-urea interactions as well as the pyridyl to iodine halogen bonds, specifically the *m*-dipyridylurea·*m*-DITFBs and *m*-dipyridylurea·*p*-DITFBs, showed higher melting points 163-164°C. In contrast, the two crystal forms of *m*-dipyridylurea with *o*-DITFB had significantly lower melting points (68-135 °C) than their urea conformer. The absence of the bifurcated urea assembly was associated with the co-crystal with the lowest melting point (68 °C for *m*-

Table 3.4. Stoichiometry of the co-crystals obtained with their corresponding melting points and the observed IR bands.

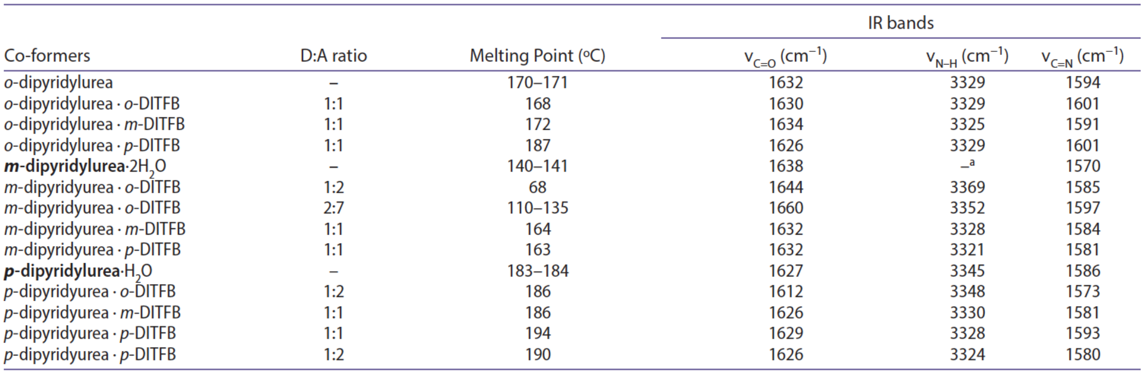

Co-formers	D:A ratio	Melting Point (ºC)	IR bands $\nu_{C=O}$ (cm^{-1})	 ν_{N-H} (cm^{-1})	 $\nu_{C=N}$ (cm^{-1})
o-dipyridylurea	–	170–171	1632	3329	1594
o-dipyridylurea · *o*-DITFB	1:1	168	1630	3329	1601
o-dipyridylurea · *m*-DITFB	1:1	172	1634	3325	1591
o-dipyridylurea · *p*-DITFB	1:1	187	1626	3329	1601
***m*-dipyridylurea**·$2H_2O$	–	140–141	1638	–[a]	1570
m-dipyridyurea · *o*-DITFB	1:2	68	1644	3369	1585
m-dipyridyurea · *o*-DITFB	2:7	110–135	1660	3352	1597
m-dipyridyurea · *m*-DITFB	1:1	164	1632	3328	1584
m-dipyridyurea · *p*-DITFB	1:1	163	1632	3321	1581
***p*-dipyridylurea**·H_2O	–	183–184	1627	3345	1586
p-dipyridyurea · *o*-DITFB	1:2	186	1612	3348	1573
p-dipyridyurea · *m*-DITFB	1:1	186	1626	3330	1581
p-dipyridyurea · *p*-DITFB	1:1	194	1629	3328	1593
p-dipyridyurea · *p*-DITFB	1:2	190	1626	3324	1580

[a]Band obscured in the dihydrate

dipyridylurea·(*o*-DITFB)$_2$ co-crystal) suggesting that this interaction plays an important role in thermal stability.

X-ray crystallography confirmed that all structures are co-crystals and that no salts have formed. We used FT-IR spectroscopy to probe the new or energetically modified hydrogen and halogen bonding interactions looking for shifts in the key vibrational bands ($\nu_{C=N}$, $\nu_{C=O}$, and ν_{N-H}) between the co-crystals and the parent dipyridylureas that would indicate altered intermolecular interactions. Most co-crystals displayed wavenumber shifts between the parent dipyridylurea co-former and the co-crystals ranging from 1 – 27 cm^{-1}. Co-crystals are known to exhibit a slight shift in vibrational bands when compared to a reference material as a result of altered intermolecular interactions.[37] Significant shifting (30-40 cm^{-1}) is often a result of salt formation but can also be a result of degradation of one or both co-formers.[37] We monitored the N···I halogen bond formation indirectly through the pyridine's $\nu_{C=N}$ band, which show shifts from 3 - 27 cm^{-1}. The relatively small observed shift of these bands make it challenging to characterize this interaction in the absence of the single crystal data.

Upon co-crystal formation, we observed that the dipyridylureas typically maintain the three-centered bifurcated interaction of the urea. Only minor shifting was observed with absolute differences between 1 - 6 cm^{-1} of the carbonyl $v_{C=O}$ band to either higher or lower wavenumbers, likely within experimental error. Interestingly, two co-crystals displayed significant shifts, larger than10 cm^{-1}, which were attributed to additional short O⋯I contacts. Specifically, the (*m*-dipyridylurea)$_2$· (*o*-DITFB)$_7$ showed a shift of 22 cm^{-1} to higher wavenumbers with O⋯I distances of 3.006(4) Å and C=O⋯I angles of 132.9° while the *p*-dipyridylurea·(*o*-DITFB)$_2$ showed a shift of 15 cm^{-1} to lower wavenumbers with O⋯I distances of 3.025(2) Å and C=O⋯I angles of 109.6(2)°. This data set suggests that the C=O vibrational band is more susceptible when closely packed to halogen atoms similar to what was reported for the macrocyclic pyridyl *bis*-urea system, which showed ~ 20 cm^{-1} shift to lower wavenumbers upon co-crystal formation with DITFBs.[20] A larger study of co-crystals with C=O⋯I interactions are needed to ascertain if this is a general trend.

An observed v_{N-H} stretch from 3321 to 3330 cm^{-1} correlated closely with the typical urea assembly motif and co-crystal structure predicted in Figure 3.3A. Disruption of the three-centered urea interaction in the *m*-dipyridylurea·(*o*-DITFB)$_2$ shifted this band to 3369 cm^{-1}. Close proximity of halogen atom crystal packing also had a large effect on the v_{N-H} band. For example, in the (*m*-dipyridylurea)$_2$·(*o*-DITFB)$_7$'s co-crystal the urea nitrogen forms and additional the N⋯I interaction (3.335(7) Å), and we observe a shift of the v_{N-H} to 3352 cm^{-1}. Similarly, the *p*-dipyridylurea·(*o*-DITFB)$_2$ co-crystal has a close contact between the urea oxygen and a neighboring iodine (3.025(2) Å) and displays the ν_{N-H} at 3348 cm^{-1}. In general, FT-IR provides a ready comparison of the urea assembly through this NH stretch as long as additional NH, OH, or protic solvents do not obscure the region.

3.3 Conclusions

In summary, we systematically investigated structures of three flexible dipyridylurea ligands and eleven of their co-crystals with *o*-, *m*-, and *p*-DITFB. The crystals of the ne3t dipyridylurea ligands all exhibited the typical bifurcated urea-urea hydrogen-bonding motif, suggesting that the position and proximity of the pyridyl nitrogen with respect to the urea moiety does not influence the urea-urea assembly. Thus, the altered assembly of *bis*-urea macrocycle, observed previously, is likely a result of the pyridyl nitrogen and urea being constrained within its cyclic framework. Comparison of calculated electrostatic potentials of the *o*-dipyridylurea ligand and the three regioisomers of DITFB correctly predicted that the co-crystals would exhibit bifurcated urea binding patterns and pyridyl-halogen interactions with DITFB. Indeed, the majority of structures exhibited 1:1 dipyridylurea: DITFB stoichiometries with typical urea assembly and short pryidyl to DITFB halogen bonds with an average N···I interaction of 80.6% of the van der Waals radii. Furthermore, the urea-urea tape motif was conserved in the majority of the co-crystal structures (10 out of 11) suggesting that the N-H···O interaction between neighboring urea molecules is the best donor-acceptor pair present in these systems. Competition between acceptors and altered assembly were observed when the two building blocks were frustrated by the relative orientation of their donors and acceptors. This is highlighted by the co-crystal structures of *m*-dipyridylurea with the constrained *o*-DITFB regioisomer, which exhibited both pyridine nitrogen N···I interactions as well as O···I interactions with the urea carbonyl that fall in the longer range of values observed (84.2-86.6 % vs. 81.5-85.3% van der Waals for O···I interactions in literature).[32,38] In comparison, the pyridyl *bis*-urea macrocycle displayed the O···I interaction in co-crystals with DITFB with shorter interaction distances of 78.1-82.0 % van der Waals,[20] suggesting that chemists can design systems to favour O···I interaction over the N···I halogen bond. Overall, simple electrostatic calculations are a useful strategy for screening building blocks for their potential to satisfy all binding sites forming both hydrogen and halogen bonds. We are currently investigating the assembly of dipyridyl substituted oxalamides with DITFBs to see if similar hydrogen and halogen bonding patterns are observed for geometrically constrained DITFB and evaluate a wider range of structures to correlate the impact C=O···I interactions have on corresponding carbonyl vibrational bands.

3.4 FUTURE WORK

We are currently screening co-crystallization of the DITFB's alongside dipyridyloxalamide counterparts to extend this study and compare the use of Spartan and the hydrogen bond propensity database as prediction tools.

3.5 EXPERIMENTAL

All compounds were characterized by ^{1}H NMR, Mass Spec, and FT-IR.

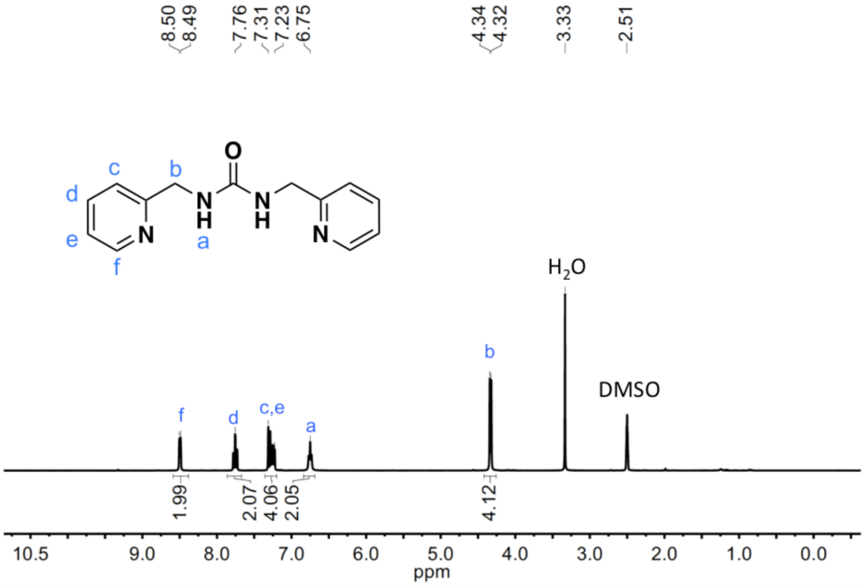

Figure 3.8. ^{1}H NMR of crystallized *o*-dipyridylurea, each proton peak is labeled with its corresponding position on the inset structure. ^{1}H-NMR (300MHz, DMSO-d) δ 8.495 (d, 2H), 7.76 (t, 2H), 7.2-7.3 (m, 4H), 6.75 (t, 2H), 4.33 (d, 4H). Water present in NMR solvent.

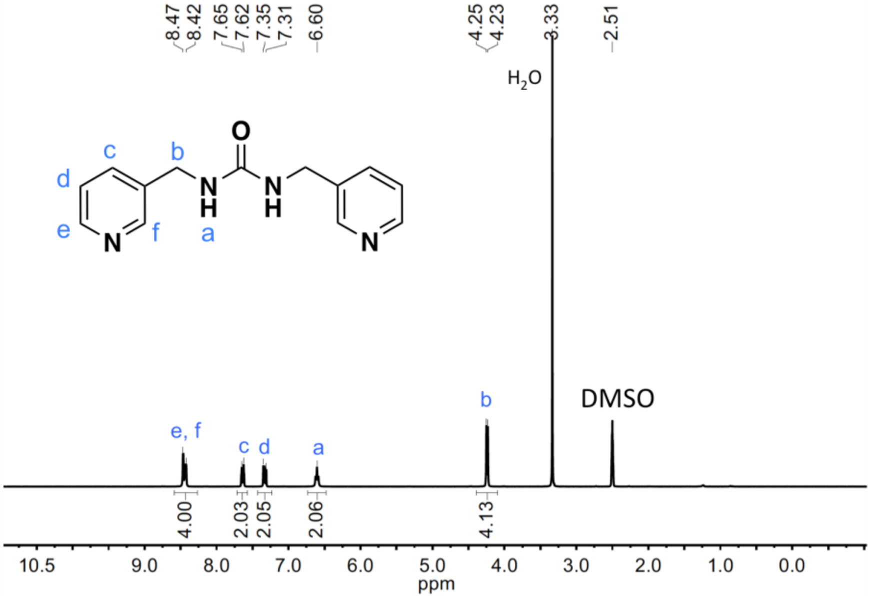

Figure 3.9. ^{1}H NMR of crystallized *m*-dipyridylurea, each proton peak is labeled with its corresponding position on the inset structure. ^{1}H-NMR (300MHz, DMSO-d) δ 8.45 (m, 4H), 7.64 (d, 2H), 7.33 (d, 2H), 6.60 (t, 2H), 4.24 (d, 4H). Water present in NMR solvent.

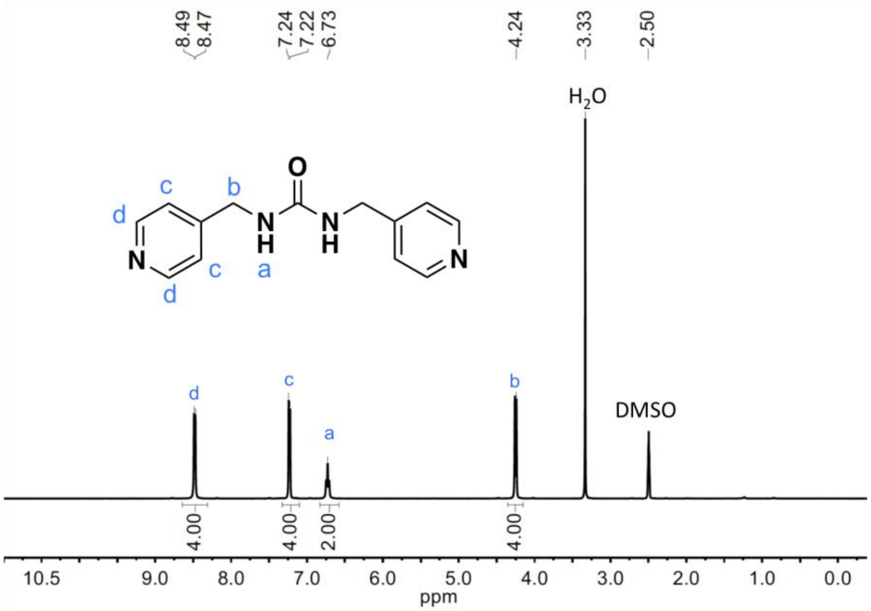

Figure 3.10 ^{1}H NMR of crystallized *p*-dipyridylurea, each proton peak is labeled with its corresponding position on the inset structure. ^{1}H-NMR (300MHz, DMSO-d) δ 8.48 (d, 4H), 7.23 (d, 4H), 6.73 (t, 2H), 4.24 (d, 4H). Water present in NMR solvent.

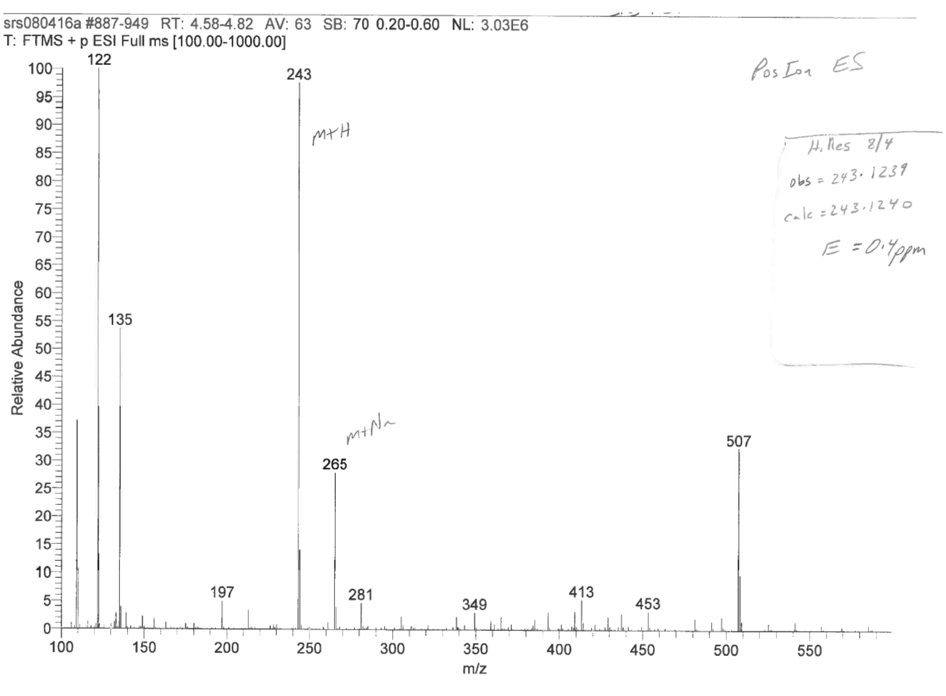

Pos Ion ES

M+H

M+Na

Hi Res 2/4
obs = 243.1239
calc = 243.1240
E = 0.4 ppm

Figure 3.11. High resolution mass spec of *o*-dipyridylurea. HRMS (EI): m/z calculated for $C_{13}H_{14}N_4O$ [M+]: 243.1240, observed: 243.1239.

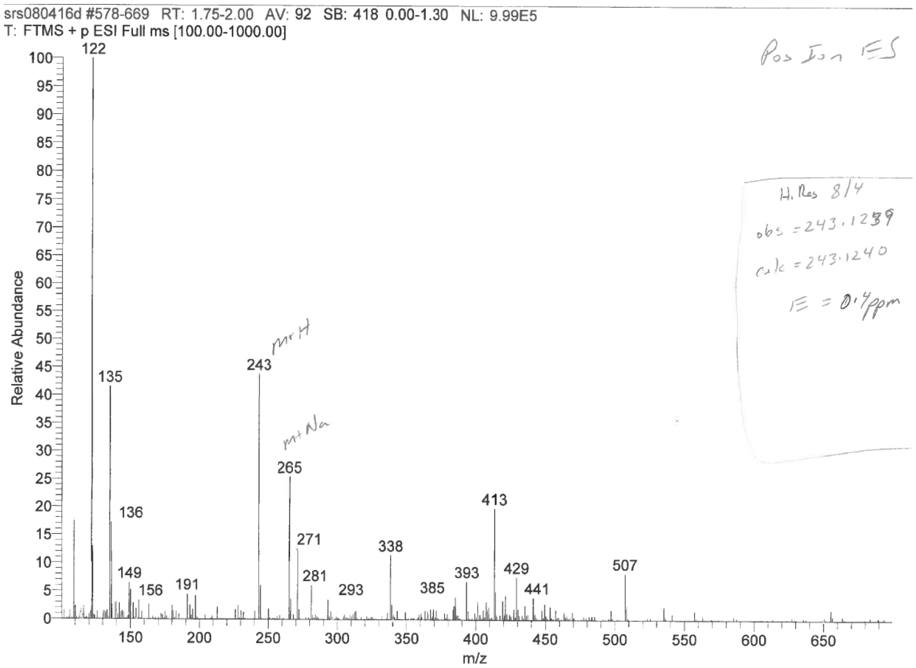

Figure 3.12. High resolution mass spec of *m*-dipyridylurea. HRMS (EI): m/z calculated for $C_{13}H_{14}N_4O$ [M+]: 243.1240, observed: 243.1239.

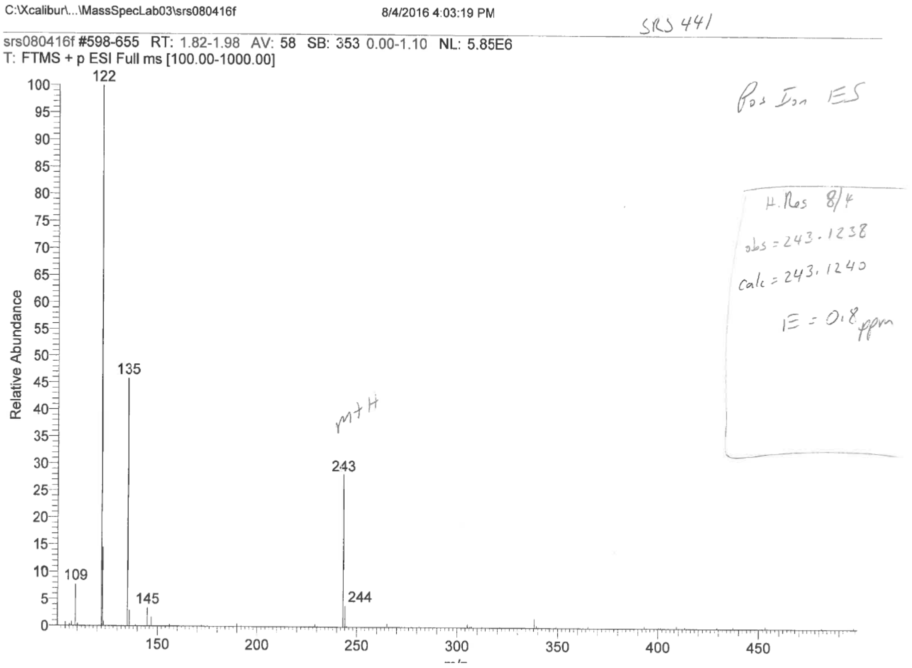

Figure 3.13. High resolution mass spec of *p*-dipyridylurea. HRMS (EI): m/z calculated for $C_{13}H_{14}N_4O$ [M+]: 243.1240, observed: 243.1238.

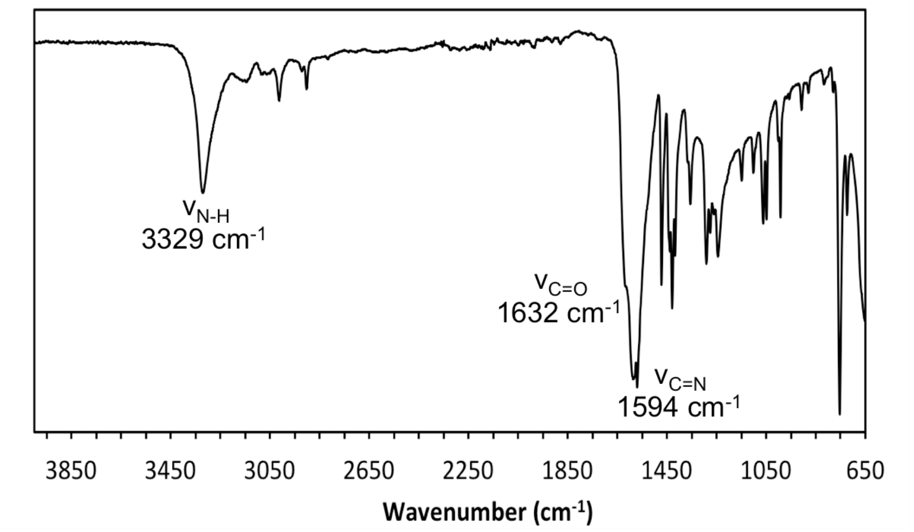

Figure 3.14. FT-IR spectra of *o*-dipyridylurea with key vibrational bands indicated with their corresponding wavenumber.

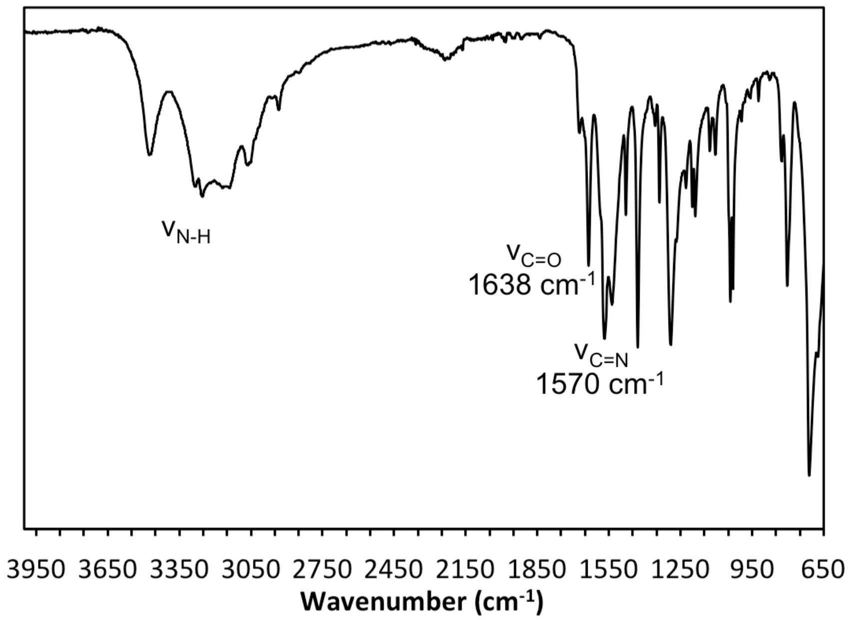

Figure 3.15. FT-IR spec of *m*-dipyridylurea with key vibrational bands indicated with their corresponding wavenumber. The dihydrate character of this co-crystal makes conclusive characterization of the NH band more difficult.

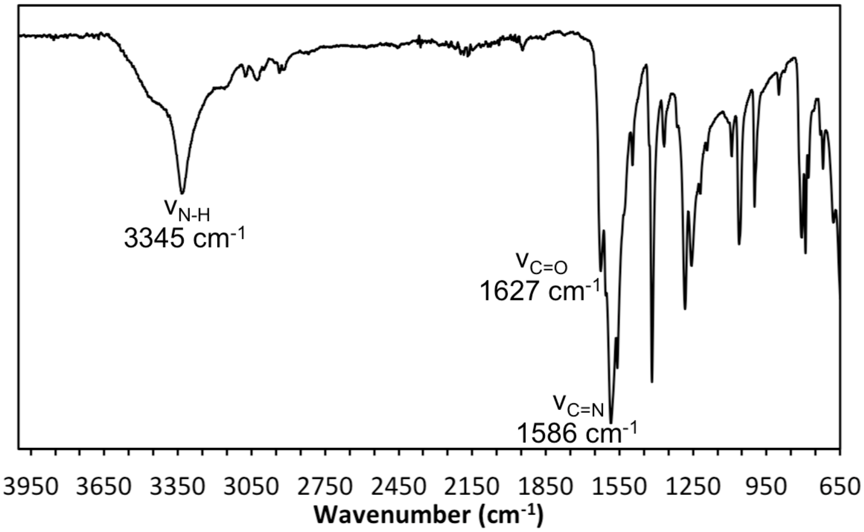

Figure 3.16. FT-IR spec of *p*-dipyridylurea with key vibrational bands indicated with their corresponding wavenumber.

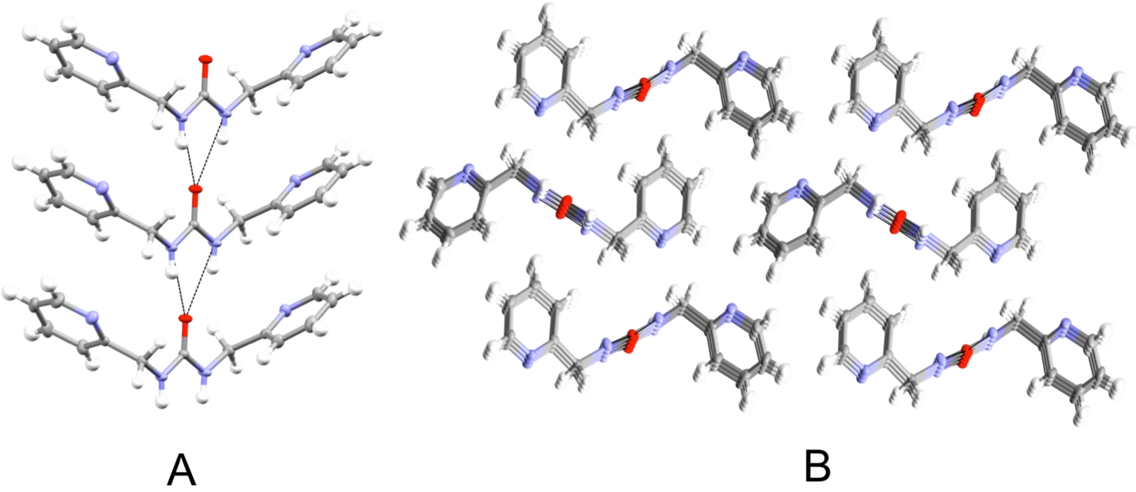

Figure 3.17. SCXRD of *o*-dipyridylurea. (A) view of the three-center urea hydrogen bonding interaction (B) View down the crystallographic *a*-axis demonstrating crystal packing.

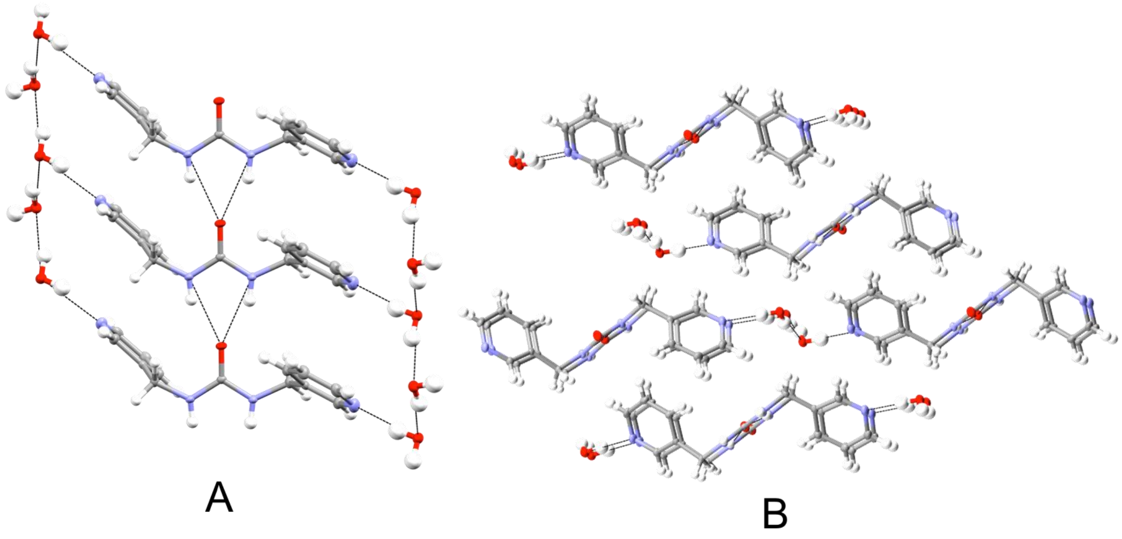

Figure 3.18. SCXRD of *m*-dipyridylurea dihydrate. (A) view of the three-center urea hydrogen bonding interaction displaying the water-to-water and water-to-pyridine interactions (B) View down the crystallographic *b*-axis demonstrating crystal packing.

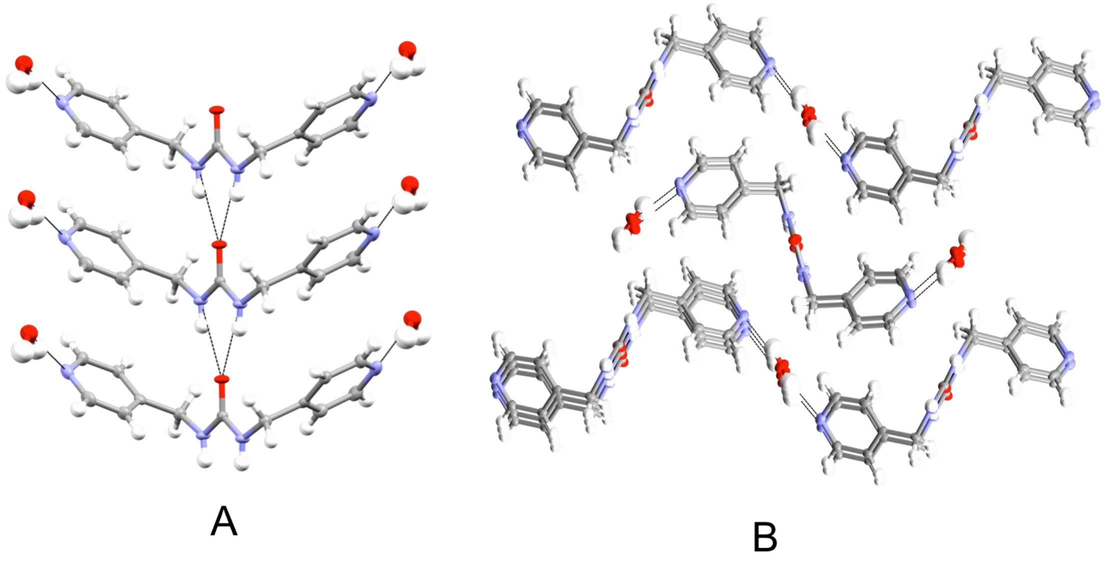

Figure 3.19. SCXRD of *p*-dipyridylurea hydrate. (A) view of the three-center urea hydrogen bonding interaction displaying the water-to-pyridine interaction (B) View down the crystallographic *c*-axis demonstrating crystal packing.

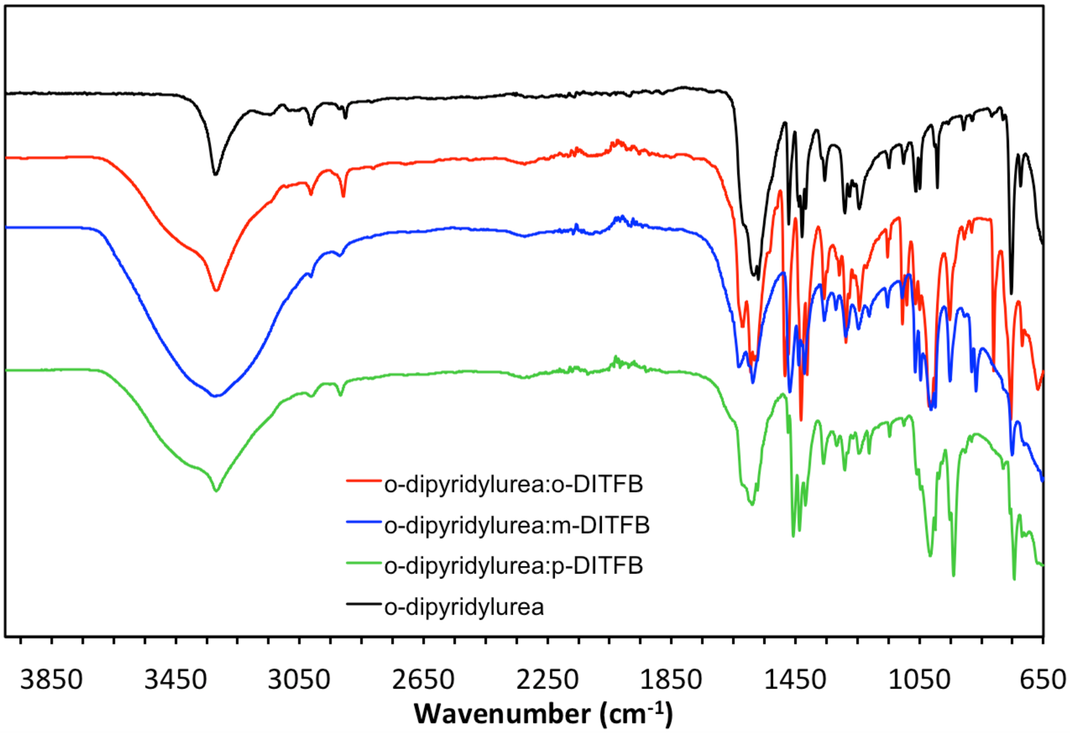

Figure 3.20. FT-IR spec of *o*-dipyridylurea·DITFB co-crystals. FT-IR spectroscopy was used to probe hydrogen and halogen bonding interactions present in the co-crystals. The three co-crystals structures of *o*-dipyridylurea and DITFBs all showed typical three-center urea hydrogen bonding interactions that are observed in the parent *o*-dipyridylurea structure, as well as additional pyridyl – iodo halogen bonds. Interestingly, the NH stretch was not significantly shifted in the co-crystals, although the peaks were broadened in the co-crystals. However, both $v_{C=O}$ (1632 to 1626-1634 cm^{-1}) and $v_{C=N}$ (1594 cm^{-1} to 1591-1601 cm^{-1}) were shifted.

***o*-dipyridylurea**

Identification code	1_DCM
Empirical formula	$C_{13}H_{14}N_4O$
Formula weight	242.28
Temperature/K	100(2)
Crystal system	monoclinic
Space group	$P2_1$

a/Å	4.5260(4)
b/Å	10.0021(8)
c/Å	13.3135(11)
α/°	90
β/°	95.911(3)
γ/°	90
Volume/Å^3	599.49(9)
Z	2
ρcalcg/cm^3	1.342
μ/mm^{-1}	0.090
F(000)	256.0
Crystal size/mm^3	0.56 × 0.44 × 0.24
Radiation	MoKα (λ = 0.71073)
2Θ range for data collection/°	5.104 to 60.096
Index ranges	$-6 \leq h \leq 6$, $-14 \leq k \leq 14$, $-18 \leq l \leq 18$
Reflections collected	28693
Independent reflections	3502 [R_{int} = 0.0384, R_{sigma} = 0.0264]
Data/restraints/parameters	3502/1/172
Goodness-of-fit on F2	1.034
Final R indexes [I>=2σ (I)]	R_1 = 0.0344, wR_2 = 0.0785
Final R indexes [all data]	R_1 = 0.0437, wR_2 = 0.0830
Largest diff. peak/hole / e Å-3	0.28/-0.20

***o*-dipyridylurea•*o*-DITFB**

Identification code	1aDMSO
Empirical formula	$C_{19}H_{14}F_4I_2N_4O$
Formula weight	644.14
Temperature/K	100(2)
Crystal system	orthorhombic
Space group	$P2_12_12_1$
a/Å	4.4908(3)
b/Å	13.7479(8)
c/Å	34.1596(19)
α/°	90
β/°	90
γ/°	90
Volume/Å^3	2109.0(2)
Z	4
ρ_{calc}g/cm^3	2.029
μ/mm^{-1}	3.035
F(000)	1224.0
Crystal size/mm^3	0.48 × 0.12 × 0.04
Radiation	MoKα (λ = 0.71073)

2Θ range for data collection/°	4.644 to 60.16
Index ranges	-6 ≤ h ≤ 6, -19 ≤ k ≤ 19, -48 ≤ l ≤ 48
Reflections collected	103423
Independent reflections	6204 [R_{int}=0.0415, R_{sigma}=0.0175]
Data/restraints/parameters	6204/0/280
Goodness-of-fit on F^2	1.122
Final R indexes [I>=2σ (I)]	R_1 = 0.0176, wR_2 = 0.0309
Final R indexes [all data]	R_1 = 0.0201, wR_2 = 0.0313
Largest diff. peak/hole / e Å^{-3}	0.41/-0.40

***o*-dipyridyl urea•*m*-DITFB**

Identification code	1bDMSO
Empirical formula	$C_{19}H_{14}F_4I_2N_4O$
Formula weight	644.14
Temperature/K	100(2)
Crystal system	monoclinic
Space group	$P2_1/c$
a/Å	4.4606(4)
b/Å	33.073(3)
c/Å	14.6219(12)
α/°	90
β/°	92.594(2)

γ/°	90
Volume/Å^3	2154.9(3)
Z	4
ρcalcg/cm^3	1.985
μ/mm^{-1}	2.971
F(000)	1224.0
Crystal size/mm^3	0.28 × 0.04 × 0.02
Radiation MoKα	(λ = 0.71073)
2Θ range for data collection/°	4.628 to 55.5
Index ranges	-5 ≤ h ≤ 5, -43 ≤ k ≤ 43, -18 ≤ l ≤ 19
Reflections collected	96670
Independent reflections	5050 [R_{int} = 0.0753, R_{sigma} = 0.0343]
Data/restraints/parameters	5050/143/315
Goodness-of-fit on F2	1.061
Final R indexes [I>=2σ (I)]	R1 = 0.0362, wR2 = 0.0644
Final R indexes [all data]	R1 = 0.0568, wR2 = 0.0692
Largest diff. peak/hole / e Å-3	1.11/-0.89

***o*-dipyridyl urea•*p*-DITFB**

Identification code	1cACN
Empirical formula	$C_{19}H_{14}F_4I_2N_4O$
Formula weight	644.14
Temperature/K	100(2)
Crystal system	monoclinic

Space group	C2/c
a/Å	31.679(2)
b/Å	4.5203(3)
c/Å	14.7400(9)
α/°	90
β/°	99.704(2)
γ/°	90
Volume/Å^3	2080.6(2)
Z	4
ρcalcg/cm^3	2.056
μ/mm^{-1}	3.077
F(000)	1224.0
Crystal size/mm^3	0.44 × 0.1 × 0.06
Radiation MoKα	(λ = 0.71073)
2Θ range for data collection/°	5.218 to 60.11
Index ranges	$-44 \le h \le 44$, $-6 \le k \le 6$, $-20 \le l \le 20$
Reflections collected	40690
Independent reflections	3060 [R_{int} = 0.0388, R_{sigma} = 0.0168]
Data/restraints/parameters	3060/0/166
Goodness-of-fit on F2	1.124
Final R indexes [I>=2σ (I)]	R1 = 0.0177, wR2 = 0.0428
Final R indexes [all data]	R1 = 0.0201, wR2 = 0.0439
Largest diff. peak/hole / e Å-3	0.54/-0.48

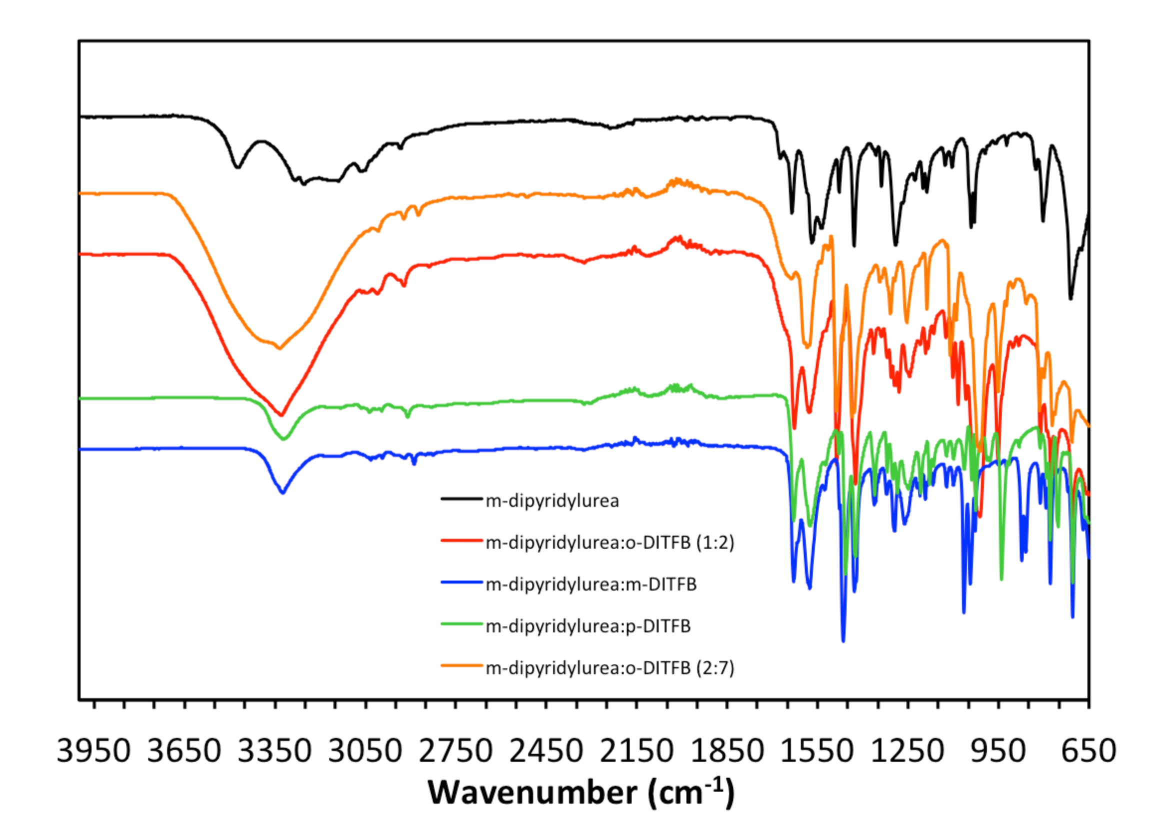

Figure 3.21. FT-IR spec of *m*-dipyridylurea·DITFB co-crystals. The co-crystals structures of *m*-dipyridylurea and DITFBs exhibited typical three-center urea hydrogen bonding interactions in nearly all cases, while all structures have additional pyridyl – iodo halogen bonds. The *m*-dipyridylurea·(*o*-DITFB)$_2$ co-crystal has disrupted urea hydrogen bonding interactions resulting in a halogen bond between the free oxygen lone pair and an iodo donor. The (*m*-dipyridylurea)$_2$·(*o*-DITFB)$_7$ has the predicted three-center urea bifurcated hydrogen bonding, although this structure does exhibit a short contact between the urea carbonyl oxygen and one of the halogen bond donors. The dihydrate character of the parent urea made characterization of NH stretch more difficult. However, the two *m*-dipyridylurea·*o*-DITFB exhibited broadening in the NH region reflecting the complex intermolecular interactions of the two co-crystals. The $v_{C=N}$ (1570 cm^{-1} to 1581-1597 cm^{-1}). The carbonyl band, $v_{C=O}$ (1638 cm^{-1}) shifted only slightly to lower wavenumbers in the *m*-dipyridylurea·*m*-DITFB and *m*-dipyridylurea·*p*-DITFB co-crystals to 1632 cm^{-1} for both co-crystals. Shifting to higher wavenumbers is observed in the (*m*-dipyridylurea)$_2$·(*o*-DITFB)$_7$ co-crystal (1638 cm^{-1} to 1660 cm^{-1}) and the *m*-dipyridylurea·(*o*-DITFB)$_2$ co-crystal (1638 cm^{-1} to 1644 cm^{-1}).

m-dipyridylurea•$2H_2O$

Identification code	BD_2
Empirical formula	$C_{13}H_{18}N_4O_3$
Formula weight	278.31
Temperature/K	100(2)
Crystal system	monoclinic
Space group	$P2_1/c$
a/Å	19.9447(9)
b/Å	4.5612(2)
c/Å	15.4649(7)
α/°	90
β/°	100.043(2)
γ/°	90
Volume/Å^3	1385.31(11)
Z	4
ρcalcg/cm^3	1.334
μ/mm^{-1}	0.097
F(000)	592.0
Crystal size/mm^3	0.3 × 0.24 × 0.04
Radiation	MoKα (λ = 0.71073)
2Θ range for data collection/°	5.35 to 60.172
Index ranges	$-28 \le h \le 28$, $-6 \le k \le 16$, $-21 \le l \le 21$
Reflections collected	65373
Independent reflections	4070 [R_{int} = 0.0390, R_{sigma} = 0.0183]

Data/restraints/parameters	4070/0/206
Goodness-of-fit on F2	1.038
Final R indexes [I>=2σ (I)]	$R_1 = 0.0362$, $wR_2 = 0.0904$
Final R indexes [all data]	$R_1 = 0.0510$, $wR_2 = 0.0973$
Largest diff. peak/hole / e Å-3	0.36/-0.21

_m_-dipyridyl urea•(_o_-DITFB)$_2$

Identification code	2aDMSO
Empirical formula	$C_{25}H_{14}F_8I_4N_4O$
Formula weight	1046.00
Temperature/K	100(2)
Crystal system	monoclinic
Space group	$P2_1/c$
a/Å	14.1182(12)
b/Å	23.9797(19)
c/Å	9.0323(8)
α/°	90
β/°	105.412(3)
γ/°	90
Volume/Å^3	2947.9(4)
Z	4
ρcalcg/cm^3	2.357
μ/mm^{-1}	4.307
F(000)	1936.0

Crystal size/mm^3	0.46 × 0.2 × 0.04
Radiation MoKα	(λ = 0.71073)
2Θ range for data collection/°	4.528 to 56.76
Index ranges	$-18 \leq h \leq 18$, $-31 \leq k \leq 31$, $-12 \leq l \leq 12$
Reflections collected	109266
Independent reflections	7339 [R_{int} = 0.0680, R_{sigma} = 0.0309]
Data/restraints/parameters	7339/0/387
Goodness-of-fit on F2	1.039
Final R indexes [I>=2σ (I)]	R1 = 0.0281, wR2 = 0.0600
Final R indexes [all data]	R1 = 0.0412, wR2 = 0.0648
Largest diff. peak/hole / e Å-3	1.17/-0.78

(*m*-dipyridyl urea)$_2$•(*o*-DITFB)$_7$

Identification code	BD_2A_11
Empirical formula	$C_{68}H_{28}F_{28}I_{14}N_8O_2$
Formula weight	3297.58
Temperature/K	100(2)
Crystal system	monoclinic
Space group	$P2_1/n$
a/Å	8.5945(4)
b/Å	23.3518(10)
c/Å	42.2742(17)
α/°	90
β/°	90.0566(13)

γ/°	90
Volume/Å^3	8484.3(6)
Z	4
ρcalcg/cm^3	2.582
μ/mm^{-1}	5.218
F(000)	6008.0
Crystal size/mm^3	0.22 × 0.08 × 0.06
Radiation MoKα	(λ = 0.71073)
2Θ range for data collection/°	4.23 to 55.562
Index ranges	$-11 \leq h \leq 11$, $-30 \leq k \leq 30$, $-55 \leq l \leq 55$
Reflections collected	292668
Independent reflections	20017 [R_{int} = 0.0571, R_{sigma} = 0.0278]
Data/restraints/parameters	20017/18/1082
Goodness-of-fit on F2	1.164
Final R indexes [I>=2σ (I)]	R1 = 0.0384, wR2 = 0.0616
Final R indexes [all data]	R1 = 0.0492, wR2 = 0.0638
Largest diff. peak/hole / e Å-3	0.77/-0.98

***m*-dipyridyl urea•*m*-DITFB**

Identification code	2B_CH$_3$CN
Empirical formula	$C_{19}H_{14}F_4I_2N_4O$
Formula weight	644.14
Temperature/K	100(2)
Crystal system	monoclinic

Space group	$P2_1/c$
a/Å	13.9125(8)
b/Å	4.5117(3)
c/Å	33.0109(19)
α/°	90
β/°	97.3790(10)
γ/°	90
Volume/$Å^3$	2054.9(2)
Z	4
ρcalcg/cm^3	2.082
μ/mm^{-1}	3.115
F(000)	1224.0
Crystal size/mm^3	0.44 × 0.02 × 0.02
Radiation MoKα	(λ = 0.71073)
2Θ range for data collection/°	4.452 to 55.328
Index ranges	$-18 \le h \le 18$, $-5 \le k \le 5$, $-43 \le l \le 43$
Reflections collected	50295
Independent reflections	4876 [R_{int} = 0.0605, R_{sigma} = 0.0358]
Data/restraints/parameters	4876/1/279
Goodness-of-fit on F2	1.131
Final R indexes [I>=2σ (I)]	R1 = 0.0447, wR2 = 0.0910
Final R indexes [all data]	R1 = 0.0620, wR2 = 0.0972
Largest diff. peak/hole / e Å-3	1.67/-1.19

_m_-dipyridyl urea•_p_-DITFB

Identification code	2cACN
Empirical formula	$C_{19}H_{14}F_4I_2N_4O$
Formula weight	644.14
Temperature/K	100(2)
Crystal system	monoclinic
Space group	$P2_1/c$
a/Å	13.1113(18)
b/Å	4.5390(6)
c/Å	35.235(5)
α/°	90
β/°	98.238(2)
γ/°	90
Volume/Å^3	2075.3(5)
Z	4
ρcalcg/cm^3	2.062
μ/mm^{-1}	3.085
F(000)	1224.0
Crystal size/mm^3	0.36 × 0.08 × 0.06
Radiation MoKα	(λ = 0.71073)
2Θ range for data collection/°	4.172 to 56.678
Index ranges	$-17 \le h \le 17, 0 \le k \le 6, 0 \le l \le 47$
Reflections collected	5302

Independent reflections	5302 [R_{int} = 0.0560, R_{sigma} = 0.0471]
Data/restraints/parameters	5302/1/280
Goodness-of-fit on F2	1.147
Final R indexes [I>=2σ (I)]	R1 = 0.0477, wR2 = 0.1140
Final R indexes [all data]	R1 = 0.0514, wR2 = 0.1152
Largest diff. peak/hole / e Å-3	1.31/-1.68

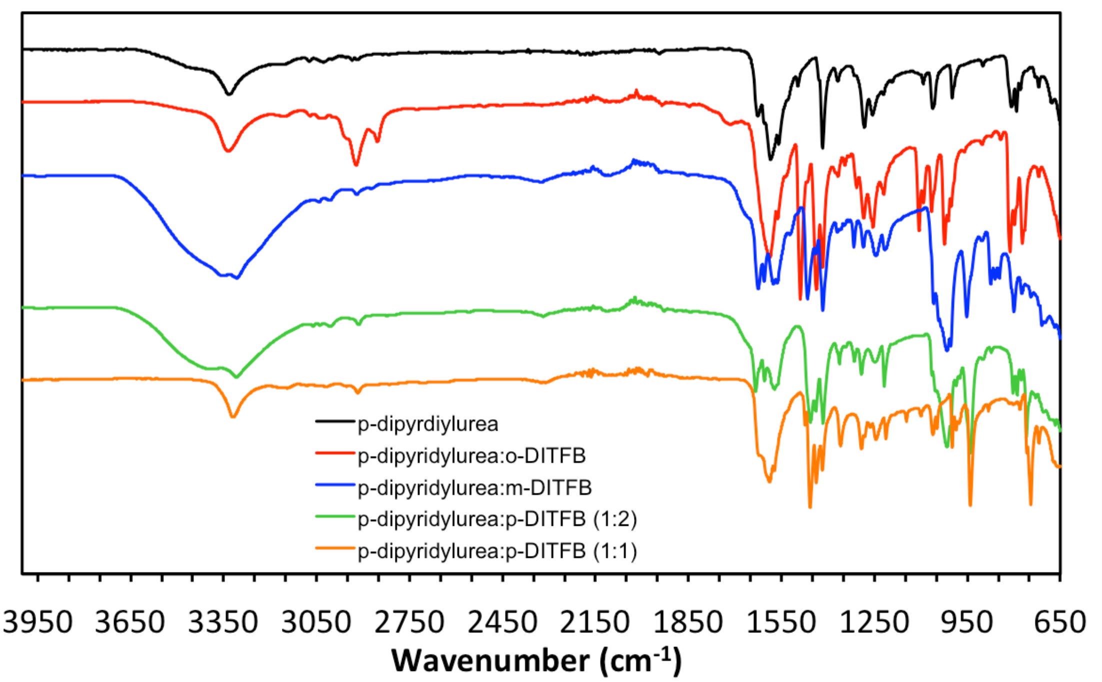

Figure 3.22. FT-IR spec of *p*-dipyridylurea·DITFB co-crystals. The co-crystals structures of *p*-dipyridylurea and DITFBs exhibited typical three-center urea hydrogen bonding interactions with pyridyl – iodo halogen bonds in all cases. Although, it should be noted that a short contact between the carbonyl oxygen and the iodo donor is observed in the crystal structure of *p*-dipyridylurea·*o*-DITFB. The NH stretch was impacted in the co-crystals, shifting to higher wavenumbers in the *p*-dipyridylurea·*o*-DITFB co-crystal (3345 cm^{-1} to 3348 cm^{-1}) and to lower wavenumbers in the rest of the co-crystal structures (3345 cm^{-1} to 3324-3330 cm^{-1}). Both the carbonyl ($\nu_{C=O}$ = 1627 cm^{-1}) and pyridyl ($\nu_{C=N}$ = 1586 cm^{-1}) bands behave similarly; exhibits shifting to higher wavenumbers for the *p*-dipyridylurea·*p*-DITFB co-crystal ($\nu_{C=O}$ = 1627 cm^{-1} to 1629 cm^{-1}) and ($\nu_{C=N}$ = 1586 cm^{-1} to 1593 cm^{-1}) while shifting to lower wavenumbers is observed for all other co-crystals ($\nu_{C=O}$ = 1627 cm^{-1} to 1612-1626 cm^{-1}) and ($\nu_{C=N}$ = 1586 cm^{-1} to 1573-1681 cm^{-1}).

p-dipyridylurea•H_2O

Identification code	BD_2
Empirical formula	$C_{13}H_{18}N_4O_3$
Formula weight	278.31
Temperature/K	100(2)
Crystal system	monoclinic
Space group	$P2_1/c$
a/Å	19.9447(9)
b/Å	4.5612(2)
c/Å	15.4649(7)
α/°	90
β/°	100.043(2)
γ/°	90
Volume/Å^3	1385.31(11)
Z	4
ρcalcg/cm^3	1.334
μ/mm^{-1}	0.097
F(000)	592.0
Crystal size/mm^3	0.3 × 0.24 × 0.04
Radiation	MoKα (λ = 0.71073)
2Θ range for data collection/°	5.35 to 60.172
Index ranges	$-28 \le h \le 28$, $-6 \le k \le 16$, $-21 \le l \le 21$
Reflections collected	65373

Independent reflections	4070 [R_{int} = 0.0390, R_{sigma} = 0.0183]
Data/restraints/parameters	4070/0/206
Goodness-of-fit on F2	1.038
Final R indexes [I>=2σ (I)]	R_1 = 0.0362, wR_2 = 0.0904
Final R indexes [all data]	R_1 = 0.0510, wR_2 = 0.0973
Largest diff. peak/hole / e Å-3	0.36/-0.21

***p*-dipyridyl urea•(*o*-DITFB)$_2$**

Identification code	3A_DCM
Empirical formula	$C_{25}H_{14}F_8I_4N_4O$
Formula weight	1046.00
Temperature/K	100(2)
Crystal system	monoclinic
Space group	$P2_1/c$
a/Å	25.7640(12)
b/Å	4.5481(2)
c/Å	25.2307(12)
α/°	90
β/°	96.6010(10)
γ/°	90
Volume/Å^3	2936.9(2)
Z	4
ρcalcg/cm^3	2.366
μ/mm^{-1}	4.323

F(000)	1936.0
Crystal size/mm^3	0.2 × 0.04 × 0.04
Radiation MoKα	(λ = 0.71073)
2Θ range for data collection/°	4.28 to 56.694
Index ranges	$-34 \le h \le 34$, $-6 \le k \le 6$, $-33 \le l \le 33$
Reflections collected	114520
Independent reflections	7281 [R_{int} = 0.0422, R_{sigma} = 0.0193]
Data/restraints/parameters	7281/0/388
Goodness-of-fit on F2	1.125
Final R indexes [I>=2σ (I)]	R1 = 0.0288, wR2 = 0.0471
Final R indexes [all data]	R1 = 0.0372, wR2 = 0.0489
Largest diff. peak/hole / e Å-3	1.32/-0.94

***p*-dipyridyl urea•*m*-DITFB**

Identification code	3bDMSO
Empirical formula	$C_{19}H_{14}F_4I_2N_4O$
Formula weight	644.14
Temperature/K	100(2)
Crystal system	triclinic
Space group	P-1
a/Å	9.2589(5)
b/Å	18.7560(11)
c/Å	24.1561(13)
α/°	97.001(2)

β/°	91.435(2)
γ/°	98.901(2)
Volume/Å^3	4109.4(4)
Z	8
ρcalcg/cm^3	2.082
μ/mm^{-1}	3.116
F(000)	2448.0
Crystal size/mm^3	0.46 × 0.12 × 0.04
Radiation MoKα	(λ = 0.71073)
2Θ range for data collection/°	4.29 to 60.188
Index ranges	$-13 \le h \le 13$, $-26 \le k \le 26$, $-33 \le l \le 34$
Reflections collected	202858
Independent reflections	24115 [R_{int} = 0.0678, R_{sigma} = 0.0476]
Data/restraints/parameters	24115/0/1113
Goodness-of-fit on F2	1.006
Final R indexes [I>=2σ (I)]	R1 = 0.0390, wR2 = 0.0656
Final R indexes [all data]	R1 = 0.0723, wR2 = 0.0744
Largest diff. peak/hole / e Å-3	1.12/-1.10

_p_-dipyridyl urea•_p_-DITFB

Identification code	3cACN
Empirical formula	$C_{19}H_{14}F_4I_2N_4O$
Formula weight	644.14
Temperature/K	100(2)

Crystal system	orthorhombic
Space group	Fdd2
a/Å	38.332(3)
b/Å	47.044(3)
c/Å	4.5676(3)
α/°	90
β/°	90
γ/°	90
Volume/Å^3	8236.6(10)
Z	16
ρcalcg/cm^3	2.078
μ/mm^{-1}	3.109
F(000)	4896.0
Crystal size/mm^3	0.46 × 0.04 × 0.03
Radiation MoKα	(λ = 0.71073)
2Θ range for data collection/°	4.25 to 60.164
Index ranges	$-54 \le h \le 54$, $-66 \le k \le 66$, $-6 \le l \le 6$
Reflections collected	101299
Independent reflections	6058 [R_{int} = 0.0421, R_{sigma} = 0.0201]
Data/restraints/parameters	6058/1/279
Goodness-of-fit on F2	1.045
Final R indexes [I>=2σ (I)]	R1 = 0.0155, wR2 = 0.0281
Final R indexes [all data]	R1 = 0.0191, wR2 = 0.0286

Largest diff. peak/hole / e Å-3	0.31/-0.22

_p_-dipyridylurea•(_p_-DITFB)$_2$

Identification code	3cDMSO
Empirical formula	$C_{25}H_{14}F_8I_4N_4O$
Formula weight	1046.00
Temperature/K	100(2)
Crystal system	monoclinic
Space group	I2/a
a/Å	25.0342(8)
b/Å	4.53820(10)
c/Å	25.7638(13)
α/°	90
β/°	100.7740(10)
γ/°	90
Volume/Å^3	2875.43(18)
Z	4
ρcalcg/cm^3	2.416
μ/mm^{-1}	4.415
F(000)	1936.0
Crystal size/mm^3	0.24 × 0.02 × 0.02
Radiation MoKα	(λ = 0.71073)
2Θ range for data collection/°	5.032 to 55.48
Index ranges	$-32 \le h \le 32$, $-5 \le k \le 5$, $-33 \le l \le 33$

Reflections collected	32026
Independent reflections	3354 [R_{int} = 0.0737, R_{sigma} = 0.0374]
Data/restraints/parameters	3354/0/194
Goodness-of-fit on F2	1.106
Final R indexes [I>=2σ (I)]	R1 = 0.0382, wR2 = 0.0552
Final R indexes [all data]	R1 = 0.0613, wR2 = 0.0600
Largest diff. peak/hole / e Å-3	1.67/-1.28

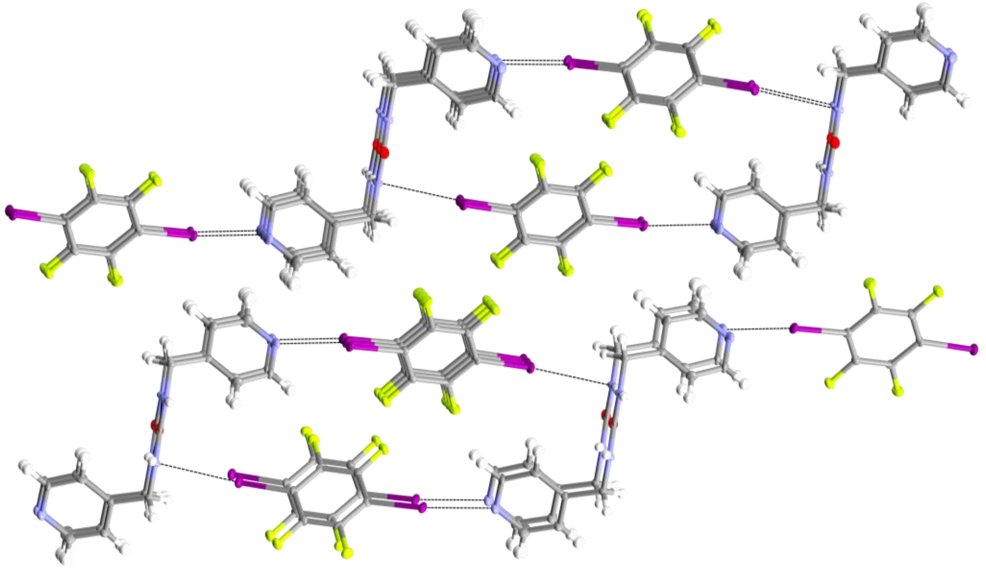

Figure 3.23. SCXRD structure of *p*-dipyridylurea·(*o*-DITFB)$_2$ which was obtained through vapor diffusion from DMSO resulting in colorless 1:2 urea: DITFB co-crystals in the monoclinic system with the space group *I2/a*. As predicted, urea hydrogen bonding columns, formed down the *b*-axis with N-H···O distances of 2.828(6) Å and N-H···O angles of N-H···O 149(5)°. The halogen bonding interactions join the columns to form 2D layers (I···N 2.825(4) Å and C-I···N 173.8(6)°). A secondary interaction is formed between the urea N-H and the activated iodine (I···N 3.207(4) Å and C-I···N 176.4(2)°)

Table 3.5. Summary table of the packing motifs observed from the SCXRD structure of each crystal.

Co-formers	Space Group	Crystal System	Packing Motif
***o*-dipyridylurea**	$P2_1$	monoclinic	2D layers
o-dipyridylurea • *o*-DITFB	$P2_12_12_1$	orthorhombic	serpentine patterned sheet
o-dipyridylurea • *m*-DITFB	$P2_1/c$	monoclinic	corrugated 2D layers
o-dipyridylurea • *p*-DITFB	C2/c	monoclinic	herringbone pattern
***m*-dipyridylurea**•$2H_2O$	$P2_1/c$	monoclinic	2D layers
(*m*-dipyridyurea)$_2$•(*o*-DITFB)$_7$	$P2_1/n$	monoclinic	Irregular packing
m-dipyridyurea • (*o*-DITFB)$_2$	$P2_1/c$	monoclinic	extended 2D chains
m-dipyridyurea • *m*-DITFB	$P2_1/c$	monoclinic	Tetrameric 2D layers
m-dipyridyurea • *p*-DITFB	$P2_1/c$	monoclinic	Linear 2D layers
***p*-dipyridylurea**•H_2O	$P2_12_12$	orthorhombic	2D layers
p-dipyridyurea • (*o*-DITFB)$_2$	$P2_1/c$	monoclinic	cluster
p-dipyridyurea • *m*-DITFB	P-1	triclinic	Undulating 2D layers
p-dipyridyurea • *p*-DITFB	Fdd2	orthorhombic	2D layers
p-dipyridyurea • (*p*-DITFB)$_2$	I2/a	monoclinic	Lamellar-like

3.6 References

1. Aakeröy, C. B.; Salmon, D. J. *Cryst. Eng. Comm*. **2005**, *7*(72), 439–448.
2. Aitipamula, S.; et al. *Cryst. Growth Des.* **2012**, *12*, 2147−2152.
3. Duggirala, N. K.; Perry, M. L.; Almarsson, Ö.; Zaworotko, M. J. *Chem. Commun.* **2016**, *52*, 640-655.
4. Bolla, G.; Nangia, A. *Chem. Commun.* **2016**, *52*, 8342-8360.
5. Bennion, J. C.; Siddiqia, Z. R.; Matzger, A. J. *Chem. Commun.* **2017**, *53*, 6065-6068.
6. Bennion, J. C.; McBain, A.; Son, S. F.; Matzger, A. J. *Cryst. Growth Des.* **2015**, *15*, 2545-2549.
7. Sinnwell, M.A.; MacGillivray, L.R. *Angew. Chem., Int. Ed. Engl.* **2016**, *55*, 3477-3480.

8. Ericson, D.P.; Zurfluh-Cunningham, Z.P.; Groeneman, R. H.; Elacqua, E.; Reinheimer, E.W.; Noll, B.C.; MacGillivray, L.R. *Cryst. Growth Des.* **2015**, *15*, 5744-5748.
9. Mukherjee, A.; Tothadi, S.; Desiraju, G. R. *Acc. Chem. Res.* **2014**, *47*, 2514-2524.
10. Cavallo, G.; Metrangolo, P.; Milani, R.; Pilati, T.; Priimagi, A.; Resnati, G.; Terraneo, G. *Chem. Rev.* **2016**, *116*, 2478 – 2601.
11. Murray, J. S.; Grice, M. E.; Politzer, P.; Etter, M. C. *Mol. Eng.* **1991**, *1*, 75-87.
12. Etter, M. C. *J. Phys. Chem.* **1991**, *95*, 4601-4610.
13. Etter, M. C. *Acc. Chem. Res.* **1990**, *23*, 120-126.
14. Aakeröy, C. B.; Spartz, C. L. Dembowski, S.; Swyre, S.; Desper, J. *IUCrJ* **2015**, *2*, 498 -510.
15. Murray, J. S.; Politzer, P. *J. Org. Chem.* **1991**, *56*, 6715-6817.
16. Murray, J. S.; Politzer, P. *WIREs Comput. Mol. Sci.* **2011**, *1*, 153-163.
17. Hunter, C. A. *Angew. Chem. Int. Ed.* **2004**, *43*, 5310 – 5324.
18. Roy, K.; Wang, C.; Smith, M. D.; Dewal, M. B.; Wibowo, A. C.; Brown, J. C.; Ma, S.; Shimizu, L. S. *Chem. Commun.* **2011**, *47*, 277-279.
19. Roy, K.; Wibowo, A. C.; Pellechia, P. J.; Ma, S.; Geer, M. F.; Shimizu, L. S. *Chem. Mater.* **2012**, *24*, 4773-4781.
20. Som, B.; Salpage, S. R.; Son, J.; Gu, B.; Karakalos, S. G.; Smith, M.D.; Shimizu, L.S. *Cryst. Eng. Comm.* **2017**, *19*, 484-491.
21. Perera, M. D.; Desper, J.; Sinha, A. S.; Aakeröy, C. B. *CrystEngComm* **2016**, *18*, 8631 -8636.

22. Reger, D. L.; Ciurtin Smith, D. M.; Shimizu, K. D.; Smith, M. D. *Polyhedron* **2004**, *23*, 711-717.

23. Schauer, C. L.; Matwey, E.; Fowler, F. W.; Lauher, J. W. *Cryst. Eng.* **1998**, *1*, 213-223.

24. Troff, R. W.; Hovorka, R.; Weilandt, T.; Lützen, A.; Cetina, M.; Nieger, M.; Lentz, D.; Rissanen, K.; Schalley, C. A. *Dalton Trans.* **2012**, *41*, 8410-8420.

25. Tzeng, B. C.; Huang, Y. C.; Chen, B. S.; Wu, W. M.; Lee, S.Y.; Lee, G.H.; Peng, S. M. *Inorg. Chem.* **2007**, *46*, 186-195.

26. Goroff, N. S.; Curtis, S. M.; Webb, J. A.; Fowler, F. W.; Lauher, J. W. *Org. Lett.* **2005***, 7*, 1891-1893.

27. **APEX3** Version 2016.5-0 and **SAINT+** Version 8.37A. Bruker AXS, Inc., Madison, Wisconsin, USA, 2016.

28. **SADABS**-2016/2: Krause, L., Herbst-Irmer, R., Sheldrick G.M. and Stalke D. *J. Appl. Cryst.* **2015**, *48*, 3-10.

29. (a) **SHELXT**: Sheldrick, G.M. *Acta Cryst*. **2015**, *A71*, 3-8. (b) **SHELXL:** Sheldrick, G.M. *Acta Cryst*. **2008**, A64, 112-122.

30. **OLEX2**: a complete structure solution, refinement and analysis program. Dolomanov, O. V.; Bourhis, L. J.; Gildea, R. J.; Howard, J. A. K.; Puschmann, H. *J. Appl. Cryst.* **2009**, *42*, 339-341.

31. Pulacchini, S.;Abrahams, I.; Eames, J.; Watkinson, M. *Supramolecular Chemistry* **2002**, *14*, 353-357.

32. Zbačnik, M.; Vitković, M.; Vulić, V.; Nogalo, I.; Cinčić, D.; *Cryst. Growth Des*. **2016**, *16*, 6381-6389.

33. Bolla, G.; Nangia, A. *Chem. Commun.* **2016**, *52*, 8342-8360.

34. McKellar, S. C.; Kennedy, A. R.; McCloy, N. C.; McBride, E.; Florence, A. J. *Cryst. Growth Des.* **2014**, *14*, 2422-2430.

35. Diax, P.; Tovilla, J. A.; Ballester, P.; Benet-Buchholz, J.; Vilar, R. *Dalton Trans.* **2007**, 3516-3525.

36. Kamiya, S.; Yamaguchi, K.; Miyahara, M.; Miyata, N. *Chem. Pharm. Bull.* **1990**, *38*, 3226-3229.

37. Wiscons, R. A.; Matzger, A. J. *Cryst. Growth Des.* **2017**, *17*, 901-906.

38. Nemec, V.; Cinčić, D. *CrystEngComm*, **2016**, *18*, 7425-7429.

CHAPTER 4

PROBING THE FORMATION OF REACTIVE OXYGEN SPECIES BY A POROUS BENZOPHENONE *BIS*-UREA HOST‡

‡DeHaven, B. A.; Liberatore, H. K.; Richardson, S. D.; Greer, A.; Shimizu, L. S. *Submitted to ACS Omega*. November 29,2018. AO-2018-033367.

4.0 ABSTRACT

Herein, we examine the photochemical formation of reactive oxygen species (ROS) by a porous benzophenone-containing *bis*-urea host (**1**) to investigate the mechanism of photooxidations that occur within the confines of its nanochannels. UV-irradiation of the self-assembled host in the presence of molecular oxygen generates both singlet oxygen and superoxide when suspended in solution. The efficiency of ROS generation by the host is lower than benzophenone, which could beneficial for reactions carried out catalytically, as ROS species react quickly and often unselectively. Superoxide formation was detected through reaction with 5,5-dimethyl-1-pyrroline *N*-oxide in methanol. However, it is not detected in $CHCl_3$, as it reacts rapidly with the solvent to generate methaneperoxy and chloride anions, similar to its parent benzophenone. The lifetime of airborne singlet oxygen ($\tau_{\Delta airborne}$) was also examined at the air-solid outer surface of the host and with quenchers loaded to probe how they impact the lifetime of singlet oxygen. Finally, we compared the efficiency and product distribution of the photooxidation of 1-methyl-1-cyclohexene with the host as a catalyst in $CHCl_3$, benzene, and benzene-δ_6. The host mediates the photooxidation in solution and produces primarily epoxide-derived products. Interestingly, in $CHCl_3$ two chlorohydrins were also formed, reflecting the formation of chloride in this solvent. Studies in benzene afforded the epoxide and a tertiary allylic alcohol. In contrast, UV-irradiation of the crystalline host•guest complex in an oxygen atmosphere produced no epoxide and afforded high conversion to three products: an enone, a tertiary allylic

alcohol, and a diol, which demonstrates the influence of encapsulation on the outcome of the reaction.

4.1 INTRODUCTION

Here, we investigate the selectivity and efficiency of reactive oxygen species (ROS) photogeneration by a self-assembled benzophenone *bis*-urea macrocycle (host **1**) and probe its utility for mediating the photooxidation of 1-methyl-1-cyclohexene (**2**) in the solid-state in comparison to suspended in solution. Macrocycle **1** presents two benzophenone (BP) photosensitizer units covalently attached to two urea groups through methylene bridges resulting in a *bis*-urea macrocycle. Self-assembly through urea hydrogen-bonding interactions affords hexagonally packed columnar nanotubes that are activated by heating to generate accessible channels that can be readily loaded with guests and applied as a nanoreactor for selective photooxidations, Figure 4.1.[1,2]

ROS are employed in a diverse range of applications spanning from wastewater treatment to photodynamic therapy for cancer treatment.[3-6] ROS are generated from simple molecular oxygen ($^3O_2$), providing an attractive pathway for industrial oxidation processes due to economical and environmental advantages over traditional oxidants, which present safety hazards and generate stoichiometric amounts of hazardous waste. Molecular oxygen can be activated through type I and type II sensitized processes.[7,8] The main species formed in type II reactions is singlet oxygen ($^1O_2$).[7] On the other hand, type I reactions produce superoxide ($O_2^{\bullet-}$), which is generated through one-electron reduction of

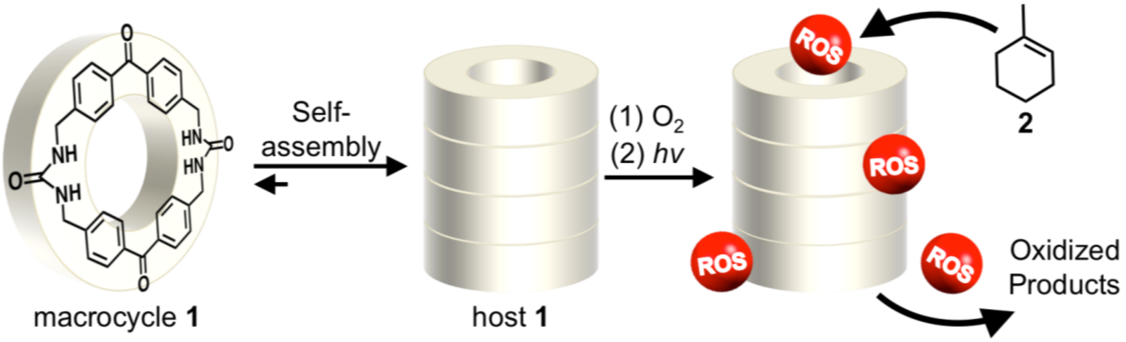

Figure 4.1. Macrocycle **1** is comprised of two BP sensitizer units covalently bound through methylene urea groups. Self-assembly through bifurcated urea hydrogen-bonding interactions results in the formation of porous host **1** nanotubes that are capable of generating ROS upon UV-irradiation.

$^3O_2$, in addition to a variety of species such as protonated superoxide $HO_2\cdot$, $ROO\cdot$, $RO\cdot$, and $\cdot OH$.[8,9,10] Whereas, $^1O_2$ is generated through a Dexter (triplet) pathway when $^3O_2$ interacts with a triplet sensitizer, often generated by visible light wavelengths.[11-13] While ROS present a green pathway for industrial oxidations, achieving high selectivity is challenging due to their inherent instability. Strategies to enhance organic selectivity of ROS reactions are under active exploration and include templation,[14] air-water interfacial effects,[15] and confinement within nanocavities and channels.[1,16,17]

Herein, we probe the mechanism of ROS generation and evaluate the host as a suspended photocatalyst in order to optimize selectivity and conversion of industrial photooxidations. Specifically, we examined the scope of ROS generated by **1** while suspended in protic methanol (MeOH) versus aprotic chloroform ($CHCl_3$). Interestingly, the detection of $O_2^{\bullet-}$ was found to be solvent-dependent. Both $O_2^{\bullet-}$ and $^1O_2$ were generated in MeOH while the former ($O_2^{\bullet-}$)

was not detected in $CHCl_3$ using EPR and a 5,5-dimethyl-1-pyrroline *N*-oxide (DMPO) trap. We determined that the $^1O_2$ quantum yield of **1** while suspended in $CHCl_3$ is low, ranging from 1-12%. Previously, selectivity of photooxidations were enhanced when a heterogeneous gas/solid reaction was carried out when the host•guest complex was simply UV-irradiated in an O_2 atmosphere.[1] Thus, we also examined the lifetime of airborne $^1O_2$ generated by a 3-phase apparatus delivering $^1O_2$ to the air-solid interface of host **1** to gain insight into how the outer wall of host **1** impacts the lifetime of $^1O_2$. The quenching of airborne $^1O_2$ was compared with the host and triphenylphosphine (Ph_3P) to give a sense of the outer wall quenching capacity.

Finally, with interfacial control of photooxidations desired, we also compared the ROS reactivity of 1-methyl-1-cyclohexene (**2**) in solution versus within the crystalline host. Host **1** was suspended as a catalyst in oxygenated solutions ($CHCl_3$ and benzene) and the photooxidation of **2** was monitored. Overall, photooxidations in solution resulted in multiple products and characterization was attempted on only key products. Upon UV-irradiation in $CHCl_3$, an epoxide and two chlorohydrins were the key products observed, which are atypical for $^1O_2$ oxidations. In contrast, in benzene the epoxide was a primary product alongside a tertiary alcohol, which is commonly observed in $^1O_2$ oxidations. We then examined the photoreactivity of the crystalline host **1•2** complex under an O_2 atmosphere to see how encapsulation within the nanochannels influences the product distribution. In this case, three different products were formed including the enone, a tertiary alcohol, and a diol, demonstrating the influence of encapsulation on the outcome of the reaction.

4.2 RESULTS AND DISCUSSION

Host **1** was synthesized as previously reported.[1,2,18] Crystallization by slow cooling in DMSO (10 mg/mL) affords white needle-like crystals with regular channels (10.5Å x 5.2Å) that are filled with DMSO.[1,2,18] The host crystals were activated by heating to 180 °C using thermogravimetric analysis (TGA) at a ramp rate of 4 °C/min.[1,2,18] Once activated, the evacuated host can be readily loaded with guest molecules by soaking the crystals in guest solutions or through vapor diffusion.[1,2] Host **1** contains two BP photosensitizer units, which assist in ROS

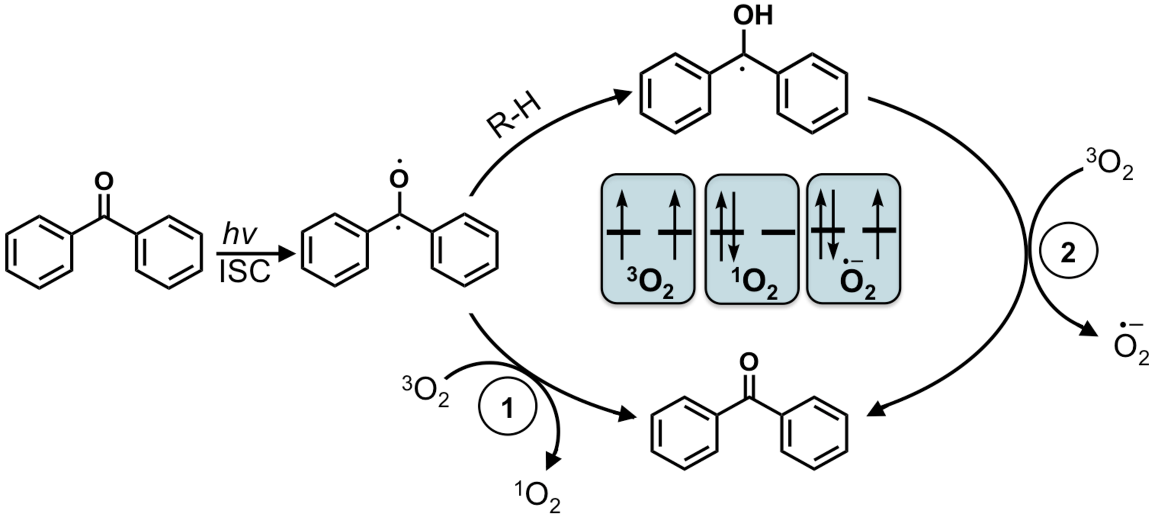

Scheme 4.1. The ground state BP is excited upon UV-irradiation to its singlet-excited state. Upon intersystem crossing the triplet excited state is formed which can interact with oxygen one of two ways: (1) through a triplet-triplet annihilation pathway which results in the formation of $^1O_2$ and the reformation of ground state BP (2) Through hydrogen abstraction to form a ketyl radical which undergoes electron transfer with molecular oxygen to generate $O_2^{\bullet-}$ and subsequently ground state BP. Blue Inset: Distribution of electrons in the highest orbitals of $^3\Sigma O_2$, $^1\Delta O_2$, and $O_2^{\bullet-}$.

formation, as the parent BP is capable of activating oxygen to generate both $^1O_2$ and $O_2^{\bullet -}$ (Scheme 4.1).[9,19] Superoxide generation by BP involves the formation of a ketyl radical, which will then undergo an electron transfer process with $^3O_2$ to form $O_2^{\bullet -}$ and subsequently peroxides, resulting in the regeneration of ground state BP, Scheme 4.1.[9,19,20] Previous work showed that UV-irradiation of the crystalline host results in the formation of persistent organic triplet radical pairs consisting of a ketyl radical and benzylic radicals in low quantity (~ 1 in 10,000 molecules).[18] Therefore, our hypothesis is that the suspended host will generate $O_2^{\bullet -}$ similarly to the parent BP, although in lower efficiency due to reduced ketyl radical production by **1** in the solid-state.

How does the host activate O_2? Electron paramagnetic resonance (EPR) spectroscopy was used to probe the types of ROS generated by host 1 upon UV irradiation while suspended in solution. EPR is a useful technique for detecting ROS due to its high sensitivity and the availability of traps for oxygen species.[21-23] Singlet oxygen can be readily detected as it reacts with 2,2,6,6-tetramethylpiperidine (TMP) to form a stable nitroxide radical, 2,2,6,6-tetramethylpiperidin-1-yl oxidanyl (TEMPO), which gives rise to a signature three-line EPR spectrum as a function of time.[21,23] Hydroxide and $O_2^{\bullet -}$ are ROS that are readily detectable by reaction with DMPO, a common spin trap that forms distinctive radical adducts (doublet of triplets) with $O_2^{\bullet -}$, hydroxide, or peroxide radicals.[21,22] The DMPO-OOH adduct is unstable with a short half-life (~1 min) and degrades to form the DMPO-OH adduct.[22,23]

To investigate if host **1** is capable of generating $O_2^{\bullet-}$, we carried out a DMPO spin trapping study in the presence of MeOH. Literature precedence demonstrates that BP activates oxygen to $O_2^{\bullet-}$ in polar protic solvents, most commonly alcohols (such as MeOH, ethanol, and 2-propanol).[9,19] Host **1** (0.11 mg, 0.2 μmol) was suspended in benzene and a stock solution of DMPO in MeOH was added to prepare a 20 mM solution. The sample was sealed under oxygen and EPR spectra were recorded over time of UV irradiation. Irradiation of the host **1** suspension resulted in the gradual formation of a four-line anisotropic spectrum. The sample was irradiated for 15 minutes in total (Figure 4.2A). An EasySpin simulation of the DMPO adduct formed upon irradiation of the host was performed using the garlic package to account for the fast motion regime and is consistent with the formation of a DMPO adduct with hyperfine splitting constants of a^N = 14.2 G and a^H = 9.2 G, which is in range of typical DMPO-OOH adducts (Figure 4.12).[24-26] The experiment was also carried out with BP as the sensitizer for comparison. It should be noted that BP is indeed soluble in $CHCl_3$ and benzene; therefore, the quenching studies carried out with BP were performed in solution. UV-irradiation of BP for 2 min in the presence of DMPO and MeOH resulted in modest formation of a four-line spectrum that overlays nicely with the spectra obtained by host **1**, with a^N = 13.8 G and a^H = 9.3 G (Figure 4.13). This result indicates that in the presence of MeOH, a polar protic solvent, the host can in fact generate $O_2^{\bullet-}$, albeit ~15x slower than BP. UV irradiation of host **1** for 15 min generates approximately half the amount of $O_2^{\bullet-}$ when compared to parent BP after just two min of UV-irradiation.

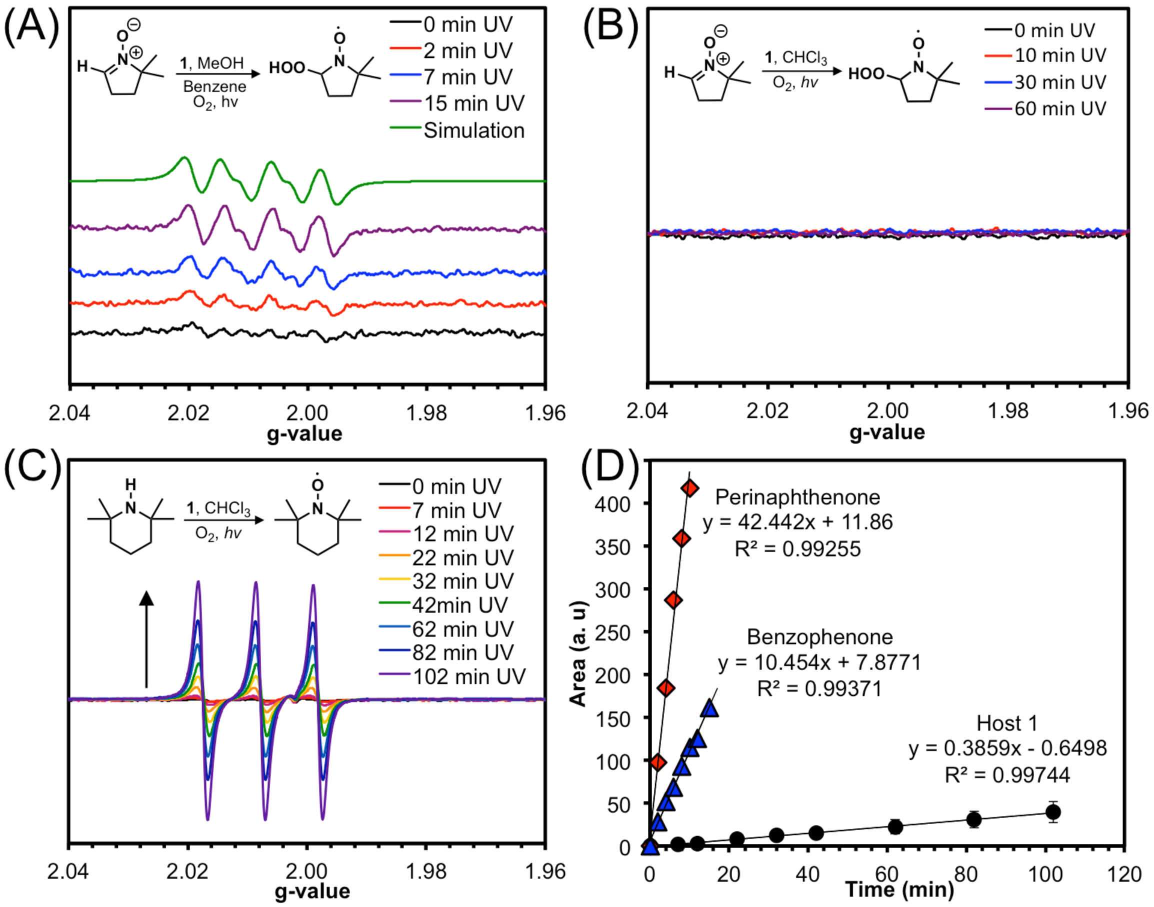

Figure 4.2. EPR studies of host **1** suspended in oxygen saturated solutions of $O_2^{\bullet-}$ and $^1O_2$ quenchers. (A) DMPO was used to trap $O_2^{\bullet-}$ in benzene in the presence **1** and methanol. (B) DMPO $O_2^{\bullet-}$ trapping experiment in chloroform in the presence **1** (C) TMP was used to chemically quench $^1O_2$ in chloroform and in the presence of **1** resulting in the formation of EPR detectible TEMPO over time of UV irradiation (D) Comparison of the TMP chemical quenching study with different photosensitizers, perinaphthenone was used as the reference and host **1** was compared to BP in solution.

To probe the formation of $O_2^{\bullet-}$ by host **1** in $CHCl_3$, the activated host (1.0 mg, 2.0 µmol) was suspended in a solution of DMPO in $CHCl_3$. Next, the solution was bubbled with O_2 gas via O_2 balloon and the stirring solution was irradiated at 350 nm in a Rayonet reactor. Aliquots of the DMPO solution (0.1 mL) were removed at various time intervals and their EPR spectra recorded to probe for the formation of $O_2^{\bullet-}$. No signals were observed for the DMPO solution pre or post UV-irradiation, indicating no significant amount of $O_2^{\bullet-}$ builds up under these conditions (Figure 4.2B). As a control, the same experiment was carried out using BP; similarly no formation of $O_2^{\bullet-}$ was detected (Figure 4.15). Roberts and Sawyer's work suggest that $O_2^{\bullet-}$ reacts with $CHCl_3$ to generate methaneperoxy ($HC(=O)OO^-$) and chloride anions,[27] although radical species cannot be ruled out. Our studies indicate that either the [$O_2^{\bullet-}$] is very low or its reaction with $CHCl_3$ is exceedingly efficient, leaving no $O_2^{\bullet-}$ to form an adduct with DMPO.

Next, the contribution of $^1O_2$ was investigated by adding activated host **1** (0.1±0.02 mg) to a Norell Suprasil quartz EPR tube. The sample was suspended in a 2.97 mM solution of TMP in $CHCl_3$ (0.2 mL) and the solution was sealed under pure O_2(g). The solution was then irradiated at 350 nm in a Rayonet reactor and EPR spectra were recorded at various time intervals. Upon irradiation of TMP and host **1** in the presence of O_2 the distinct three-line TEMPO EPR signal increased with extended irradiation time, indicating the formation of $^1O_2$ (Figure 4.2C). In order to compare the efficiency of the two ROS generation processes, the area of the EPR spectra obtained during the DMPO spin-trapping experiment was compared to the TEMPO experiment in $CHCl_3$ after 15 min of irradiation. Interestingly, the areas obtained were very similar (5.8 vs 5.1) with the $O_2^{\bullet-}$ adduct generated ~1.1x faster than $^1O_2$. The production of both $O_2^{\bullet-}$ and $^1O_2$ by **1** indicates that the host can activate oxygen in two distinct ways. In the absence of a protic solvent, one can reduce $O_2^{\bullet-}$ generation; however, in chlorinated solvents this may generate chloride anions.[27]

What is the quantum yield of $^1O_2$ generation in solution? How efficient is this crystalline host at generating $^1O_2$ versus BP or perinaphthenone? To probe this question, two indirect techniques, EPR and UV-visible spectroscopy, were employed to measure the quantum yield of $^1O_2$ generation. Both rely on a $^1O_2$ quencher whose subsequent oxidation upon irradiation can be monitored by the corresponding spectroscopic methods. In each experiment, the sensitizer (**1** or a standard) was added to an oxygen-saturated stock solution containing a known quencher such as TMP, which upon reaction with $^1O_2$ affords the stable radical TEMPO. The solution was UV-irradiated at 360 nm in a Rayonet reactor and the reaction was monitored over time by EPR spectroscopy. Figure 4.2C shows the gradual formation of TEMPO from TMP. The $^1O_2$ quantum yield ($\Phi[^1O_2]$) was determined by plotting the area of EPR signal versus time and obtaining the slope of each plot using the equation $\Phi[^1O_2]^{sample} = \Phi[^1O_2]^{ref} (m^{sample}/ m^{ref})$ where perinaphthenone was used as the reference ($\Phi[^1O_2]^{ref} = 0.97$ in $CHCl_3$), m^{sample} is the slope of the host plot, and m^{ref} is the slope of the perinaphthenone plot (Figure 2D).[23,28] By this method, we estimate the $\Phi[^1O_2]^{host}$ **^{1}** to be ~1% in $CHCl_3$. In some cases, the use of TMP in determining the quantum yield of $^1O_2$ production can be misleading when the excited photosensitizer is able to react with TMP, resulting in the $TMP^{+\bullet}$.[23] The radical cation can then undergo a reaction with molecular oxygen to form an EPR-detectable TEMPO signal that is not attributed $^1O_2$ production.[23] While this process has been observed by the parent BP it is not anticipated to occur (or be minimal at best) with the host because TMP is too large to fit into the host channels (Table 4.3).

The quantum yield of $^1O_2$ generation was also measured by UV-vis spectroscopy to further complement the EPR findings. UV-vis is a common indirect method for determining the quantum yield of $^1O_2$ generation and is carried out using a chromophore that reacts directly with $^1O_2$, which is monitored by the decrease in absorbance.[29-32] Typical $^1O_2$ quenchers for detection by UV-vis include 9,10-diphenylanthracene and 1,3-diphenylisobenzofuran, which are known to absorb and generate $^1O_2$ at the same wavelength as the host **1** sensitizer (~360 nm).[29-32] Thus, we selected 1,4-dimethylnaphthalene (DMN), a $^1O_2$ trap that absorbs at higher energy wavelengths (~290 nm) than the 360 nm required for **1**. A 2.86 mM stock solution of quencher was prepared and activated host **1** (1.1 mg, 0.13mM) was suspended in the stock solution and sealed under pure O_2. The sample was UV-irradiated with stirring in a room temperature water bath and UV-vis carried out at over time.

Figure 4.3 shows the decrease of the DMN absorbance signal with time of irradiation, indicating that the DMN reacts with $^1O_2$ to form its corresponding endoperoxide product, which does not absorb in this region. The $^1O_2$ quantum yield ($\Phi[^1O_2]$) was determined by plotting the difference between each absorbance signal versus time and obtaining the slope of each plot using the quation $\Phi[^1O_2]^{sample} = \Phi[^1O_2]^{ref}(m^{sample}/m^{ref})$ where methylene blue was used as the reference ($\Phi[^1O_2]^{ref} = 0.52$ in $CHCl_3$), m^{sample} is the slope of the host plot, m^{ref} is the slope of the methylene blue plot. From these data, we calculated the

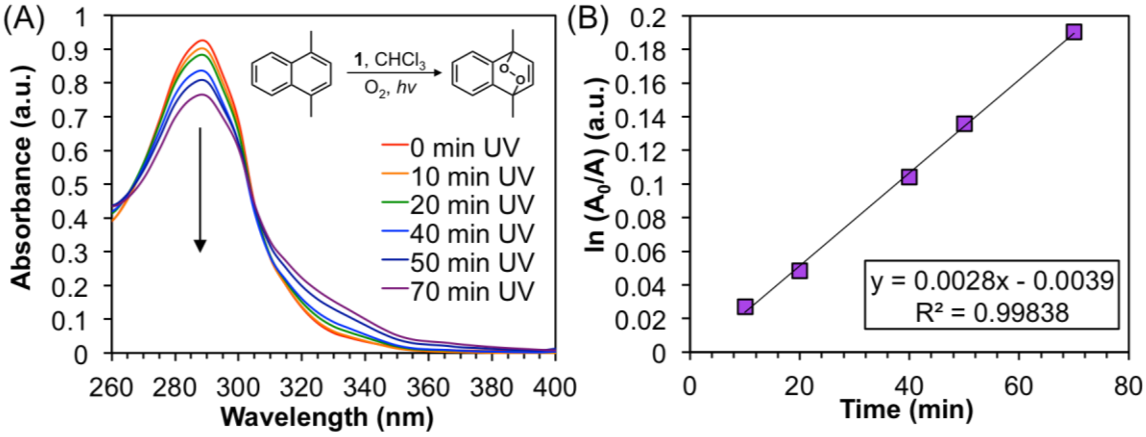

Figure 4.3. Indirect quantification of the quantum yield of $^1O_2$ generation by host **1** by monitoring the absorption loss of DMN. (A) An oxygen-saturated solution of DMN was irradiated in the presence of host **1** and the absorbance spectra was recorded over time to monitor the loss of DMN. (B) Area of UV absorbance plotted versus time of UV-irradiation for host **1**.

$\Phi[^1O_2]^{\text{host } \mathbf{1}}$ to be 12% in $CHCl_3$ via UV-vis spectroscopy.[31,32] We note that 1,4-dimethylnaphthalene-1,4-endoperoxide has a half-life ($t_{1/2}$) of 5 hours at 25 °C and can serve as a chemical source of $^1O_2$[33,34] however this $^1O_2$ release was relatively low on the timescale of our quantum yield measurements. Furthermore, it is not surprising that the $\Phi[^1O_2]$ varies between the two techniques, as they show different sensitivity.[29] Given these results, we conclude the host generates low quantities of $^1O_2$ with $\Phi[^1O_2]^{\text{host } \mathbf{1}}$ ranging from 1-12%. The low $^1O_2$ quantum yield could be advantageous for suspended host catalytic studies, as it may encourage oxidations to occur within the confines of the host channels as opposed to free in solution.

What is the lifetime of $^1O_2$ at the air-solid interface? The lifetime of $^1O_2$ (τ_Δ) is influenced by its local environment, especially when comparing its lifetime in air to its lifetime in solution.[35,36] This is because $^1O_2$ is known to undergo physical (or chemical) quenching as a result of its medium.[37,38] Previously, high selectivity was reported for the photooxidation of 2-methyl-2-butene in crystalline complexes with host **1**.[1] Thus, we next investigated the lifetime of $^1O_2$ at the air-solid interface of the host crystals. In the following phosphorescence studies, the lifetime reduction of $^1O_2$ by the **1**•DMSO complex and by triphenylphosphine (Ph_3P) were measured. Solid Ph_3P was used as a comparison because phosphines are well-known chemical quenchers of $^1O_2$ in the solution phase.[12] The lifetimes were then compared to the lifetime of $^1O_2$ in the presence of no solid. The **1**•DMSO complex was obtained through recrystallization of **1**. A series of quenchers were loaded in the channel including *N,N*-dimethyl aniline, pyridine, and *N,N,N',N'*-tetramethylethane-1,2-diamine (Table 4.3). For example, the host was activated by heating and the pyridine was loaded via vapor diffusion. The **1**•pyridine complex exhibited a host:guest ratio of 2:1.

Figure 4.4 shows the simplified experimental set up, in which an

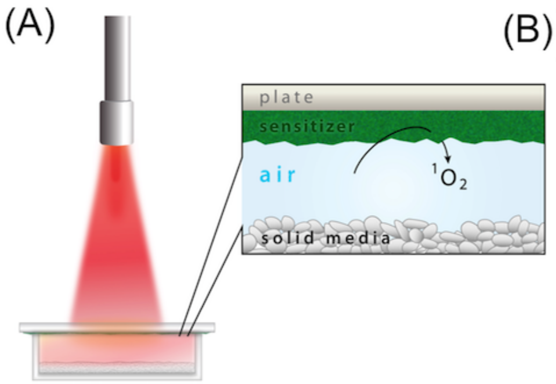

(B)

Entry	Sample	$\tau_{\Delta airborne}$(ms)
1	Pc plate	~0.15
2	**1**•DMSO + Pc plate	0.13±0.02
3	**1**•pyridine +Pc plate	0.12±0.06
4	Solid Ph_3P +Pc plate	0.10±0.03

Figure 4.4. Measurement of the $^1O_2$ lifetime at the air-solid interface. (A) Simplified experimental set up, consisting of a sensitizer plate used to generate singlet oxygen whose lifetime was measured by a photomultiplier tube through a 1270-nm bandpass filter. (B) Table of the experimental $^1O_2$ lifetimes obtained in this study.

apparatus was constructed to deliver airborne $^1O_2$ to a solid quenching agent. The reactor consisted of a sensitizing glass plate made by depositing Al(III) phthalocyanine tetrasulfonate (AlPcS) (~5 × 10^{-5} mol) onto the bottom side of a porous silica square (0.50 g, shape: 1.0 mm × 2.25 cm^2). A 0.8 mM solution of AlPcS in MeOH was deposited on the bottom face of the plate via slow evaporation. The glass plate was placed sensitizer-face down on top of a custom-made plate containing a well (sized: 1 mm × 1 cm × 1 cm). The solid trapping agent (10 mg) was placed in the well. The sensitizer plate was not in contact with the solid trapping agent and sat above it by 0.1 mm. A digital ruler with a precision of 0.01 mm was used to measure the distance between the sensitizer plate and the solid trapping agent in the well. The sensitizer plate was placed 3.0 cm below a terminus of a multimode FT-400-EMT optical fiber with an SMA 905 connector (Thorlabs, Inc). The optical fiber was connected to a 630-nm light source from a Nd:YAG Q-switched laser pumping an optical parametric oscillator (OPO) producing 5-ns ~0.2 mJ/pulses. The output of the 630-nm light from the laser yielded incident photons in a Gaussian distribution upon the sensitizer plate. The $^1O_2$ luminescence was detected by a photomultiplier tube (H10330A-45, Hamamatsu Corp.) through a 1270-nm bandpass filter (FWHM = 15 nm). The $^1O_2$ luminescence signals were registered on a 600 MHz oscilloscope and the kinetic data for the $^1O_2$ lifetime ($\tau_{\Delta \mathrm{airborne}}$) was determined by a least-squares curve-fitting procedure. The $^1O_2$ decay was observed in the 1270 nm phosphorescence upon irradiation of the sensitizer particles with 630 nm light. A slow component for the $^1O_2$ signal was observed (tenths of microseconds), which is attributed to airborne $^1O_2$ in the air gap between the sensitizer plate of origin and the solid trapping agents. A reduction of the $^1O_2$ lifetime ($\tau_{\Delta airborne}$) arises when the $^1O_2$ encounters the air/solid interface of the trapping agent.

The $^1O_2$ lifetime was observed in the 1270 nm phosphorescence range upon irradiation of the sensitizer particles with 630 nm light. We find the lifetime of airborne $^1O_2$ ($\tau_{\Delta airborne}$) generated by the apparatus to be ~150 µs and thus longer compared to $^1O_2$ solvated in benzene and toluene by ~5-fold (31 µs and 29 µs, respectively), and MeOH and ethanol by ~15-fold (10 µs and 13 µs, respectively).[39] The lifetime of $^1O_2$ in DMSO is 30 µs, but is reduced in pyridine (5.7 µs).[39] The total quenching rate constant (k_T) for Ph_3P is 8.5×10^6 M^{-1} s^{-1} and for other phosphines range from $0.1\text{-}2.0 \times 10^7$ M^{-1} s^{-1}.[40-42] The table in Figure 4 shows that the $\tau_{\Delta airborne}$ is reduced going from a sample absent of a solid trapping agent (~0.15 ms), to a sample containing solid host **1** (with DMSO or pyridine guests; 0.13 and 0.12 ms, respectively) and solid Ph_3P (0.10 ms). Other quenchers showed similar lifetimes (Figure 4.28). These data are in-line with quenching of $^1O_2$ in the solution phase. We attribute the decrease to be sensitive to factors such as the high oxophilicity of Ph_3P in solid-surface physical and chemical quenching. That is, once the $^1O_2$ was carried from the sensitizer plate to the air/solid interface of the solid host or solid Ph_3P, it was mainly physically quenched to $^3O_2$. In previous work, long and short $^1O_2$ lifetimes were found depending whether it resided within a gas bubble or in the bulk aqueous solution.[43] In a gas bubble, a $^1O_2$ lifetime of 0.98 ms has been previously observed.[43] Seeing that the lifetime of $^1O_2$ in air is decreased in the presence of the host in comparison to the Pc Plate or in a gas bubble, we wanted to next investigate ROS formation by the interior of the host.

Can host 1 be used as a catalyst to perform selective photooxidations in solutions? The oxidation of 1-methyl-1-cyclohexene (**2**) was used as a model reaction to test if host **1** can mediate its photooxidation in solution and in the solid state. Cyclohexene **2** is a good match for the size and shape of the host **1** channel and its oxidation has been studied with other sensitizers and nanoreactors. The Schenck "ene" reaction of **2** and $^1O_2$ in solution forms three key peroxides.[16,44-47] The proposed "ene" mechanism involves UV-irradiation of an oxygen-saturated solution of an alkene and a photosensitizer to first activate $^3O_2$ to $^1O_2$ through a triplet-triplet annihilation pathway. The alkene is thought to react with $^1O_2$ through a [2+2] cyclization step to form a perepoxide transition state, which subsequently undergoes ring opening to form peroxide-containing products that can be reduced to their corresponding alcohols.[45,47] With sensitizers (porphyrin or rose Bengal), photooxidations of **2** in solution forms three allylic alcohols products (Table 4.1, Entry 3-4, products **3**-**5**). Host **1** was employed under catalytic conditions in solution, where we were expecting similar products. The cycloalkene **2** (21 mM) was stirred in oxygenated $CHCl_3$ with host **1** (2 mg, 20 mol%). The suspensions were UV-irradiated for 18h and diluted with CH_2Cl_2 solutions of triphenylphosphine (21 mM) for rapid analysis. Relative conversion and selectivity were obtained by gas chromatography-mass spectrometry (GC-MS)

Table 4.1. Product Distributions in Photosensitized Oxidation of Alkenes.

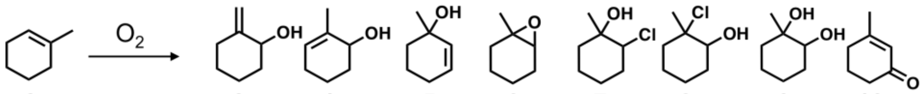

2 3 4 5 6 7 8 9 10

Entry	Conditions	% Conversion	% Selectivity							
1	Host **1** ($CHCl_3$)	92%	--	--	--	21%	24%	16%	--	--
2	Host **1** (solid-state)	97%	--	--	32%	--	--	--	13%	42%
3	RB (MeCN)[a]	60-70%	44%	20%	36%	--	--	--	--	--
4	Porphyrin($CHCl_3$)[b]	32%	42%	13%	45%					
5	Octa acid /RB[a]	60%	10%	--	90%	--	--	--	--	--
6	Na-Y / TPP[c]	~100%	88%	1%	2%	--	--	--	--	--
7	Fe(III)/SiO_2[d]	44%	--	--	--	2%	--	--	--	35%

[a]Rose-Bengal sensitized photooxidations irradiated for 4 h at rt, with octa acid nanocapsules (in D_2O) and without (in acetonitrile).[16] [b]tetraphenylporphyrin irradiated for 3 h at 0°C.[40] [c]tetraphenylporphrin-sensitized photooxidation in dichloromethane with zeolite irradiated for 1 h at rt.[41] [d]Oxidation catalyzed by Fe(III)/SiO_2 in acetonitrile for 10 hours.[47]

and the products were confirmed using standards and/or the NIST database and literature when applicable (Figures 4.24-2.27). Surprisingly, host **1** facilitated the high conversion of the alkene (92%) to afford three different products (Table 4.1, Entry 3): the epoxide **6** (21%) and two chlorohydrin constitutional isomers **7** (24%) and **8** (16%). Other minor products made up a total of 39% according to the GC trace consisting mainly of enones and ketones (Figure 4.24). Mechanistically, it is likely that the chlorohydrins arise from ring opening of epoxide **6**, or a related perepoxide, by the chloride anion. Epoxide-containing products have been reported in $^1O_2$ mediated photooxidations of cycloalkenes and are believed to be the result of either $^1O_2$ or radical pathways.[50] Literature reports the lifetime of $^1O_2$ as 207 μs in $CHCl_3$.[39] Our results suggest that both $^1O_2$ and $O_2^{\bullet-}$ are generated under these conditions. Subsequently, $O_2^{\bullet-}$ reacts with $CHCl_3$ to generate the chloride species, consistent with the EPR trapping experiments.[24] Thus, chlorinated solvents are not advisable for photooxidation reactions that generate significant amounts of $O_2^{\bullet-}$.

Next, we examined the reaction under similar conditions in benzene and benzene-δ_6 solutions, which do not react with $O_2^{\bullet-}$. The lifetime of $^1O_2$ in these solvents differs 25-fold, from 30 μs in benzene to 731 μs in the deutero benzene.[36] Aliquots (50 μL) of the reaction mixture were removed over time (4, 8, and 12 h), diluted into solutions of triphenylphosphine, and analyzed by GC-MS (Table 4.2). In general, the epoxide 6 was observed at all reaction times and similar selectivity was seen for two additional alcohols **3** and **5** (Figure 4.27). Both alcohols are commonly observed through a $^1O_2$ pathway and also reported under nanoconfinement (Table 4.1, entries 5 & 6).[16] Epoxide **6** has been observed in oxidations of **2** by enzyme P450 and by a fungal heme-thiolate protien.[48,49] Surprisingly, the 25-fold difference in $^1O_2$ lifetime did not significantly

Table 4.2. Product Distributions in Photosensitized Oxidation of Alkenes in Benzene overtime

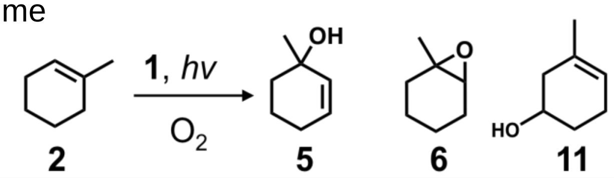

Time	% Conversion	% Selectivity		
		5	**6**	**11**
Benzene				
4	<1%	47%	21%	10%
8	35%	26%	23%	7%
12	40%	28%	29%	15%
Benzene-δ_6				
4	4%	31%	30%	5%
8	26%	25%	20%	6%
12	37%	25%	18%	11%

influence the conversion or product distribution. In summary, when employed as a suspended catalyst in solution, host **1** mediated solvent-dependent photooxidations and showed markedly different product distributions as compared with other triplet sensitizers.

To investigate the selectivity of this reaction within the nanochannels of host **1** in the solid-state, the activated host was equilibrated with **2** for at least 24 h. TGA of the host **1•2** complex displayed a one-step desorption from 25-80 °C with a weight loss of 8.2% (Figure 4.23 and Table 4.3). The host•guest stoichiometry was calculated from the weight loss and corresponded to a 2:1 host:guest ratio. Because the TGA indicates that alkene **2** slowly desorbs from the host at ambient temperature, all solid-state reactions were performed at lower temperatures (0 °C).

The crystalline complex (~16 mg) was UV-irradiated in a borosilicate vial saturated with oxygen for 5 h at 0 °C. After irradiation, the complex was immediately sonicated in a solution of triphenylphosphine (21 mM in THF) and analyzed by GC-MS (Table 4.1, entry 2). Compared with solution studies, the oxidation in the confined channels proceeds with higher conversion of **2**, 97% after 5 h vs ~ 30% after 8 h in solution. Three major products were formed: enone **10** (42%), tertiary alcohol **5** (32%), and diol **9** (13%). Unlike the solution studies, no epoxide was observed. The products enone **10** and diol **9** are not typically formed in photosensitized processes. In comparison, reaction of **2** in the Gibb's Octa Acid capsule favors the tertiary alcohol **5** with 90% selectivity at 60% conversion (Table 4.1, Entry 5).[16] While adsorption of **2** into a ZSM-5 zeolite results in the secondary allylic alcohol **3** with 88% selectivity (Table 4.1, Entry 6).[46] The unexpected diol **9** observed within our crystalline host has also been reported in the oxidation of **2** by enzyme P450.[48,51] Enone **10** has been observed in porous silica-supported iron complexes of **2** (Table 4.1, Entry 7) and is postulated to form when triplet oxygen binds with iron adhered silica nanoparticles to form a $O_2^{\bullet-}$ complex.[52] Based off of these products, we hypothesize that both ROS ($^1O_2$ and $O_2^{\bullet-}$) are produced within the channels of **1**. The difference in products observed in the crystalline host **1•2** complex versus in solution is striking and suggests a fundamental difference in the reaction mechanism.

4.3 CONCLUSIONS

In summary, we investigated ROS that were generated upon UV-irradiation of a porous BP *bis*-urea host in oxygenated solution as well as under an oxygen atmosphere in the solid-state. Overall, assembly of BP units into columnar structures reduces the production of ROS as compared to the parent BP in solution. While suspended in solution, the solid-state host was found to produce similar quantities of both $O_2^{\bullet-}$ and $^1O_2$. The quantum yield of $^1O_2$ production was estimated to be ~5% as determined by indirect methods. The detection of $O_2^{\bullet-}$ was found to be solvent-dependent, as it initiated degradation of $CHCl_3$ to form chloride species. Therefore, it is important to avoid the use of chlorinated solvents when examining the formation of $O_2^{\bullet-}$ by photosensitizers.

The lifetime of airborne $^1O_2$ was also examined at the air-solid outer surface of the host. Airborne $^1O_2$ was generated by a Pc-plate that was physically isolated from the host in the solid state. Minimal reduction in the lifetime of airborne $^1O_2$ was observed when it came in contact with the surface of host **1**. Experiments were carried out with quenchers loaded within the host **1** channels. However, all displayed similar lifetime of airborne $^1O_2$, suggesting that quenching is a surface phenomenon and this species does not access the channel interior under these conditions. Thus, we propose that ROS species involved in the air/solid reactions are primarily generated within the confined channels of the host.

Finally, photooxidation of cyclohexene **2** was used as a model reaction to probe utility of host **1**. First, host **1** was tested as a catalyst (20 mol %) in solution for the photooxidation reaction of **2** (21 mM) in $CHCl_3$, benzene, and benzene-δ_6. Despite a large variation of the $^1O_2$ lifetime from 30 μs to 731 μs in these solvents, catalytic trials with host **1** produced primarily epoxide-derived products. Interestingly, in $CHCl_3$ two chlorohydrins were also formed, which reflects degradation of the solvent by $O_2^{\bullet-}$. Studies in benzene afforded the epoxide and a tertiary allylic alcohol. The formation of the epoxide as a key product in the photooxidations reflects the proposed perepoxide transition state in $^1O_2$ mediated photoreactions.

In contrast, UV-irradiation of the crystalline host•guest complex in an oxygen atmosphere produced no epoxide and afforded the tertiary allylic alcohol with two surprising products, an enone and a diol. These are more typical of $O_2^{\bullet-}$ mediated enzymatic processes. Thus, we hypothesize that both $^1O_2$ and $O_2^{\bullet-}$ are produced within the channels of **1**. These represent key reactive species formed in the type I and type II mechanisms and it would be advantageous to be able to select a single ROS to direct more selective photooxidations. The reactions carried out in the air/solid and solution/solid interfaces suggest that selectivity arises mainly in the interior of the host. This is likely a result of confinement and/or limited mobility within the columnar channels in comparison to reactions carried out in solution. We are currently investigating the use of molecular dynamics to probe complexes of host **1** with $O_2^{\bullet-}$ and $^1O_2$ to see if these ROS species diffuse freely or adhere to the walls. We are also investigating conditions to favor control over the selectivity of ROS generation within the host channels as well as evaluating the scope of photooxidations mediated by **1**.

4.4 FUTURE WORK

Future work will focus on loading more guests inside the cavity and examining the photoreactivy. The photooxidations are the straightforward choice but photodimerizations and polymerizations could be explored within the confines of the nanochannels. Molecular dynamic computations are also of interest to determine if there is unique organization within the host channels that leads to the distinct selectivity. Finally, it is of interest to examine the photooxidations in flow, can we optimize the photooxidation process as a work around to the low amounts of host we are able to synthesize at any given time?

4.5 EXPERIMENTAL

GENERAL METHODS: All chemicals were purchased from Sigma Aldrich, VWR, or TCI Inc. and were used without further purification unless specified. ^{1}H-NMR spectroscopy in solution was performed on a Bruker Avance III HD 300 NMR spectrometer. Samples were weighed out using a Mettler Toledo

XPE206DR milligram balance. UV-irradiation of host **1** was carried out in a Rayonet RBR-200 UV reactor at 350 nm using RPR-3500A lamps in borosilicate vials or in quartz tubes. Thermogravimetric analysis (TGA) was carried out using TA instruments SDT-Q600 at a rate of 4º/min from 25-180 ºC (unless otherwise specified) with 15 min isotherms before and after temperature increase. Absorption spectra were recorded on a Molecular Devices Spectramax M2. GC-MS was carried out using Thermo Scientific (Waltham, MA) TRACE GC Ultra gas chromatograph coupled to a TSQ Quantum GC triple quadrupole mass spectrometer. Electron ionization mass spectral data was acquired in full scan mode of the first quadrupole from 33 to 650*m/z*. Samples were splitless-injected (1 µL) and an Rxi-5ms column (30 m x 0.25 mm x 0.25 µm) from Restek Corporation was used for chromatographic separations. The GC inlet was maintained at 250 °C, with a helium flow rate of 1.2 mL/min. The transfer line and ion source were maintained at 280 and 200 °C, respectively. The GC oven was held at 35 °C for 2 min, then ramped to 100 °C at a rate of 5 °C/min, followed by a second ramp at 20 °C/min to a final temperature of 300 °C and held for 15 min.

EPR STUDIES: EPR experiments were performed using a Bruker EMX plus equipped with a Bruker X-band microwave bridgehead and Xenon software (v 1.1b.66). All spectra were recorded using identical parameters at a power of 1.589 mW and modulation amplitude of 1.0 G. The double integration to obtain peak areas was performed three times and averaged in the Xenon software. Samples were sealed under pure $^3O_2$(g) and UV-irradiated in Norell Suprasil Quartz EPR tubes.

AIRBORNE $^1O_2$ LIFETIME MEASUREMENTS: An apparatus was constructed to deliver airborne $^1O_2$ to a trapping agent at its air/solid interface. The reactor consisted of a sensitizing glass plate made by depositing Al(III) phthalocyanine tetrasulfonate (AlPcS) (~50 μmol) onto the bottom side of a 0.50 g porous silica square (shape: 1.0 mm × 2.25 cm^2). A methanol solution containing 0.8 mM of AlPcS was used to deposit the sensitizer on the bottom face of the plate, after which the methanol had evaporated after 0.5 to 1 day at 25 °C. The glass plate was placed sensitizer-face down on top of a custom-made plate containing a well (sized: 1 mm × 1 cm × 1 cm). Approximately 10 mg of solid trapping agent was placed in the well. The sensitizer plate was not in contact with the solid trapping agent and sat above it by 0.1 mm. A digital ruler with a precision of 0.01 mm was used to measure the distance between the sensitizer plate and the solid trapping agent in the well. The sensitizer plate was placed 3.0 cm below the terminus of a multimode FT-400-EMT optical fiber with an SMA 905 connector (Thorlabs, Inc). The optical fiber was connected to a 630-nm light source from a Nd:YAG Q-switched laser pumping an optical parametric oscillator (OPO) producing 5-ns ~0.2 mJ/pulses. The output of the 630-nm light from the laser yielded incident photons in a Gaussian distribution upon the sensitizer plate. The airborne $^1O_2$ luminescence was detected by a photomultiplier tube (H10330A-45, Hamamatsu Corp.) through a 1270-nm bandpass filter (FWHM = 15 nm). The airborne $^1O_2$ luminescence signals were registered on a 600 MHz oscilloscope and the kinetic data for the airborne $^1O_2$

lifetime ($\tau_{\Delta airborne}$) was determined by a least-squares curve-fitting with a nonlinear least-squares procedure in Origin Software.[43]

General Synthetic Procedure

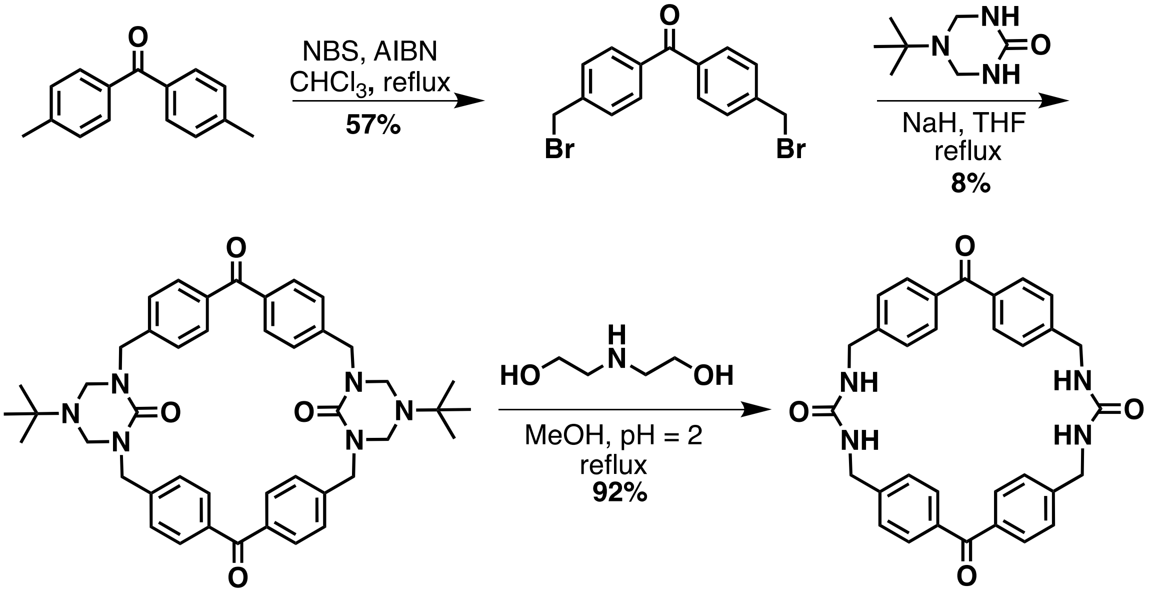

Scheme 4.2. Host **1** was synthesized as previously reported.[1-2, 18] Commercial 4,4'-dimethylbenzophenone was brominated with N-bromosuccinimide (NBS) using 2,2'-azobis(isobutyronitrile) (AIBN) as an initiator in $CHCl_3$ to yield 4,4'-bis(bromomethyl)benzophenone. The brominated benzophenone was then cyclized with triazinanone and NaH in refluxing THF to form the protected macrocycle, which was subsequently deprotected in an acidic diethanol amine aqueous/methanol mixture to afford the desired macrocycle **1**.

Preparation of Deprotection Solution: A mixture of diethanol amine (20 mL) and deionized water (50 mL) was adjusted to pH 2 via drop-wise addition of 12.1 N HCl. The pH was monitored via litmus paper.

Synthesis of 4,4'-bis(bromomethyl)benzophenone

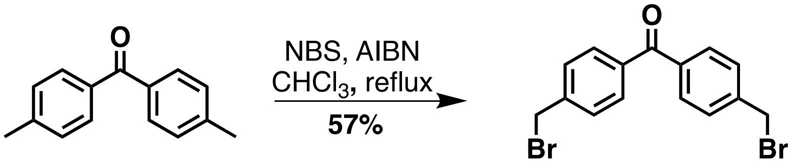

4,4'-dimethylbenzophenone (2.00 g, 9.51 mmol, 1 eq) was dissolved in chloroform (30 mL). Next, N-bromosuccinimide (NBS, 4.23 g, 23.8 mmol, 2.5 eq) and azobisisobutyronitrile (AIBN, 0.01 g, 0.06 mmol, 0.01 eq) were added, and the reaction mixture was heated at reflux under N_2 for 18 h. Excess AIBN (~2 mg) and NBS (~30 mg) were added to the reaction mixture, which was stirred for a further two hours to push the reaction to completion. The reaction was cooled to room temperature and succinimide was extracted with DI water (3x50mL) and the chloroform layer was dried under $MgSO_4$. Silica gel was added, and the solvent was removed under vacuum and loaded onto a silica gel column packed with hexanes. The product was isolated via column chromatography mixture as the last spot to yield a white solid, the column was performed using a gradient of hexanes and ethyl acetate, beginning with pure hexanes and slowly tapering to a 9:1 hexanes: ethyl acetate mixture (57%). ^{1}H-NMR: (300 MHz; $CDCl_3$) δ=7.78 (4H, d, *J*=8.1), 7.51(4H, d, *J*=8.4), 4.54 (4H, s).

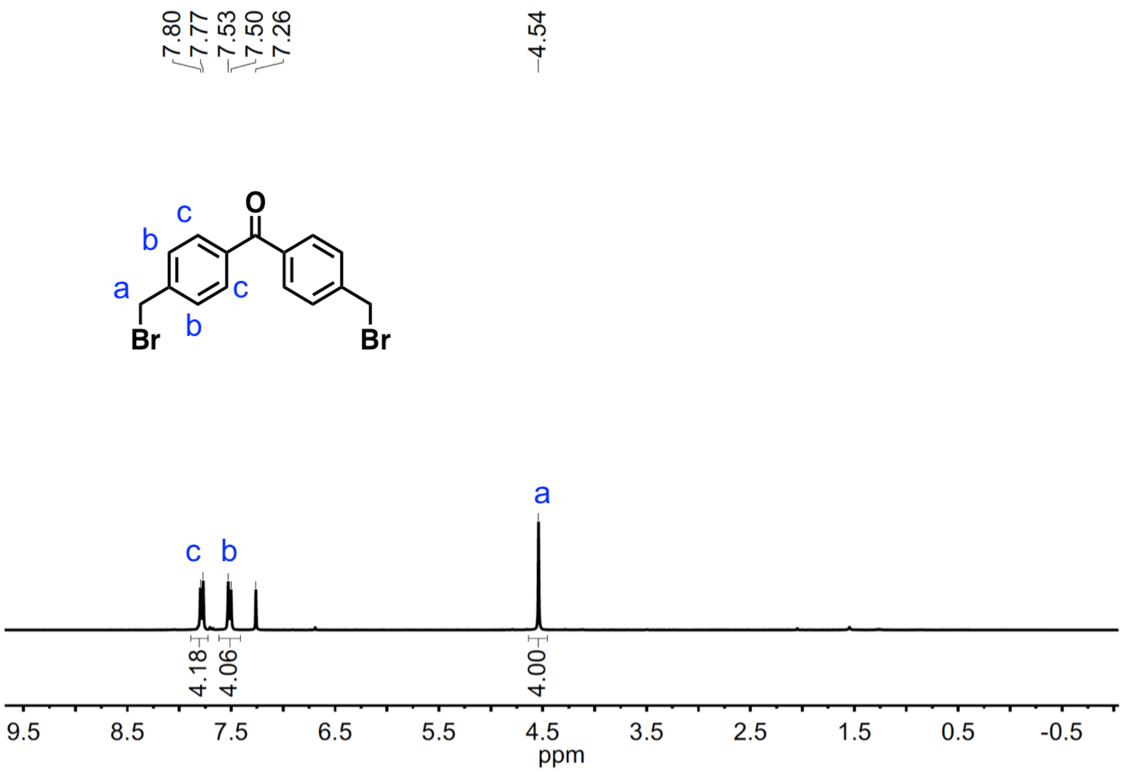

Figure 4.5. ^{1}H NMR of 4,4’-bis(bromomethyl)benzophenone in $CDCl_3$.

Synthesis of protected *bis*-urea benzophenone macrocycle 1

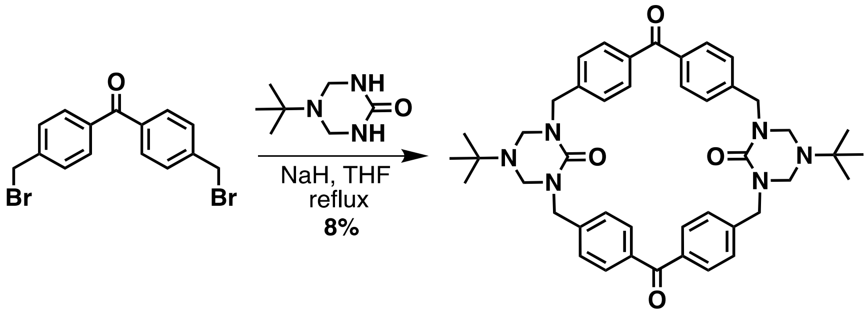

To a dry round bottom flask, still-dried THF (400 mL) was added. Next, triazinanone (0.86 g, 5.43 mmol) and NaH (60 % suspension in mineral oil, 0.88 g, 21.72 mmol) were added. The mixture was heated to reflux under N_2 atmosphere for two hours. The suspension was cooled to room temperature and a solution of 4,4’-bis(bromomethyl)benzophenone (2.01 g, 5.43 mmol in dry THF

(100 mL) was added to the stirring mixture all at once. The mixture was then heated to reflux for 48 h. Next, the reaction mixture was cooled to room temperature, neutralized with 1N HCl (~10 mL), and diluted with water (100 mL). THF was then removed under vacuum until an aqueous suspension remained. Crude product was extracted with methylene chloride (3 x 100 mL), washed with brine (150 mL), and dried with anhydrous Mg_2SO_4. Product was purified via flash silica gel column chromatography (9:1 ethyl acetate: methanol). Column fractions were left to evaporate for 3-7 days and a white precipitate was collected and dried under vacuum to yield a white solid. (0.16 g, 8%). ^{1}H-NMR (300 MHz, CD_2Cl_2) δ 7.81 (d, *J* = 8.3, 8H), 7.46 (d, *J* = 8.3, 8H), 4.65 (s, broad, 8H), 4.35 (s, 8H), 1.07 (s, 18H).

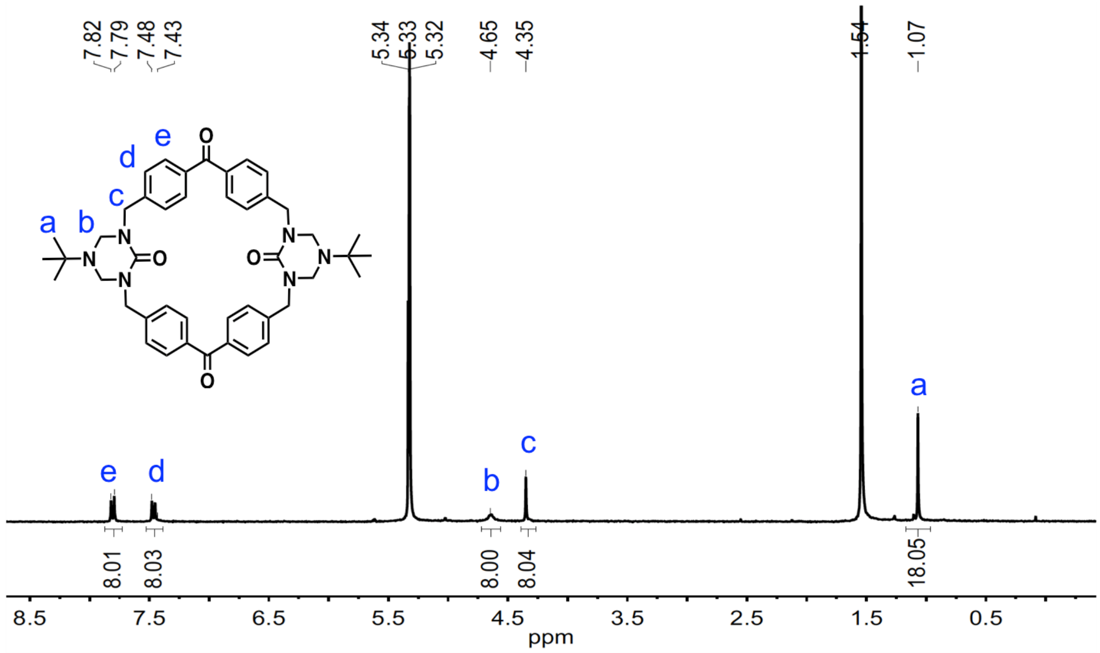

Figure 4.6. ^{1}H NMR of protected benzophenone *bis*-urea macrocycle **1** in CD_2Cl_2.

Deprotection of protected benzophenone *bis*-urea macrocycle (1)

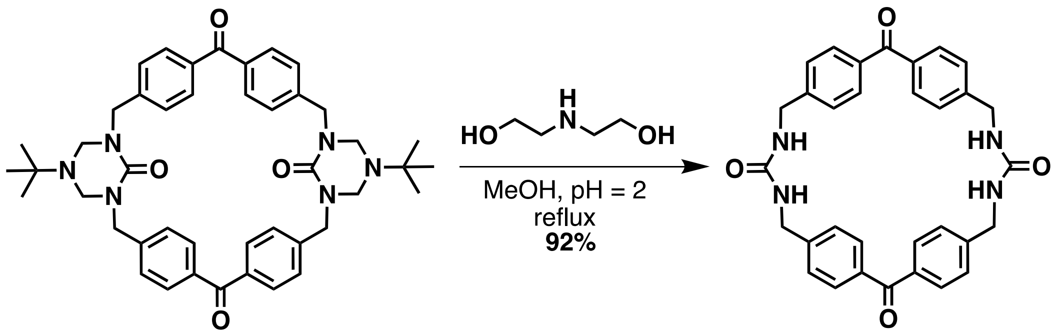

Triazinanone protected *bis*-urea benzophenone macrocycle (0.200 g, 0.28 mmol) was added to 1:1 v/v mixture of the deprotection solution (70 mL) and methanol (70 mL) was refluxed as a suspension for 48 h. The precipitate (varying in color from yellow to white) was collected via vacuum filtration and was washed with 1N HCl (20 mL), distilled water (3 x 100 mL), and dried under vacuum (0.135 g, 92%). ^{1}H-NMR (300 MHz, DMSO-δ6) δ 7.75 (d, *J*=8.3, 8H), 7.43 (d, *J*=8.3, 8H), 6.82 (t, *J*= 6.2, 4H), 4.38 (d, *J*= 5.9, 8H)

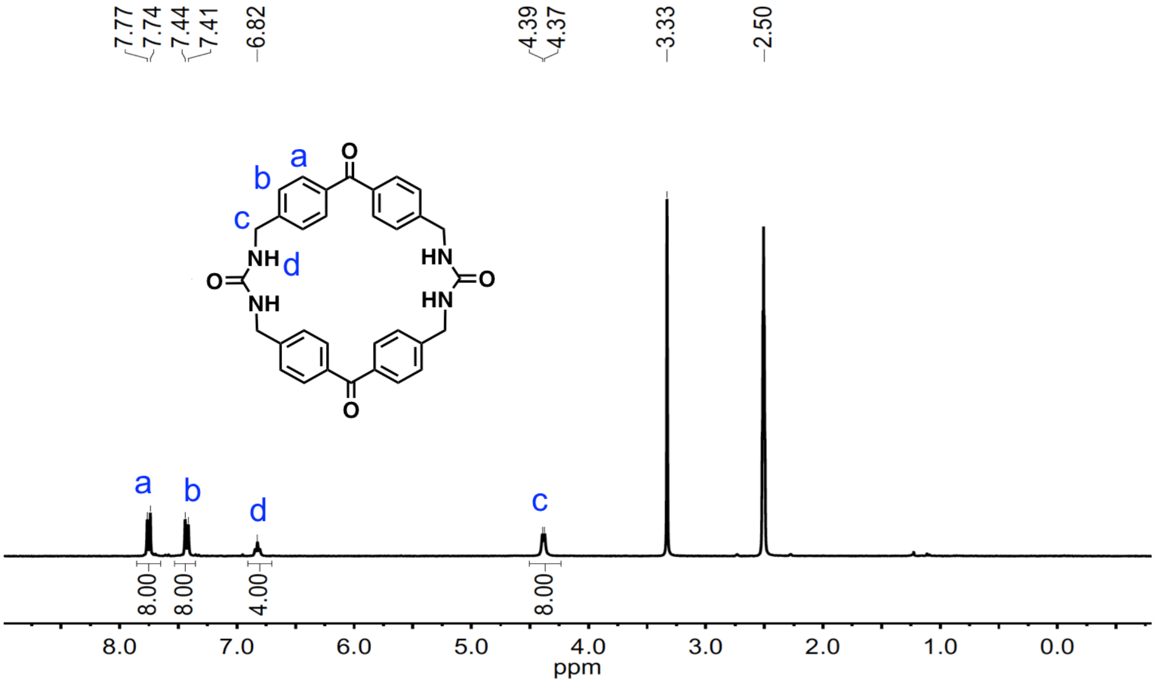

Figure 4.7. ^{1}H NMR of benzophenone *bis*-urea macrocycle **1** in δ6-DMSO.

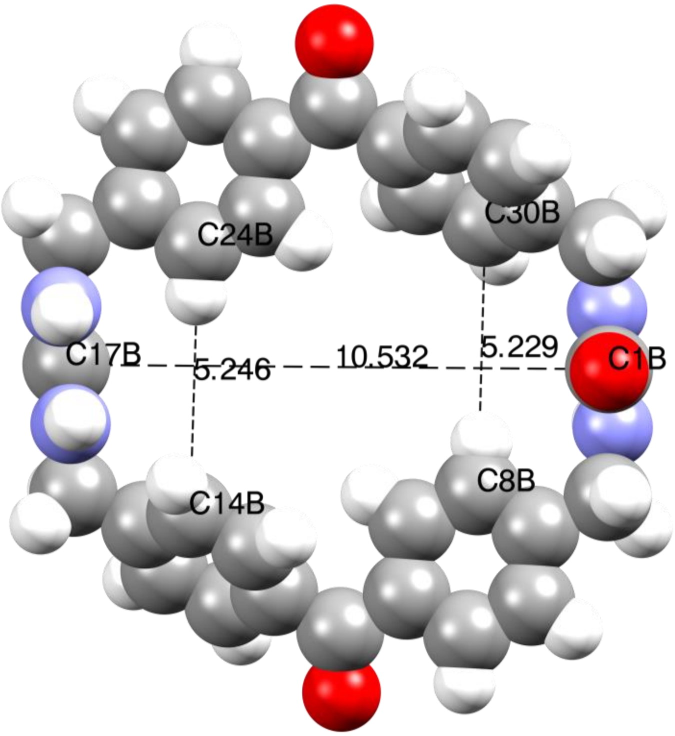

Figure 4.8. Space filling model of **1** obtained from the crystal structure[18] showing the dimensions of the host channels measured from carbon to carbon.

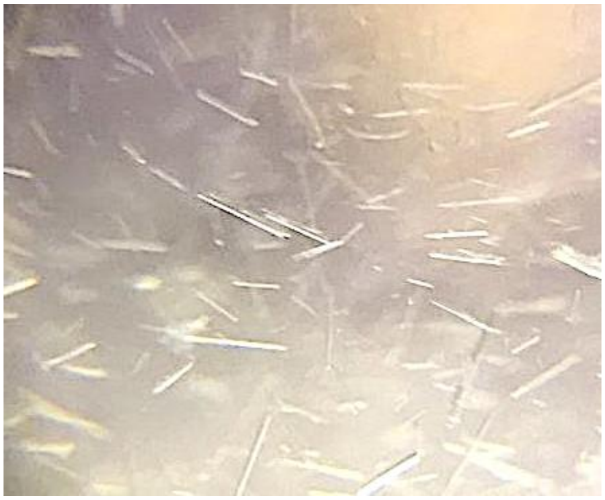

Figure 4.9. Self-assembly of macrocycle **1** results in the formation of needle-like crystals upon recrystallization in DMSO. Picture taken at 60x magnification with a LED pocket microscope.

Decolorization of DMPO using methanol

After the DMPO spin trapping study in chloroform the DMPO began to turn orange in color accompanied by a three line spectrum (a_N=15G), indicating the formation of a DMPO degradation product. Therefore, before the spin trapping study was carried out in methanol it was decolorized to remove the impurities. A traditional decolorization technique was carried out in methanol instead of water and produced similar results.[53] A 200 mM stock solution of DMPO was prepared by adding DMPO (22 μL) to a volumetric flask and was diluted to 1 mL with oxygenated methanol. Activated charcoal was added to the stock solution, which was decolorized by passing it through a 20μm syringe filter.

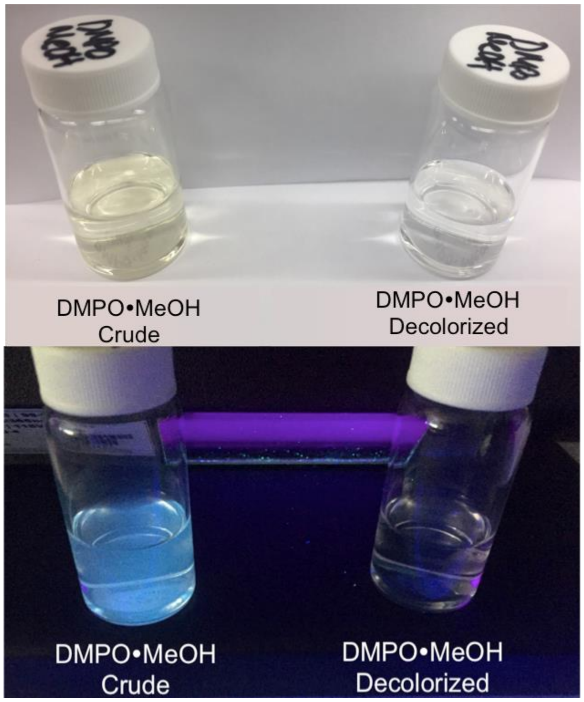

Figure 4.10. Decolorization of DMPO in MeOH, (Top) Solution before and after decolorization (Bottom) Sample under UV-light before and after decolorization.

Host 1 Superoxide Spin Trapping Experiment (Methanol)

Activated host **1** (0.11 mg, 0.2 μmol) was added to a Norell Suprasil quartz EPR tube. Next, the decolorized 200 mM stock solution of DMPO was further diluted to 20 mM into the EPR tube with oxygenated benzene using volumetric syringes. The EPR tube was further purged with oxygen for 2 minutes and sealed. An EPR spectrum was recorded pre-irradiation, the sample was then irradiated in a Rayonet UV reactor at 360 nm and EPR spectra were recorded over time.

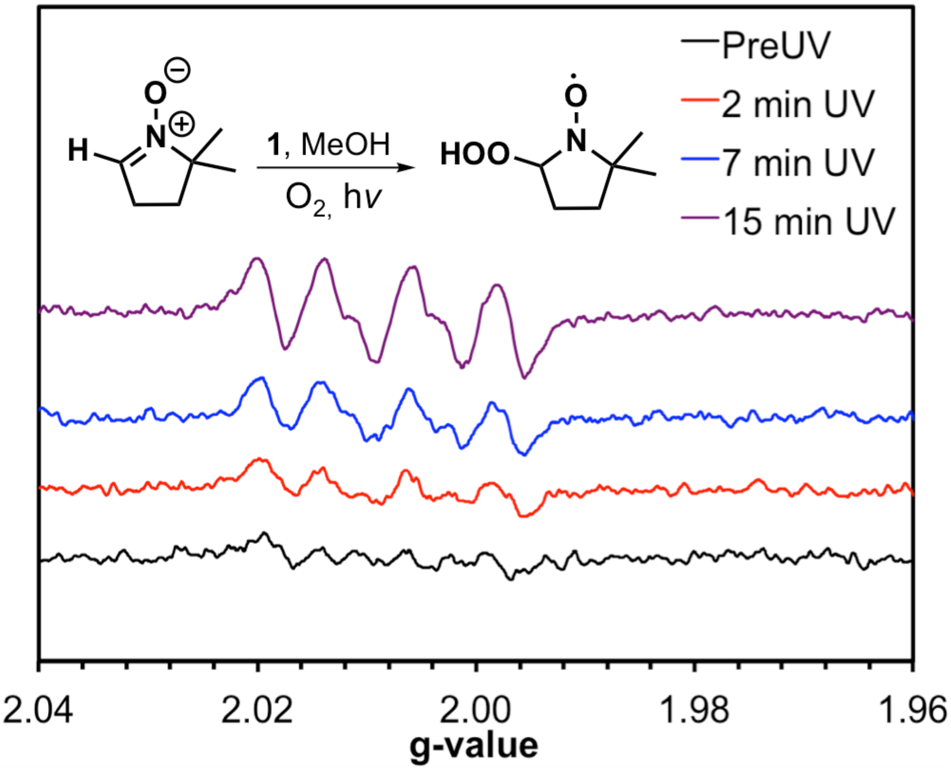

Figure 4.11. EPR spectra of host **1** in the presence of DMPO and methanol recorded over time of UV-irradiation.

Easy Spin simulation of DMPO adduct

The EPR spectrum obtained by the DMPO spin trapping experiment was simulated using the MATLAB EasySpin toolbox with the "garlic" package to account for the fast motion regime at 298K with a rotational correlation time of $1x10^{-8}$ seconds. The simulation is consistent with the formation of a DMPO adduct with an isotropic g-value of 2.0072 (PAS Components [2.0149, 2.0057, 2.0009]) and hyperfine splitting constants of a^N = 14.2 G and a^H = 9.2 G which is in range of typical DMPO-OOH adducts.

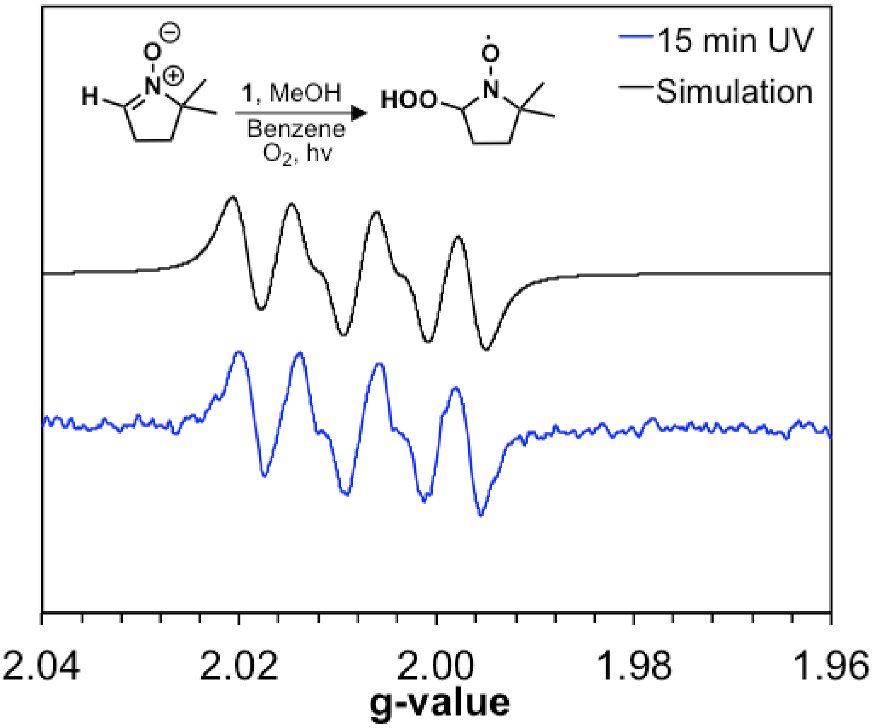

Figure 4.12. EPR spectral simulation (black line) of the DMPO adduct formed in the presence of host **1** and methanol recorded over time of UV-irradiation compared to the experimental spectra (blue line).

Benzophenone Superoxide Spin Trapping Experiment (Methanol)

Benzophenone (0.029 mg, 0.16 μmol) was added to a Norell Suprasil quartz EPR tube. Next, the 200 mM stock solution of DMPO was further diluted to 20 mM into the EPR tube with oxygenated benzene using volumetric syringes. The EPR tube was purged with oxygen for 2 minutes and sealed. An EPR spectrum was recorded pre-irradiation, the sample was then irradiated in a Rayonet UV reactor at 360 nm and EPR spectra were recorded over time. The EPR spectrum obtained by the DMPO spin trapping experiment was simulated using the same procedure on page 229. The simulation is consistent with the formation of a DMPO adduct with an isotropic g-value of 2.0076 (PAS Components [2.0159, 2.0060, 2.0009]) and hyperfine splitting constants of a^N = 13.8 G and a^H = 9.3 G which is in range of typical DMPO-OOH adducts.

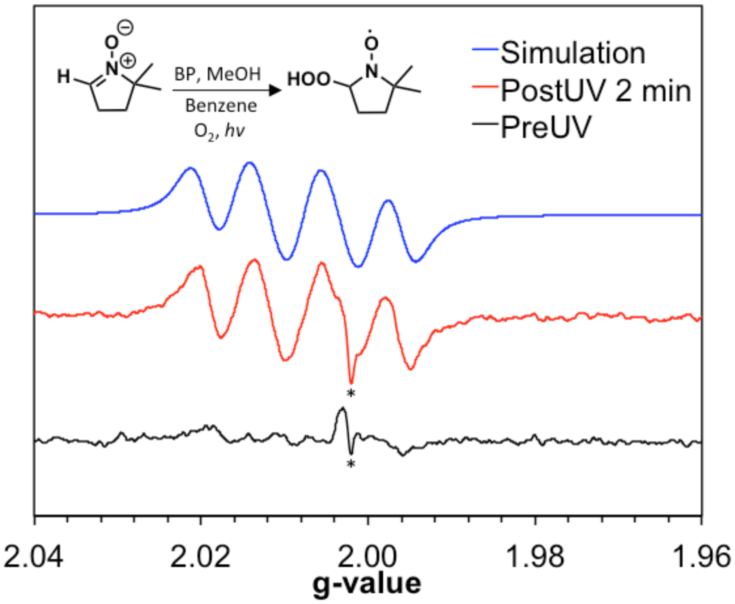

Figure 4.13. EPR spectral simulation (blue line) of the DMPO adduct formed in the presence of benzophenone and methanol recorded over time of UV-irradiation compared to the experimental spectra (red line). *indicates quartz EPR tube impurity at a g-value of 2.002.

Host 1 Superoxide Spin Trapping Experiment (Chloroform)

Host **1** (1.0 mg, 2.0 μmol) was added to borosilicate vial fitted with PTFE septum. A 0.0221 M solution of DMPO was prepared by adding DMPO (62 μL) to a 25 mL volumetric flask and diluted with chloroform. The DMPO solution was sparged under pure oxygen for 15 minutes, the volumetric flask was topped off with chloroform. The stock solution (20 mL) was added to the vial containing host **1** was added with a micro stir bar. The sample was irradiated for one hour with gentle stirring and aliquots of the DMPO solution (0.2 mL) were removed over time and EPR spectra were recorded. No DMPO adduct was formed after 1 hour of UV irradiation indicating that in polar aprotic solvents host **1** cannot form peroxides.

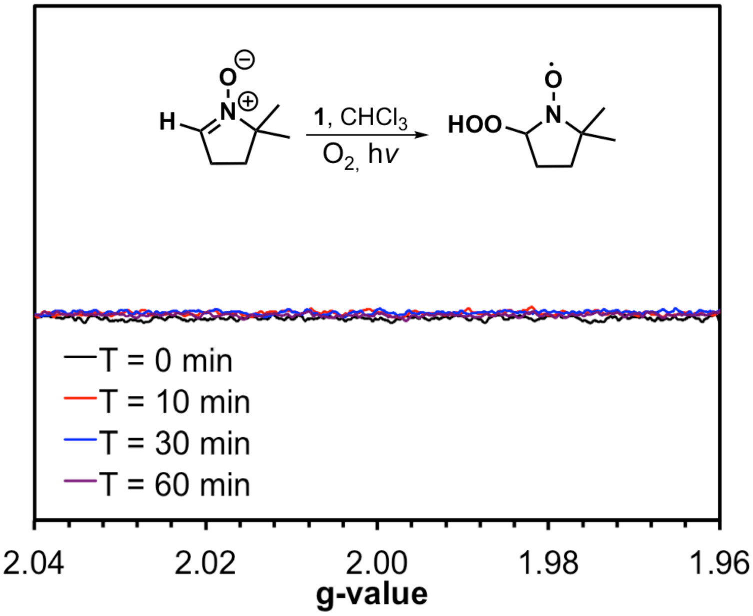

Figure 4.14. EPR spectra of host **1**•DMPO in chloroform recorded over time of UV-irradiation.

Benzophenone Superoxide Spin Trapping Experiment (Chloroform)

Benzophenone (0.7 mg, 3.8 μmol) was added to borosilicate vial fitted with PTFE septum. A 0.0221 M solution of DMPO was prepared by adding DMPO (62 μL) to a 25 mL volumetric flask and diluted with chloroform. The DMPO solution was sparged under pure oxygen for 15 minutes, the volumetric flask was topped off with chloroform. The stock solution (20 mL) was added to the vial containing benzophenone was added with a micro stir bar. The sample was irradiated for one hour with gentle stirring and aliquots of the DMPO solution (0.2 mL) were removed over time and EPR spectra were recorded. No DMPO adduct was formed after 1 hour of UV irradiation indicating that in polar aprotic solvents BP cannot form peroxides.

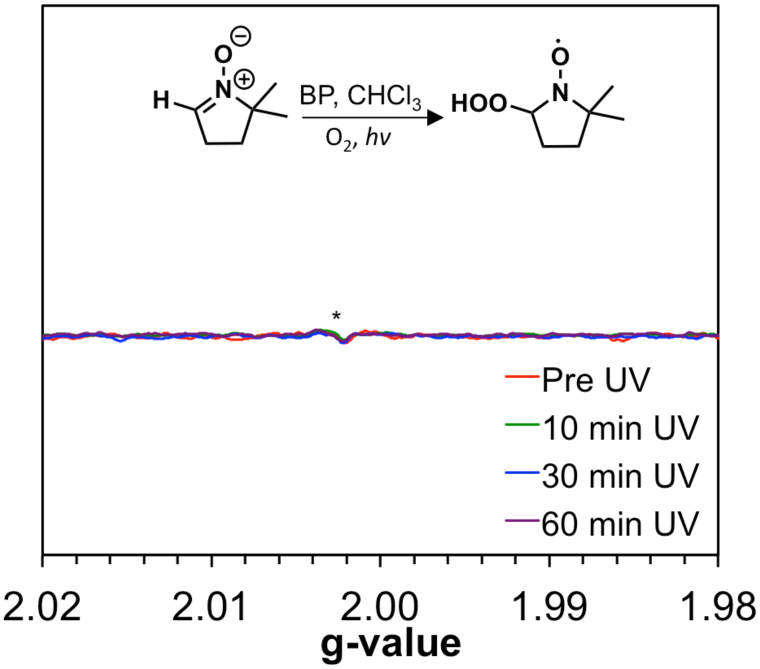

Figure 4.15. EPR spectra of BP•DMPO in chloroform recorded over time of UV-irradiation. *indicates a quartz EPR tube impurity at a g-value of 2.002.

Host 1 Singlet Oxygen Trapping Experiment (Chloroform)

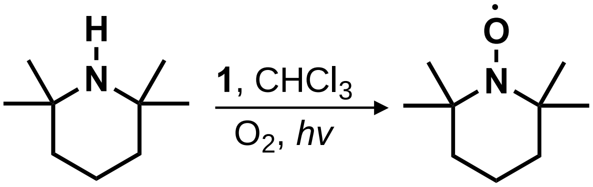

Host **1** (0.1±0.02 mg, 0.18 μmol) was added to a Norell Suprasil quartz EPR tube. A 2.9 mM stock solution of TMP was prepared by adding TMP (25 μL) to a 50 mL volumetric flask and was diluted with oxygenated chloroform. The stock solution (0.2 mL) was added to the EPR tube and sealed under oxygen. An EPR spectrum was recorded pre-irradiation and each sample was then UV irradiated and spectra were recorded over time. The sample was irradiated in a Rayonet UV reactor over time, resulting in the formation of the signature 3-line TEMPO signal.

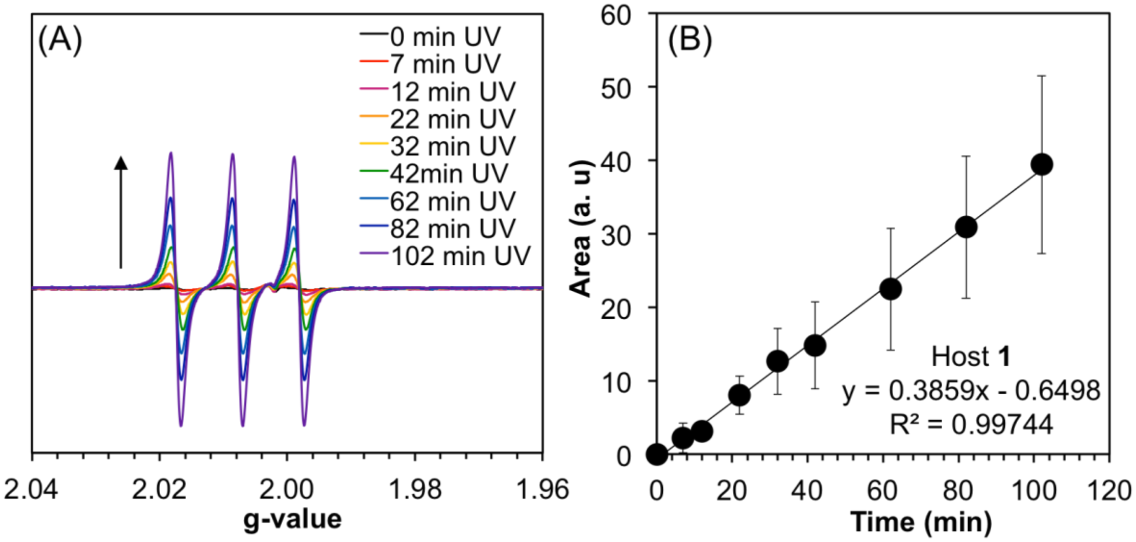

Figure 4.16. (A) EPR spectra of Host **1**•TMP in chloroform recorded over time of UV-irradiation showing the formation of the signature TEMPO EPR spectra. (B) Area of the TEMPO EPR spectra plotted versus time of UV-irradiation. The error bars represent the standard deviation between the triplicates.

Benzophenone Singlet Oxygen Trapping Experiment (Chloroform)

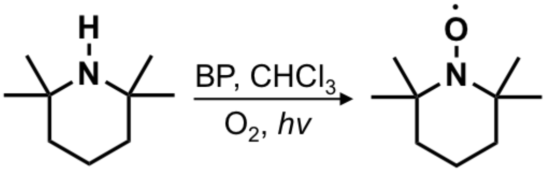

A 2.97 mM stock solution of TMP was prepared by adding TMP (25 μL) to a 50 mL volumetric flask and was diluted with oxygenated chloroform. The TMP stock solution (20 mL) was added to a 40 mL borosilicate vial with a PTFE septum followed by benzophenone (0.7 mg, 3.8 μmol). The solution was vortexed and oxygenated for 5 more minutes. The oxygenated solution (0.2 mL) was added to the EPR tube and was sealed under oxygen. An EPR spectrum was recorded pre-irradiation and each sample was then UV irradiated and spectra were recorded over time. The sample was irradiated in a Rayonet UV reactor over time, resulting in the formation of TEMPO.

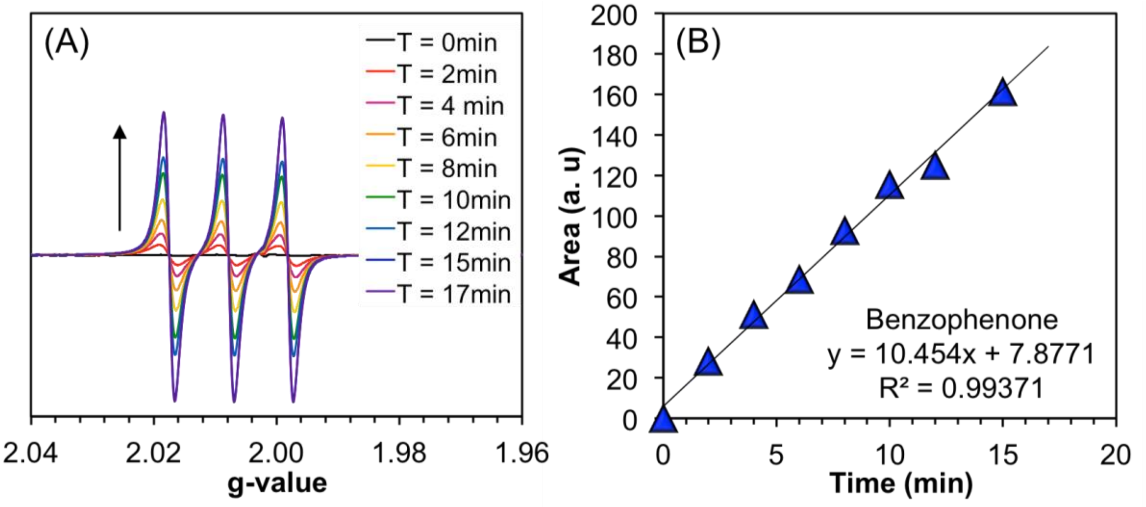

Figure 4.17. (A) EPR spectra of BP•TMP in chloroform recorded over time of UV-irradiation showing the formation of the signature TEMPO EPR spectra. (B) Area of the TEMPO EPR spectra plotted versus time of UV-irradiation.

Perinaphthenone Singlet Oxygen Trapping Experiment (Chloroform)

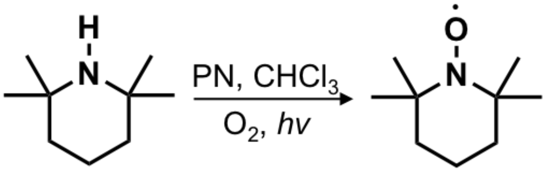

A 2.97 mM stock solution of TMP was prepared by adding TMP (25 μL) to a 50 mL volumetric flask and was diluted with oxygenated chloroform. The TMP stock solution (20 mL) was added to a 40 mL borosilicate vial with a PTFE septum followed by benzophenone (0.47 mg, 3.9 μmol). The solution was vortexed and oxygenated for 5 more minutes. The oxygenated solution (0.2 mL) was added to the EPR tube and was sealed under oxygen. An EPR spectrum was recorded pre-irradiation and each sample was then UV irradiated and spectra were recorded over time. The sample was irradiated in a Rayonet UV reactor over time, resulting in the formation of TEMPO.

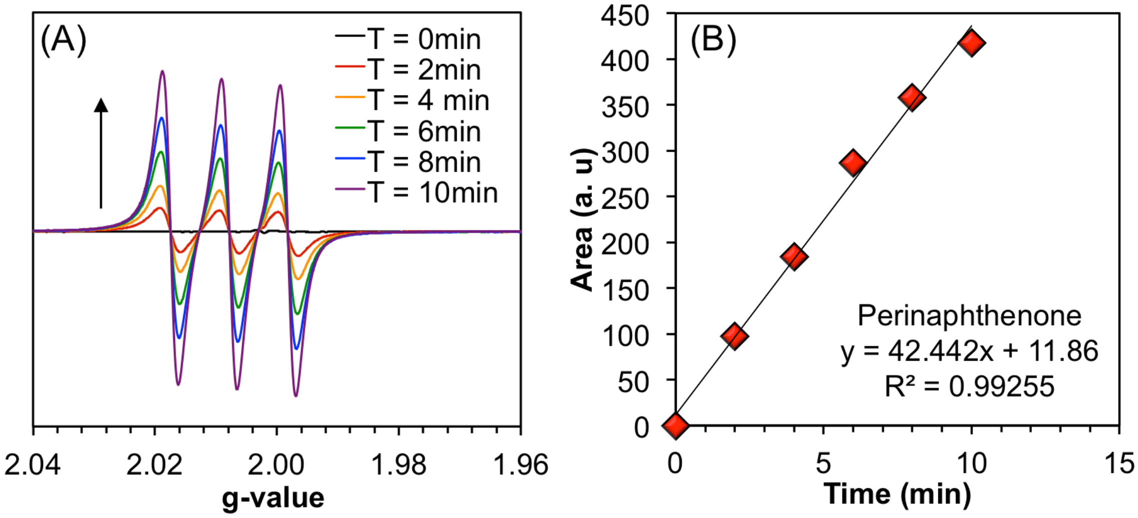

Figure 4.18. (A) EPR spectra of PN•TMP in chloroform recorded over time of UV-irradiation showing the formation of the signature TEMPO EPR spectra. (B) Area of the TEMPO EPR spectra plotted versus time of UV-irradiation.

Singlet Oxygen Quantum Yield Determination – EPR

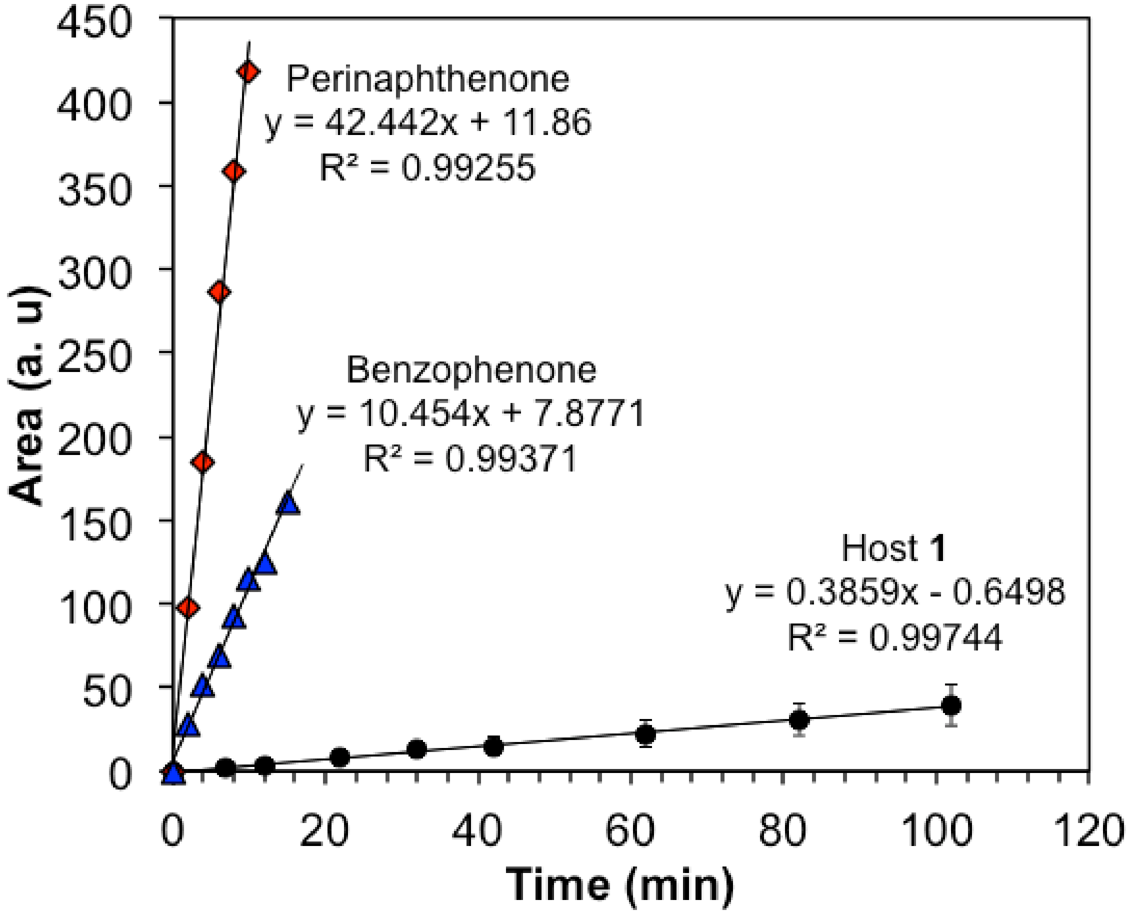

Figure 4.19. Comparison of area obtained in the formation of TEMPO for perinaphthenone, benzophenone, and host **1** spectra plotted versus time of UV-irradiation, the slopes were used to determine singlet oxygen quantum yield. Perinaphthenone was used as the reference.

$$\Phi[^1O_2]^{\text{host 1}} = \Phi[^1O_2]^{PN} \left(m^{\text{host }\mathbf{1}} / m^{PN}\right) \qquad \text{(Eq'n 4.1)}$$

$$\Phi[^1O_2]^{\text{host }\mathbf{1}} = 1\%$$

Where, $m^{\text{host }\mathbf{1}}$ = slope of host plot = 0.3859
m^{PN} = slope of reference plot = 44.442
$\Phi[^1O_2]^{PN}$ = quantum yield of reference = 0.97
$\Phi[^1O_2]^{\text{host 1}}$ = quantum yield of host **1**

Singlet Oxygen Quantum Yield Determination via UV-vis

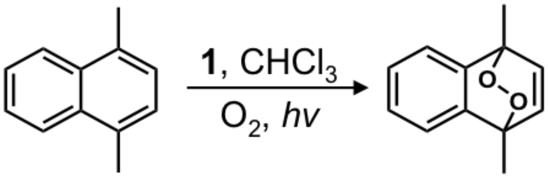

Activated host **1** (1.1 mg) was added to a stock solution of 1,4-dimethylnaphthalene in $CHCl_3$ (16 mL of a 2.86 mM soln) in a vial with septum and purged under an O_2 balloon for 10 minutes. The sample was UV-irradiated in a Rayonet reactor with gentle stirring in a room temperature water bath for 70 min. Samples (0.1 mL) were removed at 10 to 20 minute time intervals, diluted with $CHCl_3$ (1.9 mL) and monitored by UV-vis spectroscopy. Extra care was taken to ensure none of the host was removed from the reaction flask.

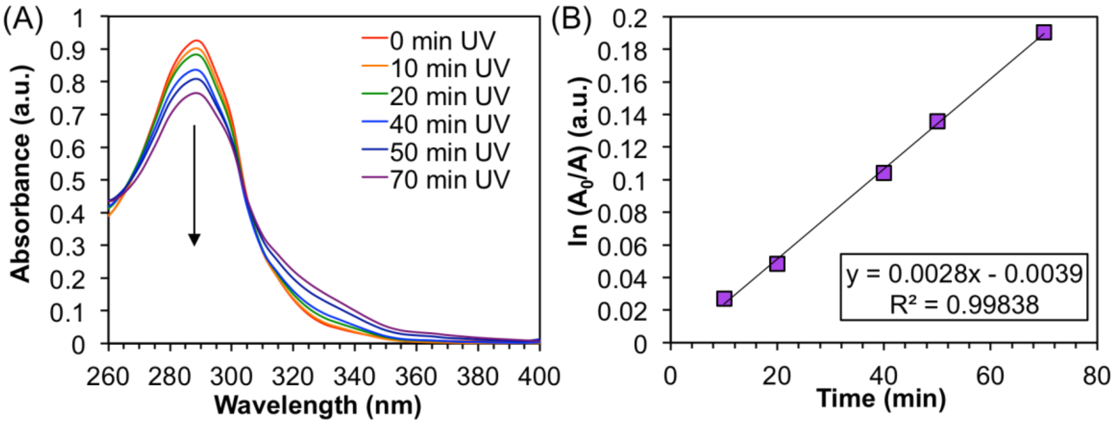

Figure 4.20. Singlet oxygen quantum yield determination of host **1** via UV-vis (A) Plot of DMN absorbance spectra over time of UV-irradiation. (B) Plot of DMN degradation versus time of UV- irradiation in presence of host **1**.

Singlet Oxygen Quantum Yield Determination via UV-vis

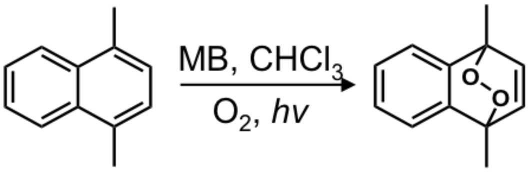

Methylene blue (0.6 mg) was added to a stock solution of 1,4-dimethylnaphthalene in $CHCl_3$ (16 mL of a 2.86 mM sol'n) in a vial with septum and purged under an O_2 balloon for 10 minutes. The sample was irradiated using a CFL 14W light bulb under gentle stirring in a room temperature water bath for 40 min. Samples (0.1 mL) were removed at 10-minute time intervals, diluted with $CHCl_3$ (1.9 mL) and monitored by UV-vis spectroscopy.

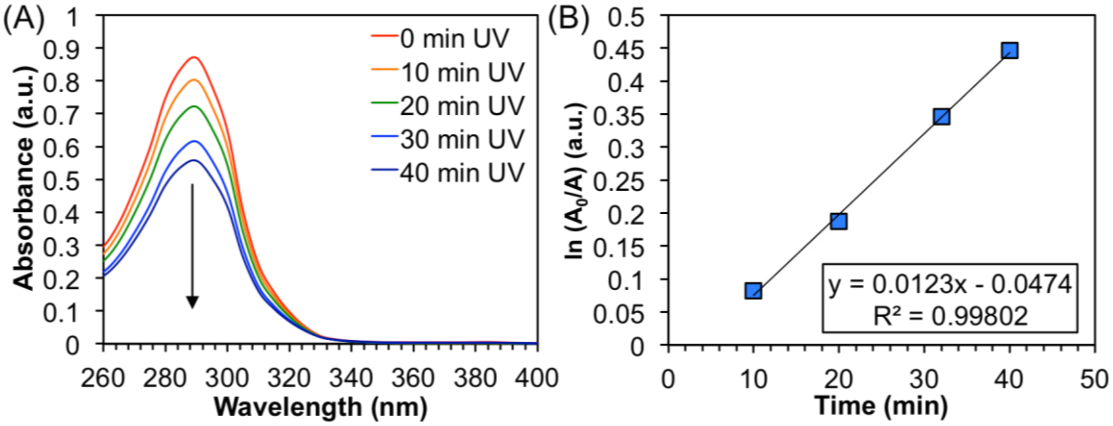

Figure 4.21. Absorption data for DMN quenching experiments sensitized by methylene blue. (A) Plot of DMN absorbance spectra over time of UV-irradiation. (B) Plot of DMN degradation versus time of UV- irradiation in presence of the reference methylene blue.

Singlet Oxygen Quantum Yield Determination via UV-vis

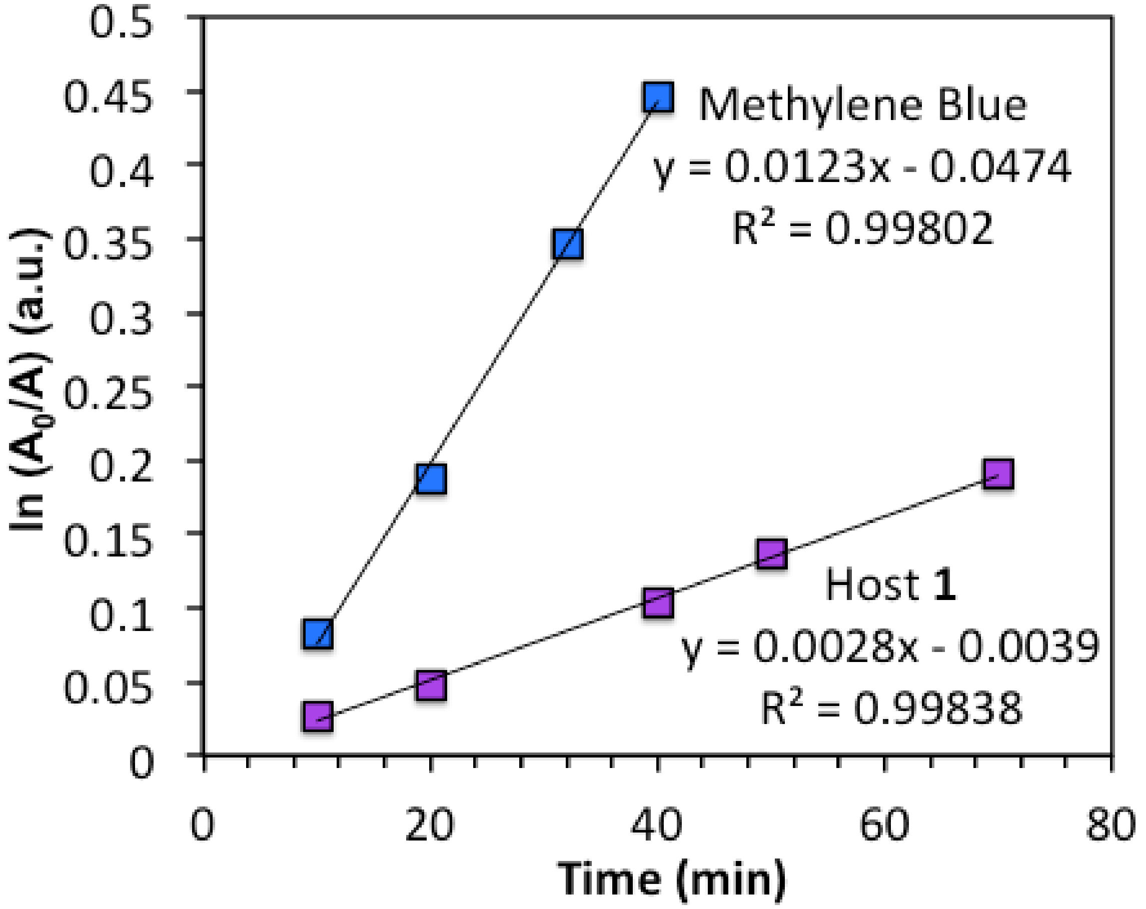

Figure 4.22. Comparison of absorptions obtained in 1,4-dimethylnaphthalene quenching experiment for methylene blue and host **1** spectra plotted versus time of UV-irradiation. The slopes were used to determine singlet oxygen quantum yield. Methylene blue was used as the reference.

$$\Phi[{}^1O_2]^{\text{host } \mathbf{1}} = \Phi[{}^1O_2]^{MB}\ (m^{\text{host } \mathbf{1}} / m^{MB}) \qquad \text{(Eq'n 4.2)}$$

$$\Phi[{}^1O_2]^{\text{host } \mathbf{1}} = 12\%$$

Where, $m^{\text{host } 1}$ = slope of host plot = 0.0028
M^{MB} = slope of reference plot = 0.0123
$\Phi[{}^1O_2]^{MB}$ = quantum yield of reference = 0.52
$\Phi[{}^1O_2]^{\text{host } \mathbf{1}}$ = quantum yield of host **1**

The host:guest ratio was determined using TGA using the following equation:

$$\boldsymbol{Host}:\boldsymbol{Guest}=\frac{\boldsymbol{mols\ of\ host}}{\boldsymbol{mols\ of\ guest}}\qquad\text{(Eq'n 4.3)}$$

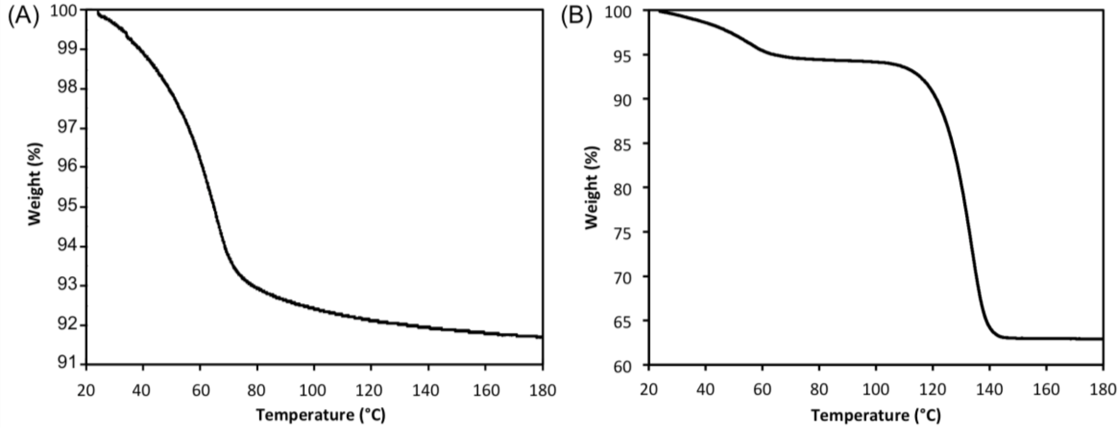

Figure 4.23. Thermogravimetric Analysis (TGA) plots were used to determine how well different guest load into host **1**. The TGA was heated at a ramp rate of 4 °C/min to 180 °C and show the removal of guest molecules from the host. Most guests displayed 1-step desorption curves. (A) TGA of the host **1•2** complex shows a one-step desorption with a weight loss of 8.2% from 20-80°C which is attributed to the loss of the alkene from the host channels. The host:guest stoichiometry was calculated from the weight loss using Eq'n 3 to be 2:1. (B) TGA of the host **1**•DMPO complex exhibited a two-step desorption curve from 20 to 140°C with a total weight loss of 37.1%. NMR suggests that the first desorption step accounts for the loss of water. The second step is attributed to the loss of DMPO which accounted for 31.3% of the weight loss, from which the host:guest stoichiometry was calculated to be 1:2. The following guests loaded were loaded: dimethylsulfoxide (DMSO), 1-methyl-1-cyclohexene (**2**), 2,2,6,6-tetramethyl piperidine (TMP), 5,5-dimethyl-1-pyrroline N-oxide (DMPO), pyridine, N,N-dimethylaniline(DMA), and N,N,N',N'-tetramethylethylenediamine (TMEDA).

Table 4.3. Host:Guest ratios calculated from TGA desorption curves.[a]

Entry	**Sample**	**Desorption Curve**	**Temperature Range (°C)**	**% Weight Loss**	**Host:Guest**
1	**1**•DMSO	1-step	45 - 145°C	12%	1:1
2	**1•2**	1-step	20 - 80°C	8.2%	2:1
3	**1**•TMP	N/A	N/A	N/A	1:0
4	**1**•DMPO	2-step	20 - 140°C	31.3%	1:2
5	**1**•pyridine	1-step	20 - 160°C	6.6%	2:1
6	**1**•DMA[b]	2-step	20 - 180°C	11.7%	2:1
7	**1**•TMEDA	1-step	20 - 128°C	8.2%	2.5:1

[a] TGA samples heated at a ramp rate of 4 °C/min to 180 °C unless otherwise specified. [b]Heated to 200°C.

Photooxidation Procedures: Recrystallized needles of 1 were activated using TGA before any photooxidations were carried out.

Catalytic Reactions: To borosilicate vials, emptied host (2.0±0.1 mg) was added followed by oxygenated solvents that were purged for 15 minutes under pure oxygen (benzene or chloroform, 1.0 mL). Next, 1-methyl-1-cyclohexene (2.5 μL) was added to each vial, which were sealed under oxygen and parafilmed. The samples were irradiated in a Rayonet reactor with gentle agitation. Following irradiation samples were tested for peroxides and quenched with triphenylphosphine. The samples were diluted with dichloromethane and examined with GC-MS.

Solid-state Reactions: 1-Methyl-1-cyclohexene was allowed to vapor load into host 1 (16.0±1 mg) for at least 24 hours. Next, each sample was cooled in a dry-ice/acetone bath and purged under pure oxygen for 15 minutes and parafilmed. The samples were irradiated for 5 hours with a Hanovia 450W medium pressure mercury arc lamp cooled in a quartz emersion well at 0 °C. Following irradiation, samples were extracted into triphenylphosphine-saturated tetrahydrofuran with sonication. The samples were diluted with dichloromethane and examined with GC-MS.

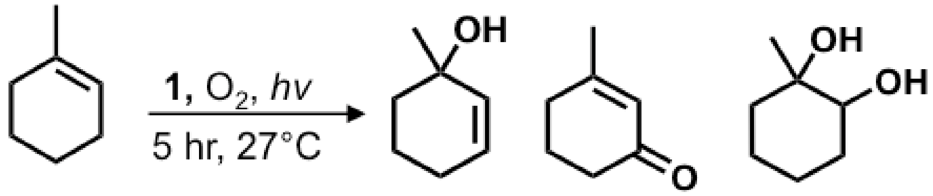

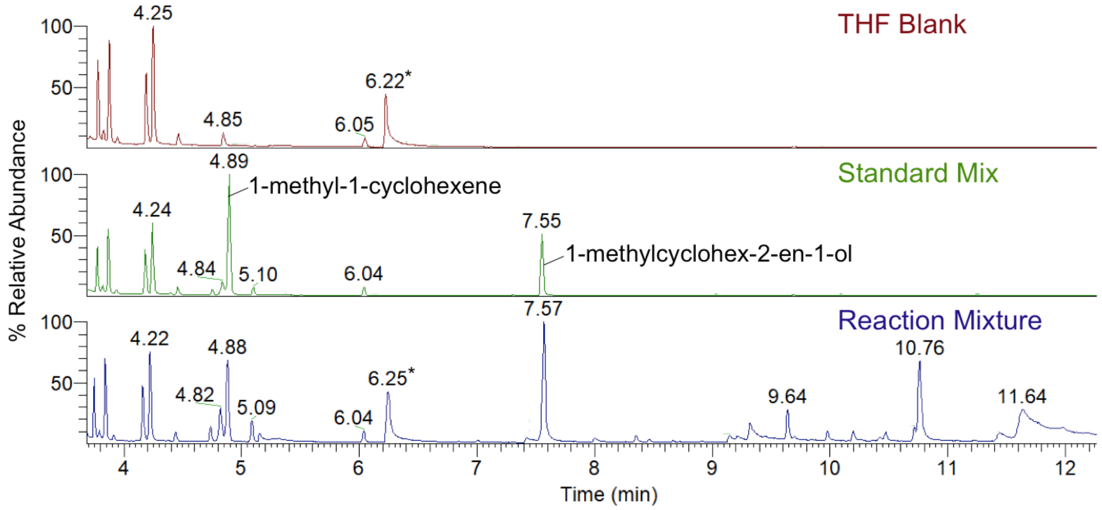

Figure 4.24. GC trace of **2** photooxidation carried out as a solid-state complex within **1** as the photosensitizer. Top: THF Blank. Middle: 1-methyl-1-cyclohexene (**2**) and 1-methyl-cyclohex-2-en-1-ol (**5**) standards. Bottom: the reaction mixture of extracted products. *DMSO contamination.

Host 1 photoxidation of 1-methyl-1-cyclohexene in chloroform

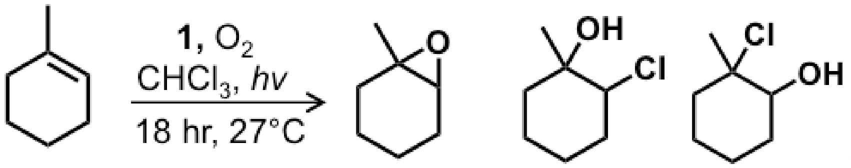

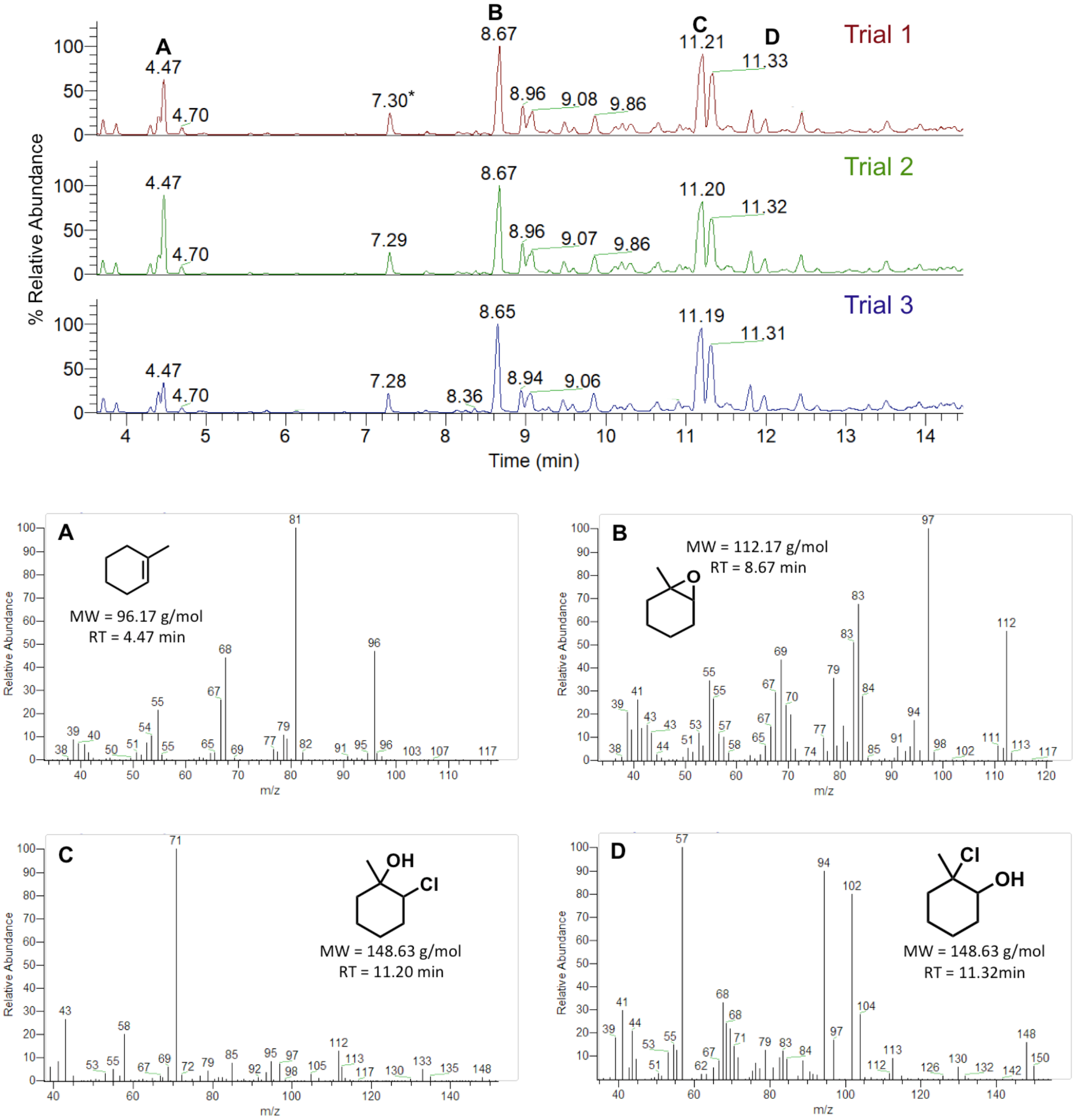

Figure 4.25. GC-MS data for the photooxidation of **2** sensitized by host **1** and carried out in chloroform. Top: GC-trace of products extracted diluted into dichloromethane (triplicates). Bottom: mass spectra of key materials: (A) starting material **2**, (B) epoxide **6**, (C) chlorohydrin **7**[54], and (D) chlorohydrin **8**[54]. *1-Methylcyclohex-2-en-1-ol (**5**) was also formed, but not as a major product, and co-elutes with cyclohexanone.

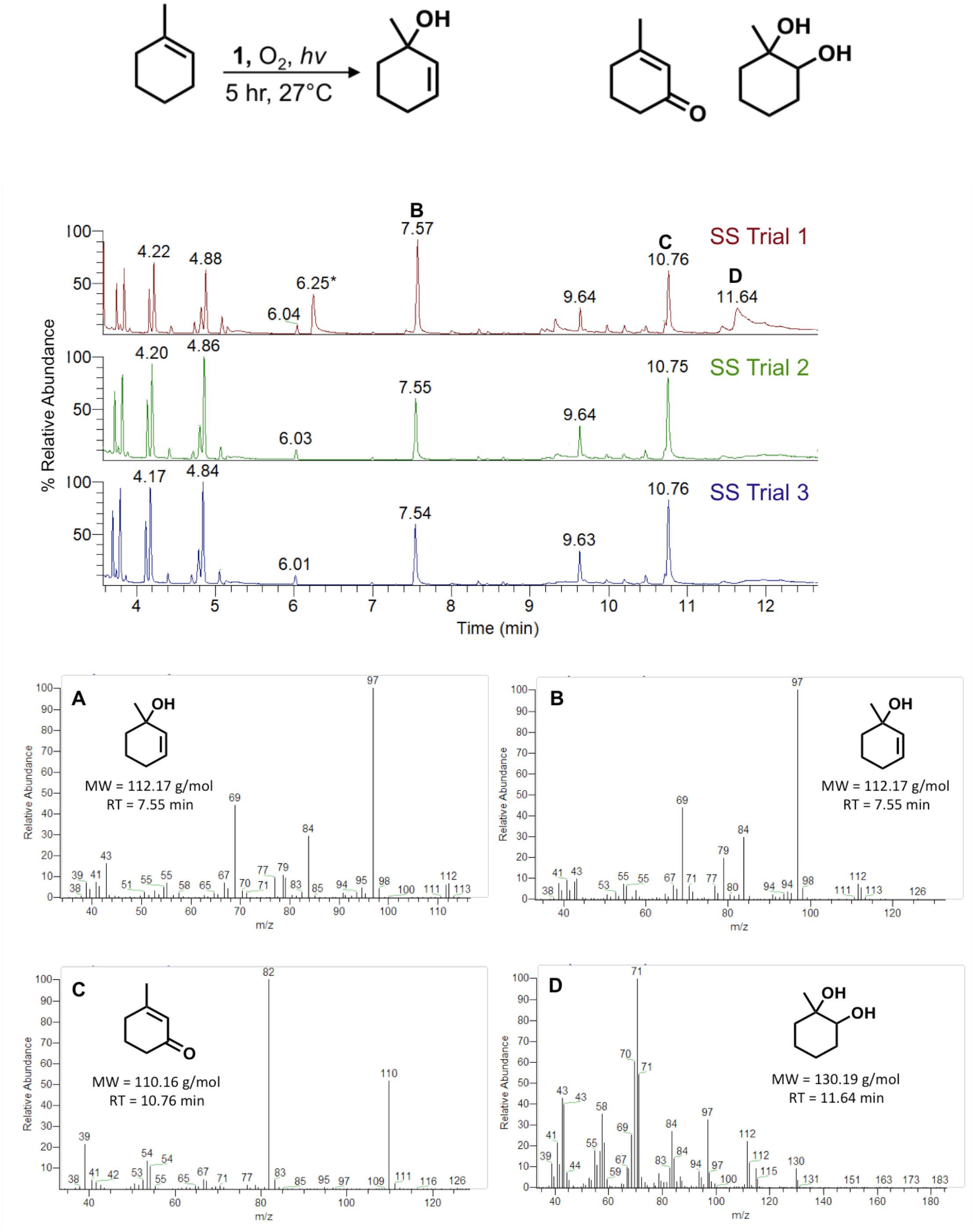

Figure 4.26. GC-MS data of **2** photooxidation carried out as a solid-state complex within **1** as the photosensitizer. Top: GC-trace of products extracted into THF. Bottom: mass spectra of key materials; (A) standard of tertiary alcohol **5**, (B) tertiary alcohol **5**, (C) enone **10**, and (D) diol **9**.

Host 1 photoxidation of 1-methyl-1-cyclohexene in benzene

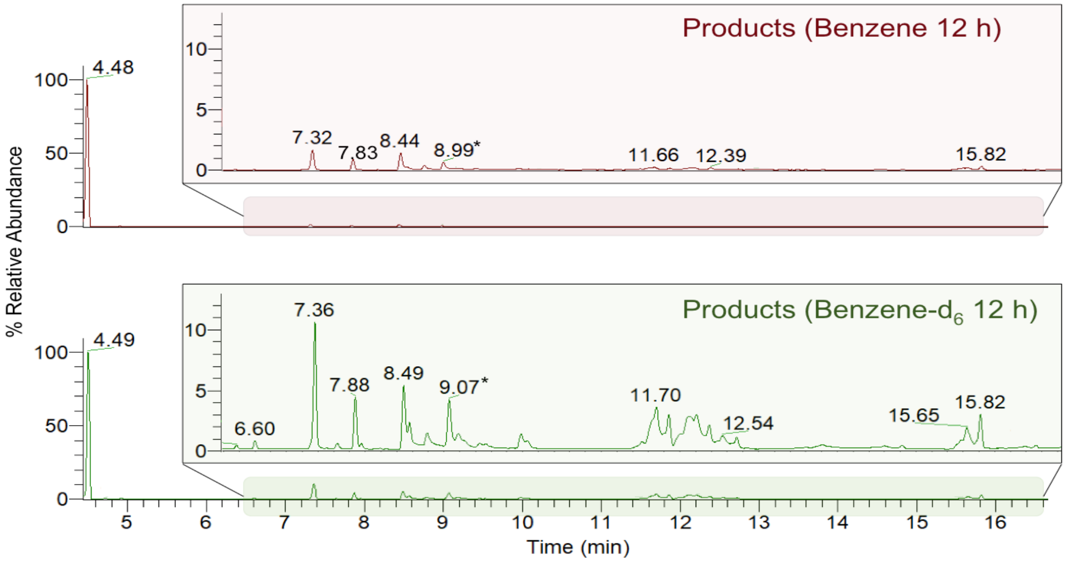

Figure 4.27. GC-MS traces of 2 photooxidation in the benzene (top) and benzene-δ_6 (bottom) mediated by 1. Due to lower conversion of starting material, a zoomed-in view of the products region of each chromatogram is also shown. *Oxidation product of solvent: phenol (top) and phenol-δ_6 (bottom)

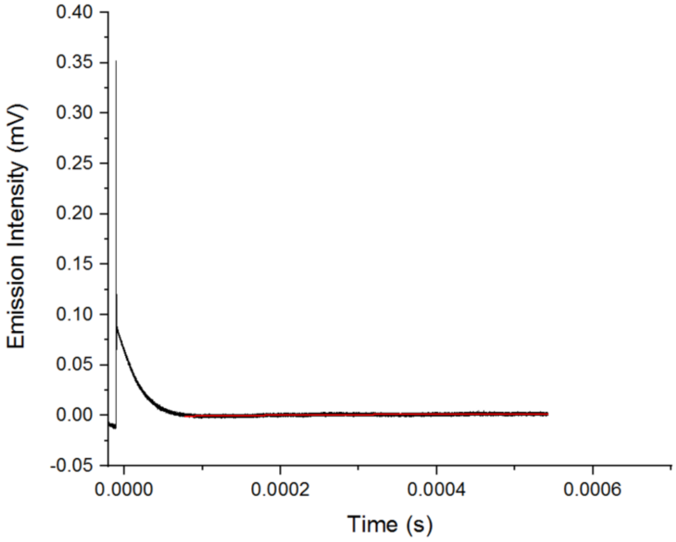

Figure 4.28. Airborne Singlet oxygen decay curve at the outer surface of host **1**. Experimental data (black line) and fitting of the airborne singlet oxygen decay component (red line) are shown. $\tau_{\Delta\text{airborne}}$ was determined by a non-linear least squares curve-fitting procedure in Origin software. All loaded quenchers (pyridine, DMSO, DMA and TMEDA) exhibited similar $\tau_{\Delta\text{airborne}}$ lifetimes.

4.6 REFERENCES

1. Geer, M. F.; Walla, M. D.; Solntsev, K. M.; Strassert, C. Shimizu, L. S. *J. Org. Chem.* **2013**, *78*, 5568-5578.
2. Dewal, M. B; Xu, Y.; Yang, J.; Mohammed, F.; Smith, M. D.; Shimizu, L. S. *Chem. Commun*. **2008**, *0*, 3909-3911.
3. DeRosa, M.; Crutchley, R. *Coord. Chem. Rev.* **2002**, *233,* 351-371.
4. Kim, H.; Kim, W.; Mackeyev, Y.; Lee, G-S.; Kim, H-J.; Tachikawa, T.; Hong, S.; Lee, S.; Kim, J.; Wilson, L. J.; Majima, T.; Alvarez, P. J. J.; Choi, W.; Lee, J. *Environ. Sci. Technol.* **2012**, *46* (17), 9606–9613.
5. Ogilby, P. R. *Chem. Soc. Rev.* **2010**, *39*, 3181-3209.
6. Dabrowski, J. M. *Adv. Inorg. Chem.* **2017**, *70*, 343-394.
7. Ghogare, A. A.; Greer, A. *Chem. Rev.* **2016**, 116, 9994-10034.
8. Baptista, M. S.; Cadet, J.; Di Mascio, P; Ghogare, A. A.; Greer, A.; Hamblin, M. R.; Lorente, C.; Nunez, S. C.; Ribeiro, M. S.; Thomas, A. H.; Vignoni, M.; Yoshimura, T. M. *Photochem. Photobiol.* **2017**, *93*, 912-919.
9. Hayyan, M.; Hashim, M. A.; AlNashef, I. M. *Chem. Rev.* **2016**, *116*, 3029-3085.
10. Lee-Ruff, E. *Chem. Soc. Rev.* **1977**, *6*, 195-214.
11. Kautsky, H.; de Bruijin, H.; Neuwirth, R.; Baumeister, W. *Ber. Dtsch. Chem. Ges.* **1933**, *66B*, 1588-1600.
12. Greer, A. *Acc. Chem. Res.* **2006**, *39*, 797– 804.
13. Foote, C. S.; Wexler, S. *J. Am. Chem. Soc.* **1964**, *86*, 3879-3880.

14. Wiegand, C.; Herdtweck, E.; Bach, T. *Chem. Commun.* **2012**, *48*, 10195-10197.
15. Malek, B.; Fang, W.; Abramova, I.; Walalawela, N.; Ghogare, A. A.; Greer, A. *J. Org. Chem.* **2016**, *81*, 6395-6401.
16. Natarajan, A.; Kaanumalle, L. S.; Jockusch, S.; Gibb, C. L. D.; Gibb, B. C.; Turro, N. J.; Ramamurthy, V. *J. Am. Chem. Soc.* **2007**, *129*, 4132-4133.
17. Chen, Y-. Z.; Wang, Z. U.; Wang, H.; Lu, J.; Yu, S-. H.; Jiang, H-. L. *J. Am. Chem. Soc.* **2017**, *139*, 2035-2044.
18. DeHaven, B. A.; Tokarski, J. T.; Korous, A. A.; Mentink-Vigier, F.; Makris, T. M.; Brugh, A. M.; Forbes, M. D. E.; van Tol, J.; Bowers, C. R.; Shimizu, L. S. *Chem. Eur. J.* **2017**, *23,* 8315 -8319.
19. McDowell, M. S.; Bakac, A.; Espenson, J. H. *Inorg. Chem.* **1983**, *22*, 847-848.
20. Sun, G.; Hong, K. H. *Text. Res. J.* **2013**, *83*, 532-542.
21. Nosaka, Y.; Nosaka, A. Y. *Chem. Rev.* **2017**, *117*, 11302-11336.
22. He, W.; Liu, Y.; Wamer, W. G.; Yin, J. –J. *J. Food Drug Anal.* **2014**, *22*, 49-63.
23. Nardi, G.; Manet, I.; Monti, S.; Miranda, M. A.; Lhiaubet-Vallet V. *Free Radic. Biol. Med.* **2014**, *77*, 64-70.
24. Buettner, G. R. *Free Radic. Biol. Med.* **1987**, *3*, 259-303.
25. Zang, L. –Y. and Misra, H. P. *J. Biol. Chem.* **1992**, *267*, 23601-23608.
26. Harbour, J. R. and Hair, M. L *J. Phys. Chem.* **1978**, *82*, 1297-1399.
27. Roberts, J. L. and Sawyer, D. T. *J. Am. Chem. Soc.* **1981**, *103*, 712-714.

28. Schmidt, R.; Tanielian, C.; Dunsbach, R.; Wolff, C. *J. Photochem. Photobiol.* **1994**, *79*, 11-17.
29. Wu, H.; Song, Q.; Ran, G.; Lu, X.; Xu, B. *Trends Anal. Chem.* **2011**, *30*, 133-141.
30. Turro, N. J.; Chow, M. –F.; Rigaudy, J. *J. Am. Chem. Soc.* **1981**, *103*, 7218-7224.
31. Ogunsipe, A.; Maree, D.; Nyokong, T. *J. Mol. Struct.* **2003**, *650*, 131-140.
32. Borah, P.; Sreejith, S.; Anees, P.; Menon, N. V.; Kang, Y.; Ajayaghosh, A.; Zhao, Y. *Sci. Adv.* **2015**, *1*, 1-8.
33. Wasserman, H. H.; Larsen, D. L. *Chem. Commun.* **1972**, *5*, 253-254.
34. Wasserman, H. H.; Wiberg, K. B.; Larsen, D. L.; Parr, J. *J. Org. Chem.* **2005**, *70*, 105-109.
35. Schweitzer, C.; Schmidt, R. *Chem. Rev.* **2003**, *103*,1685-1757.
36. Bregnhøj, M.; Westberg, M.; Jensen, F.; Ogilby, P. R. *Phys. Chem. Chem. Phys.* **2016**, *18*, 22946-22961.
37. Gorman, A. A.; Hamblett, I.; Lambert, C.; Spencer, B.; Standen, M. C. *J. Am. Chem. Soc.* **1998**, *110*, 8053-8059.
38. Liang, J. –J.; Gu, C. –L.; Kacher, M. L.; Foote, C. S. *J. Am. Chem. Soc.* **1983**, *105*, 4717-4721.
39. Wilkinson, F.; Helman, W. P.; Ross, A. B. *J. Phys. Chem. Ref. Data* **1995**, *24*, 663-1021.

40. Zhang, D.; Gao, R.; Afzal, S.; Vargas,M.; Sharma, S.; McCurdy, A.; Yousufuddin, M.; Stewart, T.; Bau, R.; Selke, M. *Org. Lett.* **2006**, *8*, 5125-5128.
41. Ho, D. G.; Gao, R.; Celaje, J.; Chung, H.-Y.; Selke, M. *Science* **2003**, *302*, 259-262.
42. Gao, R.; Ho, D. G.; Dong, T.; Khuu, D.; Franco, N. Sezer, O.; Selke, M. *Org. Lett.* **2001**, *3*, 3719-3722
43. Bartusik, D.; Aebisher, D.; Lyons, A. M.; Greer, A. *Environ. Sci. Technol.* **2012**, *46*, 12098-12104.
44. Ramamurthy, V. *Acc. Chem. Res.* **2015**, *48*, 2904-2917.
45. Chavan, S. A.; Maes, W.; Gevers, L. E. M.; Wahlen, J.; Vankelecom, I. F. J.; Jacobs, P. A.; Dehaen, W.; De Vos, D. E. *Chem. Eur. J.* **2005**, *11*, 6754-6762.
46. Chen, Y. –Z.; Wu, L. –Z.; Zhang, L. –P.; Tung, C. –H.; *J. Org. Chem.* **2005**, *70*, 4676-4681.
47. Gupta, S.; Ramamurthy, V. *ChemPhotoChem* **2018**, *2*, 655-666.
48. Bellucci, G.; Chiappe, C.; Marioni, F. *Bioorganic Med. Chem. Lett.* **1991**, *1*, 121-124.
49. Peter, S.; Kinne, M.; Ullrich, R.; Kayser, G.; Hofrichter, M. *Enzyme Microb. Technol.* **2013**, *52*, 370-376.
50. Poon, T. H. W.; Pringle, K.; Foote, C. S. *J. Am. Chem. Soc.* **1995**, *117*, 7611-7618.

51. Roiban, G. –D.; Agudo, R.; Reetz, M. T. *Tetradhedron* **2013**, *69*, 5306-5311.
52. Mao, J.; Hu, X.; Li, H.; Sun, Y.; Wang, C.; Chen, Z. *Green Chem.* **2008**, *10*, 837-831.
53. Finkelstein, E.; Rosen, G. M.; Rauckman, E. J. *Arch. Biochem. Biophys.* **1980**, *200* (01), 1-16.
54. de Andrade, V. S. C. and de Mattos, M. C. S. *Synthesis* **2016**, 48 (09), 1381-1388.

APPENDIX A

SYNTHESIS OF DIBROMONAPTHALENE TETRACARBOXYLIC DIANHYDRIDE AND PYRIDONE BINDING SITE

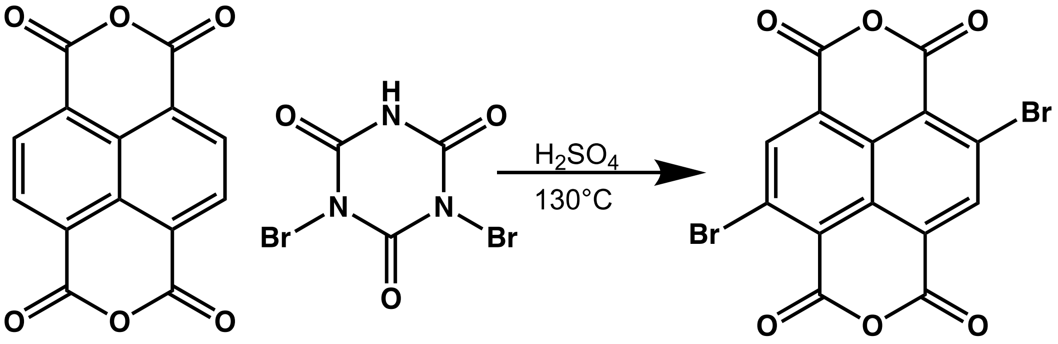

Synthesis of 4,9-dibromoisochromeno[6,5,4-*def*]isochromene-1,3,6,8-tetraone (X): A suspension of dibromoisocyanuric acid (10.4519g, 36.45 mmol) in sulfuric acid (40 mL) was added drop-wise to a stirring suspension of 1,4,5,8-naphthalenetetra-carboxylic dianhydride (5.0856 g, 18.96 mmol) in concentrated sulfuric acid (40 mL) over 45 minutes. The mixture was stirred at room temperature for 15 minutes then heated to 130 ° C and was stirred for 16 hours. The hot mixture was then poured into ice water (800 mL) and the resulting yellow precipitate was filtered and washed with acetone (250 mL), methanol (250 mL), and water (250 mL). The pale-yellow product was dried under vacuum (2.202 g, 27.13%). ^{1}H-NMR: (300 MHz; DMSO) δ=8.79 (2H, s). ESI-MS $[M + H]^+$ 423.8213.

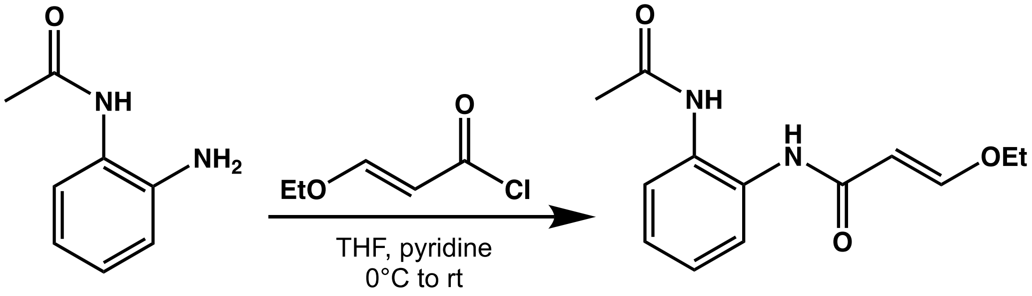

Synthesis of (*E*)-*N*- (2-acetamidophenyl)-3-ethoxyacrylamide (XI): A 25 mL round bottom flask was charged with o-acetylaminoaniline (517.9 mg, 3.45 mmol), THF (3.0 mL), and pyridine (0.443 mL, 5.42 mmol). The flask was placed in an ice-bath and stirred for five minutes to allow the solution to cool. Next, ethoxyacryloyl chloride (730.4 mg, 5.42 mmol) was added drop-wise keeping the temperature between 0-5 °C. The mixture was then warmed to room temperature and was stirred for 3 hours. The round bottom was then placed in an ice bath and the pH was adjusted to 5 with HCl (1N). Next, the mixture was diluted with DI-water (3.0 mL) and the THF was removed in vacuo. The remaining slurry was diluted with toluene (2.5 mL) and was stirred at room temperature for 15 minutes and was then placed in and ice-bath and was stirred at 0°C for one hour. The resulting solid was then collected via vacuum filtration and was washed with DI water (2x75 mL) and was then recrystallized in ethyl acetate and methanol to afford **XI** (559.9 mg, 66%) as white crystals. ^{1}H NMR (DMSO): δ = 1.28 (t, 3H, *J*=6.9), 2.06 (s, 3H), 3.96 (q, 2H, *J*=7.2), 5.61 (d, 1H, *J*=12.3), 7.11 (m, 2H), 7.49 (t, 1H, *J*= 4.8), 7.53 (s, 1H), 7.65 (dd, 1H, *J*= 1.8, 1.5), 9.13 (s, 1H), 9.39 (s, 1H). ESI-MS $[M + H]^+$ 248.

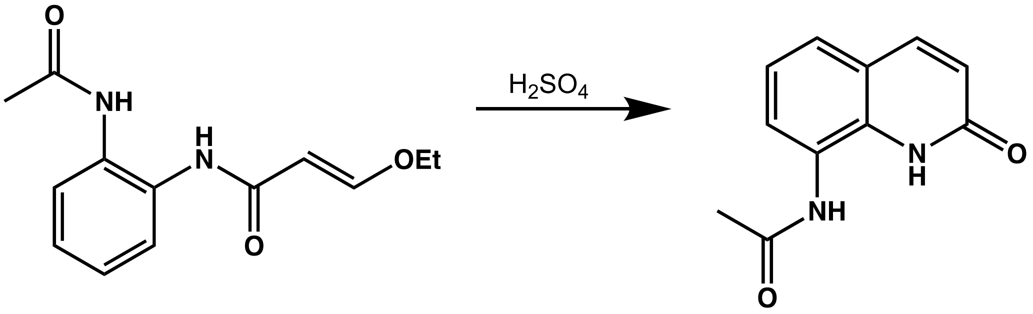

Synthethis of *N*-(2-oxo-1,2-dihydroquinolin-8-yl) acetamide (XII): XI (555.0 mg, 2.24 mmol) was slowly added to stirring sulfuric acid (5.0 mL) and was stirred and room temperature for 2.5 hours. The mixture was then precipitated into ice water (200 mL). Once the ice melted, the precipitate was collected via vacuum filtration and was washed with DI water (3 x 10 mL). The white solid was then dried under vacuum to afford **XII** as a white feathery product (249 mg, 55 %). ^{1}H NMR (DMSO): δ = 2.12 (s, 3H), 6.52 (d, 1H, *J*=8.7), 7.16 (t, 1H, *J*=7.5), 7.50 (d, 1H, *J*=7.2), 7.63 (d, 1H, *J*= 6.6), 7.93 (d, 1H, *J*=9.3), 9.52 (s, 1H), 11.05 (s, 1H). ESI-MS $[M + H]^+$ 202.

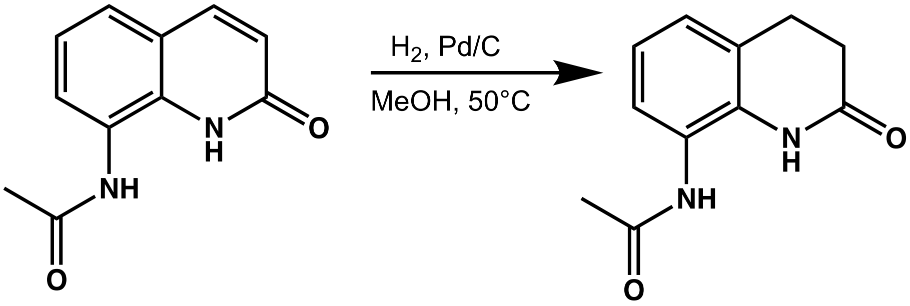

Synthesis of *N*-(2-oxo-1,2,3,4-tetrahydroquinolin-8-yl) acetamide (XIII): Crude **XII** (249.0 mg, 1.23 mmol) was placed in a 2-neck round bottom flask and methanol (15.0 mL) was added. The resulting mixture was sparged with Nitrogen for three minutes and then was charged with 10% Pd/C (140.4 mg, 1.32 mmol). The flask was then equipped with a balloon containing Hydrogen gas and the RBF was then sparged with Argon for 3 minutes before the balloon was opened to the system. Slowly the flask was heated to 50 °C until the absorption of hydrogen had ceased (20 hours). The system was closed off to the hydrogen balloon and was then purged with Nitrogen for five minutes before the balloon was removed. The solution was then filtered through a PTFE filter to remove the Pd/C catalyst and the resulting solution was concentrated under vacuum to a **XIII** as a white powder (238.7 mg, 95%). ^{1}H NMR (DMSO): δ = 2.06 (s, 3H) 2.45 (comp, 2H), 2.89 (t, 2H, *J*=7.8), 6.91 (t, 1H, *J*=7.8), 7.01 (d, 1H, *J*=6.9), 7.27 (d, 1H, *J*= 7.5), 9.35 (d, 2H, *J*=7.5).

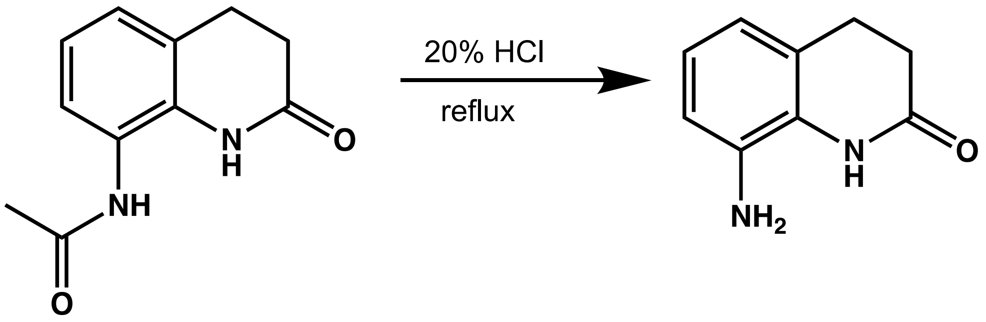

Synthesis of 8-amino-3,4-dihydroquinolin-2(1*H*)-one (XIV): A mixture of **XIII** (238.7 mg, 1.47 mmol) and 20% HCl (3.0 mL) was heated under reflux for one hour. The reaction mixture was cooled, poured onto ice water, and neutralized with 1 N NaOH. The product was extracted with ethyl acetate (3x150 mL), washed with water (2x100 mL), and dried with $MgSO_4$. The organic layer was then concentrated in vacuo. The resulting product was recrystallized with ethanol to produce brass needle-like crystals (70 mg, 37%). The crystals were submitted for XRD, and the structure was solved by by Mark Smith. ^{1}H NMR

(DMSO): δ = 2.39 (t, 2H, *J*=7.2), 2.77 (t, 2H, *J*=7.2), 5.01 (s, 2H), 6.41 (d, 1H, *J*=6.6), 6.52 (d, 1H, *J*= 7.5), 6.66 (t, 1H, *J*=7.2), 9.28 (s, 1H).

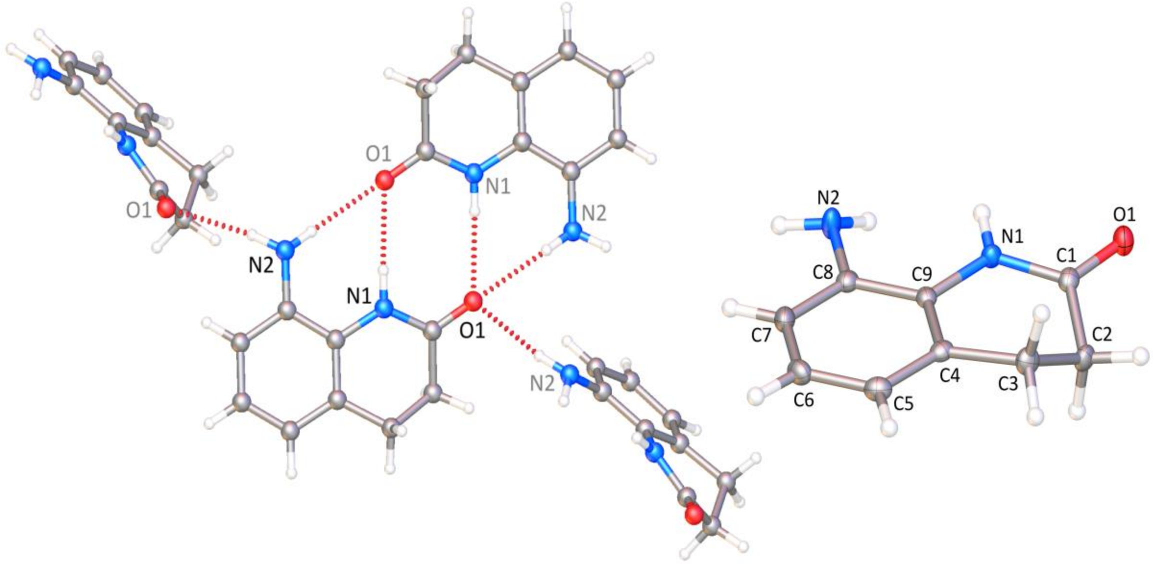

SC-XRD of 8-amino-3,4-dihydroquinolin-2(1*H*)-one (XIV): The compound crystallized as rough-textured bundles of needle crystals, from which a fragment suitable for data collection was cleaved apart. X-ray intensity data were collected at 100(2) K using a Bruker D8 QUEST diffractometer equipped with a PHOTON 100 CMOS area detector and an Incoatec microfocus source (Mo Ka radiation, l = 0.71073 Å).1 The raw area detector data frames were reduced, scaled and corrected for absorption effects using the SAINT+ and SADABS programs.1 Final unit cell parameters were determined by least-squares refinement of 7325 reflections taken from the data set. The structure was solved by direct methods with SHELXT.2 Subsequent difference Fourier calculations and full-matrix least-squares refinement against F2 were performed with SHELXL-20142 using OLEX2.3

The compound crystallizes in the monoclinic system. The pattern of systematic absences in the intensity data was consistent with the space group P21/n, which was verified by structure solution. The asymmetric unit consists of one unique molecule. Non-hydrogen atoms were refined with anisotropic displacement parameters. Hydrogen atoms were located in difference maps and refined freely. The largest residual electron density peak in the final difference map was 0.30 e-/Å3, located 0.70 Å from C4.

Identification code	BD_XIV
Empirical formula	$C_9H_{10}N_2O$
Formula weight	162.19
Temperature/K	100(2)
Crystal system	monoclinic
Space group	$P2_1/n$
a/Å	10.1403(7)
b/Å	5.6192(4)
c/Å	13.6897(9)
α/°	90
β/°	101.135(2)
γ/°	90
Volume/Å^3	765.36(9)

Z	4
ρ_{calc}g/cm^3	1.408
μ/mm^{-1}	0.095
F(000)	344.0
Crystal size/mm^3	0.2 × 0.14 × 0.08
Radiation	MoKα (λ = 0.71073)
2Θ range for data collection/°	4.6 to 55.116
Index ranges	$-13 \leq h \leq 13$, $-6 \leq k \leq 7$, $-17 \leq l \leq 17$
Reflections collected	23034
Independent reflections	1759 [R_{int} = 0.0590, R_{sigma} = 0.0211]
Data/restraints/parameters	1759/0/150
Goodness-of-fit on F^2	1.088
Final R indexes[I>=2σ (I)]	R_1 = 0.0407, wR_2 = 0.0874
Final R indexes [all data]	R_1 = 0.0510, wR_2 = 0.0914
Largest diff. peak/hole / e Å-3	0.30/-0.19

APPENDIX B

SC-XRD OF HOST 1 CRYSTALLIZED FROM PROPYLENE CARBONATE

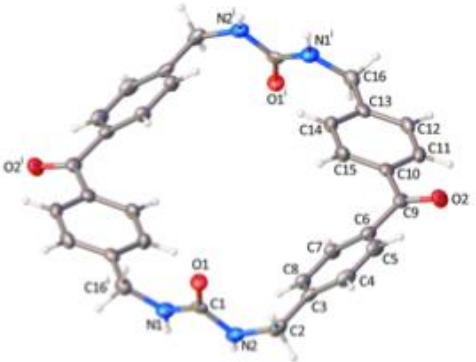

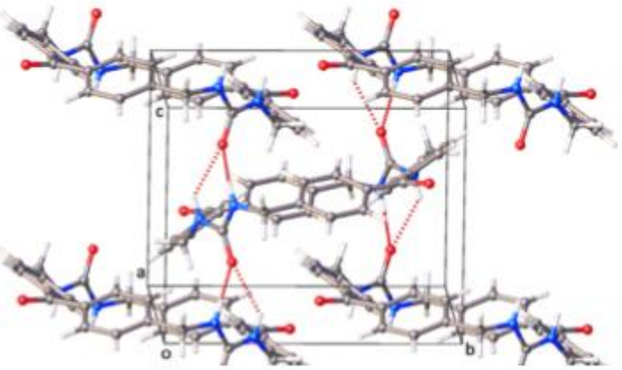

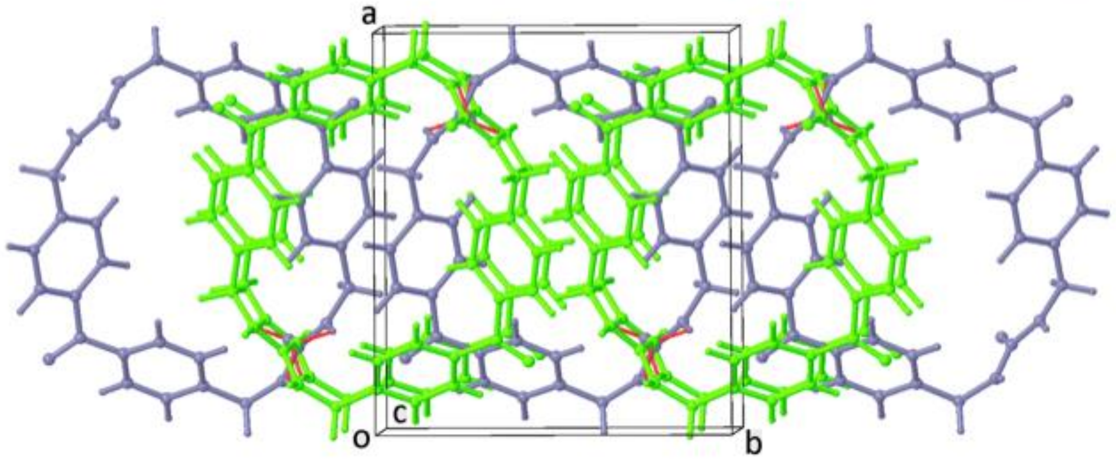

X-ray intensity data from a colorless plate crystal were collected at 100(2) K using a Bruker D8 QUEST diffractometer equipped with a PHOTON 100 CMOS area detector and an Incoatec microfocus source (Mo Ka radiation, l = 0.71073 Å).[1] The raw area detector data frames were reduced and corrected for absorption effects using the SAINT+ and SADABS programs.[1] Final unit cell parameters were determined by least-squares refinement of 9970 reflections taken from the data set. The structure was solved by direct methods with SHELXT.[2] Subsequent difference Fourier calculations and full-matrix least-squares refinement against F^2 were performed with SHELXL-2014[2] using OLEX2.[3]

The compound crystallizes in the monoclinic system. The pattern of systematic absences in the intensity data was consistent with the space group $P2_1/c$, which was confirmed by structure solution. The asymmetric unit consists of half of one molecule, which is located on a crystallographic inversion center. All non-hydrogen atoms were refined with anisotropic displacement parameters. Hydrogen atoms bonded to carbon were located in difference maps before being included as riding atoms with refined isotropic displacement parameters. Hydrogen atoms bonded to nitrogen were located in difference maps and refined freely. The largest residual electron density peak in the final difference map is 0.28 $e^-/Å^3$, located 0.71 Å from C6.

Identification code	BDHost1PC
Empirical formula	$C_{32}H_{28}N_4O_4$
Formula weight	532.58
Temperature/K	100(2)
Crystal system	monoclinic
Space group	$P2_1/c$
a/Å	12.7548(6)
b/Å	11.2321(5)
c/Å	9.1540(4)

α/°	90
β/°	94.021(2)
γ/°	90
Volume/Å^3	1308.20(10)
Z	2
ρ_{calc}g/cm^3	1.352
μ/mm^{-1}	0.091
F(000)	560.0
Crystal size/mm^3	0.22 × 0.08 × 0.02
Radiation	MoKα (λ = 0.71073)
2Θ range for data collection/°	4.838 to 52.822
Index ranges	$-15 \le h \le 15$, $-14 \le k \le 14$, $-11 \le l \le 10$
Reflections collected	46495
Independent reflections	2679 [R_{int} = 0.0476, R_{sigma} = 0.0148]
Data/restraints/parameters	2679/0/202
Goodness-of-fit on F^2	1.025
Final R indexes [I>=2σ (I)]	R_1 = 0.0334, wR_2 = 0.0833
Final R indexes [all data]	R_1 = 0.0425, wR_2 = 0.0885
Largest diff. peak/hole / e Å^{-3}	0.28/-0.19

APPENDIX C

PERMISSION TO REPRINT: CHAPTER 1

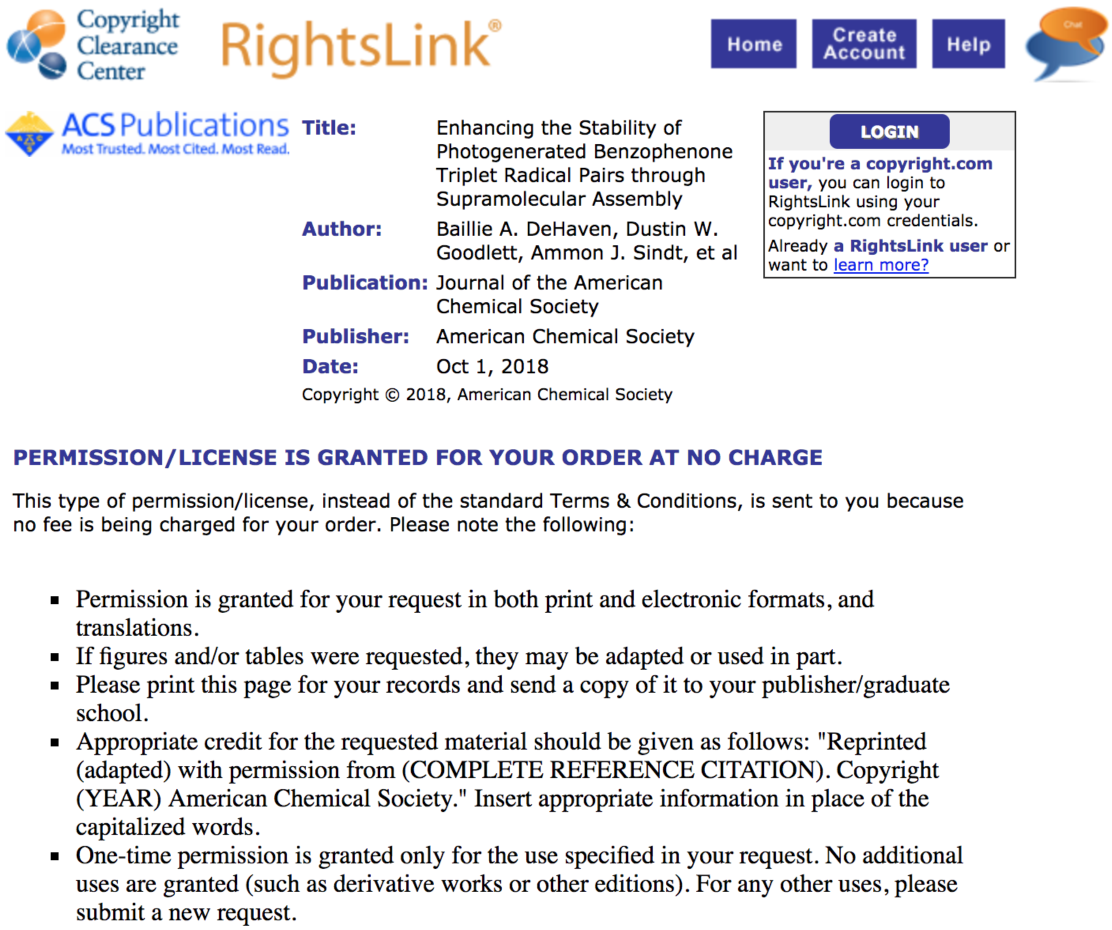

Title: Enhancing the Stability of Photogenerated Benzophenone Triplet Radical Pairs through Supramolecular Assembly

Author: Baillie A. DeHaven, Dustin W. Goodlett, Ammon J. Sindt, et al

Publication: Journal of the American Chemical Society

Publisher: American Chemical Society

Date: Oct 1, 2018

Copyright © 2018, American Chemical Society

If you're a copyright.com user, you can login to RightsLink using your copyright.com credentials.

Already **a RightsLink user** or want to learn more?

PERMISSION/LICENSE IS GRANTED FOR YOUR ORDER AT NO CHARGE

This type of permission/license, instead of the standard Terms & Conditions, is sent to you because no fee is being charged for your order. Please note the following:

- Permission is granted for your request in both print and electronic formats, and translations.
- If figures and/or tables were requested, they may be adapted or used in part.
- Please print this page for your records and send a copy of it to your publisher/graduate school.
- Appropriate credit for the requested material should be given as follows: "Reprinted (adapted) with permission from (COMPLETE REFERENCE CITATION). Copyright (YEAR) American Chemical Society." Insert appropriate information in place of the capitalized words.
- One-time permission is granted only for the use specified in your request. No additional uses are granted (such as derivative works or other editions). For any other uses, please submit a new request.

APPENDIX D

PERMISSION TO REPRINT: CHAPTER 2

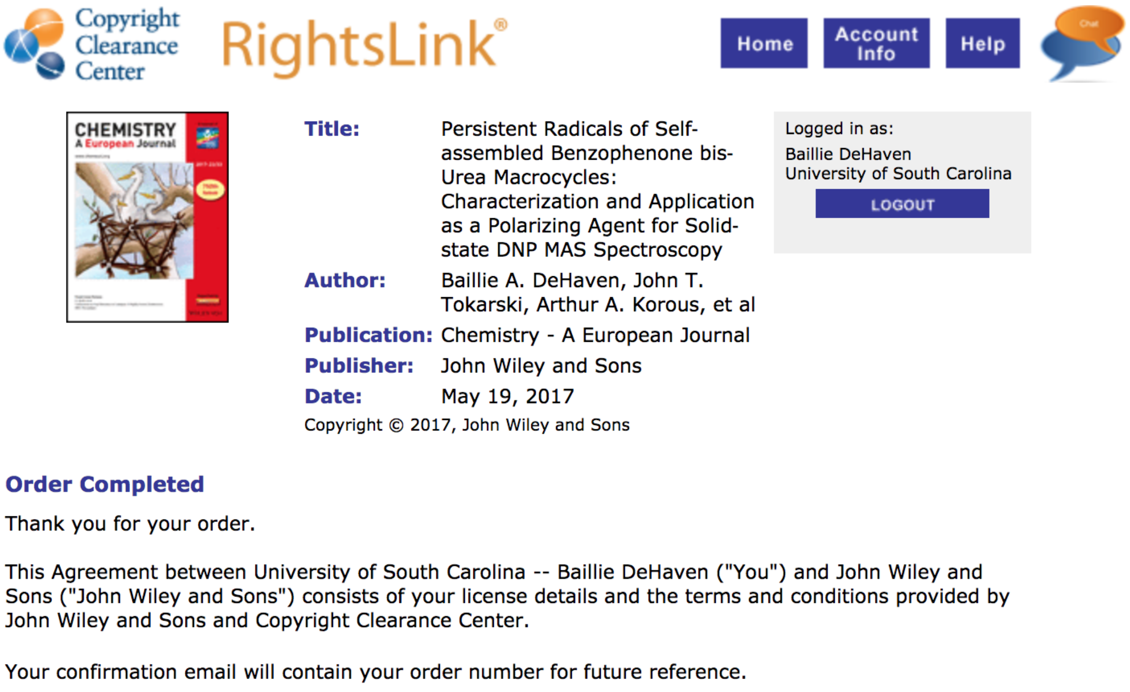

Title: Persistent Radicals of Self-assembled Benzophenone bis-Urea Macrocycles: Characterization and Application as a Polarizing Agent for Solid-state DNP MAS Spectroscopy

Author: Baillie A. DeHaven, John T. Tokarski, Arthur A. Korous, et al

Publication: Chemistry - A European Journal

Publisher: John Wiley and Sons

Date: May 19, 2017

Copyright © 2017, John Wiley and Sons

Logged in as:
Baillie DeHaven
University of South Carolina

Order Completed

Thank you for your order.

This Agreement between University of South Carolina -- Baillie DeHaven ("You") and John Wiley and Sons ("John Wiley and Sons") consists of your license details and the terms and conditions provided by John Wiley and Sons and Copyright Clearance Center.

Your confirmation email will contain your order number for future reference.

printable details

License Number	4460940794077
License date	Nov 02, 2018
Licensed Content Publisher	John Wiley and Sons
Licensed Content Publication	Chemistry - A European Journal
Licensed Content Title	Persistent Radicals of Self-assembled Benzophenone bis-Urea Macrocycles: Characterization and Application as a Polarizing Agent for Solid-state DNP MAS Spectroscopy
Licensed Content Author	Baillie A. DeHaven, John T. Tokarski, Arthur A. Korous, et al
Licensed Content Date	May 19, 2017
Licensed Content Volume	23
Licensed Content Issue	34
Licensed Content Pages	5
Type of use	Dissertation/Thesis
Requestor type	Author of this Wiley article
Format	Print and electronic
Portion	Full article
Will you be translating?	No
Title of your thesis / dissertation	Emergent Properties and applications of self-assembled benzophenone-containing materials
Expected completion date	Dec 2018
Expected size (number of pages)	250
Requestor Location	University of South Carolina 631 SUMTER ST GSRC 109 COLUMBIA, SC 29208 United States Attn: Baillie A DeHaven
Publisher Tax ID	EU826007151
Total	0.00 USD

APPENDIX E

PERMISSION TO REPRINT: CHAPTER 3

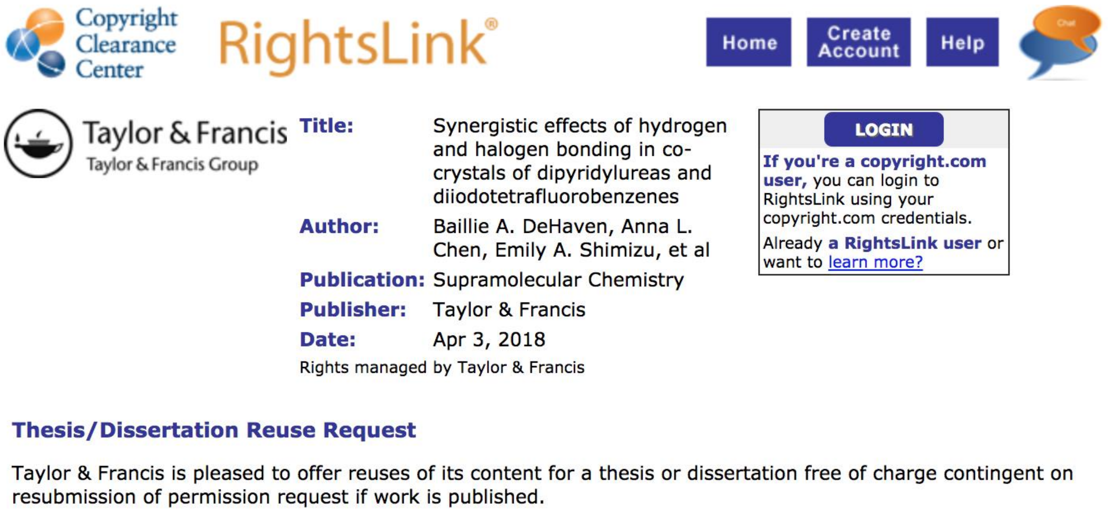

Title: Synergistic effects of hydrogen and halogen bonding in co-crystals of dipyridylureas and diiodotetrafluorobenzenes

Author: Baillie A. DeHaven, Anna L. Chen, Emily A. Shimizu, et al

Publication: Supramolecular Chemistry

Publisher: Taylor & Francis

Date: Apr 3, 2018

Rights managed by Taylor & Francis

If you're a copyright.com user, you can login to RightsLink using your copyright.com credentials.

Already **a RightsLink user** or want to learn more?

Thesis/Dissertation Reuse Request

Taylor & Francis is pleased to offer reuses of its content for a thesis or dissertation free of charge contingent on resubmission of permission request if work is published.